BEARING WORLD

www.bearingworld.org

Journal

Volume 5_2020

Editors: G. Poll _ A. Grunau _ C. Kunze

Published by
FVA sharing drive innovation
VDMA Verlag

Imprint

Bearing World Journal
Volume 5, December 2020

Published by:
Forschungsvereinigung Antriebstechnik e.V. (FVA)
Lyoner Straße 18
60528 Frankfurt am Main
Germany
www.fva-net.de

© 2020
VDMA Verlag GmbH
Lyoner Straße 18
60528 Frankfurt am Main
Germany
www.vdma-verlag.com

All rights reserved, particularly the right of duplication and disclosure, as well as translation. No part of the work may be reproduced in any form (print, photocopy, microfilm or any other method) without written consent from the publisher or saved, processed, duplicated or disclosed.

Print-ISSN 2513-1753

Volume 5_2020

Dear reader,

Globalization increasingly requires more and more international networking between research and development engineers. In response to this, the German Research Association for Drive Technology (FVA) launched the first Bearing World conference in 2016. With that inaugural meeting, the FVA initiated a very fruitful international dialogue in which researchers and developers from universities and bearing manufacturers came together with users and experts from the industry. The Bearing World conference usually is held every two years; more than 280 experts from 18 countries met at the last Bearing World conference in 2018 in Kaiserslautern, Germany, to share the latest research findings in the world of bearings. The next meeting is expected to take place in 2022.

The Bearing World Journal, which is published annually, serves to foster exchange between international experts during non-conference years by featuring peer-reviewed, high-quality scientific papers on rolling element bearings as well as plain bearings. As an international expert platform for publishing cutting-edge research findings, the journal intends to contribute to technological progress in the field of bearings.

We are now starting to prepare the 2021 edition of Bearing World Journal and are looking forward to new contributions from the scientific and industrial communities. We would like to thank all authors for their fascinating contributions to Bearing World Journal No. 5.

_ **Prof. Dr.-Ing. Gerhard Poll,** Initiator, Head of international Scientific Board
_ **Dr.-Ing. Arbogast Grunau,** President of the FVA Management Board
_ **Christian Kunze,** Editor-in-chief

Please send the paper you intend to publish in the next issue of the Bearing World Journal via e-mail as Word document to FVA (**submission@bearingworld.org**). In addition please attach a PDF document.

Bearing World Scientific Board

Scott Bair, Georgia Institute of Technology, USA
Prof. Harry Bhadeshia, University of Cambrigde, Great Britain
Prof. Stefan Björklund, KTH Royal Institute of Technology, Stockholm, Sweden
Prof. Benyebka Bou-Said, Institut National Des Sciences Appliquées (INSA) Lyon, France
Prof. Ludger Deters, TU Magdeburg, Germany
Prof. Duncan Dowson, University of Leeds, Great Britain (†)
Prof. Rob Dwyer-Joyce, University of Sheffield, Great Britain
Prof. Michel Fillon, Université de Poitiers, France
Prof. Sergei Glavastkih, KTH Royal Institute of Technology, Stockholm, Sweden
Prof. Irina Goryacheva, Russian Academy of Sciences, Russia
Prof. Feng Guo, Qingdao Technological University, China
Prof. Martin Hartl, Brno University of Technology, Czech Republic
Prof. Stathis Ioannides, Imperial College London, Great Britain
Prof. Georg Jacobs, RWTH Aachen University, Germany
Prof. Motohiro Kaneta, Brno University of Technology, Czech Republic
Prof. Michael M. Khonsari, Louisiana State University, USA
Prof. Ivan Krupka, Brno University of Technology, Czech Republic
Prof. Roland Larsson, Luleå University of Technology, Sweden
Prof. Antonius Lubrecht, Institut National Des Sciences Appliquées (INSA) Lyon, France
Prof. Piet Lugt, SKF Nieuwegin; University of Twente, Enschede, Netherlands
Prof. Jianbin Luo, State Key Laboratory of Tribology, Tsinghua University, China
Prof. Guillermo Morales-Espejel, INSA Lyon, France
Prof. Anne Neville, University of Leeds, Great Britain
Prof. Hiroyuki Ohta, Nagaoka University of Technology, Japan
Prof. Gerhard Poll, Leibniz University Hanover, Germany
Prof. Martin Priest, University of Bradford, Great Britain
Prof. Farshid Sadeghi, Purdue University, Lafayette, Indiana, USA
Prof. Richard Salant, Georgia Institute of Technology, USA
Prof. Bernd Sauer, TU Kaiserslautern, Germany
Prof. Ian Sherrington, University of Central Lancashire, Great Britain
Prof. Hugh Spikes, Imperial College London, Great Britain
Prof. Gwidon Stachowiak, Curtin University Australia, Australia
Prof. Kees Venner, University of Twente, Enschede, Netherlands
Prof. Philippe Vergne, Institut National Des Sciences Appliquées (INSA) Lyon, France
Prof. Fabrice Ville, Institut National Des Sciences Appliquées (INSA) Lyon, France
Prof. Sandro Wartzack, Friedrich-Alexander-University Erlangen-Nürnberg, Germany
Prof. John A. Williams, University of Cambridge, Great Britain
Prof. Hans-Werner Zoch, IWT Stiftung Institut für Werkstofftechnik, Bremen, Germany

Contents

Simulation Based Design of an Intelligent Hybrid Plain Bearing for Forming Machines
Clément Eberhardt, Fraunhofer Institute for Machine Tools and Forming Technology, Chemnitz, Germany 7

Calculation Method to Evaluate the Risk of WEC Occurrence in Industrial Applications Dirk-Olaf Leimann, Belgium 19

Enhancement of the Insulation Properties of Thermally Sprayed Ceramic Bearing Coatings
Elisa Burbaum, RWTH Aachen University, Germany 35

Microstructural Analysis of Bearing Steels by a Statistical Nanoindentation Technique
Esteban Broitman, Research and Technology Development, SKF B.V., The Netherlands 47

Influence of Off-Centered Gear Load Distribution on Planetary Bearing Outer Ring Creep
Felix M. Schlüter, RWTH Aachen University, Germany 57

A Fatigue Life Model for Roller Bearings in Oscillatory Applications
Georg Breslau, TU Dresden, Germany 65

The Influence of Mechanical Stresses on the Diffusion and Accumulation of Hydrogen in a Cylindrical Roller Thrust Bearing
Iyas Khader, German Jordanian University, Amman, Jordan 81

Finite Element Analysis of Two-step Deep Rolling of Bearing Steel for Expansion and Equalization of Compressive Residual Stress Profiles
Jürgen Gegner, University of Applied Science Würzburg-Schweinfurt, Germany 93

The Utilization of Production-Related Defects for Improving Operating Properties of Journal Bearings
Lars Friedrich, Chemnitz University of Technology, Germany 101

Bearing Selection for high Efficiency Worm Gear Drives
Manuel Oehler, Technische Universität Kaiserslautern, Germany 111

Dynamic Simulation of Full Complement Cylindrical Roller Bearings with a Semi-Analytical Roller End-Flange Contact Detection Method
Marius Wolf, Corporate Research, Robert Bosch GmbH Renningen, Germany 123

Surface Mutation of the Bearing Raceway During Electrical Current Passage in Mixed Friction Operation
Simon Graf, Institute of Machine Elements, Gears, and Transmissions (MEGT), Kaiserslautern, Germany 137

Full-Size Test Bench Measurements and Validation of a Novel Conical Sliding Bearing for the Main Shaft of Wind Turbines
Tim Schröder, RWTH Aachen University, Germany 149

Measuring the Kinematic Behavior of the Rolling Elements in a Spindle Bearing under Axial and Radial Loads
Hans-Martin Eckel, RWTH Aachen University, Germany 159

Microinclusions Impact on Steel Balls Fatigue Life
F. Morosi, Tsubaki Nakashima, Italy 169

Simulation Based Design of an Intelligent Hybrid Plain Bearing for Forming Machines

Clément Eberhardt[1], Christian Kraft[2], Robin Kurth[3], Hubert Schwarze[4], Thomas Päßler[5], Markus Bergmann[6], Matthias Putz[7]

[1] *Division Production Systems and Machines, Fraunhofer Institute for Machine Tools and Forming Technology, Clement.Eberhardt@iwu.fraunhofer.de*

[2] *Institute of Tribology and Energy Conversion Machinery, Clausthal University of Technology, Kraft@itr.tu-clausthal.de*

[3] *Division Production Systems and Machines, Fraunhofer Institute for Machine Tools and Forming Technology, Robin.Kurth@iwu.fraunhofer.de*

[4] *Institute of Tribology and Energy Conversion Machinery, Clausthal University of Technology, Schwarze@itr.tu-clausthal.de*

[5] *Division Production Systems and Machines, Fraunhofer Institute for Machine Tools and Forming Technology, Thomas.Paessler@iwu.fraunhofer.de*

[6] *Division Production Systems and Machines, Fraunhofer Institute for Machine Tools and Forming Technology, Markus.Bergmann@iwu.fraunhofer.de*

[7] *Division Production Systems and Machines, Fraunhofer Institute for Machine Tools and Forming Technology, Matthias.Putz@iwu.fraunhofer.de*

Abstract - The replacement of damaged journal bearings in forming machines eventuates in very high personal and material costs as well as long-term downtime. Moreover, new discontinuous forming processes (e.g. press hardening, pendulum operations) have a negative effect on the hydrodynamic pressure built up in the bearing and can lead to failure. Therefore, users and manufacturers of forming presses are looking for ways to improve the safety of this key component. In this paper, a simulation method to design an intelligent hybrid plain bearing (IHPB) and its hydraulics actuators is presented. A substitute model of the bearing composed of lookup tables is derived and integrated in a multiphysics model. An eccentricity control strategy is then developed and tested with a load profile from a deep drawing process. The results show a great potential for the performance of IHPB and its simulations.

Keywords – Hybrid-bearing, active lubrication control, journal bearing wear prevention, journal bearing multiphysics simulation, forming machine

Nomenclature

FEM	Finite element method
HD	Hydrodynamic
HS	Hydrostatic
IHPB	Intelligent hybrid plain bearing
PI	Proportional integral
ST	Steady state
$\dot{A}$, $\ddot{A}$	First and second time derivative of A
C	Damping matrix
C_R	Bearing radial clearance
E	Vector of bearing eccentricity $(\varepsilon_x, \varepsilon_y)$
F_{ext}	External force on the bearing
f_{SV}	Cut frequency of servo-valve
K	Stiffness matrix
m_b	Bearing mass
n	Shaft rotational speed
p_0	Hydrostatic supply pressure
P_{acc}	Maximum pressure of accumulator
P_N	Servo-valve nominal pressure
$P_{HS,i}$	Pressure in HS pocket i
Q_{acc}	Maximum pressure of accumulator
Q_N	Servo-valve nominal flow
$Q_{SV,i}, Q_{TOTAL}$	Volumetric flow through servo-valve i, Total volumetric through the valves
$R_{z,S}, R_{z,B}$	Roughness R_z of shaft and bearing sliding surface
V_{acc}	Volume of accumulator
$W_{t,S}, W_{t,B}$	Waviness W_t of shaft and bearing sliding surface
$y_{SV,i}$	Opening of servo-valve i, [0-1]
ε	Norm of E
$\varepsilon_x, \varepsilon_y$	Bearing eccentricity in x and y direction
$\varepsilon_{\mathrm{lim}}$	Eccentricity threshold for the active lubrication
$\varepsilon_{\mathrm{limOff}}$	Eccentricity switch off threshold for the active lubrication
φ	Bearing attitude angle
Ψ	Relative bearing clearance

1. Introduction

Operating under heavy load and low speed is critical for hydrodynamic journal bearings, but due to their simple manufacturing and low space requirement, they are used under these conditions in a wide range of applications. This bearing type often operates in the mixed friction range and therefore has a high risk of failure. This is particularly true for hydrodynamic journal bearings in mechanical presses where new technology variations (pendulum stroke, drawing with back pull or press hardening etc.) push the bearing further to its limits.

One way to overcome these new challenges is to use hybrid plain bearings. These bearings are fed with pressurized lubricant and are optimized to take advantage of the both working principles: hydrostatic and hydrodynamic [1]. The active control of the lubrication in hybrid bearings by the means of servo-valve was first theoretically considered on tilting pad bearing by Santos in 1994 [2] and then in [3] and [4] with the aim of increasing the damping and stability. The concept showed great results and was experimentally demonstrated in [5] and [6]. In these works, the hybrid behavior of the bearing and the active control are modeled by integrating a system of equations of motion and by solving modified Reynolds' equation at each time step. For high-frequency perturbation, this method demands considerable calculation time, which makes it difficult to add some degree of complexity and for example, take into account the influences of the temperature or the elastic deformations on the bearing or the rotor. As explained in [7], an alternative method is to introduce the "actively lubricated bearing calibration function". This function describes the relationship between the servo-valve input signal and the resultant force over the rotor in the frequency domain. As, in the case for vibrations reduction, the bearing movements are very small, the systems of equations can be linearized. The calibration function is then directly obtained in frequency domain through a harmonic analysis with a significant reduction of the calculation time. In order to model the performance of an actively lubricated hydrostatic plain bearing against perturbation-rejections by means of eccentricity signal and servo-valve, Rehman *et al* [8–11] neglected the hydrodynamic effects and solved the dynamic system in the time domain. When the goal of the active lubrication is to avoid wear and rotor/bearing contact with minimum power use, the hydrodynamic term of the Reynolds' equation is important. Moreover, as the rotor movements in the bearing of forming machine are highly dynamical, a harmonic analysis in a linearized position cannot be performed. More recently, Estupiñan [12] investigated an actively lubricated hybrid plain bearing for reciprocating compressor. The pressurized lubricant is injected through injectors and injections time is determined with the crankshaft position i.e. one injection per cycle and then the bearing works as a purely hydrodynamic one. Wegmann and Gold [13,14] developed an actively lubricated plain bearing for ship propulsion with specifically designed pressure sensitive mechanical valves. In the works of Estupiñan, Wegmann and Gold, the behavior of the active hydrostatic pocket are included in the numerical integration of the Reynolds' equations. Their results show good concordance with experiments. However, the coupling of these models with dynamic multiphysic ones in order to effectively develop the hydrostatic circuit and to design the active control of the IHBP, results in very complex and time intensive simulations.

In this work, a model to simulate the behavior of an intelligent hybrid plain bearing (IHPB), as presented in [15], and support its design is detailed. The IHPB has an active lubrication control based on the eccentricity between the bearing and the shaft. Thanks to a derived substitute model of the bearing and its integration in a dynamic multiphysics model, a control strategy is efficiently elaborated and tested.

2. Design of the IHPB simulation model

The IHPB is a mechatronic system composed of a hybrid bearing, hydraulic actuators for the hydrostatic lubrication, an eccentricity control algorithm and an eccentricity measurement system. This hybrid bearing is able to actively control the optimal pressure and flow rate of high pressure lubricant to prevent mixed lubrication. In order to design the bearing geometry and the active eccentricity control, a multiphysics simulation model is set up and a substitute model of the bearing is integrated in this simulation environment.

2.1 Multiphysics model

First, a simplified hydraulic dynamic model of the hydrostatic circuit is built using MATLAB/SIMULINK.

This circuit is composed of:

- A bladder accumulator, the volume of gas is modelled as ideal and adiabatic
- A servo-valve for each pair of hydrostatic (HS) pockets, modelled with the resistance equation of a control edge and a first order proportional time element (PT1) for the dynamics of the spool

A schematic of the hydraulic circuit used for the simulation model is depicted in Figure 1.

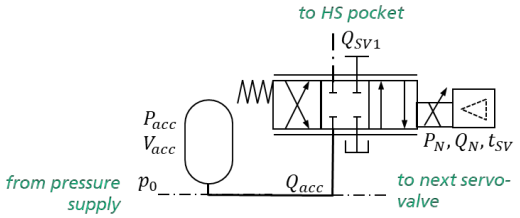

Figure 1: Schematic of the hydraulic HS circuit used. p_0 is the supply pressure, V_{acc} is the accumulator volume, P_{acc} is accumulator volume, Q_{SV1} is the lubricant flow through the servo-valve 1, P_N is the valve nominal pressure, Q_N is the nominal flow and f_{SV} the cut frequency of the valve.

The maximum pressure of the accumulator (or supply pressure) p_0, volume V_{acc} of the accumulator as well as the nominal flow Q_N, nominal pressure P_N and cut frequency of the servo-valves f_{SV} are important parameters for the proper functioning of the IHPB. They are determined thanks to the multiphysics model.

The hydraulic model is then combined with a substitute dynamic model of the hybrid bearing. Because of the strong non-linearity of the bearing dynamic, prior generated lookup tables are used. These tables are coupled with the equation of motion in order to fully describe the behavior of the IHPB. The inputs of the lookup tables are the bearing eccentricity (ε_x, ε_y), the shaft rotational speed (n), and the volumetric flow rate of each pair of HS pockets ($Q_{SV,i}$). Two outputs (or the data in the tables) are the stiffness and damping matrix of the bearing (K and C), which include the stiffness and damping in both x and y directions and the cross coupling terms. The other outputs are the pressures in the bearing HS pockets ($P_{HS,i}$). Finally, the inputs of the substitute model are the flow rates ($Q_{SV,i}$), the rotational speed (n), and the external forces applied on the bearing (F_{ext}). The outputs are the pressures in HS pockets ($P_{HS,i}$) and the bearing eccentricity (ε_x, ε_y). A schematic of the bearing substitute model is presented in Figure 2.

Each time step a new volumetric flow rate through the HS pockets ($Q_{SV,i}$) is calculated using the equation of flow resistance in the servo-valve (Eq. 1) and used as input for the lookup tables.

$$Q_{SV,i} = y_{SV,i} \frac{Q_N}{\sqrt{P_N}} \sqrt{P_{acc} - P_{HS,i}} \qquad (Eq.\ 1)$$

$y_{SV,i}$ is the opening of the valve i. The pressure in the HS pocket i is given by the corresponding lookup table of the bearing substitute model.

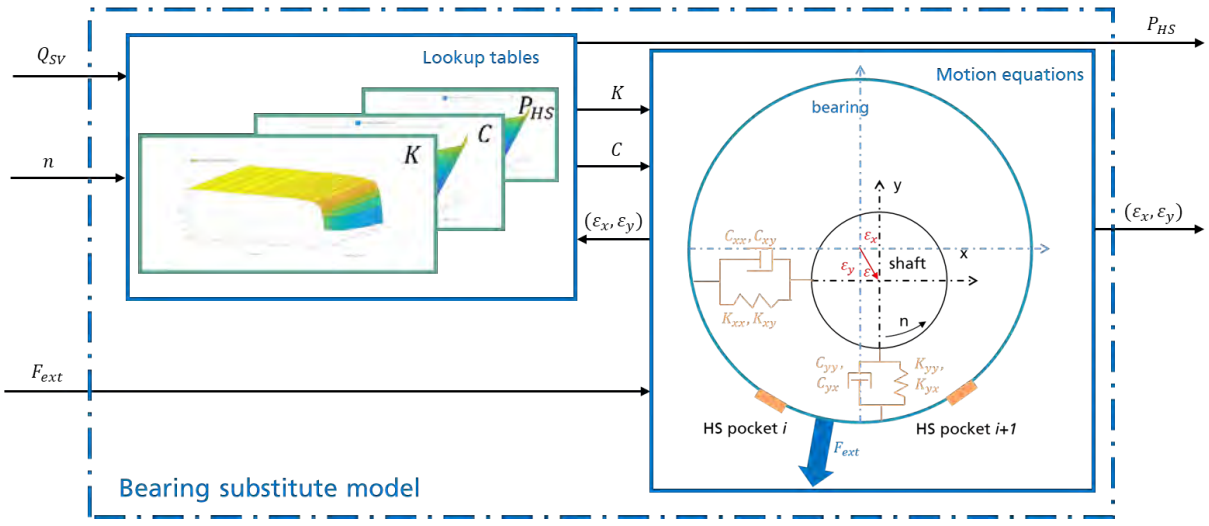

Figure 2: Schematic representation of the bearing substitute model. F_{ext} is the external force applied on the bearing.

Every new positions of the bearing are then deduced from the dynamic equation of motion applied on the bearing (Eq. 2) and used as input for the lookup tables.

$$m_b \cdot \ddot{E} = C \cdot \dot{E} + K \cdot E + \frac{F_{ext}}{C_R} \qquad (Eq.\ 2)$$

m_b is the bearing mass and F_{ext} the extern forces on the bearing. The stiffness matrix K and the damping matrix C are read from the corresponding lookup table of the bearing substitute model, $E, \dot{E}, \ddot{E}$ are the eccentricity vector $(\varepsilon_x, \varepsilon_y)$ and its first and second temporal derivatives.

To complete the model, a bearing eccentricity control is added as presented in Figure 3. In this bloc different control strategies can be implemented and tested. The multiphysics model allows a fast prototyping of control structures and trigger conditions for the active hydrostatic support.

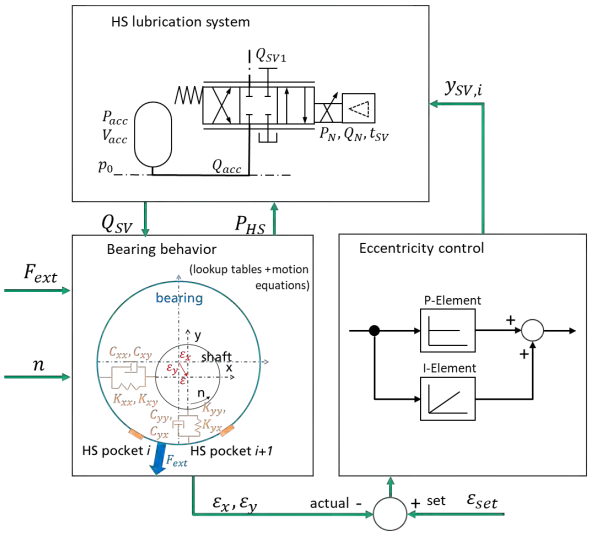

Figure 3: Schematic representation of the intelligent hybrid plain bearing multiphysics mode. . ε_{set} is the set eccentricity of the active eccentricity control and $y_{SV,i}$ is the servo-valve input.

2.2 Derivation of the hybrid bearing lookup tables

To be able to describe the journal bearing behavior and create a lookup table, the operating conditions in the lubricating gap have to be calculated. This is done with the journal bearing calculation program COMBROS R [16]. It enables the non-isothermal calculation of the static and dynamic characteristics of lubricated journal bearings. The basis for describing the flow in the lubricating gap is the solution of the extended Reynolds equation, which can be derived from the Navier-Stokes equations and the continuity equation. With the dimensionless parameters

$$\Pi = \frac{p\, C_R^{\,2}}{(\eta_0\, \omega\, r^2)},\ \varphi = \frac{x}{r},\ \bar{y} = \frac{y}{C_R},\ \bar{z} = \frac{z}{r},$$
$$H = \frac{h}{C_R},\ \eta^* = \frac{\eta}{\eta_0},\ \phi = \omega\, t \qquad \textit{(Eq. 3)}$$

the Reynolds equation can be written as

$$\frac{\partial}{\partial\varphi}\left(\frac{H^3}{12\,\eta^*}\frac{\partial\Pi}{\partial\varphi}\right)+\frac{\partial}{\partial\bar{z}}\left(\frac{H^3}{12\,\eta^*}\frac{\partial\Pi}{\partial\bar{z}}\right)= \frac{1}{2}\,\frac{\partial}{\partial\varphi}(\rho^*\, f_c\, H)+\frac{\partial}{\partial\phi}(\rho^*\, H) \qquad \textit{(Eq. 4)}$$

where ρ* is the relative lubricant density. In the cavitation model used, it is equivalent to the degree of filling [17].

The flow in the lubrication gap is strongly influenced by the thermal conditions. As a result of dissipation due to internal friction, a three-dimensional temperature distribution is formed in the lubricant film. In order to take this into account in the extended Reynolds' differential equation as a result of the Navier Stokes equations, the mean values for the three-dimensional viscosity distribution are calculated using (Eq. 5):

$$\eta_p^* = \frac{1}{12\,\tilde{F}_2},\ f_c = 2\left(1-\frac{\tilde{F}_1}{\tilde{F}_0}\right),\ \tilde{F}_0 = \int_0^1 \frac{d\tilde{y}}{\eta^*},$$
$$\tilde{F}_1 = \int_0^1 \frac{\tilde{y}\ d\tilde{y}}{\eta^*},\ \tilde{F}_2 = \int_0^1 \frac{\tilde{y}}{\eta^*}\left(\tilde{y}-\frac{\tilde{F}_1}{\tilde{F}_0}\right) d\tilde{y}. \qquad \textit{(Eq. 5)}$$

For this purpose, the three-dimensional temperature distribution in the lubricating film must be known, which is determined by the solution of the energy differential equation

$$\frac{1}{\mathrm{Pr}\ \mathrm{Re}_0\,\psi}\left(\psi^2\frac{\partial^2\vartheta}{\partial\varphi^2}+\frac{\partial^2\vartheta}{\partial\bar{y}^2}+\psi^2\frac{\partial^2\vartheta}{\partial\bar{z}^2}\right)+ \eta^* K_t\left\{\left(\frac{\partial\bar{u}}{\partial\bar{y}}\right)^2+\left(\frac{\partial\bar{w}}{\partial\bar{y}}\right)^2\right\}=\bar{u}\frac{\partial\vartheta}{\partial\varphi}+\bar{v}\frac{\partial\vartheta}{\partial\bar{y}}+\bar{w}\frac{\partial\vartheta}{\partial\bar{z}}. \qquad \textit{(Eq. 6)}$$

The influence of the temperature-dependent viscosity, is taken into account using (Eq. 7):

$$\eta = 0{,}18 mPas_1 \cdot \left(\frac{ISOVG\cdot\rho}{\eta_1}\right)^{\left(\frac{159.56\ °C}{\vartheta+95\ °C}-0.18193\right)}. \qquad \textit{(Eq. 7)}$$

More detailed calculation method can be found in [17].

From the field size distributions, which are determined based on of the solutions of the partial differential equations introduced previously, bearing characteristic values can be determined by integration, which characterize the operating behavior of the bearing. The restoring force of the lubricating film due to a static external load is obtained by

integrating the lubricating film pressure, which is the result of the solution of Eq. 4, over the journal surface

$$\begin{pmatrix}\bar{\Pi}_x\\ \bar{\Pi}_y\end{pmatrix}=\begin{pmatrix}\dfrac{1}{4\ B/D}\displaystyle\int_0^{2\pi}\int_0^{2B/D}\Pi\ \sin\varphi\ d\bar{z}\ d\varphi\\ \dfrac{1}{4\ B/D}\displaystyle\int_0^{2\pi}\int_0^{2B/D}\Pi\ \cos\varphi\ d\bar{z}\ d\varphi\end{pmatrix}. \qquad \textit{(Eq. 8)}$$

The additional restoring forces for a bearing load of sufficiently small magnitude that varies over time can be determined with the result of a linear perturbation calculation. For this purpose, the following approximations are made for the temporal change of the gap and the pressure under the condition of rigid walls

$$\begin{aligned}&H(\varphi,\bar{z})=H_{st}(\varphi,\bar{z})-\bar{X}\sin\varphi-\bar{Y}\cos\varphi,\\&\frac{\partial H}{\partial\tau}(\varphi,\bar{z})=-\bar{X}'\sin\varphi-\bar{Y}'\cos\varphi,\\&\Pi(\varphi,\bar{z})=\Pi_{st}(\varphi,\bar{z})+\left(\frac{\partial\Pi}{\partial X}\right)_{st}\bar{X}+\\&\left(\frac{\partial\Pi}{\partial Y}\right)_{st}\bar{Y}+\left(\frac{\partial\Pi}{\partial\bar{X}'}\right)_{st}\bar{X}'+\left(\frac{\partial\Pi}{\partial\bar{Y}'}\right)_{st}\bar{Y}'.\end{aligned} \qquad \textit{(Eq. 9)}$$

Figure 4 shows the dimensional parameters of the linear perturbation calculation.

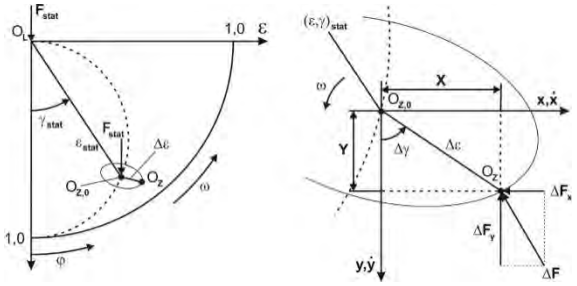

Figure 4: Dimensional quantities of the linear perturbation calculation

By inserting the linear approach of Eq. 9 into the generalized Reynolds differential Eq. 4, the four perturbation equations [18] result, assuming that all other changes are negligibly small:

$$\begin{aligned}&\frac{\partial}{\partial\varphi}\left[\frac{H_{st}^3}{12\eta_p^*}\frac{\partial}{\partial\varphi}\left(\frac{\partial\Pi}{\partial X}\right)_{st}\right]+\frac{\partial}{\partial\bar{z}}\left[\frac{H_{st}^3}{12\eta_p^*K_z}\frac{\partial}{\partial\bar{z}}\left(\frac{\partial\Pi}{\partial X}\right)_{st}\right]=\\&-\frac{1}{2}\frac{\partial}{\partial\varphi}\left(\rho^*f_C\sin\varphi\right)+\frac{\partial}{\partial\varphi}\left[\frac{3H_{st}^2\sin\varphi}{12\eta_p^*}\frac{\partial\Pi_{st}}{\partial\varphi}\right]+\frac{\partial}{\partial\bar{z}}\left[\frac{3H_{st}^2\sin\varphi}{12\eta_p^*}\frac{\partial\Pi_{st}}{\partial\bar{z}}\right],\end{aligned} \qquad \textit{(Eq. 10)}$$

$$\begin{aligned}&\frac{\partial}{\partial\varphi}\left[\frac{H_{st}^3}{12\eta_p^*}\frac{\partial}{\partial\varphi}\left(\frac{\partial\Pi}{\partial Y}\right)_{st}\right]+\frac{\partial}{\partial\bar{z}}\left[\frac{H_{st}^3}{12\eta_p^*}\frac{\partial}{\partial\bar{z}}\left(\frac{\partial\Pi}{\partial Y}\right)_{st}\right]=\\&-\frac{1}{2}\frac{\partial}{\partial\varphi}\left(\rho^*f_C\cos\varphi\right)+\frac{\partial}{\partial\varphi}\left[\frac{3H_{st}^2\cos\varphi}{12\eta_p^*}\frac{\partial\Pi_{st}}{\partial\varphi}\right]+\frac{\partial}{\partial\bar{z}}\left[\frac{3H_{st}^2\cos\varphi}{12\eta_p^*}\frac{\partial\Pi_{st}}{\partial\bar{z}}\right],\end{aligned} \qquad \textit{(Eq. 11)}$$

$$\frac{\partial}{\partial\varphi}\left[\frac{H_{st}^3}{12\eta_p^*}\frac{\partial}{\partial\varphi}\left(\frac{\partial\Pi}{\partial X'}\right)_{st}\right]+\frac{\partial}{\partial\bar{z}}\left[\frac{H_{st}^3}{12\eta_p^*}\frac{\partial}{\partial\bar{z}}\left(\frac{\partial\Pi}{\partial X'}\right)_{st}\right]=-\rho^*\sin\varphi, \qquad \textit{(Eq. 12)}$$

$$\frac{\partial}{\partial\varphi}\left[\frac{H_{st}^3}{12\eta_p^*}\frac{\partial}{\partial\varphi}\left(\frac{\partial\Pi}{\partial Y'}\right)_{st}\right]+\frac{\partial}{\partial\bar{z}}\left[\frac{H_{st}^3}{12\eta_p^*}\frac{\partial}{\partial\bar{z}}\left(\frac{\partial\Pi}{\partial Y'}\right)_{st}\right]=-\rho^*\cos\varphi \qquad \textit{(Eq. 13)}$$

It should be noted that all implicit dependencies of the pressure itself must be linearized and the solution functions of equations 10 to 13 must generally be determined iteratively. This includes, for example, the linear dynamic volume flow balance, which is the basis for the correct formulation of the boundary conditions for the fault equations. By integrating the solution functions over the shaft surface analogous to equation 8, one obtains the four stiffness (γ_{ik}^*) and damping coefficients (β_{ik}^*) according to

$$\begin{aligned}\gamma_{ik}^*&=\frac{1}{4\ B/D}\int_0^{2\pi}\int_0^{2B/D}\left(\frac{\partial\Pi}{\partial q_k}\right)\left((i-1)\cos\varphi-(i-2)\sin\varphi\right)d\bar{z}\ d\varphi,\\\beta_{ik}^*&=\frac{1}{4\ B/D}\int_0^{2\pi}\int_0^{2B/D}\left(\frac{\partial\Pi}{\partial q_{k+2}}\right)\left((i-1)\cos\varphi-(i-2)\sin\varphi\right)d\bar{z}\ d\varphi\end{aligned} \qquad \textit{(Eq. 14)}$$

with $i,k = 1,2$ and $q_n = \bar{X},\ \bar{Y},\ \bar{X}',\ \bar{Y}'$ for $n = 1$ to 4. The dynamic lubricating film restoring force thus results in

$$\begin{pmatrix}\bar{\Pi}_x\\ \bar{\Pi}_y\end{pmatrix}=\begin{pmatrix}\bar{\Pi}_x\\ \bar{\Pi}_y\end{pmatrix}_{st}+\begin{pmatrix}\gamma_{11}^* & \gamma_{12}^*\\ \gamma_{21}^* & \gamma_{22}^*\end{pmatrix}\cdot\begin{pmatrix}\bar{X}\\ \bar{Y}\end{pmatrix}+\begin{pmatrix}\beta_{11}^* & \beta_{12}^*\\ \beta_{21}^* & \beta_{22}^*\end{pmatrix}\cdot \qquad \textit{(Eq. 15)}$$

The dimensional stiffness coefficients follow from this to $K_{ik}=\gamma_{ik}^*\cdot(2\ B\ \eta_0\ \omega)/\psi^3$. The dimensional damping is obtained according to $C_{ik}=\beta_{ik}^*\cdot(2\ B\ \eta_0\ \omega)/(\omega_s\psi^3)$. Detailed descriptions of the perturbation calculation for the extended form of the Reynolds' differential equation can be found in [18–21]. Also all descriptions of the used variables used for the description of hydrodynamics are explained there.

With these model assumptions contained in the journal bearing calculation software COMBROS R [16], it is possible to generate accurate lookup tables of the HS pocket pressures ($P_{HS,i}$) bearing stiffness (K) and

damping matrix (C) of the lubricant film depending on the input values: bearing eccentricity eccentricity (ε_x, ε_y) and shaft rotational speed.

3. Use case: Deep drawing process

To validate the IHPB concept a bearing prototype to be tested on a test rig is designed using the previously described multiphysics model structure.

3.1 Definition of load case and bearing parameters

The test load case is derived from the load profile of the main bearing of an eccentric press connecting rod during a deep drawing forming process. The load and rotational speed of the test case is then downsized (Figure 5) to fit the test rig dimensions.

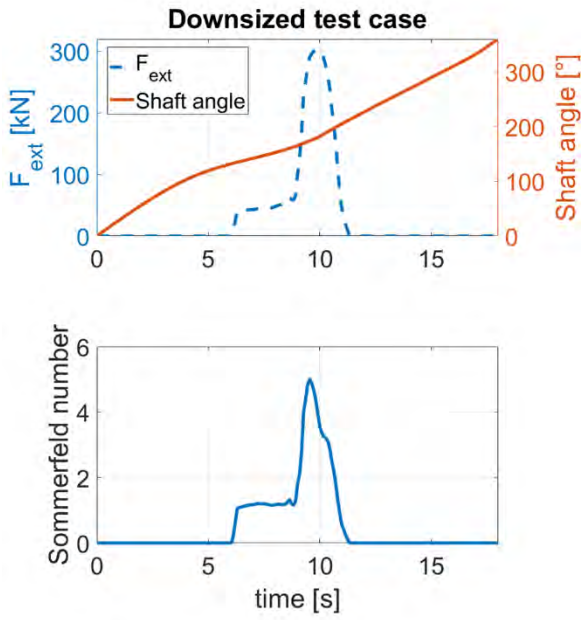

Figure 5: Load case for the IHPB design. Lubricant ISO VG150 at temperature 40°C, relative clearance of 0.667‰*, diameter of 300 mm and bearing width of 98 mm*

A bearing diameter of 300mm is chosen in accordance to the maximum capacity of the bearing test rig. A typical relative bearing clearance $\Psi = 0.667‰$ is chosen for this kind of application. A conventional lubricant ISO VG 150 fed at a temperature of 40°C is defined. The bearing width is then set so that the bearing faces is shortly overloaded during the load case. As shown in Figure 5 with the evolution of the Sommerfeld number, the bearing is partially in heavy load domain (Sommerfeld number > 3) for a chosen bearing width of 98 mm. This combination of load case and bearing parameters corresponds to the journal bearing of a machine which is slightly used over its capacities and is therefore endangered. Based on this bearing, hydrostatic pockets and an eccentricity control are designed.

3.2 Hybrid bearing geometry design

A traditional bearing geometry from the mechanical press industry was chosen. A circular cylindrical radial slide bearing without additional geometric recesses (e.g. transverse grooves) is defined as test bearing.

In order to carry out a simulative potential estimation, the simple circular cylindrical hydrodynamic plain bearing with hydrostatic pockets (HS) was supplemented. The main objective is to avoid the critical operating condition of the bearing while at the same time achieving high energy efficiency (minimum hydrostatic volume flow and pressure) of the resulting hybrid plain bearing. This is achieved by a small number of HS pockets and a controlled operation of the hydrostatic support. The use of both operating mechanisms (hydrodynamic and hydrostatic) is crucial to reduce hydrostatic oil consumption. The positions of the HS pockets were therefore selected in a way that they are not located in the main load zone to prevent backflow, but still in the effective area of the lubricating film of the bearing (optimization). For this reason, the pockets are positioned in the area of the pressure build-up and directly behind the expected pressure maximum. In order to avoid an impairment of the hydrodynamic contact area, a flat, large-area pocket geometry of the HS pockets has been used.

In order to ensure sufficient tilting rigidity in the lubricating film when the shaft is tilted towards the bearing bush in hybrid operation, two separate HS pockets with a common feed and corresponding chokes were defined on an angular coordinate. For the positioning of the hydrostatic pockets several variation calculations were carried out. Figure 6 shows the position's influence of the hydrostatic pockets on the load carrying capacity.

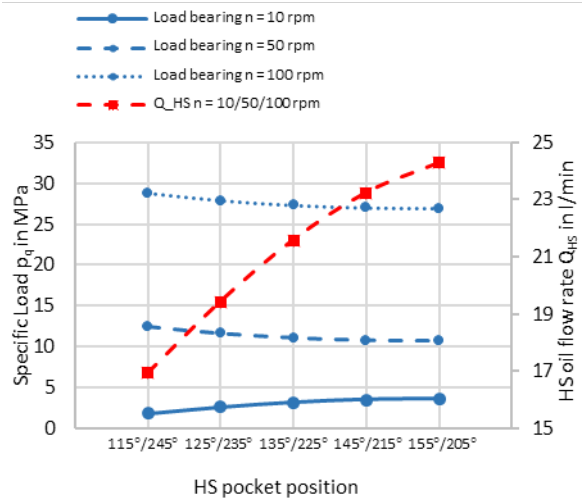

Figure 6: Influence of the HS pocket position on the hydrostatic oil supply and load capacity

With lower hydrodynamics, the load-bearing capacity increases with a smaller distance of the pockets (155°/205°) from the main load zone at 180°, while the opposite behavior occurs with increasing circumferential speed. At higher speeds, more widely spaced pocket arrangements would be better and at lower speeds, a more closely spaced pocket arrangements would be better. The predicted oil flow rate Q_{HS} is nearly the same for all speeds. For this, a medium positioning (145°/215°) was chosen as the most favorable compromise with regard to limiting a maximum system admission pressure of approx. 300 bar.

Finally, the geometrical parameters of the repository are shown in Table 1.

Table 1: Geometric bearing parameters

Parameter	**Value**
Bearing type	journal
Bearing width b	98 mm
bearing diameter d	300 mm
Clearance Ψ	0,667 ‰
Low pressure oil support	2x (90/270°)
High pressure oil support	4x (2x145°/2x215°)

Figure 7 shows the plain bearing bushing with the mounting collar on the front and the oil supply pockets

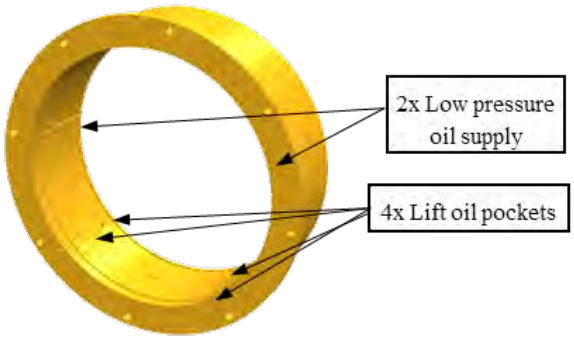

Figure 7: IHPB bushing

The deformation behavior of the bearing carrier was determined with the help of influence number matrices that were calculated a priori. These matrices form an input quantity for the bearing calculation program COMBROS R [16], so that the deformation influence due to the compressive load can be calculated. Figure 8 shows an example of a deformation field of the bearing bush surface.

The positive deformation values in the range of 90° and 270° show that the plain bearing bushing tends to ovalize. In addition, in the main load zone at 180° there is a slight opening of the gap towards the bearing edge. However, the bearing characteristics such as the maximum lubricant film pressure p_{max} and the minimum gap height h_{min} do not show any significant change due to the deformation. Only the hydrostatic oil flow rate and the displacement angle of the shaft journal are influenced by taking the deformations into account, as shown in Figure 9. Thus, when taking the deformations into account, the hydrostatic oil flow rate increases with the deformations due to the lateral opening of the bearing in the main load zone are taken into account, while the shaft is displaced slightly more in the direction of rotation.

For the parameter range under consideration, no significant change in the operating behavior of the bearing due to the deformation influence is expected.

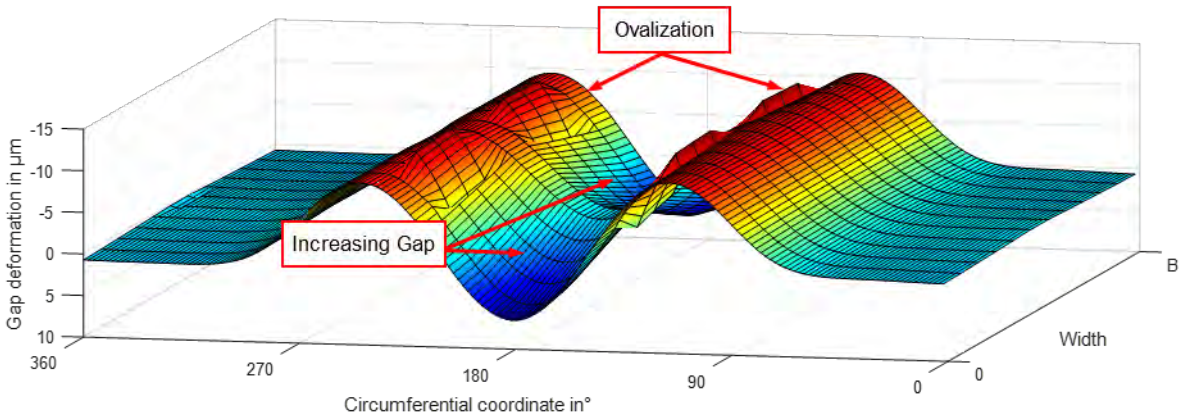

Figure 8: Calculated lubrication gap deformation of the test bearing (T_{sup} = 40 °C, F = 200 kN, ISO-VG 150)

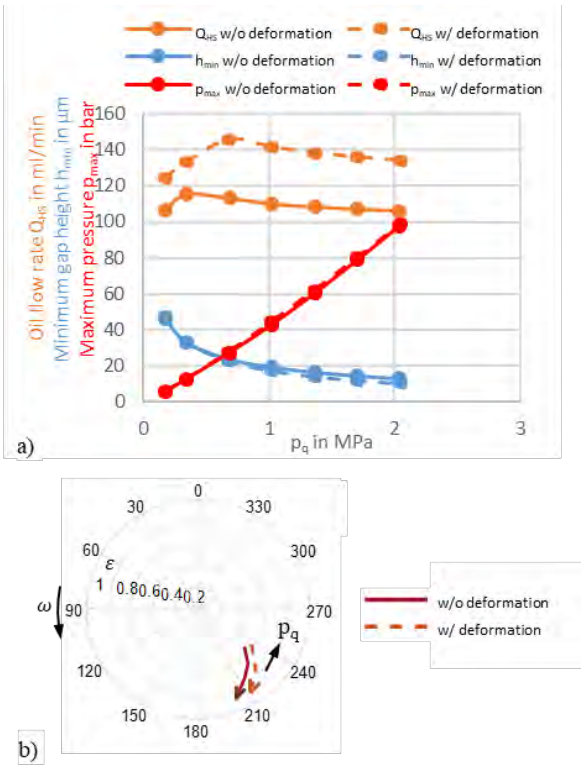

Figure 9: Calculated influence of the deformation behaviour of the test bearing under static load; a) bearing characteristics, b) journal displacement (T_{sup} = 40 °C, F = 200 kN, ISO-VG 150)

Using the method detailed in 1.4 and considering the defined geometry and deformation of the bearing, the substitute model of the bearing is derived.

3.3 Active hydrostatic design

After the successful design of the hybrid bearing with an optimal position of the HS pockets to not disturb the hydrodynamic operation, the eccentricity control strategy and the parameters of the HS hydraulic circuit have to be determined with the multiphysics model and the integrated substitute model of the bearing.

In this work, the hydrostatic support is activated, once the eccentricity ε exceeds a threshold ε_{lim}. A proportional integral (PI) control is then set to stabilize the eccentricity at the value of the threshold ε_{lim} by controlling the voltage input of the servo-valves. Lang [22] defined the mixed lubrication limit as the sum of the roughness R_z and waviness W_t of bearing and shaft. As the oil flow is proportional to the cubic of the lubricating gab, the threshold ε_{lim} is set at this mixed lubrication limit to be as high as possible and thus maintain a minimal oil consumption through the HS pockets (Eq. 16).

$$\varepsilon_{lim} = 1 - \frac{R_{z,S} + R_{z,B} + W_{t,S} + W_{t,B}}{C_0} \qquad (Eq.\ 16)$$

C_R is the journal bearing radial clearance. A surface roughness R_z of 6.3 µm for the bearing and the shaft is considered as a typical value in forming machines. Furthermore, the manufacturing process of these two components is precise enough to neglect the waviness W_t. With these assumptions, (Eq. 16) is reduced to (Eq. 17).

$$\varepsilon_{lim} \approx 1 - \frac{12{,}6 \cdot 10^{-6}}{C_0} = 0.87 \qquad (Eq.\ 17)$$

In order to optimize the lubrication, the control is deactivated when the bearing is considered in a safe state, which is given for an eccentricity ε smaller than $\varepsilon_{limOff} = 0.83$.

To minimize the leakage in pure hydrodynamic functioning, the valves exhibit a positive spool overlap, so that the valves close if no hydrostatic support is needed. Servo-valves D1FP from Parker have been chosen. They present a very good dynamic response of 350Hz at input signal between -5 and 5%, which is very important for this kind of control.

A schematic of the closed loop control system is depicted in Figure 10.

The control strategy and valve parameters are then implemented in the SIMULINK model of the IHBP. Results of simulation are illustrated in Figure 11.

A simulation comparison of the load case with and without HS support indicates a reduction of the maximal eccentricity of nearly 0.1 (from 0.96 to 0.87). The control is also very robust, the eccentricity is precisely stable at the set value with very small overshooting. The pressure in the 4 hydrostatic pockets (P_{HS12} and P_{HS34}) is always below 80 bar which allows to determine a supply pressure $p_{sup} = 100$ bar for the accumulator. As depicted in the first and third graphics of Figure 11, the HS pressure values in the pockets and the total lubricant flow Q_{Total} through the two valves follow perfectly the bearing load. P_{HS12} is up to 10 bar above P_{HS34} when the load profile is maximal. This corresponds to a hydrodynamic pressure difference caused by the shaft velocity. The total flow doesn't exceed 0.6 l/min. A total volume of 16 ml lubricant pro process cycle is calculated for this load case. With this value and the supply pressure p_0, the hydraulic aggregate and the accumulator can easily be designed. A nominal flow $Q_N = 6\,l/min$ of the valves for a nominal pressure $P_N = 35\,bar$ is chosen, so that the valve input voltage during the control is relatively broad for the electronic precision and close to the 5% span of the valve maximum input for an optimal dynamic response. Simulations with these parameters indicate an input between 0 and 6% of the maximal valve input.

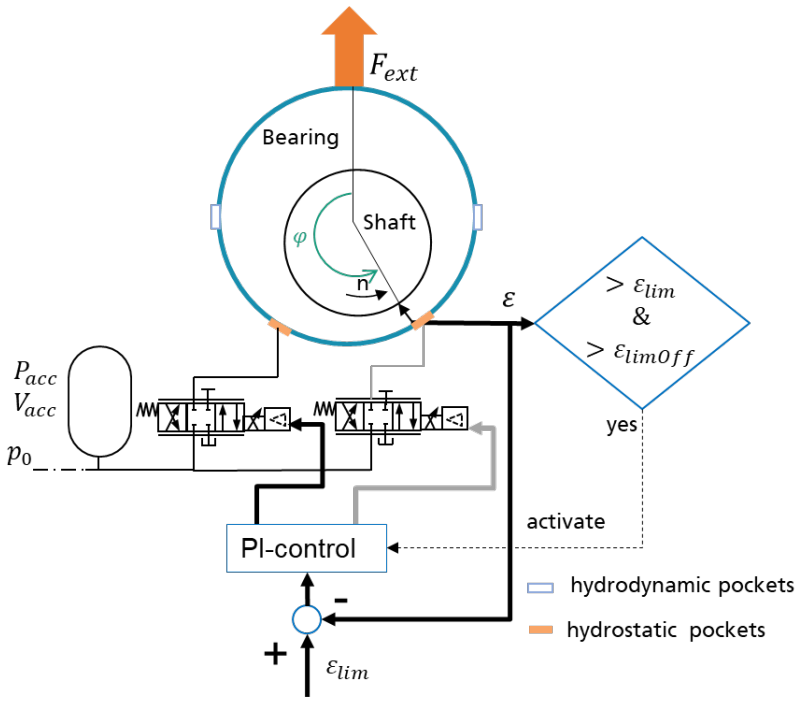

Figure 10: Closed loop control of the IHPB

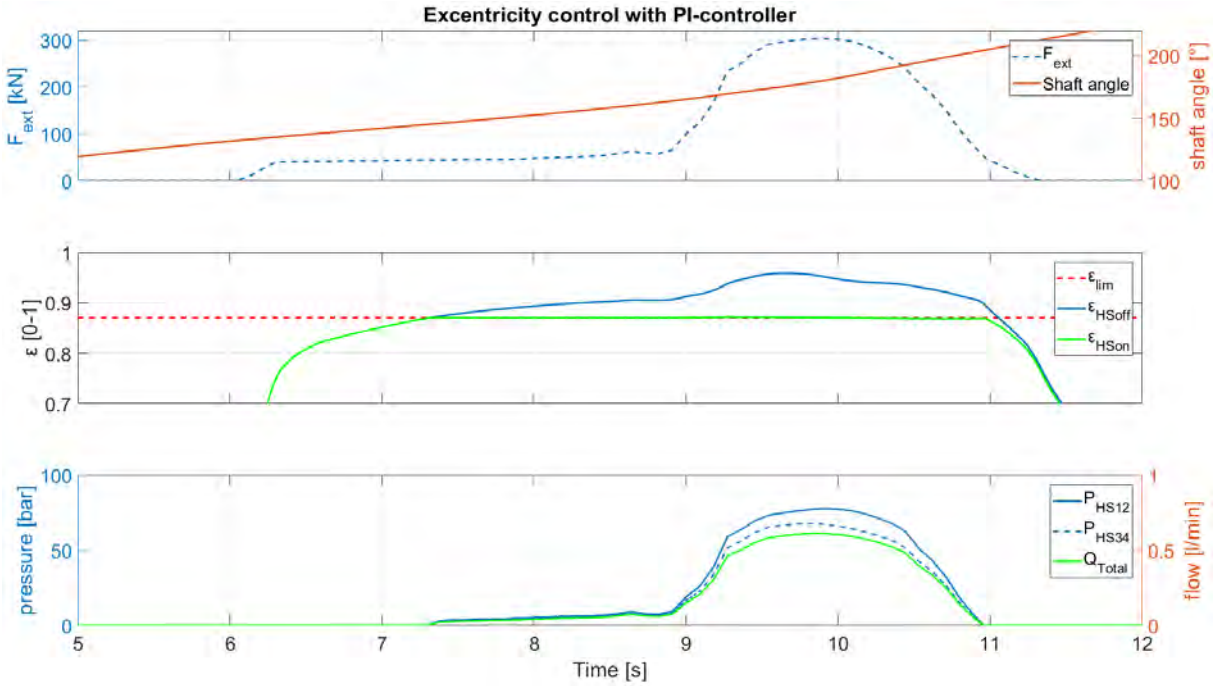

Figure 11: Simulation results of the IHPB control strategy

3.4 Performance evaluation of the designed IHPB

To evaluate the performance of the designed hybrid bearing with the PI based eccentricity control strategy from 1.8, simulations with different load step are conducted. For this performance evaluation, a constant rotational speed of 10 rpm is set and the lubricant is fed with a temperature of 40 °C.

In Figure 12 a comparison of the eccentricity with and without HS support is presented. For load step smaller than 30 kN (10 kN and 20 kN in Figure 12) the eccentricity is below the threshold and the HS support is not activated. To prevent wear on the running surface, the support is activated for the next load steps. It represents an eccentricity reduction of 8% for 120 kN and more than 11% for the three other loads (220 kN, 320 kN and 420 kN). For a maximal lubricant use of 0.8l/min. The eccentricity evolution shows that the closed loop response of the IHPB is very fast, robust (very few overshooting) and precise. At 420 kN the pressure in the first two HS pockets reaches 100 bar, which is the limit of the pressure supply. It can be concluded that the designed IHPB allows an increase of the maximal bearing load of nearly 1400% (from 30 kN to 420 kN) without endanger the bearing safety.

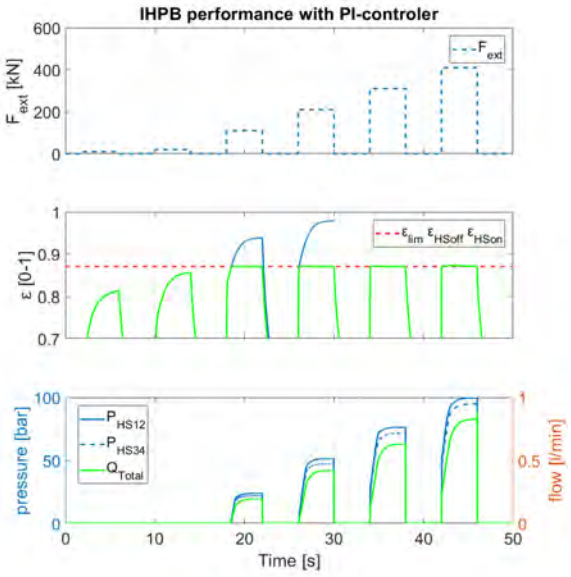

Figure 12: Performance evaluation of the IHPB with step load (10, 20, 120, 220, 320, 420 kN) at 10rpm and 40°C.

4. Conclusions

The simulation method described in this work has shown very good results in the modeling of a hybrid plain bearing in a multiphysics environment. A substitute model of the bearing is first derived using the thermo-elasto-hydro-dynamic code COMBROS R. This simplified model is composed of lookup tables, which consider the nonlinear behavior of the bearing. It is then coupled with a hydraulic model of the

hydrostatic lubricant supply. Based on this, an intelligent bearing eccentricity control was tested, and the hydrostatic actuators were finer designed. According to the simulations performed with a downsized load case from a forming process, the control strategy derivate from a PI-controller presents great precisions and stability. The safety of the IHPB was guaranteed with an optimal use of lubricant and hydraulic power. Simulation with step load has shown that the response of the system is fast and that the IHPB enables an increase of the bearing maximal load up to 1400%. This IHPB was manufactured and tested in a plain bearing test rig at the Fraunhofer-Institute for Machine Tools and Forming Technology (IWU). The results presented in this paper are in accordance with the experiments detailed in [23].

For more confidence in the developed technology an extended comparison with experimental data would be necessary. Nevertheless, this method is very versatile and can be exerted to validate other use cases, actuators and control strategies. Moreover, the lookup table of the substitute bearing model can be enhanced to take into account the influence of other bearing behavior, such as the lubricant temperature, the bearing deformation or the shaft misalignment.

Acknowledgment

This article displayed the research work performed by the Fraunhofer-Institute for Machine Tools and Forming Technology (IWU) and the Institute of Tribology and Energy Conversion Machinery (ITR). It was supported by the German Federation of Industrial Research Association eV (AIF) within the framework of the industrial collective research (IGF) program (IGF No. 19220 BG). The authors gratefully acknowledge the support received from the funding organizations, from German Machine Tool Builders' Association (VDW) and from all those involved in the project.

References

[1] Bassani R., and Piccigallo B., 1992, Chapter 9 Hybrid Plain Journal Bearings, *Hydrostatic lubrication*, Bassani R., and Piccigallo B., eds., Elsevier, Amsterdam, pp. 288–300. DOI: 10.1016/S0167-8922(08)70093-2.

[2] Santos I. F., 1994, “Design and evaluation of two types of active tilting pad journal bearings,” *The active control of vibration: IUTAM symposium*, Mechanical Engineering Publ. Ltd, Bath, UK, September 5–8, 1994, pp. 79–87.

[3] Nicoletti R., and Santos I. F., 2001, “Vibration control of rotating machinery using active tilting-pad bearings,” *2001 IEEE/ASME International Conference on Advanced Intelligent Mechatronics. Proceedings (Cat. No.01TH8556)*, IEEE, Como, Italy, July 8-12, 2001, pp. 589–594. DOI: 10.1109/AIM.2001.936530.

[4] Nicoletti R., and Santos I. F., 2003, “Linear and non-linear control techniques applied to actively lubricated journal bearings,” Journal of Sound and Vibration, **260**(5), pp. 927–947. DOI: 10.1016/S0022-460X(02)00951-3.

[5] Santos I. F., and Scalabrin A., 2003, “Control System Design for Active Lubrication With Theoretical and Experimental Examples,” Journal of Engineering for Gas Turbines and Power, **125**(1), pp. 75–80. DOI: 10.1115/1.1451757.

[6] Salazar J. G., and Santos I. F., 2015, “Exploring integral controllers in actively-lubricated tilting-pad journal bearings,” Proceedings of the Institution of Mechanical Engineers, Part J: Journal of Engineering Tribology, **229**(7), pp. 835–848. DOI: 10.1177/1350650115570697.

[7] Varela A. C., and Santos I. F., 2014, “Tilting-Pad Journal Bearings With Active Lubrication Applied as Calibrated Shakers: Theory and Experiment,” Journal of Vibration and Acoustics, **136**(6), p. 251. DOI: 10.1115/1.4028452.

[8] Rehman W. U., Guiyun J., Iqbal M. N., Luo Y.-X., Wang Y.-Q., Rehman S. U., Bibi S., Saleem F., Azhar I., and Shoaib M., 2018, Intelligent Servo Feedback Control for Hydrostatic Journal Bearing, *Intelligent Computing and Internet of Things*, Li K., Fei M., Du D., Yang Z., and Yang D., eds., Springer Singapore, Singapore, pp. 352–364. DOI: 10.1007/978-981-13-2384-3_33.

[9] Rehman W. U., Luo Y.-X., Guiyun J., Wang Y.-Q., Yun X., Iqbal M. N., Zaheer M. A., Azhar I., Elahi H., and Xiaogao Y., 2017, “Control of an oil film thickness in a hydrostatic journal bearing under different dynamic conditions,” *29th Chinese Control And Decision Conference (CCDC)*, IEEE, Chongqing, China, Mai 28-30, 2017, pp. 5072–5076. DOI: 10.1109/CCDC.2017.7979395.

[10] Rehman W. U., Jiang G.-Y., Luo Y.-X., Wang Y.-Q., Khan W., Rehman S. U., and Iqbal M. N., 2018, “Control of active lubrication for hydrostatic journal bearing by monitoring bearing clearance,” Advances in Mechanical Engineering, **10**(4), 1-17. DOI: 10.1177/1687814018768142.

[11] Rehman W. U., Guiyun J., Luo Y.-X., Wang Y.-Q., Iqbal M. N., Rehman S. U., and Bibi S., 2019, “Linear extended state observer-based control of

active lubrication for active hydrostatic journal bearing by monitoring bearing clearance," ILT, **71**(7), pp. 869–884. DOI: 10.1108/ILT-09-2017-0263.

[12]Estupiñan E. A., 2009, "Feasibility of applying controllable lubrication techniques to reciprocating machines," Ph.D. thesis, Technical University of Denmark.

[13]Wegmann R., Gold S., Brökel K., and Weber J., 2013, "Numerische Simulation und experimentelle Verifikation von kombiniert hydrostatisch-hydrodynamisch wirkenden Radialgleitlagern großer Abmessungen," *10. VDI-Fachtagung Gleit- und Wälzlagerungen, Gestaltung, Berechnung, Einsatz,* Schweinfurt, 23.-24. April, pp. 219–232.

[14]Gold S., 2015, "Auslegung, Analyse und Erprobung eines lastgesteuerten Hybrid-Gleitlagers für Schwerlastanwendungen am Beispiel Pod-Antrieb," Ph.D. thesis, Technische Universität Dresden, Dresden.

[15]Kurth R., Tehel R., Päßler T., Putz M., Wehmeyer K., Kraft C., and Schwarze H., 2019, "Forming 4.0: Smart machine components applied as a hybrid plain bearing and a tool clamping system," Procedia Manufacturing, **27**(2019), pp. 65–71. DOI: 10.1016/j.promfg.2018.12.045.

[16]Hagemann T., 2012. *Dokumentation Radialgleitlagerberechnungsprogramm*, FVV, Frankfurt a. M.

[17]Hagemann T., 2011, "Ölzuführungseinfluss bei schnell laufenden, hoch belasteten Radialgleitlagern unter Berücksichtigung des Lagerdeformationsverhaltens," Ph.D. thesis, Technische Universität Clausthal.

[18]Fuchs A., 2002, "Schnelllaufende Radialgleitlagerungen im instationären Betrieb," Ph.D. thesis, Technische Universität Braunschweig.

[19]Mittwollen N., 1990, "Betriebsverhalten von Radialgleitlagern bei hohen Umfangsgeschwindigkeiten und hohen thermischen Belastungen: Theoretische Untersuchungen," Ph.D. thesis, Technische Universität Karlsruhe.

[20]Mermertas Ü., 2007, "Nichtlinearer Einfluss von Radialgleitlagern auf die Dynamik schnelllaufender Rotoren," Ph.D. thesis, Technische Universität Clausthal.

[21]D.-C. Han, 1979, "Statische und dynamische Eigenschaften von Gleitlagern bei hohen Umfangsgeschwindigkeiten und bei Verkantung," Ph.D. thesis, Technische Universität Karlsruhe.

[22]Lang O. R., and Steinhilper W., 1978. *Gleitlager: Berechnung und Konstruktion von Gleitlagern mit konstanter und zeitlich veränderlicher Belastung*, Springer Berlin Heidelberg, Berlin, Heidelberg, s.l. DOI: 10.1007/978-3-642-81225-5.

[23]Eberhardt C., Kurth R., Kraft C., Schwarze H., Päßler T., Bergmann M., and Putz M., 2021, "Experimental Validation of an Intelligent Hybrid Plain Bearing Active Control," Journal of Tribology, **143**(4), p. 288. DOI: 10.1115/1.4048384.

Calculation Method to Evaluate the Risk of WEC Occurrence in Industrial Applications

Dirk-Olaf Leimann[1]

[1] *Belgium, dirkolaf63@msn.com*

Abstract – White Etching Crack WEC is a premature subsurface initiated failure mode. WEC can occur on bearing components in industrial applications and is reported in wind turbine gear boxes, automotive and other applications. The failure mode leads to severe bearing failures and is initiated from a sub-surface crack, sometimes seen in combination with so called butterfly's and seldom related to inclusions. The proposed calculation method will give an estimation of the risk of WEC failure, taking real operating and lubrication conditions into account.

The method, based on the model of Leimann, is an analytic and experienced based method with new calculation elements and hypotheses as the introduction of a time dependant stress level for the occurring and permissible stresses. The equations for determining the risk of WEC failure consist of 3 parts, first part are stresses, calculated with known approaches, second part is a time factor, based on contact cycles, third part are influence factors, derived from publications or experience. This approach leads to an estimation of the risk on WEC failures and enables an engineer to use design, load ,material, lubricant, ambient and geometry criteria to adjust the safety against this failure mode.

Keywords – Model of Leimann, Rolling Bearings failures, White Etching Crack WEC, time dependant stress levels, design tool

Introduction

The failure mode white etching crack WEC is subsurface initiated and leads to severe bearing damages.

The damage looks like craters on the contact surface or cracks crosswise the raceway. The failure is initiated from sub-surface cracks and under stress levels, lower than the fatigue limits would allow.

The method of Leimann [3] is developed from an analytic and experienced based background. It is the first calculation method, that is able to give an estimation for the risk of the occurrence probability of WEC under real load, operating and lubricating conditions. The method is based on new hypotheses and insights and will be explained in this paper more in detail. It is validated for radial and axial rolling bearings and copes with field and test observations. The method can be applied to calculate point and line contact on ball and roller bearings. The approach leads to an estimation of the risk of the occurrence of the WEC failure and enables the user to change design, load, geometry, material, lubricant and ambient conditions to adjust the safety against the probability of the occurrence of the WEC failure and enables therefore the user to avoid this failure mode.

This failure mode is also known under names as: white structure flaking, flaking at early stage, subsurface initiated flaking or white flaking structure and other.

When this failure was observed, it was always the question, why does this failure only harms one bearing in a gear unit and why not the neighbour or other bearings in the unit, even if they have the same operating and load conditions. The proposed method gives answers to this question.

Due to the WEC failures in wind turbine gear boxes, careful considerations were done to increase the reliability of wind turbine gear boxes by substitute rolling bearings by journal bearings [12]. This process is ongoing.

The proposed method for WEC helps to make decisions to future designs, based on comparable reliable solutions and economical facts.

General approach

Calculation methods for gears and bearings with respect to failures modes were developed over decades and the methods, published in standards, are a combination of scientific approach and experience based insights and formulae.

Still there are a lot of bearing failure modes, where no international calculations are agreed (table 1).

One reason could be, that companies have different experiences with those failure modes due to, may be, different design and manufacturing processes. In the most standards it is also mentioned, that the user shall compare to own experience and chose the actions with respect to those.

The standards are build on experience and tests, carried out on small scaled components and test rigs with set up conditions, to allow short testing times, so that a high number of tests can be carried out to get statistical verification. But material behaviour, manufacturing processes and operating conditions on bigger sizes of those mechanical components can be different.

When a field failure turns up, where no standard with clear limits is available, experience and insight is requested to find solutions to avoid the failure. For industrial applications (automotive applications might differ), there are not enough field failures to have statistical data.

The proposed model could help the engineer, to find solutions in case of insufficient statistical data.

The general approach is based on the observation, that:

A time dependence of permissible and occurring stresses exists

And an understanding, that in a certain material depth, not the maximum permissible stress is valid but a depth dependant permissible stress.

Further the idea is, to compare a few failures with a lot of not failed components in detail and with respect to stresses.

The model is build on a comparison between occurring stresses and permissible stresses and uses correction factors, taking into account field observations, manufacturing processes and negative and positive experiences.

It is very important to consider all kind of possible stresses and factors, therefore it is necessary to study the matter thoroughly.

The basic formulae of the model is:

$$\sigma_{Y(M)} = \Sigma\sigma_{Y(M)} \times f_{time} \times \beta \ldots \quad (Eq.\ 1)$$

With σ, as the synonym for stresses, f_{time} , as the time factor and factors β... for influences, discussed later in this paper. All stresses are seen as scalar.

For permissible stresses the formulae is:

$$\sigma_{pY(M)} = \Sigma\sigma_{pY(M)} \times f_{time\_p} \times \beta \ldots \quad (Eq.\ 2)$$

And for occurring stresses the formulae is:

$$\sigma_{oY(M)} = \Sigma\sigma_{oY(M)} \times \Sigma f_{time\_o} \times \beta \ldots \quad (Eq.\ 3)$$

With the permissible stress and the occurring stress, a safety factor is calculated and compared to the field observations. It is important to balance and calibrate the stresses and factors, so that the safety factor is able to differentiate, whether the component fails or not.

The basic formulae for the safety factor is:

$$\mathbf{S}_{\text{failure-mode}} = \frac{\sigma_{pY(M)}}{\sigma_{oY(M)}} \quad (Eq.\ 4)$$

This model fits for 2 observed failure modes with significant numbers of field failures on the industrial application wind turbine gear unit. These failure modes are Tooth Flank Fracture TFF and White Etching Cracks WEC. For both failure modes, some knowledge and experience was available when they occurred, but this knowledge was insufficient to find solutions and give to an engineer instructions on, how to avoid this failure mode in the future.

As already mentioned, every solution may be different between applications and manufactures due to different processes and designs and executions.

This might be for instance an explanation, why the proposed calculation method for TFF in ISO/TS 6336-4 [21] with the proposed safety factor or exposure rate did not fit to the experience and standard reported in [5,6].

This paper will demonstrate the experience of the model with respect to WEC.

Situation

There are a few standardized calculation methods available for bearings. For wind turbine gearboxes the standard IEC 61400-4 [1] gives an overview on bearing failure modes, the available calculation methods and limits. The outlook of those failure modes is documented in ISO 15243 [2]. In table 1, a survey is given about failure modes and the public state of the art standardized rolling bearing calculation method and the calculation result, not taken into account technical reports.

Table 1: Failure modes versus calculation methods

Failure Mode ISO 15243 / IEC 61400-4	Calculation Standard	Calculation Criteria / Result	Failure outlook
Subsurface initiated fatigue	**ISO 281**	**Lifetime**	**Pitting**
Surface initiated Fatigue	not available	not available	**Micro Pitting**
Adhesive Wear	not available	not available	**Wear**
Moisture Corrosion	not available	not available	**Rust**
Frictional Corrosion	not available	not available	**Rust, Deformation**
Excessive Voltage	not available	not available	**Black Spots, craters**
Current leackage	not available	not available	**Craters**
Overload	**DIN ISO 76**	**Static Safety Factor**	**Plastic Deformation**
Indentations from Debris	**ISO 281 Beiblatt 4**	**Lifetime**	**Pitting**
Indentations from Handling	not available	not available	**Pitting**
White Etching Structures	not available	not available	**WEC**
Hairline Crack	not available	not available	**WEC**

In the publication from Johan Luyckx [4], pictures and failure rates (table 2, 16, 21) are shown with respect to WEC damage and gear box population of wind turbine gear boxes.

Table 2: Gear box population versus failure rate [4]

execution	Gear box population	WEC failure rate	occurrence after
Through hardened	**1000**	**40% - 70 %**	**2 years**
	400	**40%**	**14 month**

On rolling bearings, the WEC subsurface cracks start between 20 µm up to 1,5 mm below the contact surface of the raceways and sometimes the roller surface. The cracks develop to the surface resulting in pitting, craters and flaking or axial hairline cracks. The damage develops very fast and is severe. The WEC failure mode is a premature failure mode and occurs far before the calculated lifetime is reached. With regular standard and not coated bearings, this failure is reported during the first 24 month of operation. (Figure 1)

Figure 1: Lifetime bath curve

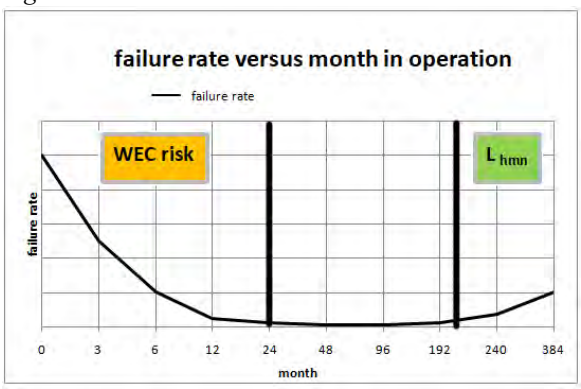

A lot of WEC failures on bearings are observed on the wind turbine application [4], especially with 1,5 to 2,5 MW gear units. WEC failures occur on planet shaft bearings PS, low speed intermediate shaft LSIS bearings, high speed intermediate shaft HSIS bearings and high speed shaft HSS bearings.

Figure 2 shows an example of a 2 MW wind turbine gearbox with one planet stage and 2 helical stages [12]. Here, Taper roller bearings TRB and cylindrical roller bearings CRB are used.

Figure 2: Wind turbine gearbox

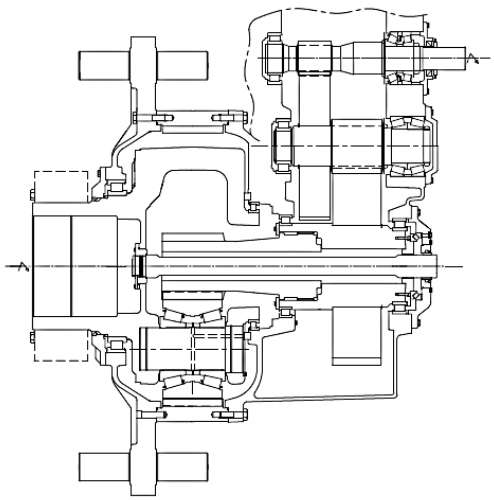

The Method of Leimann [3]

The calculation method is based on the insights, gained from the calculation method for tooth flank fracture TFF acc. to the method of Leimann [6]. This is standardized in the Belgium Standard NBN E 23-402 [5]. Additional extensions for rolling bearings are documented in [3]. This means, that for the calculation of the risk of the occurrence of WEC, changes were done in the formulae of the method for TFF and also additional hypotheses and formulae were added.

The WEC bearing calculation method is based on 10 hypotheses or elements:

Hypotheses or elements for permissible stresses with respect to rolling bearings

1. The Hertzian stress in the rolling contact leads to a compressive stress in the material depth in the direction of the force and this compressive stress is proposed as increasing the material value similar to the approach of taking residual stresses into account
2. In addition, it is proposed that all compressive stresses in this direction increase the material value
3. A correction factor f_c Hertz for the permissible stress is introduced to comply with observations
4. A time factor $f_{\text{time p}}$ is introduced with respect to number of rolling contacts per route
5. A surface factor β_c is introduced for the contact between roller and raceway
6. A material factor β_M is introduced to take into account material properties and decreasing and increasing effects on the safety value as hydrogen, current or voltage flow or special bearing steel

Hypotheses or elements for occurring stresses with respect for rolling bearings

7. A time factor $f_{\text{time o}}$ is introduced with respect to the number of rolling contacts per route
8. A notch factor β_k is introduced based on material qualities and observations
9. A variable X- factor is introduced for the calculation of the half width local contact to take into account a different stress behaviour in the material depth

Hypotheses or elements for the material depth y_M for the stress comparison

10. The evaluation depth y_M is introduced and related to the elastic deformation δ_K in the contact between the roller and the raceway under load. The elastic deformation δ_K is multiplied with a design specific factor Z

With these hypotheses or elements the basic equations for the calculation of the permissible and occurring stress are:

Permissible stress:

$$\sigma_{\text{permissible (yM)}} = (\sigma_{\text{p-HV(yM)}} + \sigma_{\text{p-Hertz(yM)}} \times f_{\text{cHertz}} + \sigma_{\text{p-residual(yM)}}) \times \beta_M \times \beta_c \times f_{\text{time p}} \quad \textit{(Eq. 5)}$$

Occurring stress:

$$\sigma_{\text{occurring (yM)}} = (\sigma_{\text{o-comp Hertz(yM)}} + \sigma_{\text{o-hoop(yM)}} + \sigma_{\text{o-friction(yM)}}) \times \beta_{\text{k(yM)}} \times f_{\text{time o}} \quad \textit{(Eq. 6)}$$

The load or force used in the calculation should be calculated according to:

$$P_{\text{calculation}} = P_{\text{application}} \times K_A \times K_v \times Y_{\text{WEC}} \quad \textit{(Eq. 7)}$$

The safety factor for WEC, $S_{\text{WEC (yM)}}$ is calculated as:

$$S_{\text{WEC (yM)}} = \frac{\sigma_{\text{permissible (yM)}}}{\sigma_{\text{occurring (yM)}}} \qquad \textit{(Eq. 8)}$$

The safety value against the risk of the occurrence of WEC S WEC (yM) shall comply with values of own experience or should comply with the values given in table 3.

Table 3: Safety values to estimate the risk of failure

Safety factor $S_{WEC\ (yM)}$ if no additional WEC driver is present or assumed	**< 0,95**	**0,95 ... 1,05**	**> 1,05**
	unsafe **high probability of failure**	**action required** **could occasionally fail**	**safe** **should not fail under the defined operating conditions**
Safety factor $S_{WEC\ (yM)}$ if an additional WEC driver is present or assumed	**< 1,15**	**1,15…1,2**	**> 1,2**
	unsafe **high probability of failure**	**action required** **could occasionally fail**	**safe** **should not fail under the defined operating conditions**

Definition of the critical depth

The WEC crack ignition can be between 20 µm up to 1,5 mm below the contact surface. It is essential, to make the comparison between the occurring and the permissible stress in a material depth below the contact surface, where the crack ignition is supposed to start. Observations have shown, that this depth is dependent on the bearing type as axial bearing, radial bearing, ball bearing and roller bearing. As a measure for the determination of the critical depth, the deformation δ_K under the load $P_{calculation}$ is taken, multiplied by the factor Z, depending on the bearing type.

$$y_M = \delta_K \times Z \qquad \textit{(Eq. 9)}$$

The figures 2 and 3 show the definition of y_M with respect to axial and radial bearings.

Figure 2: axial bearing

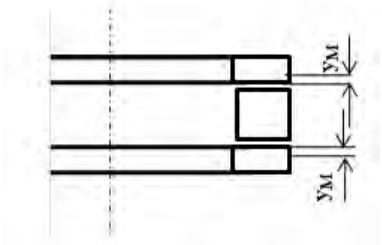

Figure 3: radial bearing

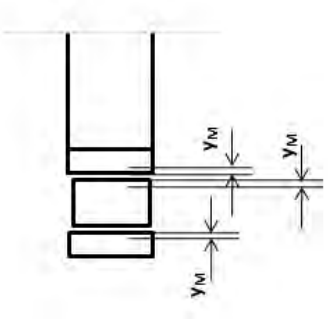

Several calculations with respect to y_M and S WEC were carried out and compared with experience values to find the factor Z for the different bearing types.

The images, figures 4 and 5 show WEC damages taken from the publication Loos [20] with the friendly permission of Schaeffler Technologies, Herzogenaurach, Germany.

Figure 4: white etching cracks [20]

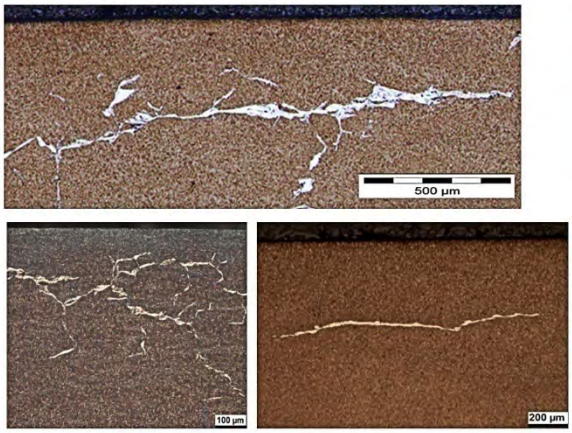

Figure 5: white etching cracks [20]

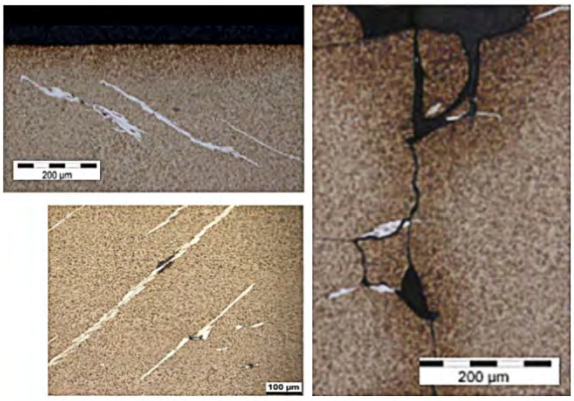

These images give an idea about the depth of the crack network.

Hypotheses 9 for determination of stresses

During the development of the method for the calculation of tooth flank fracture TFF [5,6] it turned out, that the stress levels in a certain material depth y_M do not fit to the common calculation formulae of the half width contact value b.

The modified half width contact value b^* in this method is calculated with a variable factor X instead of a fix number as:

$$b^* = \sqrt{\frac{X \times P_{calculation} \times (1-\nu^2)}{\pi \times E \times l \times \left(\frac{1}{d_1}+\frac{1}{d_2}\right)}} \qquad (Eq.\ 10)$$

With: ν = 0,3; E = 2,1 x 10^5 N/mm² and l = length mm

The value X can take on values from 1 to 4

Preferably it is: X = 2.

The time factor f_{time}

(or correction factor for the time dependent stress values)

During the development of the calculation method for tooth flank fracture TFF [5,6], research results were published, where TFF was reproducible with small modules on spur gears, but could not be reproduced on spur gears with bigger modules. In [5,6] an explanation was postulated, which said, that stresses do not suddenly disappear, if the load passes a contact point. There is a release and also loading time present. This resulted in the definition of a time factor or stress relieve factor f_{time}. With this definition, the presence of a bending moment on spur gears could be explained.

On bearings, the contact sequences due to speed and number of rollers change the stress values. The calculation method for the time factor is new and the equations first published in [27]. The equations are experienced based and lead to a high consensus with the observations of the calculated bearings.

For bearings the basic formulae of the time factor for permissible stresses is:

$$f_{time\_p} = \left(\left(\frac{N_c}{10000}\right)^{\frac{1}{6}} \times 1{,}2\right)^{corr} \qquad (Eq.\ 12)$$

For the occurring stress the basic formulae of the time factor is:

$$f_{time\_o} = N_c{}^{\frac{1}{50}} \times corr \qquad (Eq.\ 13)$$

With the number of contacts N_c and a correction factor *corr*.

The factors β…

Beta-factors (β…) are factors, which take increasing and decreasing effects on the risk of WEC failure mode into account. A lot of research was done and published during the last decades with respect to drivers and counter measures of the WEC failure mode. The results of those research works are used in this method and transferred into β-factors and approximated with fixed numbers due to the variance of the influence parameters. Some factors are more explained in results and discussion.

The material factor β_M

(or factor to take into account influences, that increase or decrease the permissible material values)

It is known, that some conditions may increase the risk of the WEC failure mode by weakening the material as:

- Electric current or voltage flow E
- Hydrogen H
- Oil chemistry CH

and, that some features can decrease the risk of this failure mode as:

- Material properties M
- Special materials M

The material factor β_M takes these so called drivers and counter measures into account. The factor can have values between 0,6 and 1,2 and comes from experience or research results and is:

$\beta_M = 1$ for standard bearing steels and normal operating conditions.

For weakening conditions the factor is:

$\beta_M \leq 0{,}95$

and for strengthening conditions the factor is:

$\beta_M \geq 1{,}1$.

The notch factor β_k

During the development of the method for tooth flank fracture TFF [5,6] it has been seen, that premature failures due to cracks below the contact surface can also start at small and hard inclusions. Therefore a notch factor was defined with respect to the size of the inclusion.

Bearing steel has much smaller inclusions than standard gear steels, so the critical size for bearings is defined in a first approach as 0,2 mm. This size of critical inclusion is chosen, because there are no failures reported with the root cause inclusion. What has been reported are so called butterfly´s [4]. There is today no common understanding about, that these butterfly´s with sized up to 150 µm to 250 µm could cause WEC. It might be also, that debris of hard and smooth particles can have some impact similar to inclusions, so the recommendation is, to use this approach also for these matters. According to [5,6] the calculation formulae for the notch factor is:

$$\beta_{k\,(yM)} = 1 + \frac{(l+w+h)^3}{Const} \qquad (Eq.\ 14)$$

With Const = 20 ....540 mm³ depending on the material quality used. This factor is based on [5].

Surface factor β_c

There are also contact surface related conditions that can increase or decrease the WEC risk.

These are:

- black oxidized surfaces BO
- other surface refinements S
- manufacturing quality Q
- grinding burns G

The material factor β_c takes these drivers or countermeasures into account. This factor can also have values between 0,8 and 1,2 and comes from experience or research results and is:

$\beta_c = 1$ for standard surfaces and normal operating conditions.

For weakening conditions the factor is:

$\beta_c \leq 1$

and for strengthening conditions the factor is:

$\beta_c \geq 1{,}1$.

Results and discussion

Based on the approach above a lot of calculations were carried out. Also industrial applications and research results from publications with failed and non failed bearings were calculated on the occurrence of WEC.

The total of all calculated cases provided the following distribution:

The percentage of the non failed bearings of all calculated cases is 74 % and the percentage of bearings failed due to WEC is 26 %.

The effectiveness of the proposed method is:

$e \geq 99$ % , means, less than 1 % of the calculated cases do not comply with the observations.

The average safety factor of non failed bearings is 1,208 compared at an average material depth y_M = 0,24 mm and an average Hertzian stress of p_H = 1400 MPa with min 515 MPa and max 4170 MPa. The average safety factor of failed bearings due to WEC damage is 0,920 compared at an average material depth y_M = 0,3 mm and an average Hertzian stress of p_H = 1332 MPa with min 429 MPa and max 3900 MPa.

These results support the limits shown in table 3.

The average speed of the non failed bearings is 1219 rpm with a min of 7,5 rpm and a max of 10500 rpm and the failed bearings have an average speed of 986 rpm with a min of 14,9 rpm and a max of 10500 rpm.

An interesting observation here is, that, out of the range of stress levels and material depth, where the crack ignition starts, they are more or less the same for failed and non failed bearings.

The average value of the speed of failed bearings is lower than the speed for not failed bearings.

An explanation could be, that the time factor has a significant influence on the increase of the material value due to compressive stresses.

The following results show some cases in detail with respect to research results from FVA (Forschungsvereinigung Antriebstechnik e.V. Frankfurt) and several publications, see references.

FVA 541 I with high load and normal load [7]

When this research was initiated, there was a strong believe, that the WEC damage in wind turbine gear boxes could be caused by overload events, leading to an initial crack, and under normal load conditions, the crack will develop further. For this research task, a new test set up was designed for the cylindrical bearing Type 206 and condition monitoring was added to recognize the early stage of a coming failure. The high load was a value of C/P = 2,5 followed by a lower load of C/P = 4. This lower load value is near to values used in planet stages of wind turbine gear boxes (C/P = 5 to 7) and was chosen to get reasonable testing times, the high load value was a value estimated as harmful. The tests were carried out with 3 speed levels, one of those speed levels represents the speed of the high speed shaft of a 60 Hz wind application. During all tests, no WEC damage was found. The calculation results according to the proposed method confirm, that no WEC damage can be expected.

Table 4: Calculation results FVA 541 I [7]

bearing type	-	**NJ 206**	**NJ 206**	**NJ 206**	**NJ 206**
contact	-	**IR**	**OR**	**IR**	**OR**
Hertzian stress p_H	MPa	2998	2504	2395	1977
speed	rpm	1700	1700	1700	1700
C / P	-	2,5	2,5	4	4
driver	-	none	none	none	none
WEC	-	**NO**	**NO**	**NO**	**NO**
depth y_M	mm	0,28	0,28	0,18	0,18
S $_{WEC\ yM}$	-	**1,291**	**1,105**	**1,216**	**1,077**

FVA 707 I with low reference oil [8]

In FVA 707 I [8], a radial bearing NU 206 and 2 axial bearings 81212 and 81206 were tested. To create the WEC damage mode, a so called low reference oil was used. The research succeeded in producing WEC on a so called FE8 test stand on the axial cylindrical bearings types 81212 and 81206. One of the reported observation was, that WEC could only be observed, if also pitting damage was present. On the tests with the radial bearing type NU 206, no WEC could be produced after 1000 hrs where the calculated lifetime was much higher.

The next tables show the results of the calculations. The bearing types and sizes are well known from testing and without a driver, no WEC damages are reported in literature. With the special low reference oil used in this research, WEC could be produced.

Table 5: Calculation results FVA 707 I 81212 [8]

bearing type	-	**81212**	**81212**
Hertzian stress p_H	MPa	1900	1900
speed	rpm	300	300
driver	-	none	low reference oil
WEC	-	**NO**	**YES**
depth y_M	mm	0,4	0,4
S $_{WEC\ yM}$	-	**> 1,1**	**0,948**

Table 6: Calculation results FVA 707 I 81206 [8]

bearing type	-	**81206**	**81206**
Hertzian stress p_H	MPa	1900	1900
speed	rpm	300	300
driver	-	none	low reference oil
WEC	-	**NO**	**YES**
depth y_M	mm	0,22	0,22
S $_{WEC\ yM}$	-	**> 1**	**0,899**

Table 7: Calculation results FVA 707 I NU 206 [8]

bearing type	-	**NU 206**	**NU 206**
Hertzian stress p_H	MPa	1900	1900
speed	rpm	750	750
driver	-	none	low reference oil
WEC	-	**NO**	**NO *after 1000 hrs***
depth y_M	mm	0,08	0,08
S $_{WEC\ yM}$	-	**> 1,1**	**> 0,97**

The results of the proposed calculation method with respect to the proposed safety factor in table 3 confirm the observations of the tests.

Electric current or voltage flow [9,10,13]

As already mentioned earlier, there is a strong belief, that electric and / or current flow is a major driver for WEC failures. This was observed on test benches used in [9,10,13]. In practice and on a wind turbine as example, it is very difficult to measure this and to determine values for voltage and current. However, Loos reported in [9,13] results on a cylindrical roller bearing NU 207 and Kawamura and Mikami [10] and Loos [9] report on results on a ball bearing 6203.

The reported results on the NU 207 from Loos [9] are, that WEC was produced on the outer ring by the driver electric current flow. Table 8 gives the results of the proposed calculation method.

Table 8: Calculation results on NU 207 [9]

bearing type	-	**NU207**	**NU207**	**NU207**	**NU207**
contact	-	**IR**	**OR**	**IR**	**OR**
Hertzian stress p_H	MPa	2400	1900	2400	1900
speed	rpm	2000	2000	2000	2000
C / P	-	> 4	> 4	> 4	> 4
driver	-	none	none	E	E
WEC	-	**NO**	**NO**	**NO**	**YES**
depth y_M	mm	0,21	0,21	0,21	0,21
S $_{WEC\ yM}$	-	**> 1**	**> 1**	**> 1**	**0,937**

The next results are on a ball bearing type 6203. As well as Loos [9], Kawamura and Mikami [10] report WEC damage by applying electric current.

The result of the proposed calculation method can be seen in table 9.

Table 9: Calculation results on 6203 [9,10]

bearing type	-	**6203**	**6203**
Hertzian stress p_H	MPa	2150	2150
speed	rpm	10500	10500
C / P	-	10	10
driver	-	none	E
WEC	-	**NO**	**YES**
depth y_M	mm	0,1	0,1
S $_{WEC\ yM}$	-	**> 1**	**0,932**

Low load conditions and high oil volume flow with so called slip conditions

When the first WEC failures were observed, there was the assumption, that roller slip is a driver of this failure mode. Over the years, also the idea raised, that low load condition in combination with slip conditions could be a driver [11].

Loos [11] examined low load conditions in combination with high loads under high oil volume flow. The result was, that if only high loads were applied, no WEC was found and with a combination of 50 % high load and 50 % low load, WEC arises.

The tested bearing was a NU 222.

The result of the calculation method is shown in table 10.

Table 10: Calculation results on NU 222 [11]

bearing type	-	**NU222**	**NU222**
bearing Load	kN	90	6
C / P	-	3,8	57,5
driver	-	none	SLIP
WEC	-	**NO**	**YES**
depth y_M	mm	0,58	0,05
S $_{WEC\ yM}$	-	**> 1,2**	**0,828**

A comparison of the results above is done to low load conditions and normal oil volume flow. In [23], a cylindrical roller bearing was tested with respect to smearing. No WEC damages are reported. In [25] special research was done on the effect of slip and dynamic. When comparing the results according to the proposed method this is confirmed (table 11).

Table 11: Calculation results on oil volume flow [11,23,25]

bearing type	-	**NU ...**	**NU 215**	**NU 222**
source	-	**[11]**	**[25]**	**[23]**
shaft diameter d_1	mm	160	75	110
C / P	-	66	42	57,5
oil flow	-	normal	high	high ++
WEC	-	**NO**	**YES**	**YES**
depth y_M	mm	0,05	0,05	0,05
S $_{WEC\ yM}$	-	**1,2**	**< 0,8**	**0,817**

Hydrogen

Also hydrogen was always assumed as a driver as well.

In [22], Uyama from NSK did research on the influence of hydrogen on WEC damage. For his research he used an axial ball bearing type 51305. 3 different hydrogen contents were examined and reported. The influence is severe.

While using the proposed method, the material factor $\beta_{M\,(H)}$ could be defined. The factor turned out as:

$\beta_{M\,(H)} \leq 0{,}75$ for the lowest hydrogen content.

Table 12 shows the result of the calculation.

Table 12: Calculation results on 51305 [22]

bearing type	-	**51305**	**51305**
Hertzian stress p_H	MPa	3800	3800
speed	rpm	1000	1000
driver	-	none	H
WEC	-	**NO**	**YES**
depth y_M	mm	0,2	0,2
S $_{WEC\ yM}$	-	**> 1,3**	**< 1**

The question was, where does hydrogen in a gear unit come from and how could hydrogen be generated.

One suspect was, that water, bound in the oil that is used as lubricant, supports the hydrogen origination. However, a lot of research was already carried out with respect to water and lubricants. In [14] the influence of water content in high reference oils was examined. Bearings for this examination were a spherical roller bearing 22206 and a ball bearing 6206.

Even with the highest water content of 5000 ppm, no WEC could be found during all tests. Table 13 shows the calculation results with applying the factor derived from table 12.

Table 13: Calculation results on 22206 and 6206 [14] with $\beta_{M\,(H)} = 0{,}75$.

bearing type	-	**22206**	**22206**	**6206**	**6206**
Hertzian stress p_H	MPa	2400	2400	3600	3600
speed	rpm	5000	5000	5000	5000
C / P	-	2,7	2,7	2,7	2,7
driver	-	none	H	none	H
WEC	-	**NO**	**NO**	**NO**	**NO**
depth y_M	mm	0,14	0,14	0,21	0,21
S $_{WEC\ yM}$	-	**> 1,5**	**> 1,0**	**> 1,5**	**> 1,0**

As the results show, the WEC safety is high for the bearings used in [14], so no WEC could be expected, what is confirmed by the research results.

In [14] Brenner gives values for the maximal comparable stress according to the maximum shear stress criterion and the related depth with respect to the loads in table 13. For the spherical roller bearing 22206, the comparable stress is 1340 N/mm² at a depth of $y_M = 0{,}12$ mm , the occurring stress $\sigma_{occurring}$ according to the proposed method at the depth $y_M = 0{,}12$ mm is 1536 N/mm², taking all occurring stresses into account.

For the ball bearing 6206, the comparable stress is 2032 N/mm² at a depth of $y_M = 0{,}12$ mm , the occurring stress $\sigma_{occurring}$ according to the proposed method at the depth $y_M = 0{,}12$ mm is 2237 N/mm², taking all occurring stresses into account.

It can be noticed, that the calculated stresses according to the proposed method are in the range of what could be calculated with the shear stress criterion.

Why WEC on wind turbine gear boxes?

The application wind turbine has a big variant in load and speed conditions. In IEC 61400-4 [1] those load conditions are explained in more detail.

Figure 6 shows a generic power -speed curve, projected to the bearing NJ 206 used in FVA 541 I [7] “Bearing lifetime Wind gearboxes”.

Figure 6: fictive power curve wind turbine and WEC risk

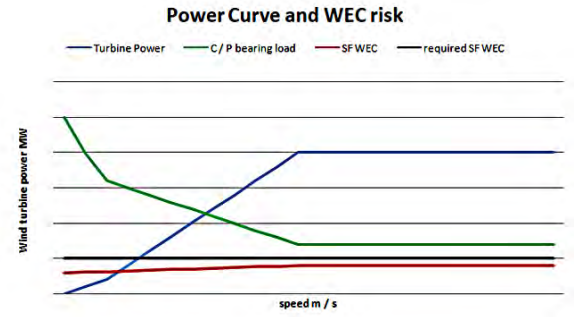

From this figure it can be seen, that lower loads (high C/P values) are even more harmful than high load values.

If drivers are present, the risk of WEC occurrence grows.

Calculation results for big bearings tested on a big size bearing test rig [17,18]

In [17] a big size bearing test rig is introduced and in [19] a method to determine slip conditions on roller bearings. These conditions were important for the tests, documented in [18]. Engelen reports in [18] about tests on bearings with size ...2336 .. with different additional drivers as: cage slip energy, heathcote slip, DC voltage and load reversal.

WEC was found on 2 (4) bearings CRB-3 on the outer raceway, by applying cage slip energy. No WEC was found on 2 CRB-1 bearings, where DC voltage was applied. Table 14 shows the results of the calculation according to the proposed method.

Table 14: Calculation results of of the method for test cases from [18]

bearing type		**..2336 ref**	**..2336**	**..2336**
Type		**-**	**CRB1**	**CRB3**
Hertzian stress p_H	MPa	> 1000	> 1000	> 1000
p_{max} outer ring	MPa	1900	1900	1710
oil type	-	VG 320	A	C
test time	h	-	1500	1500,00
driver	-	**none**	**E**	**SLIP**
depth crack started	mm	-	-	**0,294**
WEC	-	**NO**	**NO**	**YES**
occurrence	-	-	0 of 2	**2 of 4**
depth y_M calculated	mm	0,3	0,3	**0,3**
$S_{WEC\ yM}$	-	**> 1,1**	**> 1**	**0,924**

The calculation results copes with the observations. The calculated critical depth y_M is exactly the value, that was measured on the failed bearings.

The safety value of 0,924 indicates the observation about the population failed.

Drivers and counter measures demonstrated on a fictive NJ 206 wind bearing

As mentioned above, this calculation method enables an engineer to use design criteria to avoid WEC. These drivers and counter measures are explained in more detail by using the bearing from FVA 541 I [7] "Bearing lifetime Wind gearboxes" as a fictive case.

In a first step, operating conditions are defined, which have a high probability of WEC failure for this bearing size and type. The next step is, to go more in detail how drivers and counter measures change the risk to get WEC.

It is supposed, that the bearing NJ 206 is used on a high speed intermediate shaft of a wind turbine gear box. This is a position, where WEC damages have been reported. To find speed and load conditions (table 15) the requirements mentioned in IEC 61400-4 [1] are used.

Table 15: load speed conditions fictive case

Load and speed conditions HSIS NJ 206			
required bearing life ≥	L_{h10}	h	40000
max Hertzian contact stress	p_H	MPa	1650
estimated shaft speed	n	rpm	400
dynamic capacity	C	kN	46
bearing load	P	kN	4
C / P	-	-	11,5

The assumed oil in the calculation is a proven high reference PAO oil, that is common in wind turbines. The oil temperature is estimated with 60°C.

Table 16: Results of the NJ 206 reference case with WEC risk

bearing type	-	**NJ 206**	**NJ 206**
contact	-	**IR**	**OR**
Hertzian stress p_H	MPa	1590	1431
speed	rpm	400	400
C / P	-	11,5	11,5
Lifetime L_{h10}	h	142000	142000
oil viscosity at 60°C ν	mm²/s	138	138
driver	-	none	none
counter measure	-	none	none
WEC	-	**YES**	**YES**
depth y_M	mm	0,07	0,07
$S_{WEC\ yM}$	-	**0,954**	**0,906**

With the fictive conditions from table 15, WEC can be expected on the reference NJ 206.

The calculated safety values are in line with the average safety values mentioned in results and discussion for WEC endangered bearings.

Counter measures to decrease the risk of getting WEC mentioned in this paper are black oxidizing BO and for instance the special CrNiDur steel mentioned in [15]. BO is a common improvement of the raceway surface and this technology is available from bearing manufactures.

There are probably a lot of counter measures with respect to surface and material improvements, the one, where improvements have been reported [4] is black oxidizing BO.

Table 17: population and WEC failure rate for BO

execution	Gear box population	WEC failure rate	observed after
BO	**1150**	**0%**	**2 years**

The next table shows the results if these improvements are applied.

Table 18: Results of the NJ 206 reference case with counter measures as improvement by BO and material

bearing type	-	**NJ 206**	**NJ 206**	**NJ 206**	**NJ 206**
contact	-	**IR**	**OR**	**IR**	**OR**
Hertzian stress p_H	MPa	1590	1431	1590	1431
speed	rpm	400	400	400	400
C / P	-	11,5	11,5	11,5	11,5
Lifetime L_{h10}	h	142000	142000	142000	142000
oil viscosity at 60°C ν	mm^2/s	138	138	138	138
driver	-	none	none	none	none
counter measure	-	BO	BO	M	M
WEC	-	**NO**	**YES**	**NO**	**NO**
depth y_M	mm	0,07	0,07	0,07	0,07
S $_{WEC\ yM}$	-	**> 1**	**< 1**	**> 1**	**> 1**

In this example, only the special material can improve the WEC resistance on the inner ring IR and outer ring OR raceway. BO could improve the safety factor on IR, but not solve the problem on OR. This is in line with some field observations, where also BO coated bearings failed. The question for special materials is the availability of those and the costs.

If negative drivers are present, the safety values decreases, what is shown in table 19.

Table 19: Results of the NJ 206 reference case with negative drivers

bearing type	-	**NJ 206**	**NJ 206**	**NJ 206**	**NJ 206**
contact	-	**IR**	**OR**	**IR**	**OR**
Hertzian stress p_H	MPa	1590	1431	-	-
speed	rpm	400	400	400	400
C / P	-	11,5	11,5	-	-
Lifetime L_{h10}	h	142000	142000	-	-
oil viscosity at 60°C ν	mm^2/s	138	138	138	138
driver	-	E	E	slip	slip
counter measure	-	none	none	none	none
WEC	-	**YES**	**YES**	**YES**	**YES**
depth y_M	mm	0,07	0,07	0,07	0,07
S $_{WEC\ yM}$	-	**< 0,85**	**< 0,85**	**< 0,7**	**< 0,7**

As it can be seen in table 19, if drivers are present, the risk increases severely.

Alternative roller bearing solutions by using the proposed method to compare

In Annex C of the IEC 61400-4 [1] bearing design considerations are given as calculations methods to calculate the contact stress and also criteria to bearing life and designs.

The tables C3 – C6 give explanations to the different designs. Table C7 explains symbols for classifying the designs in suitable (S), suitable with restrictions (SR), unsuitable (U) and no experience (NE) with respect to located and non and cross located bearing uptakes. Table C10 gives recommendations for the high speed intermediate shaft HSIS conditions from table 15.

As the NJ 206 could be a non locating bearing (NL) or a cross located bearing (CL) some alternative bearing designs are applicable.

With respect to the required lifetime and maximum contact stress, the alternative bearing options are shown in table 19 for more or less same dimensions.

Table 20: alternative bearing type solutions to reference NJ 206

alternative bearing options							
execution			**ref**	**ref**	**alt**	**alt**	**alt**
Type	**-**	**-**	CRB	CRB	SRB	SRB	TRB
size	**-**	**-**	NJ 206	NJ 206	22 206	22 206	30 206
bearing uptake	**-**	**-**	NL	CL	NL	CL	CL
classification	**-**	**-**	S	SR	SR	SR	SR
shaft diameter	**d**	**mm**	30	30	30	30	30
width	**b**	**mm**	16	16	20	20	17
dynamic capacity	**C**	**kN**	46	46	64	64	44

The above bearing alternatives have almost the same dynamic capacity and the same bearing width and same inner and outer diameter.

The next table 21 shows the results of the alternative bearings. In the table, only the raceway (IR, OR) with the lowest safety factor is mentioned.

Table 21: alternative bearing type solutions to reference NJ 206 and calculation results

bearing type	-	**NJ 206**	**NJ 206**	**22 206**	**22 206**	**30 206**	**30 206**
contact	-	**OR**	**OR**	**IR**	**IR**	**OR**	**OR**
Hertzian stress p_H	MPa	1590	1431	990	990	1435	1435
speed	rpm	400	400	400	400	400	400
C / P	-	11,5	11,5	16	16	10,9	10,9
Lifetime L_{h10}	h	142000	142000	427000	427000	118000	118000
oil viscosity at 60°C ν	mm²/s	138	138	138	138	138	138
driver	-	none	none	none	none	none	none
counter measure	-	**none**	**M**	**none**	**BO**	**none**	**BO**
WEC	-	**YES**	**NO**	**YES**	**YES**	**YES**	**NO**
depth y_M	mm	0,07	0,07	0,06	0,06	0,09	0,09
S $_{WEC\ yM}$	-	**0,906**	**> 1**	**0,849**	**< 1**	**0,917**	**> 1**

The results show, that it is possible to prevent the reference bearing NJ 206 from WEC. The alternatives are a cylindrical bearing NJ 206 from special bearing steel or a design change to a bearing solution with taper roller bearings 30206 with BO.

The spherical roller bearing is no option. This copes also with observations, specially with respect to the wind turbine gear box application.

Case carburizing

Another discussion is about using case carburized bearings to avoid WEC damage.

The reported failure rates are in table 22.

Table 22: Failure rates on case carburized bearings reported in [4,24]

execution	**gear box population**	**WEC failure rate**	**observed after**
CC [4]	**75**	**2,700%**	**14 month**
CC [24]	**500**	**0,002%**	**3 years**

More detailed information about the reported failures on case carburized bearings in comparison with through hardened bearings can be found in [24].

The comparison makes visible, that case carburized bearings can be an alternative.

Table 23 give results on a comparison between through hardened steel and case carburized steel of a NJ 2334 bearing on a low speed intermediate shaft LSIS, table 24 gives results about 2 different case carburized steel bearings for a rotor shaft.

In the table CC means case carburized and TH through hardened.

Table 23: Results on a NJ 2334 LSIS, reported in [24]

bearing execution	-	**INT-A**	**INT-B**
Type	**NJ 2334**		
Hertzian stress p_H	MPa	1583	1756
Heat treatment	-	CC	TH
speed	rpm	86,12	86,12
driver	-	none	none
WEC	-	**NO**	**YES**
depth y_M	mm	0,6	0,5
S $_{WEC\ yM}$	-	**1,009**	**0,981**

One reason for the performance of the NJ 2334 CC was assumed in [24] due to the presence of residual stress. While there is probably additional tensile stress (35-100 MPa) in the TH bearing, the XRD measurement of residual stress in the CC bearing gave -400 MPa at 500 µm depth. In the calculation of the proposed method a value of -370 MPa at 600 µm depth was taken into account, which lead to an increase of the material value of 135 MPa. This makes a differences. In figure 3 and 4 [24] can be seen, that the crack network varies from 0,3 mm to 0,8 mm. The evaluation depth in the proposed method is 0,5 – 0,6 mm.

Table 24: Results on Taper Roller Bearings TRB on a rotor shaft reported in [24]

bearing execution	-	**ROT-C**	**ROT-D**
Type	-	**TRB**	**TRB**
Hertzian stress p_H	MPa	1634	1798
Heat treatment	-	CC	CC
speed	rpm	13,66	13,66
driver	-	none	none
WEC	-	**NO**	**YES**
depth y_M	mm	0,27	0,31
S $_{WEC\ yM}$	-	**0,995**	**0,892**

In ROT-D bearing WEAs were found in a depth ranging from 400 – 600 µm. The evaluation depth in the proposed method is 0,3 mm.

It can be seen, that the proposed method is also able to make these differentiations based on the definition of the safety factor from table 3.

Influence of oil chemistry CH

In [26] the influence of oil chemistry is reported. Tests were carried out with so called WEC and non-WEC oils. As a result it is reported, that oils with Zink DithioPhosphate in combination with Na sulfonate and or Ca sulfonate could cause WEC. The next table 25 gives an idea, how strong this influence can be. Oil chemistry could be compared to the influence of hydrogen as discussed above with a factor $\beta_{M(CH)} \leq 0{,}7$.

Table 25: Influence of oil chemistry CH as reported in [26] and calculated according to the proposed method

	unit	**ref cal**	**given depth 0,12**	**CH**
Type		**81212**		
speed	rpm	750	750	750
driver	-	none	none	**CH**
WEC	-	**NO**	**NO**	**YES**
depth y_M	mm	***0,3***	***0,12***	***0,12***
S $_{WEC\ yM}$	-	**> 1,1**	**> 1,4**	**< 1**

Can a journal bearing substitute the reference bearing NJ 206?

As already mentioned in the introduction, the WEC field failures lead to questioning the reliability of rolling bearings in wind turbine gear box applications. In [12], an alternative journal bearing concept was introduced for a 2 MW wind turbine gear box. At this moment, only limited experience of the use of journal bearings in wind turbine gear units is public available.

The question is, can a journal bearing substitute the fictive NJ 206 reference bearing.

From [12] reference values are taken for the comparison for this example.

With journal bearings, there are some basic values available [16] for the comparison, as the relation between bearing width and shaft diameter and the projected surface stress. A common value for the width / diameter relation is about 0,5 and for permissible stresses is 5 – 7 MPa. According to experience and chosen materials these values could differ.

Table 26 shows the data and results for the alternative journal bearing.

Based on these simple values, also a journal bearing solution should be possible.

Table 26: alternative journal bearing solutions to the fictive reference NJ 206 based on insights of [12]

bearing type	-	**NJ 206**	[14]	**alt 206**
Roller or Journal	-	**R**	J	**J**
load	kN	**4**	1100	**4**
Hertzian stress p_H	MPa	1431	-	-
specific bearing load p	MPa	-	9,17	**8,33**
limit value ISO 7209-3 p_{lim}	MPa	-	**5 - 7**	**5- 7**
speed	rpm	400	42	400
shaft diameter d	mm	30	400	30
width b	mm	16	300	16
value b / d	-	-	0,75	0,53
C / P	-	11,5	-	-
Lifetime L_{h10}	kh	142	-	-
oil viscosity at 60°C ν	mm²/s	138	138	138
driver	-	none	none	none
counter measure	-	none	none	none
WEC	-	**YES**	-	-
depth y_M	mm	0,07	-	-
S $_{WEC\ yM}$	-	**0,906**	-	-

Conclusions

The proposed method has a mechanical based safety extended with the effect of time dependant stresses. Increasing and decreasing effects on the safety against the risk of WEC failures are taken into account by factors. The method is able to calculate the probability and the risk of the occurrence of WEC damages on rolling bearings in industrial applications.

The approach is able to differentiate the conditions in a way, that the calculations results cope with field and test bench observations. This means, a differentiation between a failed bearing and its non failed neighbour is possible.

The method can be used for these conditions:

Speed 5 – 12000 rpm
Contact stress 300-4500 MPa
Bearing types:
Radial and axial bearings
Cylindrical roller bearings
Taper roller bearings
Spherical roller bearings
Ball bearings

The proposed method is a design tool. With this calculation method, a designer can examine a lot of alternatives and can chose the most reliable and economical solution.

The method enables also to select the type of bearing as rolling bearing versus journal bearing, based on economically and mechanical data.

Outlook

This method is seen as a starting point and further research could increase the accuracy of the factors or extend the approach.

Required input data for the proposed calculation method

Table 27: Input data for the proposed calculation method

Symbol	Description	Unit
z	number of rollers	-
D_w	roller diameter	mm
L_w	roller length	mm
d	bearing inner diameter	mm
d_1	inner raceway diameter	mm
d_2	outer raceway diameter	mm
D	outer diameter	mm
D_m	pitch diameter	mm
b	bearing width	mm
e	equivalent contact angle	-
ν_1	oil viscosity at operating temperature	mm²/s
HV	hardness	HV
p_H	Hertzian surface contact stress	N/mm²
$T_{cal\ PH}$	Torque used for calculation p_H	Nm
p_r	hoop stress	N/mm²
P	bearing load	kN
n	shaft speed	rpm
K_A	application factor ISO 6336-6 flank	-
K_V	dynamic factor ISO 6336 Method B	-

Symbol, description, units

Symbols	description	unit
b^*	Modified half width contact Hertz	mm
Const	Factor for cleanliness	mm³
corr	Correction factor	-
d_1	raceway bearing inner ring	mm
d_2	raceway bearing outer ring	mm
E	modulus of elasticity	N/mm²
f_{cHertz}	correction factor for $\sigma_{p\text{-}Hertz(yM)}$	-
f_{time_o}	cycle related correction factor for strength values	-
f_{time_p}	cycle related correction factor for strength values	-
h	height of a material inclusion	mm
K_A	application factor	-
K_v	dynamic factor	-
l	length of a materia inclusion	mm
N_c	Number of contacts	-
$P_{application}$	equivalent bearing load from application	N
$P_{calculation}$	bearing load for calculation	N
p_H	contact stress Hertz	MPa
w	width of a material inclusion	mm
X	correction factor for calculation half width	-
y_M	material depth for the calculation of S_{WEC}	mm
Y_{WEC}	special WEC Factor	-
β_c	surface factor	-
$\beta_{k\ (yM)}$	notch factor	-
β_M	material factor	-
δ_K	elastic deformation under load	mm
ν	Poisson number	-
$\sigma_{\ occurring\ (yM)}$	Occurring stress number in material depth	N/mm²
$\sigma_{o\text{-}comp\ Hertz\ (yM)}$	Occurring stress from Hertzian stress at depth y_M	N/mm²
$\sigma_{p\text{-}residual(yM)}$	Permissible stress from residual stress at depth y_M	N/mm²
$\sigma_{p\text{-}Hertz(yM)}$	Permissible stress from Hertzian stress at depth y_M	N/mm²
$\sigma_{p\text{-}HV(yM)}$	Permissible stress from material strength at depth y_M	N/mm²
$\sigma_{o\text{-}hoop\ (yM)}$	Occurring stress from hoop stress at depth y_M	N/mm²
$\sigma_{o\text{-}friction\ (yM)}$	Occurring stress from friction stress at depth y_M	N/mm²
$\sigma_{\ permissible\ (ym)}$	permissible stress in material depth	N/mm²
Z	factor for Y_M depending on bearing type	-

References

[1] NN, Wind Turbines- Part 4, Design requirements for wind turbine gear boxes, IEC 61400-4, Genève, 2012

[2] NN, Rolling bearings - Damage and failures - Terms, characteristics and causes, ISO 15243, Beuth, Berlin, 2004

[3] Dirk Leimann, Calculation of White Etching Crack WEC Load Carrying Capacity acc. to the Method of Leimann, Tagungsband DMK 2019, Dresden 2019

[4] Johan Luyckx, „WEC failuremode on rollerbearings“, VDI Wissensforum, Tagung Gleit- und Wälzlager Schweinfurt, Düsseldorf 2011

[5] NBN E 23-402 :2019, Tandwielen, Berekening van tandflankbreukbelastbarheid, Engrenages, Calcul de la capacité de charge en cas de fracture du flanc de la dent, Bruxelles, 2019

[6] D. Leimann, Vergleichspannung für Zahnflanken, Offenlegungsschrift DE 10 2017 209 512 A1, München, 2018

[7] B.Hacke et all, FVA Forschungsvorhaben Wälzlegerlebensdauer Windgetriebe, Vorhaben Nr. 541 I, Forschungsvereinigung Antriebstechnik E.V., Frankfurt, Heft 967, 2011

[8] C. Bongardt, M-O Özel et all, Risse auf Lageringen, Gefügeveränderungen in Wälzlagerringen mit Rissen als Folgeschaden, Vorhaben FVA 707 I, Heft 1121, 2014

[9] J. Loos et all, Einfluss hoher elektrischer Ströme auf die WEC- Bildung in Wälzlagern, Tagungsband ATK 2016, Aachen, 2016

[10] T.Kawamura, H.Mikami, Development of a NH103A Long-life Grease for Automotive Components, NTN technical review no. 75, NTN Osaka, Japan, 2008

[11] J. Loos et all, factors increasing the risk of WEC-formation in large size bearingswith full film fluid lubrication, FVA Bearing World 2016, Frankfurt, 2016

[12] D. Leimann, M. van den Doncker, Berechnung- und Testerfahrungen von gleitgelagerten Planetenrädern in einem 2 MW Windkraftgetriebe, Getriebe aktuell, 7. Ausgabe, VDI Wissenschaftsforum, September 2015

[13] J. Loos et all, WEC Bildung in Wälzlagern, VDI Fachkonferenz an Lagern, VDI, Düsseldorf, 2016

[14] D. Brenner, Einfluss von Wasser in Hochleistungsölen auf die Wälzlagerlebensdauer, Dissertation Fakultät Maschinenbau, Magdeburg, Shaker Verlag, 2009

[15] Brochure “Materials for Rolling Bearing Technology”, Schaeffler, Herzogenaurach, 08-2015

[16] NN, Hydrodynamic plain journal bearings under steady-state conditions – circular cylindrical bearings, part 3, ISO 7902-3, Genève, 1998

[17] K. Engelen, M. Ooms, D. Leimann, Slip behavior on roller bearings in wind turbine gear boxes, VDI Berichte Gleit- und Wälzlagerungen, VDI Verlag, Düsseldorf, 2015

[18] K. Engelen et al, WEC reproduction on large size roller bearings, CWD Tagungsband, Aachen, 2017

[19] D. Leimann, K. Engelen, Rolling- Element Bearing for a Gearing, US 2016/0169288 A1, US patent office, 2016

[20] J. Loos et all, Bearing Currents as WEC-Trigger in Wind Turbines, Tagungsband CWD 2019, Aachen, 2019

[21] NN, Calculation of load capacity of spur and helical gears - Part 4: Calculation of tooth flank fracture load capacity, ISO/TS 6336-4:2019-01, Genève, 2019

[22] H. Uyama, the mechanism of white structure flaking in rolling bearings, wind turbine tribology seminar, NREL, Broomfield, Colorado, US

[23] R.D. Evans, Classic Bearing Damage Modes, wind turbine tribology seminar, NREL, Broomfield, Colorado, US

[24] R. Errichello et al, Investigations of bearing failures associated with white etching areas (WEAs) in wind turbine gear boxes, Power Transmission Engineering, Chicago, IL, US, 2014

[25] B. Tarigan, Entstehung von White Etching Cracks in schlupfbehafteten Zylinderrollenlagern bei torsionaler Drehdynamik, Dissertation, TU Clausthal, Clausthal, 2018

[26] J.T. Carey and J.W.H. Franke et al, Lubricant effects on white etching cracking failures in thrust bearing test rig, ExxonMobil, Schaeffler, Hannover Fair Presentation, April 2017

[27] Leimann, D, Calculation method to evaluate the Risk on WEC occurrence in Industrial Applications, Bearing World presentation, FVA, Frankfurt, Germany, 2020

Enhancement of the Insulation Properties of Thermally Sprayed Ceramic Bearing Coatings

Kirsten Bobzin[1], Wolfgang Wietheger[1], Martin A. Knoch[1], Elisa Burbaum[1], Tim Hosenfeldt[2], Nazlim Bagcivan[2], Mehmet Öte[2], Astrid Heckl[2], Björn Müller[2], Carsten Kunde[3], Anna-Lena Elsner[3]

[1] *Surface Engineering Institute, RWTH Aachen University, info@iot.rwth-aachen.de*
[2] *Oberflächentechnologie, Schaeffler Technologies AG & Co. KG, info.de@schaeffler.com*
[3] *Diamant Metallplastic GmbH, info@diamant-polymer.de*

Abstract– Thermally sprayed ceramic coatings partly include desired inhomogeneities like pores, which can be filled by sealers. Common bearings for drive trains in rail vehicles with electrical engines are coated with ceramics by thermal spraying for electrical insulation. The lifetime of these bearings can be reduced by the electrical characteristics of modulated frequency converters in electrical engines. High frequencies and a strong increase of the voltage may lead to a premature breakdown of the bearing. This breakdown is identifiable by electrical discharge machining of the bearing surface and caused by the functional failure of the ceramic coating at high frequency currents. Therefore, a novel measurement approach for the reproducible validation of the electrical insulation properties of coating materials is developed. With this approach, the influence of the frequency on the alternating current resistance (impedance) of different coatings is investigated at frequencies between 100 mHz and 5 MHz under dry and moist conditions. Furthermore, XRD measurements are used to examine the phase composition in the ceramic coatings. The microstructure and inhomogeneities are evaluated by optical and electron microscopy. Correlations between impedance results, XRD measurements and the coating microstructure have been identified. Increased impedance is measured for the samples produced with feedstock material with a grain fraction of -22 +5 µm. The investigated increased micro-crack density and the reduced large pore content of these samples lead to increased impedance in dry and moist ambient conditions.

Keywords – thermal spraying, atmospheric plasma spraying, electrical insulation, impedance measurement

1. Introduction

Since the European Union has decided that the CO_2-emission rates for 2030 must be reduced by 32 % compared to 1990 [1], electro mobility has been gaining a tremendous increase of interest in the last decade. Additionally to the decarbonisation of transport, the efficiency of electrical transport systems should be increased. For this, efficient electrical engines in modern rail vehicles were developed. These engines experience high voltages with steep increases due to the frequency modulators. These conditions can reduce the lifetime of bearings in drive trains without sufficient electrical insulation due to parasitic discharges damaging the raceway by electro erosion. Consequently, commercially available bearings are coated on the outer ring with alumina (Al_2O_3) to successfully protect bearings from electrical discharges in current drivetrains. However, future engine developments and extreme environmental conditions with high air humidity levels might require an improved insulation. Therefore, Al_2O_3-based high performance coating systems are being developed.

Thermal spraying (TS) is a coating technology with the possibility to coat complex geometries and to apply a broad variety of feedstock materials [2]. Feedstock materials are used mostly in form of powder or wires. The particles of the feedstock material are molten in or in front of a torch and accelerated towards a substrate by the carrier gas. Properties like particle temperature or velocity vary between the different TS-processes and process parameters. Moreover, the coating properties can be modified by selective adjustment of the process parameters, which influence the coating microstructure and phase composition.

Ceramic-coated bearings used in systems with electrical engines are, in general, deposited by atmospheric plasma spraying (APS), which is schematically displayed in Figure 1. In the APS-process, a hot plasma jet with temperatures up to T = 20,000 K [3] is generated between an anode and a cathode. To generate an arc inside the torch, a voltage is applied between the two electrodes. The incoming process gas mixture of Argon and Hydrogen is ionised and forms a plasma jet. In general, the current I between depends on the applied voltage and the electrical conductivity. In plasma spraying, the current is controlled by adjusting the applied voltage to control the power input. As the plasma temperature is well above the melting point of oxide ceramics, it is possible to coat the outer surfaces of rolling bearings with alumina using APS. [4]

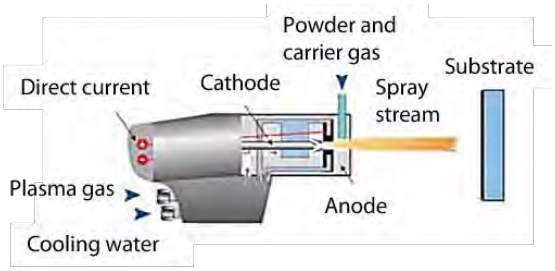

Figure 1: Schematic of the APS process [5]

In general, alumina as sintered bulk material is known for its high electrical resistance of $\rho = 4\text{-}13 \cdot 10^{10}\ \Omega\,m$ [6], which can vary due to

variation of the coating microstructure from $\rho = 5 \cdot 10^7 3 \cdot 10^{10}$ Ω m for thermally sprayed coatings [7]. The main difference between sintered alumina and thermally sprayed alumina coatings is the content of the α-alumina phase. In contrast to sintered alumina, thermally sprayed alumina coatings consist predominantly of metastable γ-alumina [8]. The reason for the high γ-alumina content in TS-coatings is the high cooling rate during coating deposition [3]. The thermodynamically stable α-alumina phase has an oxide sub lattice with a hexagonal closest packing (hcp) structure. The metastable γ-alumina phase is present in a defect spinel structure (Fig 2, (a)). This causes a change in the electrical resistance, in the water absorption and in the coating microstructure. In contrast to α-alumina, γ-alumina is strongly hygroscopic and can be even used as a catalyst due to its high water absorption [9].

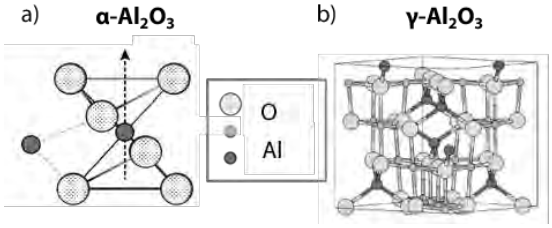

Figure 2: Crystallographic structure of (a) α- and (b) γ-alumina [10, 11]

In general, the water absorption of alumina coatings for electrical insulation should be limited. In case of bearings for electrical drive trains, steep voltage increases and high voltage amplitudes already pose high demands on the coatings. Therefore, these an organic sealer is used for the coatings, as water uptake could result in a reduced electrical resistance of the coating.

During the TS-process, particles from the feedstock material are molten or partly molten in the free-jet and accelerated towards the substrate's surface. They flatten on the surface and solidify, forming a layered coating structure. The particle states, when hitting onto the substrate, depend on the particle injection in the plasma jet and the particle size and lead to differences in particle velocity and temperature. Due to the difference in the particles states, the coating microstructure exhibits in-homogeneities, which are displayed in Figure 3. The microstructure of a TS-coating consist of a three dimensional interconnected network of pores and micro-cracks. These pores and micro-cracks of a TS-coatings for bearings are usually filled by an organic sealer with the overall aim to reduce the water infiltration into the coating along the pores and micro-cracks [12]. Therefore, to reduce the overall water absorption of the TS-coating the performance of the sealer is of great importance. Sealer infiltration is affected by the coating microstructure, which, in turn, changes when the process parameters are adjusted to modify the α-alumina content [7].

To increase the electrical resistance of the established alumina bearing coatings, the influence of the microstructure and the phase content on the impedance is investigated. Therefore, different coating micro-structures were specifically adjusted by a variation of the TS-process and the choice of feedstock material. These samples were subjected to a comparative study with focus on the impedance values in dry and moist conditions over a frequency range of 100 mHz ≤ f ≤ 5 MHz, the coatings porosity and the process-related phase content. The predominant mechanisms influencing the electrical insulation were determined.

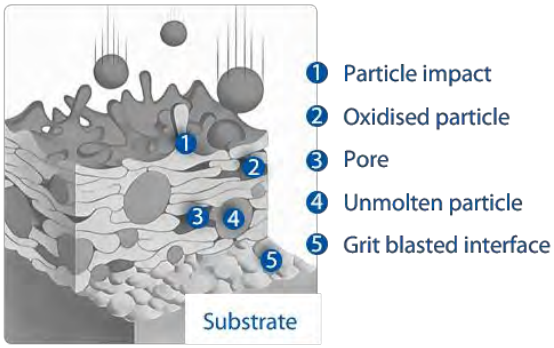

Figure 3: Schematic representation of the characteristics of a thermally sprayed ceramic coating after [3]

2. Experimental procedures

The experimental methods and corresponding theoretical background are presented in this chapter. The TS-coating as the matrix material and the applied sealer as a filler are investigated with the overall aim to increase the performance of this composite coating system.

2.1. Sample preparation

The investigated samples where coated using the APS-system TriplexPro-210 by Oerlikon Metco with a Ø = 9 mm plasma nozzle. Two different alumina feedstock powders, Metco 6051 with a grain fraction of -22 +5 µm and Metco 6062 with a grain fraction of -45 +15 µm from Oerlikon Metco, were applied on 100Cr6-steel substrates, which are conventionally used for rolling bearing materials. The flat substrate samples were rotating during the coating process to imitate the relative motion of a radial bearing during coating deposition. The free-jet was perpendicular to the sample's surface during the whole process. The directions of motion are displayed in Figure 4.

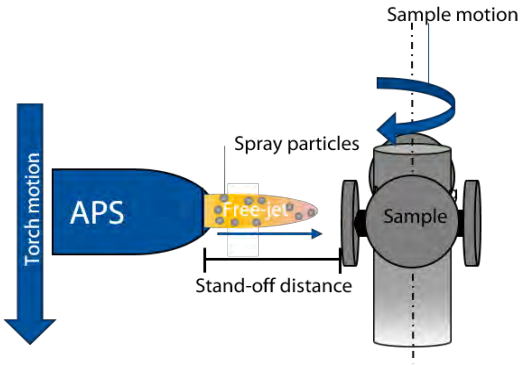

Figure 4: Schematic of the samples motion and mounting during the thermal spraying process

To evaluate the influence of the microstructure and the α-/γ-alumina content on the electrical properties of the coatings, the stand-off distance s was varied, whereas all other process parameters in Table 1 remained constant. A residual coating thickness t_r of t_r = 250 µm after grinding was targeted.

Table 1: Process parameters of APS process

Current I [A]	450
Process gas $Q_{Ar/H2}$ [SLPM]	66
Surface velocity v_S [mm/s]	750
Powder feed rate Metco 6062 [g/min]	21.5
Powder feed rate Metco 6051 [g/min]	18.0
Stand-off distance s [mm]	120, 150
Residual coating thickness t_r [µm]	> 250 µm

To ensure reproducibility and comparability among the different samples for further investigations, all samples were post-treated identically. The samples were first sealed in the as-sprayed state with an epoxy-based sealer from Diamant Metallplastic GmbH. The sealer was applied uniformly with a pipette on each sample.

After the solidification of the sealer, the organic top coat was removed by grinding. To ensure the same conditions for the samples, the samples were then uniformly ground by a cup grinder. This also ensures plane parallel samples for further investigations. Afterwards, the samples were cleaned using an ultrasonic ethanol bath before they were conditioned in different air humidity levels (r. h.) for a week at room temperature (RT). The considered humidity levels were 5 r. h. and 100 r. h. to compare the samples, on the one hand, in dry conditions without the influence of water and, on the other hand, under extreme environmental conditions with high air humidity levels.

2.2. Impedance measurement

The samples were taken from the conditioning chamber and measured within two minutes in order to keep the humidity levels constant. The newly developed measurement set-up is displayed in Figure 5. The sample is placed between two electrodes, which are connected with the potentiostat Reference600+ from Gamry Instruments. The clamp presses the electrodes and the sample together to ensure good contact. Between the lower electrode and the grounding steel plate, an insulating material is placed. The grounding plate is in contact with a faraday's cage, which surrounds the electrode-sample-electrode stack. This prevents possible influences of the surrounding electromagnetic fields on the impedance measurement.

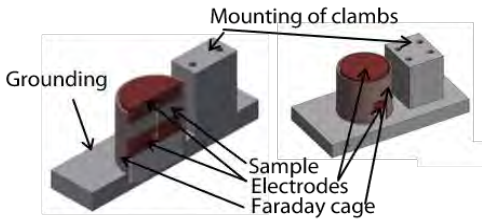

Figure 5: Newly developed measurement set-up for impedance measurement of flat specimen

The ceramic coating surrounded by the steel substrate of the bearing ring and the steel housing can be considered as an ideal plate capacitor for further analysis. Regarding a equivilant circuit diagramme the capacity C and the ohmic resistance R is in parallel. The steel is electrically conductive and the ceramic coating represents an insulating dielectric between the plates, separating the charge. The capacity C is given in *Eq. 1:*

$$C = \varepsilon_0 \, \varepsilon_r \, \frac{A}{d} \qquad \textit{Eq. 1}$$

In the geometry factor $\frac{A}{d}$, the measured area A is divided by the thickness d of the dielectric. The electrical field constant ε_0 is a natural constant and the dielectric constant ε_r presents a material constant. For sintered bulk Al_2O_3, the dielectric constant is $\varepsilon_{r,Al2O3} = 9{,}4$ at f = 1 MHz [13]. The microstructure of the thermally sprayed coatings, as well as the different α- and γ-alumina-contents, can influence the dielectric constant. Pawlowski found a difference in the dielectric constants of sealed and unsealed TS-coatings [7]. The sealed coatings exhibit a lower dielectric constant. In general, the dielectric constant decreases with increasing frequency. In case of an alternating current (AC), the dielectric constant ε_r is a complex variable (see *Eq. 2*):

$$\varepsilon_r = \varepsilon_r' - j\varepsilon_r'' \qquad \textit{Eq. 2}$$

The real part ε_r' is dependent on the polarisation and the imaginary part ε_r'' indicates the dielectric loss [14]. j represents the imaginary unit.

The overall insulation behaviour of bearing coatings in the application of train vehicles is a result of the electrical insulation of the different materials present in the coating, such as organic sealer, ceramic coating and water from the surrounding atmosphere. Polarisation is defined as the sum of dipole moments per unit of volume and can mainly be detected in insulating materials exposed to an electric field (E-field). Without applied E-field, the dipoles are compensated. The dipole moments are induced in ceramics due to the shift of the anionic and cationic crystallographic sub-lattices based on the applied AC current. Figure 6 displays the different polarisation mechanisms with and without applied E-field. Figure 7 shows a superstition of the different polarisation mechanisms, which reduces with increasing frequency and therefore, results in a decreasing ε_r'. The electron and ion polarisation exists in every material. The electron polarisation is based on the shift of the electrons to the atomic nucleus by the E-field (Figure 6 a)). In ion polarisation, anions are shifted against cations (Figure 6 b)). Both polarisation mechanisms reduce the electrical insulating character of the material when a resonance with the applied AC current occurs. This effect occurs at $10^{11} \leq f \leq 10^{13}$ Hz for ion and at $10^{14} \leq f \leq 10^{15}$ Hz for electron polarisation (Figure 7). The space charge polarisation fails first at low frequencies. This polarisation mechanism mainly depends on the charge separation at grain boundaries (Figure 6 d)). With increasing frequency, these charge separation cannot be uphold as electrons in the material oscillate with a lower amplitude in the applied E-field and thus, the insulation based on charge separation breaks down. The orientation polarisation is based on permanent dipoles based on different electronegativity of the atomic bonds, where charge is asymmetrically distributed in the bonding. These permanent dipoles occur in a preferred direction with applied E-field (Figure 6 c)). [15]

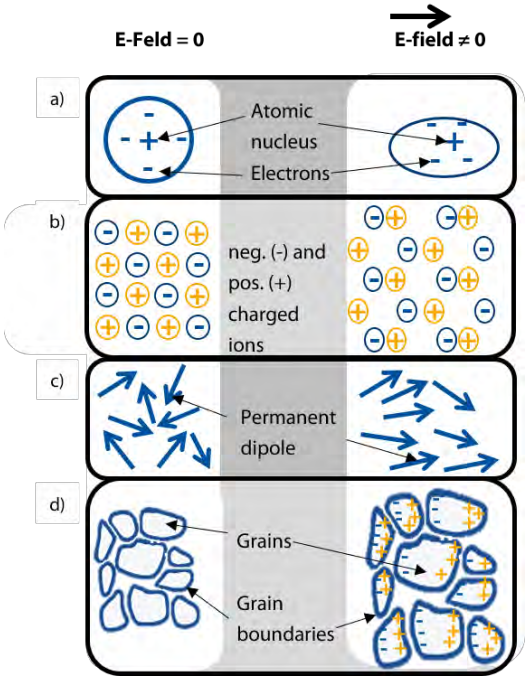

Figure 6: Schematic figure of different polarisation mechanisms: (a) Electron polarisation, (b) Ion polarisation, (c) Orientation polarisation and (d) Space charge polarisation after [15]

Figure 7 shows that at $10^{-4} \leq f \leq 10^{-2}$ Hz, the space charge polarisation and at $f < 10^{10}$ Hz the orientation polarisation relaxes. In contrast to the before mentioned ion and electron polarisation, the orientation and space charge polarisation break down by relaxing which is visible in Figure 7. The reason for this is that these polarisation types cannot resonate with the frequency of the applied E-field due to mechanical reorientation processes of the charges. [16]

In conclusion, the overall electrical resistance is a superposition of all active polarisation mechanisms. Consequently the resistance decreases with decreasing remaining polarisation mechanisms [15].

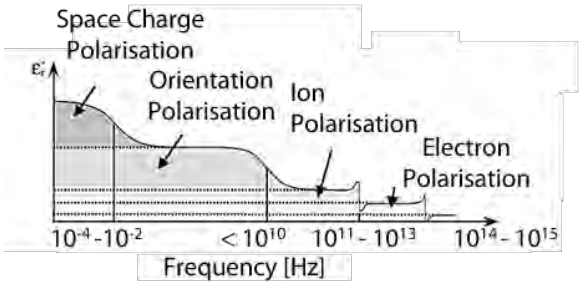

Figure 7: Mechanisms of polarisation loss after [15]

Regarding the dielectric losses ε_r'' of AC-current on a capacitor, the impedance is investigated. The impedance Z is the AC-resistance and depends on the ohmic resistance R and the reactance X, see Eq. 3:

$$Z = R + jX \qquad \text{Eq. 3}$$

Wherein the reactance of a capacitor $X = Z_C = -\frac{1}{fC}$. The overall impedance of the parallel connection of an ideal plate capacitor is given in Eq. 4:

$$Z = \frac{1}{\frac{1}{Z_R} + \frac{1}{Z_C}} \qquad \text{Eq. 4}$$

With Z_R = R, the overall impedance consists of a frequency independent ohmic part (red dotted line, Figure 8) and a frequency dependent capacitance part Z_C (yellow dotted line, Figure 8). The measured impedance is a nett impedance curve following the path of the lowest impedance, which is coloured black in Figure 8.

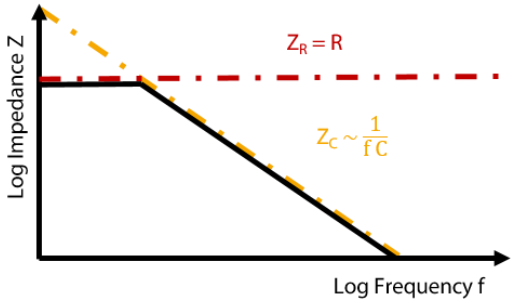

Figure 8: Schematic of an impedance measurement curve with a frequency independent ohmic resistance part (red dotted) and a capacitance part (yellow dotted), the black line is the net curve

To evaluate the electrical insulation of the coatings impedance measurements have been conducted. Taking into account the intended use case of rolling bearings for drive-trains of electrical vehicles, a frequency range of 0.1 Hz ≤ f ≤ 5 MHz with a voltage amplitude of û = 3.54 V, which includes the maximum voltage amplitude and frequency for this measurement cell, was used. Bearings might be exposed to high r. h. levels. Therefore, to compare the difference in water absorption of the samples and consequently the change in impedance among the different coatings, the samples were conditioned at different humidity levels. Each measurement was conducted twice; each presented data point is the mean value of both measured values.

2.3. Evaluation of the microstructure

The properties of a coating are determined by chemical composition, coating microstructure and phase composition or crystallographic micro-structure. The metastable γ-alumina phase is predominantly present in TS-alumina due to the high cooling rates during the coating deposition. Moreover, the process parameters as well as the grain fraction of the feedstock material can be used to influence the phase composition and coating microstructure of the TS-coating.

Cross-sections of the samples in the as-sprayed condition were prepared for evaluation of the microstructure. To ensure a good reproducibility and high stability of the coating during metallographic preparation, vacuum embedding has been used. All samples were ground and polished uniformly.

The optical microscope Zeiss Axio Imager 2 (Oberkochen, Germany) was used to analyse the cross-sections. A polarisation filter was used to ensure a good material contrast between pores and matrix. With the software, ImageJ by Fiji [17] the porosity analysis could be conducted by optical image analysis. The presented values may deviate from known values as the used polarisation diminishes phase contrasts of different alumina phases as well as contaminations. This would falsify the given porosity values. The result is therefore not the porosity itself but the content of large pores. These pores are assumed to be a challenge regarding sealer infiltration. In addition to this value, the combined content of porosity and micro-cracks was determined using SEM-images with Phenom XL from Zeiss (Jena, Germany).

Both measurements of the porosity were conducted on three different positions. The measurement area of the large pore content is 600 x 150 µm² and for the SEM porosity and micro-crack measurement is 250 x 200 µm².

2.4. Evaluation of alumina phases

The investigation of the alumina phase was conducted by X-ray diffraction with the XRD 3000 from Seifert (Schnaittach-Hormersdorf, Germany). CuK_α radiation with a wavelength of $\lambda_{CuK\alpha} \approx 1.54$ Å was used [18]. The peak positions of alumina is given by the International Centre for Diffraction Data (ICDD) card 00-046-1212 for α- and 00-056-457 for γ-alumina. The investigation of the content of α- and γ-alumina in the coating is conducted qualitatively as addition to the impedance and porosity measurement.

3. Results and discussion

For the following section the samples notation is set up from the feedstocks' grain fraction with F for fine and C for coarse powder. The following number is the off-stand-off distance s = 120 or 150 mm. The last part of the notation is the relative air humidity (r.h) the sample was conditioned in for a week.

3.1. Impedance results

All investigated samples, which were conditioned at 5 r.h, are displayed in Figure 9. The upper figure shows the complete frequency range of the measurement. The impedance of the samples decrease with increasing frequency. For a more detailed view, the critical range, in which the impedance is the lowest, of 1 MHz ≤ f ≤ 5 MHz is displayed in Figure 9 b). Sample C-150 exhibits the lowest impedance with $Z_{5MHz,C\text{-}150} = 1.3\ \Omega{*}cm^2$. This comparison shows the properties of the samples in

dry conditions. Consequently, pores inside the TS-coating can improve the electrical insulation.

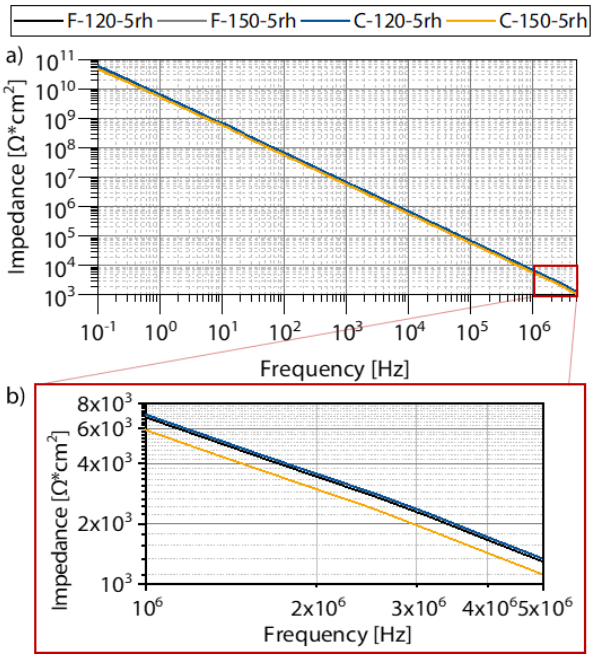

Figure 9: Impedance curve of all samples conditioned at 5 r. h. with an overview of the total measurement range (a) and the same curve at detail view in the range of $10^6 \leq f \leq 5 \cdot 10^6$ Hz (b)

As bearings in real applications might experience extreme atmospheric conditions like high air humidity, the impedance measurement was also conducted with samples conditioned in 100 % r. h. over one week (see Figure 10). In contrast to the impedance measurement of samples conditioned in 5 r. h., the 100 r. h. samples F-120 and F-150 follow an almost frequency independent slope in the range of $10^{-1} \leq f \leq 3 \cdot 10^{-1}$ Hz, which indicates an onset of the ohmic part, compare Figure 8. Reason for the visible frequency independent ohmic resistance part of the impedance curve is the reduced ohmic resistance Z_R, due to absorbed water in the coating system. The samples coated with the coarse feedstock material additionally exhibit an increase of the impedance in the range of $10^{-1} \leq f \leq 1$ Hz. A possible explanation for this phenomenon could be a decrease of the ohmic resistance based on the presence of water in the coating system. Niittymäki et al. [19] made a similar observation, that impedance values at lower frequencies are more sensitive to the amount of water in the system than values at higher frequencies. Further investigations need to be conducted to verify this hypothesis.

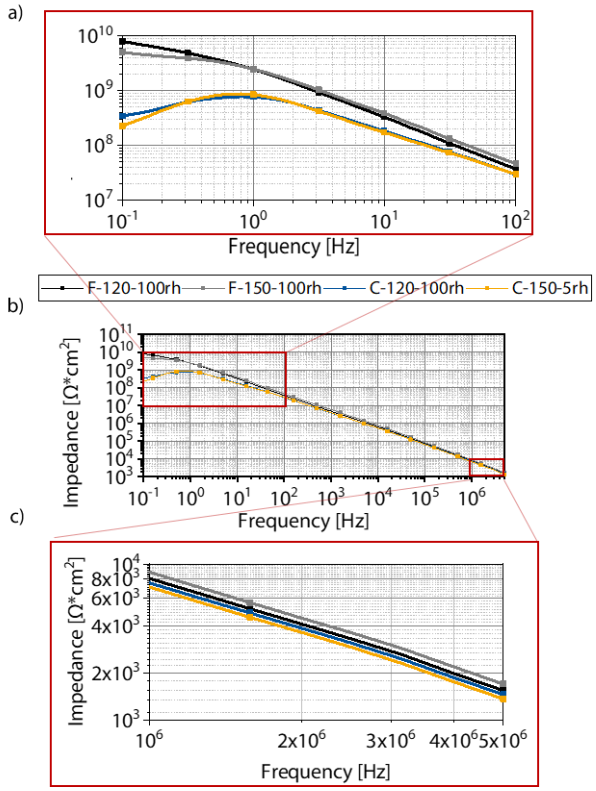

Figure 10: Impedance curves of all samples conditioned at 100 r. h. with an overview of the total measurement range (b) and the same curve at detail view in the range of $10^{-1} \leq f \leq 10^2$ Hz (a) and in the range of $10^6 \leq f \leq 5 \cdot 10^6$ Hz (c)

The samples with the fine feedstock material exhibit a higher impedance than the samples with the coarse feedstock material. Therefore, it is possible that the F-120 and F-150 samples have a lower water absorption then the C-120 and C-150 samples.

To compare the influence of the relative humidity on each sample, a comparison of each sample conditioned in 5 r. h. and 100 r. h. is displayed in Figure 11. Furthermore, Table 2 compares the values of the impedances at f = 0.1 Hz and f = 5 MHz. It can be seen that the F-samples exhibit the highest impedance at 100 r.h and f = 5 MHz, whereas the highest impedance at 5 r. h. and f = 5 MHz was found at C-120 and F-150. In accordance to the literature [19], decrease of impedance with the increased air humidity is only found at small frequencies. At f = 0.1 Hz the impedance of the samples decreases about one order of magnitude for both F-samples and two orders of magnitude for the C-samples, when exposed to high air humidity.

In contrast to this, the increased air humidity does not exhibit a strong influence on the impedance at f = 5 MHz. Contrary to the expectations, the impedance even slightly increases for the 100 r. h. samples at f = 5MHz. This effect might be caused by water absorbed to the hybrid system of sealer and ceramic coating, which can influence the dominant polarisation mechanisms. Due to the defects of the TS-coating, the different alumina phase contents and the present sealer, the impedance curves differ from the ideal plate capacitor. This change causes a

different slope of the capacitive part of the impedance curve. Additionally, water also changes the slope of the impedance curves according to Küchler [14], which can be seen in Figure 11 when comparing the different impedance curves of the same sample qualitatively.

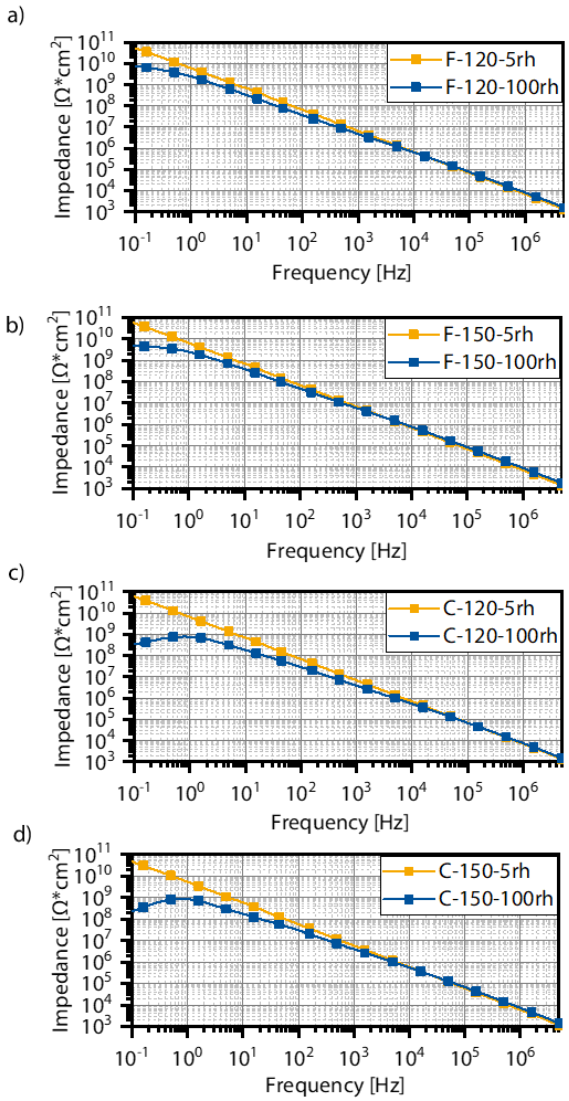

Figure 11: Comparison of impedance of F-120 (a), F-150 (b), C-120 (c) and C-150 (d) conditioned in 5 r. h. and 100 r. h.

In conclusion, the F-samples exhibit the best insulation properties for this measurement conditions in combination with the selected sealer. This is clearly shown by the relatively low decrease of the impedance at f = 0.1 Hz from 5 r. h. to 100 r. h., indicating a lower water absorption. In dry conditions, the lowest impedance is found in the C-150 sample, which might be caused by the microstructure and alumina phase contents in this coating.

Table 2: Comparison of the impedance results of different samples at f = 0.1 Hz and f = 5 MHz

sample	r. h.	$Z_{0.1\ Hz}$ [GΩ*cm²]	Z_{5MHz} [kΩ*cm²]
F-120	5	54.2	1.3
	100	7.9	1.5
F-150	5	56.8	1.3
	100	5.1	1.7
C-120	5	60.3	1.1
	100	0.3	1.5
C-150	5	46.6	1.3
	100	0.2	1.3

3.2. Microstructure

The light microscopic images with polarisation filter of the four different samples are shown in Figure 12. The high contrast between large pores (black) and the coating (bright) was achieved by using a polarisation filter.

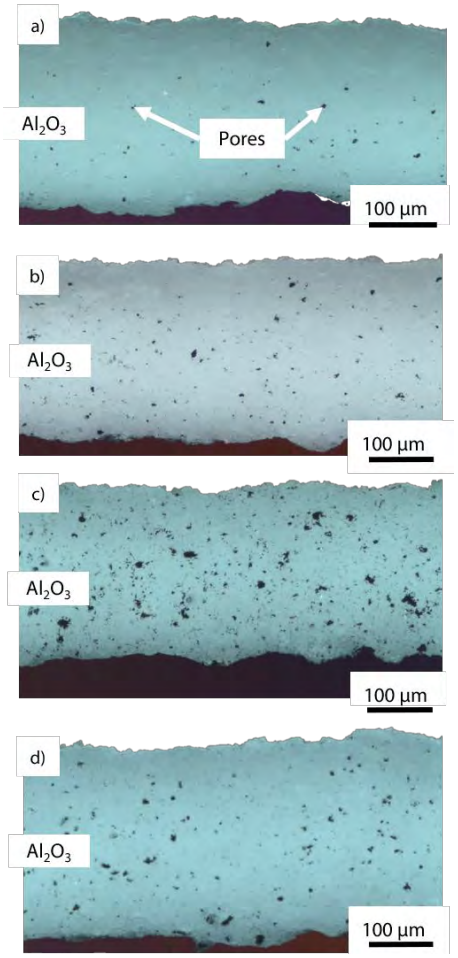

Figure 12: Light microscopic images with polarisation filter of cross-sections of the investigated samples a) F-120, b) F-150, c) C-120 and d) C-150 in the as-sprayed state

The content of large pores of each sample, measured based on light-microscopic images, is displayed in Table 3. It is obvious that with increasing grain fraction of the feedstock material there is also an increase of the large pore content visible.

In relation to Figure 10, it can be seen that at low frequencies, when exposed to 100 % r. h., the fine powders exhibit the highest impedance. This correlates to the low porosity values from Table 3. As large pores are usually not completely filled by the sealer, such a partially filled pore can be considered as a reservoir for water. The presence of water decreases the electrical insulation. Consequently, with this sealer and TS-coating combination, fine powders result in a denser ceramic coating, which reduces the water absorption and increases the impedance.

Table 3: Porosity measurement by light microscopy of three different positions of given samples in an area of 600 x 150 µm²

sample	Large pores [%]	Standard deviation
F-120	0.3	0.2
F-150	1.6	0.7
C-120	11.5	7.7
C-150	5.3	2.5

Comparing the impedance results of all samples conditioned in moist conditions, both C-samples show almost the same impedance curve at low frequencies. This correlates to the increased content of large pores of these samples compared to the F-samples, as the large pores of the TS-coating probably were not filled completely by the sealer and water was absorbed to the coating system. C-120 is approximately twice as porous as C-150, but regarding Figure 10 b) the impedance measurement does not show a great difference between the two samples. This might be explained by the hypotheses that the sealer fill the pores up to a certain content of large pores and limits water absorption into the coating. When the content of pores cannot be filled by the sealer properly, the impedance decreases.

A closer view on the cross section with scanning electron microscopy (SEM) was conducted to evaluate micro-cracks and small pores in the TS-coating. The SEM images of the investigated samples are displayed in Figure 13. As the SEM images are based on the interaction of electrons from the SEM with the atoms of the investigated sample, the colours are dependent on the material composition. The higher the mass of the atoms, the brighter the colour.

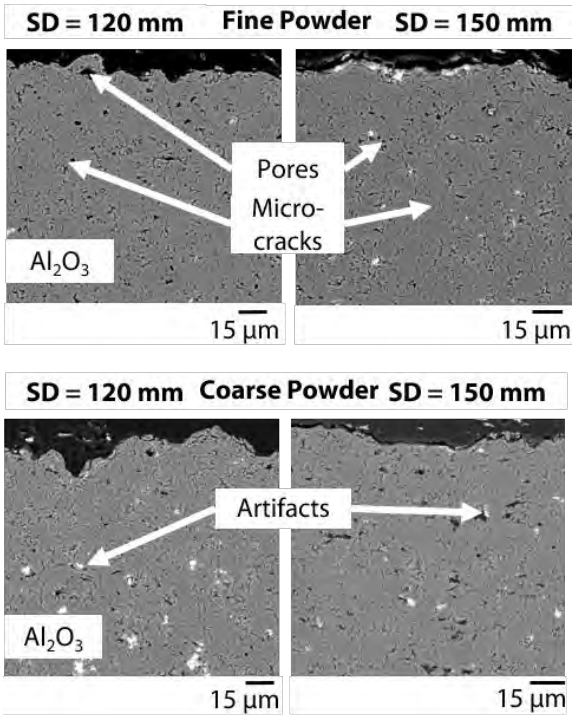

Figure 13: SEM images of cross-sections of the investigated samples with pores, micro-cracks and contaminants from the metallographic preparation

Micro-cracks are a few micro-metres or less long and usually exhibit a width of w < 1 µm. Figure 14 exemplarily displays micro-cracks found in all samples. The micro-cracks can appear perpendicular to the flattened splats and along their boundaries.

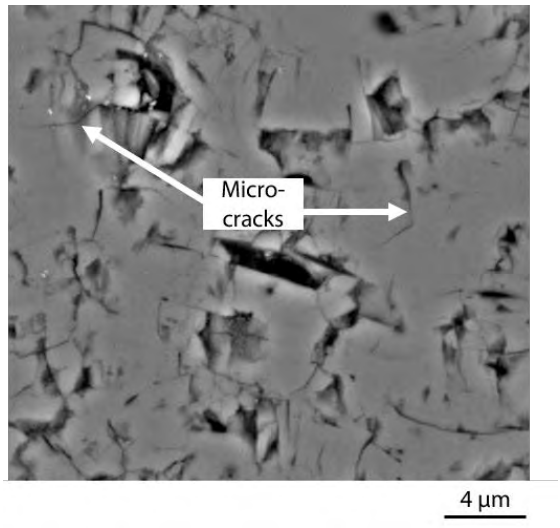

Figure 14: Detail view of F-150 as example for pores and micro-cracks in ceramic TS-coatings

The micro-crack and pore contents where determined with the ImageJ software in an area of 250 x 200 µm². The micro-crack and pore contents are given in Table 4.

Table 4: Content of micro-cracks and pores measurement by SEM of three different positions of given samples in an area of 250 × 200 µm²

Sample	Micro-crack and pore content [%]	Standard deviation
F-120	18.4	2.9
F-150	18.3	0.1
C-120	15.0	2.1
C-150	15.3	1.8

In contrast to Figure 12 and Table 3, Table 4 indicates that the F-samples and the C-120 sample are in the same range of porosity and micro-crack content. As the F-samples had, compared the C-samples, a lower content of large pores, the C-sample's micro-crack content is, relative to the total porosity and micro-crack content, lower than for the F-samples. This result correlates to the impedance measurement, in which the F-samples exhibit the highest impedance for 100 r. h. and low frequencies. The high impedance at 100 r. h. can result from the lower water up-take due to the potential higher fill level of the sealer. Micro-cracks, in theory, improve the infiltration of the sealer into the coating.

As the sealer is applied on the top of the samples, it infiltrates the coating by filling the network of pores and micro-cracks. The micro-cracks are characteristic for ceramic coatings as they form during the rapid solidification of the spray particles when hitting the substrate's surface [20, 21]. These micro-cracks have a much smaller radius as the pores. If the sealer infiltration were compared to a capillary effect, a smaller capillary radius r would predominantly influence the infiltration depth. This hypothesis has been made by Kuutilla at al. [22] and considers predominantly the capillary force ΔP in Eq. 5. It also includes the surface energies of the solid-vapour phase interface γ_{SV} and the solid-liquid phase interface γ_{SL}. In the present case, the ceramic coating is the solid phase, the liquid phase is the sealer and the vapour phase is the surrounding air:

$$\Delta P = \frac{2\,(\gamma_{SV} - \gamma_{SL})}{r} \qquad \text{Eq. 5}$$

Consequently, the infiltration depth of the sealer can be enhanced by reducing the radius r and reducing the surface energy γ_{SL}. Regarding this, the surface energy difference between the solid TS-coating and the liquid sealer should be decreased. In this study, the same sealer is investigated for the same coating material with different coating porosities. Therefore, the surface energy can be neglected for further consideration in this work.

In case of TS-coatings, the sealer must displace gases in the porous network when infiltrating the TS-coating. Therefore, the Washburn equation (Eq. 6) is used with the same hypothesis, which again correlates to the assumption from Eq. 5, that the infiltration is improved with decreasing pore radius r:

$$L = \frac{r\,\gamma_{LV}\,\cos\Theta}{4\eta v} \qquad \text{Eq. 6}$$

With infiltration depth L, surface energy of the liquid-vapour phase interface γ_{SV}, wetting angle Θ, viscosity of the liquid η, and the infiltration rate v. [22]

Summarised, the F-samples show the lowest content of large pores but the highest pore content including the micro-cracks. This indicates a high content of micro-cracks in the coating. Regarding the theoretical basis of Eq. 5 and Eq. 6, the smaller the pore radius the higher the sealer infiltration depth. These results correlate to the impedance values indicating a lower water absorption of the F-samples. Consequently, the newly developed F-samples indicate the best performance with the considered epoxy-based sealer.

3.3. Phase analysis

As mentioned in the beginning, different present alumina phases can result in various material properties. Figure 15 illustrates the difference in the XRD-measurement of the feedstock material and the TS-coatings. In the feedstock material, the α-phase is predominantly present, whereas in the TS-coating the γ-phase is the main phase.

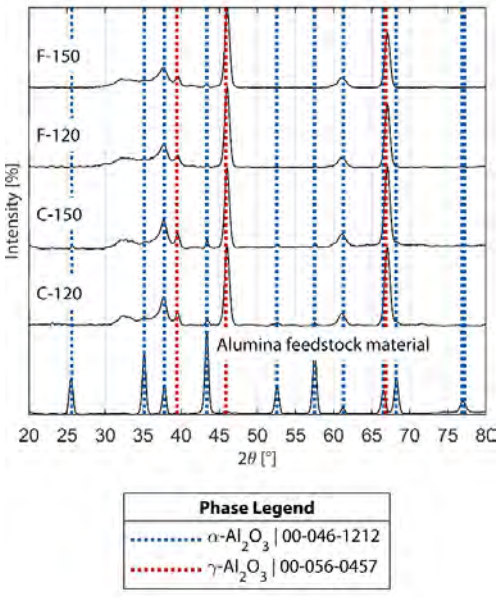

Figure 15: Normalised XRD diffractograms of the coatings and the feedstock material

The evaluation of the phase content between the different samples is conducted qualitatively. For this, the diffractogram in Figure 16 is normalised to the highest γ-peak at 2θ ≈ 46.13° of each sample and the α-peak at 2θ ≈ 37.74° is displayed in detail. Based on the higher peak-intensity of the C-samples, the α-content of the C-samples is assumed to be higher than in the F-samples.

Additional to this observation, the C-samples exhibit α-peaks at 2θ ≈ 43.3° and 2θ ≈ 57.43°, which are not visible for the F-samples. These observations indicate an increased stability for the α-phase for coarse feedstock materials. It would also underline the theory of Davis [3], that the formation of the γ-phase is connected to the cooling rate. Therefore, coarser particles lead to a higher stability of the α-phase, as they have a lower surface to volume ratio and the core of the splats might exhibit a lower temperature during the spraying process.

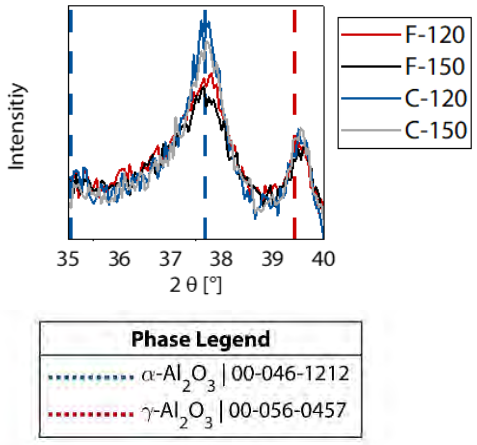

Figure 16: Detailed view on the XRD measurement normalised to 2θ ≈ 46.13 on the range of 2θ = 36-39°

The theory discussed in section 1, that an increased α-content can result in a lower water absorption and consequently in higher electrical insulation, is not verifiable within this work. The impedance curves in Figure 10 display a higher water absorption for the C-samples, which have a higher α-content. These results underline the fact, that a change in the phase-content due to different process parameters is directly related to a change in the microstructure of the coating. Consequently, the microstructure of the coating combined with the chosen sealer is predominantly influencing the electrical insulation properties of the coating system.

4. Conclusions

To summarise the results of this study, Figure 17 shows the impedances for the samples conditioned at 5 r. h. and 100 r. h. at f = 0.1 Hz on the right y-axes. These impedance values indicate the tendency of water absorption of each sample by the reduction of impedance. The investigation of the large pore content in addition to the content of pores and micro-cracks is displayed on the left y-axes.

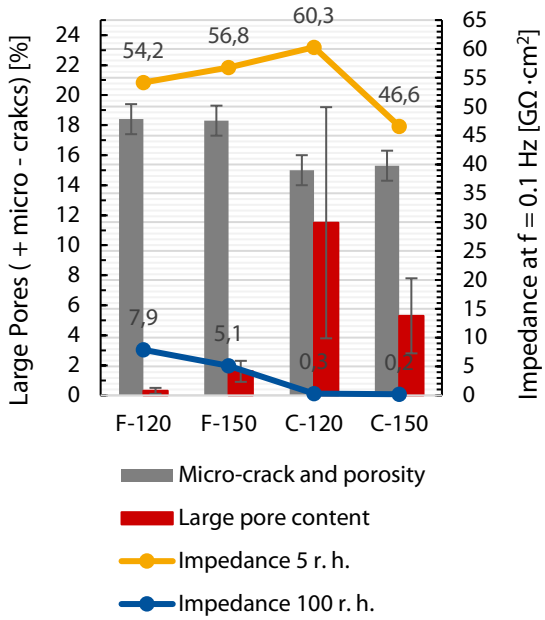

Figure 17: Summary of the porosity, pore and micro-crack content and impedance results at f = 0.1 Hz of the investigated samples

The overview highlights the decrease of the impedance value of 100 r. h. conditioned samples from fine to coarse feedstock material. Regarding this, also a tendency of increasing large pore content is visible. In contrast, the F-samples exhibit an overall higher micro-crack and porosity value then the C-samples. This indicates a decreased large pore content but relatively higher micro-crack density of the F-samples, which could be beneficial for the infiltration of the sealer due to the high capillary forces.

The impedance values of the 5 r. h.-samples is directly correlated to the porosity of the samples. Comparing only samples of the same feedstock materials, an increased large pore content leads to an increased impedance in the 5 r. h.-samples. The observation underlines the hypothesis, that pores can increase the electrical insulation in dry conditions. This result only correlates within the samples of the same feedstock material. Sample F-150 has a lower content of large pores than samples C-150 but the impedance of F-150 is higher. This result indicates an additional influence of the overall microstructure of the coatings inclusively the micro-crack content, which is higher for the F-samples.

The high standard deviation at the porosity of the C-120 sample is ascribed to different measurement positions. Since for each individual measurement an area of 600 x 150 µm² is chosen, the porosity might vary within the sample. Despite this, Figure 12 c) underlines the higher porosity of sample C-120 compared to other samples, as it appears to be the most porous samples within this study.

For further investigations, a feedstock material with narrow grain distribution should be analysed. Besides the stand-off distance further process parameters like current I or the process gas flow rate Q could be varied as well to produce suitable microstructures for specific sealers. Since the phase content did not show a predominant influence on the impedance values, the stabilisation of the α-alumina phase must be considered in combination with the coating microstructure. Different sealers could also be adapted and investigated for the different coatings to increase the overall performance of the hybrid coating system.

In conclusion, with APS alumina coatings with different microstructures can be reproducibly applied. The developed measurement set-up for impedance measurements is suitable to compare different coating systems exposed to different ambient conditions. Additionally to this, the developed F-samples exhibit increased electrical insulation for the investigated combination with the sealer from Diamant Metall-plastic GmbH. Therefore, fine feedstock material is recommended for an increased electrical insulation of the outer rings of the bearing in electrical engine.

5. Acknowledgment

The authors greatly acknowledge the financial support from the German Federal Ministry of Education and Research for the financial support of the research project ELIOMAS (03XP0167C). The project is funded according to a decision of the German Federal Parliament.

The paper was supported by FVA e.V.

References

[1] European Commission, Communication from the comission to the european parliament, the council, the european economic and social comittee and the comittee of the regions, 15 (2014) , 1–22.

[2] Bobzin, K., Öte, M., Königstein, T., Zhao, L., and Wietheger, W., Coatings and Surface Treatments for Friction and Wear Control, In G.E. Totten (Editor), ASM Handbook, Volume 18: Friction, Lubrication, and Wear Technology, Materials Park, ASM International (2017) , 614–622, DOI: 10.31399/asm.hb.v18.a0006419.

[3] Davis, J. R. (2004. *Handbook of thermal spray technology*. ASM International, Materials Park, OH.

[4] Bobzin, K. (2013. *Oberflächentechnik für den Maschinenbau*. Wiley-VCH, Weinheim.

[5] Gemeinschaft Thermisches Spritzen (Assoc. of Thermal Sprayers) e.V.,, Thermal Spray Processes, Linspray brochure - Gases and know-how for thermal spraying (2008.

[6] Prudenziati, M., Development and the Implementation of High-Temperature Reliable Heaters in Plasma Spray Technology, J Therm Spray Tech, 2 (2008) , 234–243.

[7] Pawlowski Lech, The Relationship between Structure and Dielectric Properties in Plasma-Sprayed Alumina Coatings, Surface and Coatings Technology, 35 (1987) , 285–298.

[8] McPherson, R., Formation of metastable phases in flame- and plasma-prepared alumina, J Mater Sci, 6 (1973) , 851–858, DOI: 10.1007/BF02397914.

[9] Levin, I. and Brandon, D., Metastable Alumina Polymorphs: Crystal Structures and Transition Sequences, Journal of the American Ceramic Society, 8 (1998) , 1995–2012, DOI: 10.1111/j.1151-2916.1998.tb02581.x.

[10] Kouwenberg, J.J.M. (2018. *Fluorescent Nuclear Track Detectors for Alpha Particle Measurement*. Delft University of Technology.

[11] Streitz, F. H. and Mintmire, J. W., Energetics of aluminum vacancies in gamma alumina, Phys. Rev. B, 2 (1999) , 773–777, DOI: 10.1103/PhysRevB.60.773.

[12] Kim, H.-J., Odoul, S., Lee, C.-H., and Kweon, Y.-G., The electrical insulation behavior and sealing effects of plasma-sprayed alumina–titania coatings, Surface and Coatings Technology, 3 (2001) , 293–301, DOI: 10.1016/S0257-8972(01)01044-1.

[13] Hülsenberg, D. (2014. *Keramik*. *Wie ein alter Werkstoff hochmodern wird*. Technik im Fokus 2. Springer Vieweg, Berlin.
[14] Küchler, A. (2009. *Hochspannungstechnik*. Springer Berlin Heidelberg, Berlin, Heidelberg.
[15] Schaumburg, H. (1994. *Keramik*. Werkstoffe und Bauelemente der Elektrotechnik. Vieweg+Teubner Verlag, Wiesbaden.
[16] Ivers-Tiffée, E. and Münch, W. v. (2007. *Werkstoffe der Elektrotechnik*. *Mit 40 Tabellen*. Teubner, Wiesbaden.
[17] Schindelin, J., Arganda-Carreras, I., Frise, E., Kaynig, V., Longair, M., Pietzsch, T., Preibisch, S., Rueden, C., Saalfeld, S., Schmid, B., Tinevez, J.-Y., White, D. J., Hartenstein, V., Eliceiri, K., Tomancak, P., and Cardona, A., Fiji: an open-source platform for biological-image analysis, Nature methods, 7 (2012) , 676–682, DOI: 10.1038/nmeth.2019.
[18] Nissan Maskil and Moshe Deutsch, Structure and wavelength of the Cu K alpha 2 x-ray emission line, Physical review. A, General physics, 8 (1988) , 2947–2952, DOI: 10.1103/PhysRevA.37.2947.
[19] Niittymaki, M., Lahti, K., Suhonen, T., and Metsajoki, J., Effect of temperature and humidity on dielectric properties of thermally sprayed alumina coatings, IEEE Trans. Dielect. Electr. Insul., 3 (2018) , 908–918, DOI: 10.1109/TDEI.2018.006892.
[20] Ohmori, A. and Li, C.-J., Quantitative characterization of the structure of plasma-sprayed Al2O3 coating by using copper electroplating, Thin Solid Films, 2 (1991) , 241–252, DOI: 10.1016/0040-6090(91)90114-D.
[21] Vardelle, A., Moreau, C., Akedo, J., Ashrafizadeh, H., Berndt, C. C., Berghaus, J. O., Boulos, M., Brogan, J., Bourtsalas, A. C., Dolatabadi, A., Dorfman, M., Eden, T. J., Fauchais, P., Fisher, G., Gaertner, F., Gindrat, M., Henne, R., Hyland, M., Irissou, E., Jordan, E. H., Khor, K. A., Killinger, A., Lau, Y.-C., Li, C.-J., Li, L., Longtin, J., Markocsan, N., Masset, P. J., Matejicek, J., Mauer, G., McDonald, A., Mostaghimi, J., Sampath, S., Schiller, G., Shinoda, K., Smith, M. F., Syed, A. A., Themelis, N. J., Toma, F.-L., Trelles, J. P., Vassen, R., and Vuoristo, P., The 2016 Thermal Spray Roadmap, J Therm Spray Tech, 8 (2016) , 1376–1440, DOI: 10.1007/s11666-016-0473-x.
[22] Knuuttila, J., Sorsa, P., and Mäntylä, T., Sealing of thermal spray coatings by impregnation, J Therm Spray Tech, 2 (1999) , 249–257, DOI: 10.1007/s11666-999-0002-2.

Microstructural Analysis of Bearing Steels by a Statistical Nanoindentation Technique

Esteban Broitman[1], Mohamed Y. Sherif[2], Boris Minov[3], Urszula Sachadel[4]

[1] *Research and Technology Development, SKF B.V., Esteban.Daniel.Broitman@skf.com*
[2] *Research and Technology Development, SKF B.V., Mohamed.Sherif@skf.com*
[3] *Research and Technology Development, SKF B.V., Boris.Minov@skf.com*
[4] *Research and Technology Development, SKF B.V., Urszula.Sachadel@skf.com*

Abstract– The microstructure of ASTM 52100, X30CrMoN15-1, and AISI M62 steel samples, analyzed by optical and scanning electron microscopy and by X-ray diffraction, were correlated to the mechanical properties measured at macro- and nanoscale. The distribution of hardness determined from multiple nanoindentation measurements was deconvoluted, obtaining an estimate of the microstructural constituents, and corresponding plastic and elastic properties at nanoscale.

Keywords – nanoindentation, steel, hardness, statistical nanoindentation, ASTM 52100, X30CrMoN15-1, AISI M62

1. Introduction

The precise knowledge of bearing steel microstructures is of vital importance to understand their tribological performance. Standard microstructural characterization, carried out by optical and electron microscopy together with X-ray diffraction, is usually correlated to the hardness determined by Rockwell or Vickers indentation. The obtained hardness values by these techniques are generally used as a parameter to evaluate the steel resistance against indentation deformation at macro- and microscale. However, the mechanical significance of the steel phases and other microscale inhomogeneities cannot be analyzed by macro and micro-mechanical techniques. The use of instrumented nanoindentation provides a way to measure the mechanical response of these phases at an appropriate scale (~ 10^{-6} m). The use of nanoindentation data together with macro- and microindentation information can be used for multiscale mechanical modelling that could predict the steel mechanical performance for a given composition and microstructure.

Despite of the significant body of research on the hardness of bearing steels at macro- and microscale, their deformation behavior at nanoscale received less attention. Therefore, there is still a need for fundamental understanding of the local deformation behavior of the steels with respect to the local microstructure, which can be used to their optimization. Nanoindentation has been carried out to study individual hard and soft phases in low carbon steel [1], high carbon steel [2], TRIP steels [3], tool steel [4], dual phase steels [5], high speed steel [6], and stainless steel [7].

In the first part of the paper, the background of the indentation techniques to measure hardness of homogeneous materials at macro, micro-, and nanoscale is described. In the second part, the microstructure of ASTM 52100, X30CrMoN15-1, and the powder metallurgy AISI M62 steel samples, analyzed by optical and scanning electron microscopy and X-ray diffraction, are correlated to the mechanical properties measured by multiple nanoindentations. Finally, the distribution of the hardness and modulus of elasticity determined from the nanoindentation observations are deconvoluted, and the results are correlated to the microstructure.

2. Theoretical Remarks

2.1. Indentation Hardness

The hardness of a solid material can be defined as a measure of its resistance to a permanent shape when a constant compressive force is applied. In metals, ceramics, and most of polymers, the hardness is related to the plastic deformation of the surface. Hardness has also a close relation to other mechanical properties like strength, ductility, and fatigue resistance, and therefore, hardness testing can be used in the industry as a simple, fast, and relatively cheap material quality control method [8].

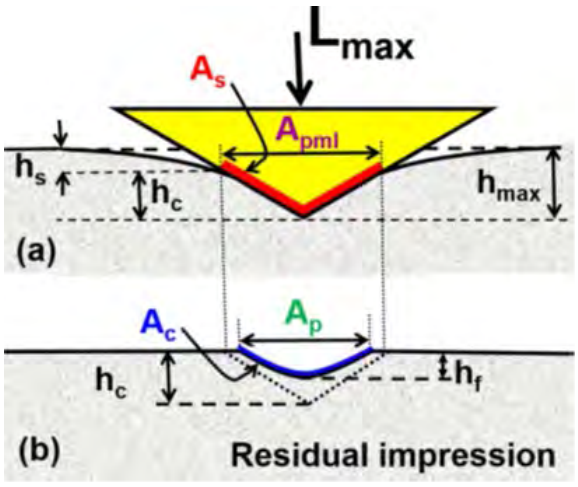

Figure 1: (a) Elasto-plastic deformation at the maximum applied load L_{max}; (b) plastic deformation after releasing the load (Adapted from [8]*).*

At macro- and microscale, the indentation hardness is defined in three different ways, as illustrated in Figure 1. Brinell and Vickers define hardness as the applied load L divided by the actual area A_c of the impressed curved surface. Meyer and Knoop hardness are defined as the ratio of the applied load L to the projected areas A_p of the indent. Finally, the Rockwell, Shore, IHRD, and Buchholz tests determine the hardness by measuring the depth of penetration of an indenter under a large load [8].

At nanoscale, the nanoindentation hardness is defined as:

$$H_{IT} = L_{max} / A_{pml} \qquad (Eq.\ 1)$$

where A_{pml} is the projected area contact at the maximum applied load L_{max} [8]. In this method, the maximum load ranges between few μN and about 500 mN, while penetrations will vary from few nm to about few μm. The indented area results to be very small (nanometer or few micrometers size), and as a consequence, the use of optical microscopy is not possible like in macro- and micro-indentation tests. However, Oliver and Pharr developed in the 1990s a method to accurately calculate hardness H and elastic modulus E from the indentation load-displacement (L-h) data, without need to measure the deformed area [9].

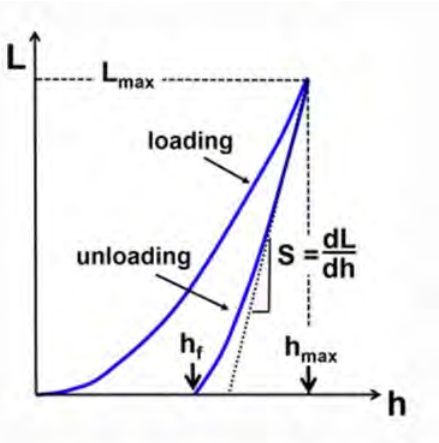

Figure 1: Load–unload curve during nanoindentation (Adapted from [8]).

During the nanoindentation process, the indenter penetrates the sample until a predetermined maximum load L_{max} is reached, with a corresponding penetration depth h_{max}. When the indenter is withdrawn from the sample, the unloading displacement is also continuously monitored until the zero load is reached and a residual penetration depth h_f is measured (Fig. 2). The slope of the upper portion of the unloading curve, S = dL/dh, is called the elastic contact stiffness.

Assuming that pileup is negligible, an elastic model [9] shows that the amount of sink-in h_s (indicated in Fig. 1) is given by:

$$h_s = \varepsilon L_{max}/S \qquad (Eq.\ 2)$$

where ε is a constant that depends on the geometry of the indenter, which for Berkovich and cube-corner indenters has a value ε = 0.75 [9].

The contact depth h_c can be estimated, from figure 1 and eq. 2 as:

$$h_c = h_{max} - h_s = h_{max} - \varepsilon L_{max}/S \qquad (Eq.\ 3)$$

If we assume that we have an ideal Berkovich indenter, the projected area at maximum load A_{pml} can be calculated as:

$$A_{pml} = \sqrt[3]{3}\, tan^2(\alpha/2) h_c^2 = 24.56 h_c^2 \qquad (Eq.\ 4)$$

where α = 130.6° is the angle of the Berkovich indenter [8]. Combining eq. (2), (3), and (4) into equation (1) we obtain:

$$H_{IT} = L_{max} / (h_{max} - \varepsilon L_{max}/S)^2 \qquad (Eq.\ 5)$$

Under the given assumptions, equation (5) shows a way to calculate the hardness of the material using the experimental data from figure 2.

Even if they are carefully manufactured, the indenter tips are usually blunted and/or can have other defects, or they become imperfect after few nanoindentations, so equation (4) is not always valid. In that case, it is necessary to evaluate an empirically determined indenter area function:

$$A_{pml} = f(h_c) = 24.56 h_c^2 + C_1 h^1 + C_2 h^{1/2} + C_3 h_c^{1/3} + \ldots \qquad (Eq.\ 6)$$

where the fitting parameters C_i can be obtained by performing nanoindentation tests on materials with known hardness. The most used material used for the fitting is fused quartz, with a known hardness H = 9.25 GPa [8].

The nanoindentation technique allows also to calculate the elastic modulus of the material by using:

$$S = \frac{2}{B\sqrt{\pi}} E_r \sqrt{A_{pml}} \qquad (Eq.\ 7)$$

where B = 1.034 for indenters of triangular cross-section [8] [9], and E_r is the reduced elastic modulus of the contact defined by:

$$\frac{1}{E_r} = \frac{1-\vartheta^2}{E} + \frac{1-\vartheta_i^2}{E_i} \qquad (Eq.\ 8)$$

where E and ν are the elastic modulus and Poisson's ratio of the sample and E_i and ν_i the elastic modulus and Poisson's ratio of the indenter.

If we try to determine the hardness of homogeneous materials with dimensions of many decimeters (a relatively ''infinite'' material when comparing with the sizes of a macroscale indentation), we probably won't be able to measure different values of indentation hardness measured at different length scales. However, a difference will appear when we try to indent a polycrystalline material with inhomogeneous features of microscale length. While macroscale indentations will give a material average hardness, nanoscale tests can indicate variations in different parts of the sample microstructure because the size of the indentations is usually of few micrometers and the indentation depth can be in the order of tens of nanometers. A nanoindentation can give hardness and elastic modulus variations

in different grains, precipitates, phases and grain boundaries [10].

2.2. Statistical Nanoindentation

2.2.1. Two-phases material

Let's consider a material composed of two phases with different mechanical properties, being phase 2 the "matrix" and phase 1 characterized by a length scale D. (Figure 3).

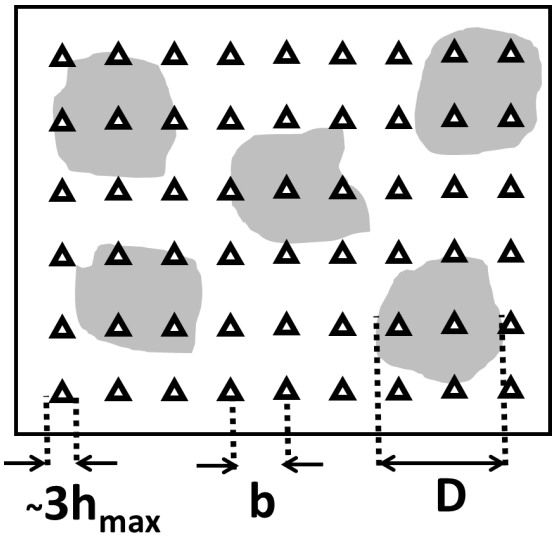

Figure 3: A material with a matrix having one phase with a characteristic size D. The indentations have a size ~3h_{max} and the distance between the indents is b.

If the indentation size (which is ~ 3h_{max} [8]) is much bigger than the than the size D of phase 2 (h_{max} » D), the properties extracted from this indentation will be the average value corresponding to a macro-scale indentation test. On the other hand, if the indentation depth h_{max} is much smaller than the size of phase 2 (h_{max} « D), then a single indentation test in a place far enough from the boundary between the phases can give full information of the phase. In addition, if a large number of tests N (N»1) are done on a grid of distance characteristic b (Figure 3), where b > 10 h_{max} to avoid interference between individual indentation tests, an analysis that includes histograms of mechanical properties can be obtained. Figure 4 is a schematic example of how a histogram (frequency diagram) could be represented for a matrix material of mean hardness H_2 ±σ_2 with a softer phase of mean value H_1 ± σ_1.

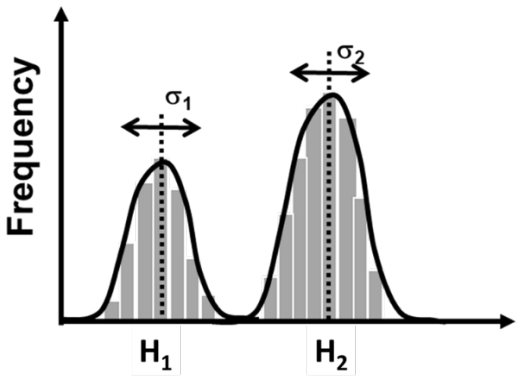

Figure 4: Histogram representing a matrix of hardness H_2 with a softer phase material of hardness H_1..

2.2.2. N-phases material

We can generalize the previous assumption extending to a material of n phases. Let's suppose that each phase i has a mechanical property x (x = H or E) with a discrete histogram of values following a Gaussian distribution. We also assume that the phases do not mechanically interact. The data can be analyzed by deconvoluting the discrete experimental distribution values P(x) of the mechanical property x by the sum of n theoretical probability distribution functions p_i (one for each mechanically different phase:

$$p_i(x) = \frac{1}{\sqrt{2\pi\sigma_i^2}} \exp\left(-\frac{(x-\mu_i)^2}{2\sigma_i^2}\right) \qquad (Eq.\ 9)$$

where μ_i is the arithmetic mean of all Ni values of phase i, while the standard deviation σi or root mean square deviation, is a measure of the dispersion of these values:

$$\mu_i = \frac{1}{N_i} \sum_{k=1}^{N_i} X_k \quad (Eq.\ 10)$$

$$\sigma_i^2 = \frac{1}{N_i - 1} \sum_{k=1}^{N_i} (x_k - \mu_i)^2 \quad (Eq.\ 11)$$

The overall frequency distribution of the mechanical property x will have a probability density function P(x):

$$P(x) = \sum_{i=1}^{n} f_i \; p_i(x) \qquad (Eq.\ 12)$$

where f_i is the volume fraction of the phase i and:

$$\sum_{i=1}^{n} f_i = 1 \quad (Eq.\ 13)$$

From the practical point of view, the function P(x) can be fitted to the experimental data by finding fi, σi and μ_i that are minimizing the standard error:

$$\min \sum_{l=1}^{m} \frac{[y(x_l) - p(x_l)]^2}{m} \qquad (Eq.\ 14)$$

or maximizing R-square, also known as the coefficient of determination (COD), which is calculated as:

$$R^2 = 1 - \frac{\sum_{l=1}^{m}[y(x_l)-p(x_l)]^2}{\sum_{l=1}^{m}\left[y(x_l)-\frac{1}{m}\sum_{l=1}^{m}y(x_l)\right]^2} \quad (Eq.\ 15)$$

where x_l and $y(x_l)$ are the l-th (x,y) coordinates values of the experimental results, and m is the number of "bins" used to build the experimental frequency density. The mean, standard deviation, and volume fraction values of each phase i can be determined by the deconvolution analysis with the condition of minimizing the standard error or R^2.

2.2.3. Selection of indentation depth and number of bins

To identify each of the n-phase property (hardness or elastic modulus), we need to generalize the assumptions of section 2.2.1. In the case of coatings characterization, there is a rule of tomb that the indentation depth should be smaller than the thickness of the coating in order to avoid the influence from the substrate hardness [8]. We can use a similar rule, and establish that, for a multiphase material, the maximum nanoindentation depth needs to be $h_{max} < D/10$, where D is the smallest microstructural length-scale of the material (see figure 3). At the same time, we need also to comply with an inferior limit: $h_{max} > d$, the largest heterogeneity of the indented material.

Different bin sizes can reveal different features of the data. Using a low number of bins will reduce the noise due to sampling randomness but could hide important details about the data distribution; on the other hand, the use of narrow-size bins increases the precision of density estimation but also increases the noise data. There are many methods to estimate the number of bins or their width. We utilize the Freedman-Diaconis rule that determine the number and width by the number of measurements and its spread [11]:

$$Bin\ width = 2\,\frac{IQR(x)}{\sqrt[3]{n}} \quad (Eq.\ 16)$$

where IQR(x) is the interquartile range of the data (i.e., range containing the 50% of all data) and n is the number of measurements.

3. Experimental Conditions

Three quenched and tempered steel samples, ASTM 52100, X30CrMoN15-1, and AISI M62, were selected for the study. The samples were sectioned, ground, polished with 1 µm diamond paste, and then electropolished. Microstructure studies were carried out by optical microscopy using etched specimens (Leica DM6000-M) and by X-ray diffraction (Bruker D8 DISCOVER). The diffractometer was operated at 50 kV and 50 mA, using Zr-filtered Mo Kα1,2 radiation. A step-scan mode was employed over the scanned θ-2θ range of 15-63°, with angular step width of 0.02°, the collection time being for 10 s at each step.

Nanoindentation experiments have been performed with a diamond Berkovich indenter with a tip radius of approximately 150 nm. The employed equipment was a NHT from CSM Instruments (now Anton Paar) with a vertical displacement resolution of 0.01 nm, a force resolution of 0.02 µN, an internal noise uncertainty of 0.3 nm, and thermal drift at room temperature below 0.05 nm/min [12]. Multi-indentations were carried out at L_{max} = 20 mN in grids of 20x25 indents with a space between indents b = 7 µm. It has been shown that the metallographic polishing process can affect nanoindentation results due to the presence of surface roughness and surface mechanical damage [13] [14] [15]. In this work we followed the results of Bublíková *et al*, who demonstrated that a mechanical polishing followed by electropolishing ensures reliable results in nanoindentation experiments and minimizes the indentation size effect for loads higher than 5 mN [15].

4. Results and Discussion

4.1. Optical Microscopy

Figure 5 shows the steel microstructures. Figure 5a exhibits a typical ASTM 52100 bearing steel microstructure with an uneven distribution of carbides, while the X30CrMoN15-1 steel (Figure 5b) reveals that they are well distributed. The AISI M62 steel microstructure (Figure 5c) displays the presence of several carbides clusters.

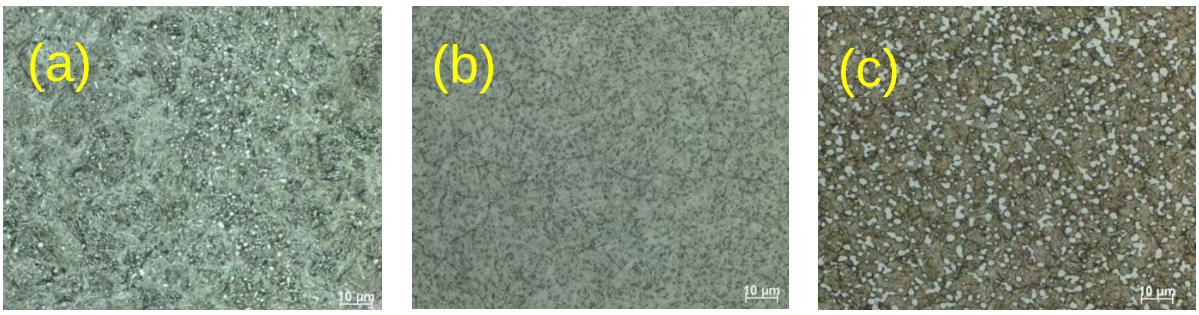

Figure 5 Microstructure of (a) ASTM 52100, (b) X30CrMoN15-1, (c) AISI M62.

Table 1: A summary of the Rietveld refinement results in wt.%. (*) Amount is too small to be certain of the phase's presence.

	ASTM 52100	X30CrMoN15-1	AISI M62
α-Fe (matrix)	86.2 ± 0.1	76.8 ± 0.6	75.9 ± 0.4
Austenite	6.4 ± 0.1	1.8 ± 0.1	2.2 ± 0.5
Cementite	7.4 ± 0.1	-	-
Fe_2Mo_4C (M_6C)	-	-	9.4 ± 0.1
VC	-	-	4.3 ± 0.1
Fe_3W_3C (M_6C)	-	-	7.7 ± 0.3
Mo2C hexagonal	-	0.1 ± 0.1(*)	0.4 ± 0.4
Cr_7C_3	-	20.2 ± 0.4	-

4.2. XRD analysis

Two X-ray spectra were acquired per microstructure, and the Rietveld method was used to identify and quantify phases present (Table 1). For the ASTM 52100 steel, the calculated retained austenite content was 6.4±0.1 wt.%. However, for the AISI M62 and X30CrMoN15_ microstructures, very small amount of retained austenite was found at 1.8±0.1 and 2.2±0.5 wt.%, respectively. The AISI M62 microstructure was estimated to contain also a total of 17.1 wt.% of the M6C-type of carbide on average, as well as 4.3±0.1 wt.% vanadium carbide.

4.3. Indentation Hardness and Elastic Modulus

The macroscale hardness of the steels, measured by Vickers (10 kgf) and by Rockwell C (150 kgf) according to standards ISO 6507-1 [13] and ISO 6508-1 [14], respectively, are shown in Table 2. The moduli of elasticity E displayed in the table have been provided by the steel suppliers. The nanoindentation hardness H_{IT} and elastic modulus E_{IT} in Table 2 are calculated as the mean value and corresponding error of 500 measurements. For the elastic modulus calculation, a Poisson's ratio value of 0.30 has been assumed for the three steels.

Even if Vickers and nanoindentation hardness are measured in the same scale (MPa), it should be noted that the values cannot be directly compared. Vickers hardness HV is calculated as the maximum applied load L_{max} divided by the contact area A_c of the indent after the indenter has been released, while the nanoindentation hardness H_{IT} is calculated as L_{max} divided by the projected contact area A_{pml} of the indent *at the maximum load* (see Figure 1). A geometrical equivalence between A_c and A_{pml} can be established only in materials that fully deform plastically, which is not the case for steels.

Table 2: Macro- and nanoscale mean values of hardness and elastic modulus for the three steel microstructures.(*) Elastic modulus values E at macroscale provided by the steel suppliers.

	HV10 (MPa)	HRC (150 kgf)	E* (GPa)	H_{IT} (MPa)	E_{IT} (GPa)
ASTM 52100	7280 ± 30	61.4 ± 0.1	210	8184 ± 59	212.7 ± 1.1
X30CrMoN15-1	6850 ± 20	58.4 ± 0.2	223	7970 ± 150	221.4 ± 2.3
AISI M62	9230 ± 80	67.9 ± 0.1	241	9690 ± 190	260.9 ± 4.3

Figure 6 is an example of the load-displacement curves for the average hardness nanoindentation of the three studied steels: (a) ASTM 52100, (b) X30CrMoN15-1, (c) AISI M62. The Hertzian elastic contact deformation solution curve, deduced from Hertz theory equation [15]:

$$L = \frac{4}{3} E_r R^{1/2} h^{3/2} \qquad (Eq.17)$$

(where R is the radius of the indenter) is also indicated as a dotted line. Since neither a rapid slope change in the loading curves nor pop-out elbows in the unloading curves were observed in all indentations, it is deduced that no deformation-induced transformations have been triggered during the nanoindentation.

4.4. Statistical Indentation Results

Figures 7 (a-c) display the nanoindentation hardness histograms for ASTM 52100, X30CrMoN15-1 and AISI M62 steels, respectively. The hardness histogram for ASTM 52100 (Figure 7a) reveals four different deconvoluted peaks, at 6.76, 8.14, 9.17, and 9.63 GPa. The X30CrMoN15-1 steel shows a pronounced peak centered at 8.94 GPa, plus a wide peak at about 5.06 GPa (Fig. 7b). Finally, the AISI M62 steel peaks were found at 10.03 and 6.09 GPa (Fig. 7c). The number of peaks in all histograms, which are found by fitting multiple Gaussian peaks and maximizing the coefficient of determination R-square as explained in section #2.2, are not only correlated with the phases identified by X-ray analysis (Table 1) but also related to the complexity of the observed microstructures (Figure 5).

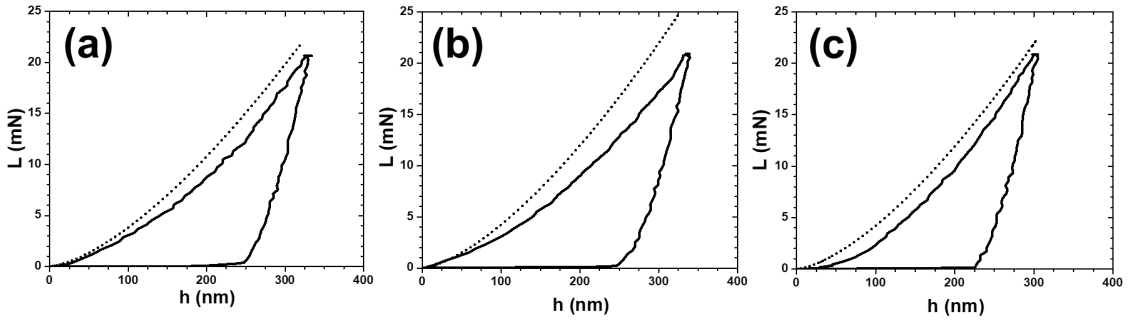

Figure 6: Nanoindentation load-displacement curve for (a) ASTM 52100, (b) X30CrMoN15-1, (c) AISI M62 (full line) and the corresponding theoretical elastic Hertz solution curve (dotted line).

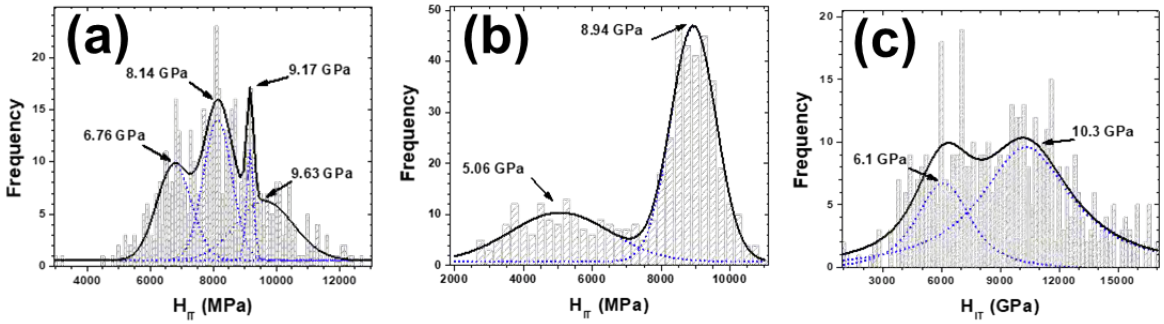

Figure 7: Microstructure of (a) ASTM 52100, (b) X30CrMoN15-1, (c) AISI M62.

There has been some steel studies showing multi-indent nanoindentation hardness histograms for DP980 [5] [16], multiphase Q&P [17], AISI 304L stainless [18], and dual-phase [19] steels. However, all these studies concentrated only on showing individual phases distributions without any analysis. A more elaborated use of statistical nanoindentation to study multiphase phase distribution has only be done for stainless steel [20] [21] and SM490 steel [22]. Haušild *et al* studied the distribution of the phases at different stainless steel deformation levels; they observed that the Gaussian hardness peaks moved to higher values with the increase of deformation, in agreement with results obtained by using x-ray diffraction during *in-situ* tensile testing [20]. Roa *et al* studied the dependence of nanoindentation hardness with crystallographic orientation of austenite grains in metastable stainless steels [21]. They correlated the data of each indentation with electron backscatter diffraction (EBSD) characterization to conclude that the hardness of (001) and (101) grains were lower than (111) grains. Finally, Pham and Kim studied the welded zones of SM490 steel [22]. They found out that the weld zone contained three phases: low stiffness ferrite, high stiffness ferrite, and pearlite. While all the aforementioned authors studied different steels, all agree in the idea that the hardness for the different phases observed by the statistical nanoindentation analysis were consistent with results from other methods found in the literature.

When we compare the results of statistical analysis in Figure 7 with the results found by X-ray diffraction (XRD) analysis (Table 1) we can notice that the number of phases apparently does not coincide. For instance, for ASTM 52100 we found 5 peaks (Figure 7a), but the Rietveld refinement results show the presence of only 3 phases. We need to consider that, in fact, the histograms reflect not only the response from the phases in the sample, but also the effect of grain boundaries, different grain sizes and orientations, non-uniform chemical distributions and dislocation density within grains. Furthermore, our approach in Section #2.2 considers phases that follow a simple mixing rule; in fact, the mixing rule should be more complicated as it will depend on non-linear stress distribution around the indentation zone.

However, the results shown in Figure 7 can be interpreted as a characteristic fingerprint for each steel. From this point of view, the nanoindentation statistical analysis can be considered as a kind of “hardness spectroscopic analysis” where each steel will show an own number of characteristic “peaks” centered in characteristic “hardness” values. Following this spectroscopy analogy, Haušild results [20] showing that the center of the steel Gaussian hardness peak moves according to the deformation of the sample, and Roa results [21] describing how the position of the Gaussian hardness peak depends on the orientation of the phase, behave in a similar fashion to what is observed for the same phenomena through the corresponding XRD peak shifts.

5. Conclusions

A statistical nanoindentation technique has been used for first time to compare three different bearing steel microstructures. The distribution of the mechanical properties determined from multiple nanoindentation measurements was deconvoluted. The results show that this nanoindentation technique can be used to generate hardness histograms that reflect unique characteristics (fingerprints) for the different bearing steel mechanical properties.

6. Bibliography

[1] I. de Diego-Calderón, M. J. Santofimia, J. M. Molina-Aldareguia, M. A. Monclús und I. Sabirov, "Deformation behavior of a high strength multiphase steel at macro- and micro-scales," *Materials Science and Engineering: A,* Bd. 611, pp. 201-211, 2014.

[2] R. Hossain, F. Pahlevani, M. Z. Quadir und V. Sahajwalla, "Stability of retained austenite in high carbon steel under compressive stress: an investigation from macro to nano scale," *Scientific Reports,* Bd. 6, p. 34958, 2016.

[3] Q. Furnémont, M. Kempf, P. J. Jacques, M. Göken und F. Delannay, "On the measurement of the nanohardness of the constitutive phases of TRIP-assisted multiphase steels," *Materials Science and Engineering: A,* Bd. 328, Nr. 1-2, pp. 26-32, 2002.

[4] F. Pöhl, A. Weddeling und W. Theisen, "Mechanical Characterization of Hard Phases by Means of Nanoindentation," in *Proceedings of the International Symposium on Wear Resistant Alloys for the Mining and Processing Industry CBMM*, Campinas, 2018.

[5] M. D. Taylor, K. S. Choi, X. Sun, D. K. Matlock, C. E. Packard, L. Xu und F. Barlat, "Correlations between nanoindentation hardness and macroscopic mechanical properties in DP980 steels," *Materials Science and Engineering: A,* Bd. 597, pp. 431-439, 2014.

[6] H. Zhu, Q. Zhu, A. Kosasih und A. K. Tieu, "Investigation on mechanical properties of high speed steel roll material by nanoindentation," *Materials Research Innovations,* Bd. 17, pp. 35-39, 2013.

[7] S. Chen, Y. Miyahara und A. Nomoto, "Crystallographic orientation dependence of nanoindentation hardness in austenitic phase of stainless steel," *Philosophical Magazine Letters,* Bd. 98, Nr. 11, pp. 473-485, 2018.

[8] E. Broitman, "Indentation Hardness Measurements at Macro-, Micro-, and Nanoscale: A Critical Overview," *Tribology Letters,* Bd. 65, p. 23, 2017.

[9] W. Oliver und G. Pharr, "An improved technique for determining hardness and elastic modulus using load and displacement sensing indentation experiments," *Journal of Materials Research,* Bd. 7, Nr. 6, p. 1564–1583 , 1992.

[10] A. C. Fischer-Cripps, Nanoindentation, New York: Springer-Verlag , 2011.

[11] D. Freedman und P. Diaconis, "On the histogram as a density estimator: L2 theory," *Probability Theory and Related Fields,* Bd. 57, Nr. 4, p. 453–476, 1981.

[12] Anton Paar, Mechanical Characterization of Materials, Ostfildern: Anton Paar, 2016.

[13] S. Pathak, D. Stojakovic, R. Doherty und S. R. Kalidindi, "Importance of surface preparation on the nano-indentation stress-strain curves measured in metals," *Journal of Materials Research,* Bd. 24, Nr. 3, pp. 1142-1155, 2009.

[14] M. C. Wurz, F. Pape, M. Wark und H. H. Gatzen, "Investigation of Liquid Additives on the Nano-Hardness of NiFe during Polishing," *Tribology Online,* Bd. 6, Nr. 1, pp. 113-116, 2011.

[15] P. Bublíková, H. K. Namburi und D. Marušáková, "Optimization of Surface Properties for Nanoindentation Studies on Nuclear Structural Materials," *Materials Science Forum,* Bd. 891, pp. 67-72 , 2017.

[16] International Organization for Standardization, "ISO 6507-1-2005: Metallic Materials—Vickers Hardness Test—Part 1: Test Method," International Organization for Standardization, Geneva, 2005.

[17] International Organization for Standardization, "ISO 6508-1: Metallic Materials - Rockwell Hardness Test - Part 1: Test Method," International Organization for Standardization, Geneva, 2016.

[18] H. Hertz, "Über die Berührung fester elastischer Körper (On the contact of elastic solids)," *Journal für die reine und angewandte Mathematik,* Bd. 92, pp. 156-171, 1881.

[19] G. Cheng, F. Zhang, A. Ruimi, D. P. Field und X. Sun, "Quantifying the effects of tempering on individual phase properties of DP980 steel with nanoindentation," *Materials Science and Engineering A,* Bd. 776, pp. 240-49, 2016.

[20] G. Cheng, K. S. Choi, X. Hu und X. Sun, "Determining individual phase properties in a multi-phase Q&P steel using multi-scale indentation tests," *Materials Science and Engineering A,* Bd. 652, pp. 384-395, 2016.

[21] K. S. Mao, C. Sun, Y. Huang, C.-H. Shiau, F. A. Garner, P. D. Freyer und J. P. Wharry, "Grain orientation dependence of nanoindentation and deformation-induced martensitic phase transformation in neutron irradiated AISI 304L stainless steel," *Materialia,* Bd. 5, p. 100208, 2019.

[22] A. Khosravani, C. M. Caliendo und S. R. Kalidindi, "New Insights into the Microstructural Changes During the Processing of Dual-Phase Steels from Multiresolution Spherical Indentation Stress–Strain Protocols," *Metals,* Bd. 10, p. 18, 2020.

[23] P. Haušild, V. Davydov, J. Drahokoupil, M. Landa und P. Pilvin, "Characterization of strain-induced martensitic transformation in a metastable austenitic stainless steel," *Materials & Design,* Bd. 31, Nr. 4, pp. 1821-1827, 2010.

[24] J. J. Roa, G. Fargas, A. Mateo und E. Jiménez-Piqué, "Dependence of nanoindentation hardness with crystallographic orientation of austenite grains in metastable stainless steels," *Materials Science and Engineering A,* Bd. 645, pp. 188-195, 2015.

[25] T.-H. K. S.-E. Pham, "Determination of mechanical properties in SM490 steel weld zone using nanoindentation and FE analysis," *Journal of Constructional Steel Research,* Bd. 114, pp. 314-324, 2015.

[26] International Organization for Standardization, "ISO 6508-1: Metallic Materials—Rockwell Hardness Test—Part1: Test Method," International Organization for Standardization, Geneva, 2016.

Influence of Off-Centered Gear Load Distribution on Planetary Bearing Outer Ring Creep

Felix M. Schlüter[1], Georg Jacobs[1], Dennis Bosse[1], Tim Schröder[1]

[1] *Chair for Wind Power Drives, RWTH Aachen University, felix.schlueter@cwd.rwth-aachen.de, georg.jacobs@cwd.rwth-aachen.de, dennis.bosse@cwd.rwth-aachen.de, tim.schroeder@cwd.rwth-aachen.de*

Abstract:

Planetary bearing outer ring creep is one of the relevant mechanical issues in most wind turbine gearboxes in the field today. Bearing ring creep causes wear and debris and any measure should be taken to reduce creeping movements. Off-centered gear load distributions have been identified as a relevant influence on outer ring creep in the literature, but have not been investigated yet.

After a description of the test bench used for this investigation, the independently measured creep behavior of two bearing rings of a planetary bearing arrangement under varying gear load distributions is presented. For the investigated planetary gear, both rings only show so called gear creep at high loads for all gear load distributions applied.

For the extreme case investigated with an axis inclination on 120 µm it was observed that the creep behavior of the two bearing rings inverted when compared to the centered gear load distribution without axis inclination. It is speculated that this is due to the off-centered gear load distributions in both tooth engagements of the planetary gear partially compensating the tilting moment caused by the gear's helix angle.

The case investigated with only 60 µm axis inclination shows a creep speed of close to zero for both rings at about 50% torque. As the gear load distribution can be influenced during the design process of the gears, slight modifications towards this gear load distribution could be a possible measure to reduce creep in the future.

Keywords: Planetary Bearing, Creep, Test Bench, Wind Turbine, Gear Load Distribution

1. Introduction

The share of wind power has increased rapidly in recent years and in in 2019 for the first time constituted the largest share amongst all energy sources in Germany [1]. As the cost pressure on the entire supply chain of wind turbines (WT) increases to be more competitive, improving the reliability of WTs has become one of the major challenges today [2]. To improve the reliability of today's complex WTs, understanding the detailed causes of damages becomes essential. Due to high downtimes per failure caused by time-consuming repair, mechanical damages in the gearbox are of particularly high interest in this context.

Bearing ring creep – especially bearing outer ring creep – is one of the mechanical issues in planetary bearings which on average require two to three costly repairs over the design life time of a WT [3]. This usually involves a replacement of the entire gearbox as uptower repairs are often not possible. Bearing ring creep is a phenomenon occurring especially in WT planetary bearings due to rapidly increasing gearbox torque density [4] and high specific loads. Together with elastic surrounding structures [5] due to lightweight constructions, deformations within the gearbox increase. With gear teeth engagements being sensitive to misalignments, uneven gear load distributions can be the result.

The phenomenon of bearing ring creep has been investigated extensively on small scale model test benches by means of simulations and experiments [5] and is well understood within the parameter range investigates so far. However, uneven gear load distribution as well as multiple-row bearing concepts, as commonly seen in WT planetary gears, have been identified as highly relevant influences on ring creep [5], but have not been investigated under realistic load conditions yet. Therefore, a metrological investigation as presented in this paper is necessary.

2. Bearing Creep in Planetary Bearings

Bearing ring creep is one of the relevant mechanical issues in current WT gearboxes [5,6] and can occur at various positions, for example at the planet carrier bearing [7,8], the planetary pin seat and the planetary bearing [5,9]. Ring creep in planetary bearings – mostly outer ring creep [9,10] – leads to planetary bearing failure due to misalignment and ultimately breaking of components [5]. Also, fretting corrosion can be caused, leading to secondary failure modes in the entire gearbox due to debris.

Planetary bearing outer ring creep can be divided into two independent mechanisms which provoke opposing tangential movements of the bearing outer ring in the planetary gear: roller-induced creep and gear creep [5,9].

Figure 1 shows the direction of movement of these two creep mechanisms. The pin is stationary, the gear rotates counterclockwise and the gear forces act from the left and the right. The direction of creep of a bearing ring is determined relative to the rotational direction of the roller set to the observed bearing ring. Roller-induced creep leads to a tangential movement of the bearing ring in the direction of rotation of the roller set – according to [11] this is defined as positive.

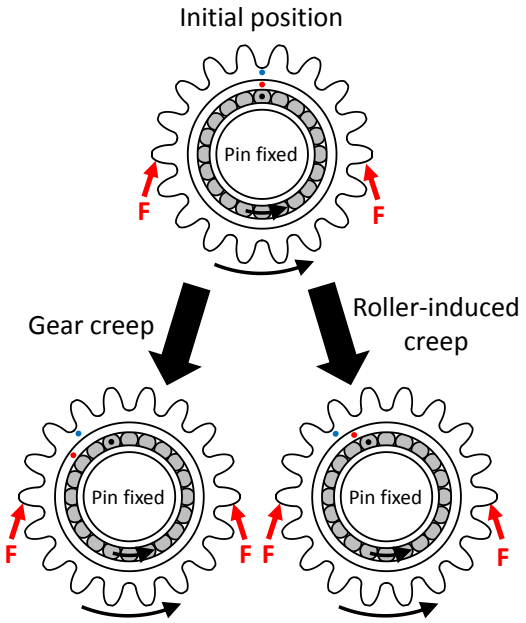

Figure 1: Possible tangential creep effects in planetary bearings according to [5].

Positive creep is shown in the lower right gear in Figure 1. While the gear rotates counterclockwise by a certain angle (blue dot on gear), the roller set rotates in the same direction, but by a smaller angle (black dot on roller). Therefore, in relative view to the gear, the rotation of the roller set is clockwise. Roller-induced creep drives the bearing ring in this (clockwise direction), indicated by the red dot on the bearing ring.

Gear creep – shown in the lower left gear in Figure 1 – drives the bearing ring against the relative rotational direction of the roller set to the gear. Therefore, the bearing ring (red dot) rotated slightly more than the gear (blue dot). Both mechanisms will be shown in experimental results in this paper.

For laboratory scale bearings, validated FE-models exist [5] to quantitatively simulate the influence of numerous parameters on creep behavior, e. g the influence of interference fit, torque, bearing width and number of rollers. However, the influence of off-centered gear load distributions – as presented here – has not been modelled yet. With the results presented in this publication, models taking this influence into account could validated. Through this, investigations regarding creep in planetary bearings could be carried out simulatively in the future – and therefore at reduced cost.

3. Experimental Setup

To fully describe the test setup, this chapter is divided into four sub-chapters. First, it is described why the experimental investigations were carried out on a three-shaft test rig while maintaining realistic kinematic conditions for the bearings and gears under test. Then, a short overview of the overall setup as a bracing rig is given. The main functionality – a unique kinematic adjustment system – is described afterwards, followed by the measurement setup necessary for the investigations presented.

3.1. Equivalent mechanical system

In this contribution, experimental investigations of outer ring creep of a WT planetary bearing are presented. As the planetary bearing and planetary gear in a WT gearbox rotate about two axis simultaneously, accessibility to measurement signals is challenging. Therefore, a component test bench was designed and set up which comprises of a stationary planetary pin, two double-row cylindrical roller bearings as the planetary bearing arrangement and two helical gears to substitute ring and sun gear engagement.

A cut view of a planet gear in the original gearbox and the planet gear in the equivalent model test gearbox is shown in Figure 2. In this figure, the yellow arrows represent the load distributions acting in the two tooth engagements with the planetary gear. The “Rotor side” in the planetary gearbox corresponds with the “Outer side” of the test gearbox – the same applies to the “Generator side” and the “Bracing side”.

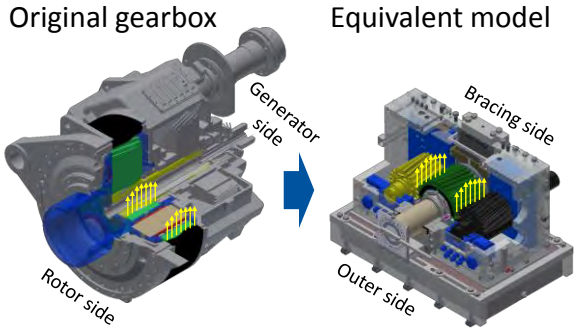

Figure 2: Equivalent mechanical system for detailed investigation of planetary bearing outer ring creep.

The rotational bearing speed as well as gear and bearing forces are transferred to the test bench from a scaled 2.75 MW WT gearbox from a generic research nacelle – the “FVA Nacelle”. Further information on the “FVA Nacelle” can be found in [12]

3.2. Mechanical bracing rig

To increase energetic efficiency during testing, the test bench is set up as a mechanical bracing rig. The torque is applied via a rotating hydraulic torsion motor. A separate electric motor sets the entire test rig into motion. The concept is shown in Figure 3.

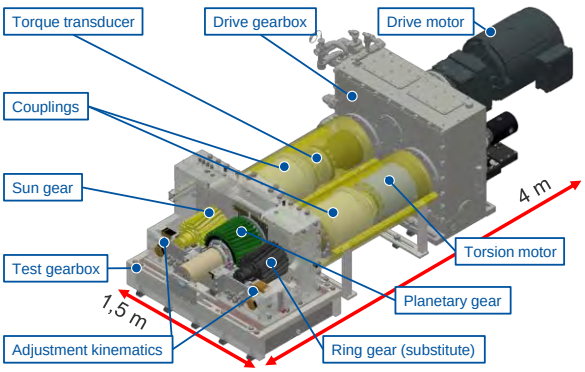

Figure 3: Mechanical bracing rig with test gearbox, drive gearbox, torsion motor and drive motor.

Table 1 provides basic mechanical information on the gears and bearings used in the test gearbox.

Table 1: Key data on gears and bearings in the used test gearbox.

	Variable	Value
Sun and ring gear	Number of teeth	22
	Width	234 mm
Planet gear	Number of teeth	33
	Module	9.5 mm
	Rel. rim thickness	3.5 (x Module)
	Width	226 mm
	Helix angle	7.6°
Bearing	Type	SL185030
	Number of bearings	2
	Outer Diameter	225 mm
	Static Load Rating	1.39 MN/bearing
	Press fit outer ring	55-65 µm (middle of R6/h6 acc. to [13])

The investigated planetary bearing arrangement – two double row, full complement cylindrical roller bearings with an outer diameter of 225 mm – is typical for planetary stages in WT gearboxes of up to ~2 MW. The planetary gear with a helix angle of 7.6° has a relative rim thickness of 3.5 modules and therefore is only slightly thicker than the allowed minimum for WT gearboxes according to [13].

The press fit of the outer rings in the planetary gear was machined and precisely measured to be middle of the range of R6/h6 – the recommended fit according to IEC61400 [13]. This is important as the fit is a key parameter with very high influence on bearing ring creep [14].

3.3. Kinematic adjustment system

The built up test bench allows the precise reproduction of the loading situation of a planetary bearing in a WT gearbox. This loading situation comprises of rotational speeds and torque as well as the gear load distributions in both tooth engagements which result from elastic deformations in a WT gearbox. A detailed description of gear load distributions from system deformations in WT gearboxes as well as load distribution measurements on gears and bearings from this test bench can be found in [15].

For the presented investigations, a unique kinematic adjustment system was developed. The basic concept is shown in Figure 4. The adjustment system comprises of a pair of eccentric bushings for vertical positioning and a separate pair for horizontal positioning. Each of the four support bearings in the test gearbox have this adjustment system, giving the test bench 8 degrees of freedom to influence the load situation on the tooth engagements of the planetary gear.

In the test gearbox, both pinion shafts push the planetary gear up. Therefore, elevating a support bearing of one of the pinion shafts leads to an increasing flank load share on this side of the pinion shaft. The gear load distribution has a significant influence on the bearing load distribution – especially in wide gears as they are common in WT gearbox planetary stages.

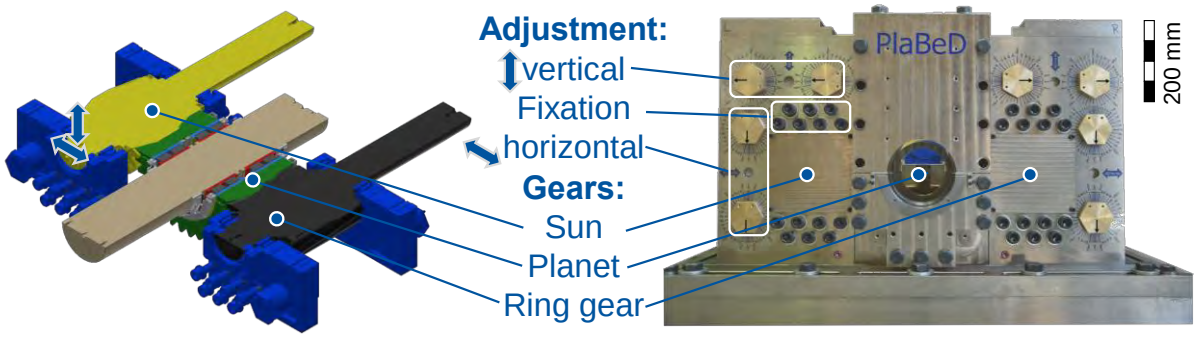

Figure 4: Kinematic adjustment system for active variation of gear load distribution in the test gearbox.

3.4. Measurement setup

Figure 5 shows the sensor setup which is used to evaluate outer ring creep. The figure only shows the three distance sensors. However, another three are installed in the same manner, leading to a total of six distance sensors used. Therefore, the distance measurement of each component is conducted redundantly to increase the precision. Each distance sensor delivers four peaks per revolution due to 4 grooves machined into the planetary gear and magnets fixed to the bearing outer rings. To obtain tangential creep measurements, signals from the distance sensors are evaluated as incremental encoders. For each component, the average from both sensors is used to calculate creep. Five strain gauges are equally spaced over the width of the gear on each pinion shaft and are used to evaluate the gear load distribution in this tooth engagement. Two teeth are applied with strain gauges and the average of both strain gauges is presented as the resulting gear load distribution.

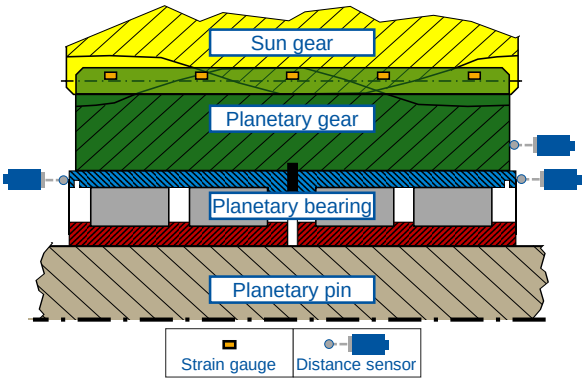

Figure 5: Measurement setup for gear load distribution and bearing outer ring creep.

3.5. Presented test scenarios

For the graphs presented in chapter 4, load levels at a constant rotational speed of 75 rpm at the sun gear

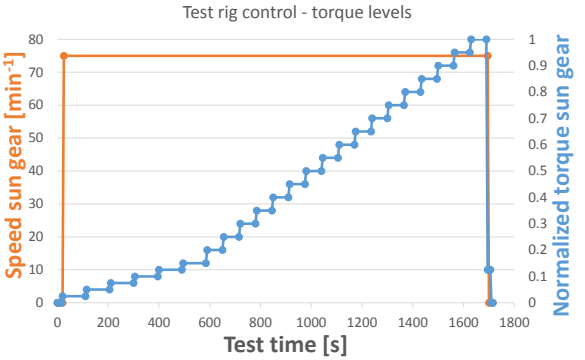

Figure 6: Torque and speed during evaluated tests.

To investigate the influence of off-center gear load distributions on outer ring creep, the described kinematic adjustment system was used to provoke these off-center distributions in both tooth engagements. In this contribution, the "overload"-scenario is compared to the "nominal scenario". Qualitatively, this is shown in Figure 7

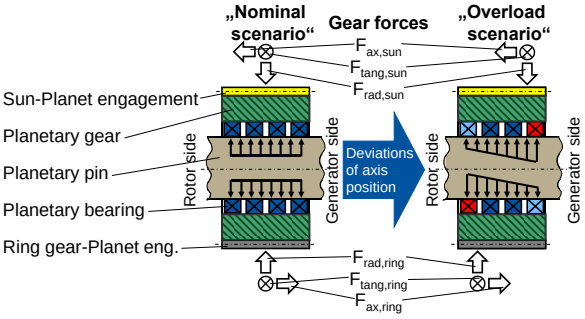

Figure 7: Schematic representation of centered ("nominal scenario") and off-centered ("overload scenario") gear load distributions on a planetary gear.

The "nominal scenario" represents the gear load distributions of a perfectly designed and machined planetary gear operating at its nominal design torque. Under these conditions, all elastic deformations (e.g. torsion of the sun gear and the planetary carrier as well as tilting of the planetary gear) are compensated by the gear modifications, most importantly the flank line modifications.

The "overload scenario" represents a gearbox operating above its nominal design torque. This does occur in any gearbox as the nominal design torque is usually around 70-80% of the specified gearbox torque. [16]. At this "overload scenario" the torsion of the sun gear increases, leading to a higher load share on the generator side – in the presented test bench this correlates with the bracing side. At the engagement of the planetary gear with the ring gear, the increased torsion of the planetary carrier increases the load share on the rotor side – correlating with the outer side in the test bench.

The "nominal scenario" was set by calculating the positioning value of the support bearings in a *RIKOR* [17] model that takes into account all shaft deformations and bearing stiffnesses. These values were then set with the kinematic adjustment system described earlier. For the "overload scenario" an axis inclination $f_{H\beta(\beta)}$ of 120 µm was set for each tooth engagement. This was done in opposing directions for sun and ring gear shaft in two steps – further referred to as "50% off-centered" and "100% off-centered".

4. Results and discussion

During the experiments presented in this contribution, torque was applied at constant levels during evaluation intervals. Due to intentionally short testing times and low rotational speeds, the total number of revolutions of the test bench is low and the total creep angle therefore negligible during the presented measurements. This is important to mention as the effects of wear and conditioning of the friction coefficient in the bearing seat – an important phenomenon described in the literature [11] – can be neglected this way.

Creep measurements will be presented without quantitative axis labelling as this is a sensitive matter to the industrial project partners involved in the project. The "outer side" bearing correlates to the rotor-sided bearing in a WT gearbox, the "bracing side" bearing to the generator-sided bearing. Both figures showing creep are scaled the same for x- and y-axis to allow a direct comparison. To be consistent with the definition given in [11], positive values on the y-axis represent roller-induced creep whereas negative values represent gear creep.

4.1. Gear load distributions

Figure 8 shows the gear load distribution at the sun gear at 80% of the maximum torque possible at the test bench. Three different kinematic adjustment configurations are shown. For each configuration the gear load distribution is shown through the measured strain values at the 5 marked positions along the gear width. In addition, the vertical line with the same color and markers represents the horizontal position of a single resulting force – see schematic representation in Figure 7. This value is a way to quantify, how far off-centered a gear load distribution is.

The black line with triangles shows a centered gear load distribution with a resulting force that is off-centered towards the bracing side (BS) by only about 2 mm. Compared to the gear width of 226 mm this is negligibly small.

The green line with squared markers shows the gear load distribution where the kinematic adjustment of the support bearings was only moved by 50% – the resulting axis inclination $f_{H\beta(\beta)}$ therefore is 60 µm. The resulting force is about 21 mm off-centered towards the bracing side.

Finally, the red line with circular markers shows the gear load distribution for an axis inclination $f_{H\beta(\beta)}$ of 120 µm – defined as the "100% overload scenario".

It can be observed that the measured strain on the outer side is further reduced while it is further increased on the bracing side. The resulting force is 29 mm off-centered towards the bracing side.

The axis inclination for the substituted ring gear was set to be exactly the opposite. Therefore, the gear load distributions and resulting forces show the opposite behavior and are not presented here.

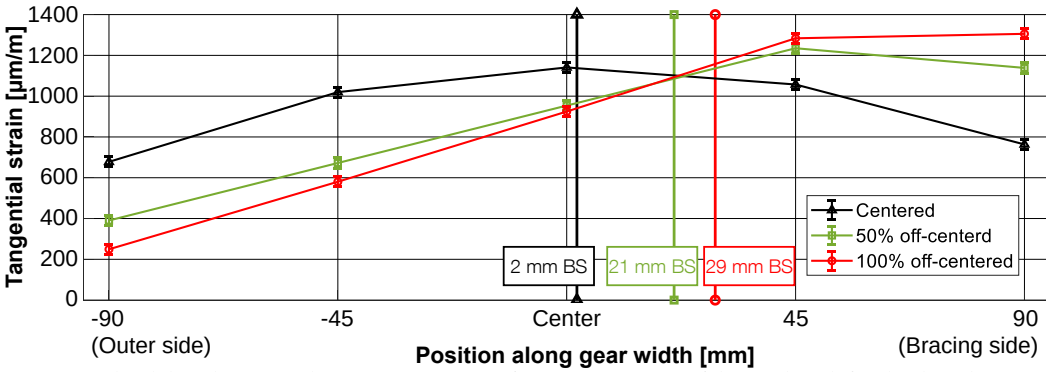

Figure 8: Gear load distribution at the sun gear at 80% of maximum torque of the test bench for the three kinematic adjustment configurations "centered", "50% off-centered" and "100% off-centered".

4.2. Bearing ring creep at centered gear load distributions ("nominal scenario") and comparison to literature

Figure 9 shows the normalized tangential creep speed for both outer rings over the torque applied for the centered gear load distribution shown in Figure 8.

Each data point represents the total creep angle that the bearing ring moved in the planetary gear in an evaluation interval divided by the time of the interval. Torque was constant during each interval as shown in Figure 6 and the intervals had a length of 60 s each. Due to very low creep speeds at low torque, an interval length of 90 s was used to increase the accuracy.

A few observations can be made from these curve:

1) As expected, the creep speed is zero for both rings when no or very low torque is applied.
2) The bearing ring on the bracing side starts creeping at a lower torque than the outer sided ring, see area marked grey.
3) Both bearing rings show (positive) roller-induced creep at low to medium torque levels.
4) Both bearing rings show (negative) gear creep at medium to high torque.
5) At high torque, the increase of gear creep over torque is approximately linear.

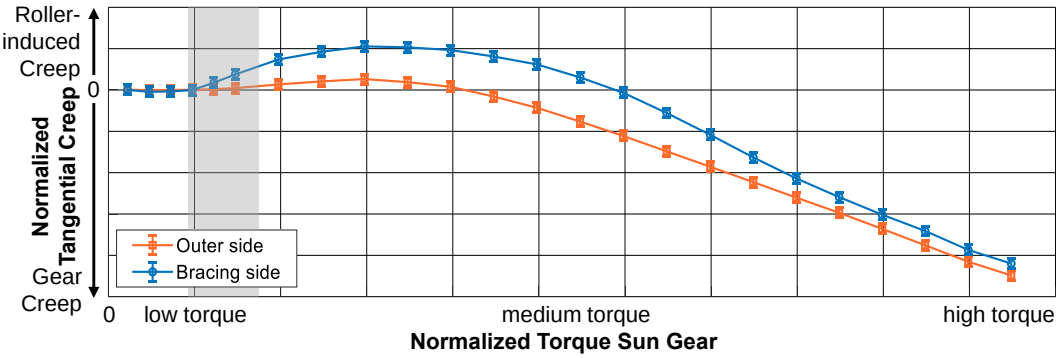

Figure 9: Normalized tangential creep of both bearing outer rings over normalized sun gear torque at centered gear load distributions.

Assuming a friction coefficient of 0.3, the results correlate very well with simulative literature findings [5] for the outer side bearing ring. The bearing ring on the bracing side, however, shows a behavior that differs from [5] – there it shows gear creep over the entire load range whereas the results presented here show positive creep first and negative gear creep only for higher load – see blue curve in Figure 9. One possible explanation is the differing relative gear rim thickness. The planetary gear presented in this contribution has a relative gear rim thickness of 3.5 modules whereas the simulations in [5] used for comparison have a relative gear rim thickness of only 2.2 modules. When comparing the presented measurements of the bearing ring on the

bracing side to a simulated relative gear rim thickness of 4.5 in [5], the results qualitatively correlate better. However, the results for both bearing rings correlate very well to measurements performed on a 2.75 MW wind turbine on a system test bench [9] with a planetary gear rim thickness of 4.0 modules. There, the generator-sided bearing ring (correlating to the bracing side bearing ring in the test bench presented here) shows roller-induced creep at low torque and gear creep at high torque while the rotor-sided bearing ring shows gear creep only over the entire torque range.

4.3. Bearing ring creep at off-center load distributions ("overload scenario")

Figure 10 shows the creeping behavior of the two bearing outer rings over the applied torque for the two different off-centered gear load distributions shown in Figure 8.

The following basic observations can be made from Figure 10:

1) Under the "off-centered" configuration, both bearing rings start creeping at a much lower torque compared to the "centered" configuration in Figure 9.
2) At low torque, the outer side bearing ring creeps in positive direction and the bracing side bearing ring creeps in negative direction.
3) From approximately 25 to 50 % torque, the bearing ring on the bracing side creeps in positive direction.
4) At high torque, both bearing rings creep in negative direction (gear creep).
5) At high torque, the increase of gear creep over torque is approximately linear.

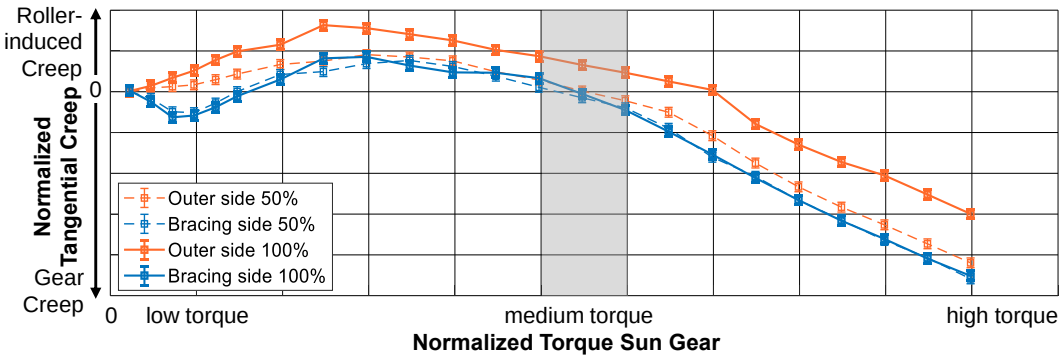

Figure 10: Normalized tangential creep of both bearing outer rings over normalized sun gear torque at 50% and 100% off-centered gear load distributions.

When comparing the "100% off-centered" configuration (thick lines) to the "centered" configuration in Figure 9, it can be observed that the overall behavior of the two bearing rings inverted as the curve of the outer side bearing ring shows higher values over the entire torque range.

Next, a closer look will be taken at the thin curves in Figure 10 – showing the configuration with only half the amplitude of axis inclination applied through the kinematic adjustment system. The inverted behavior that was observed for the "100% off-centered" configuration appears to already show for half the axis inclination applied. Also, the creep limit appears to be the same for both shown configurations and both rings start creeping at very low torque.

Even though the creep behavior of both rings is different at low torques, they show almost the same behavior above ~25% of torque. As both thin curves are in the (positive) range of roller-induced creep in the low/medium torque range and show clear gear creep at high torque, they cross the "zero creep line" in the torque range marked grey in Figure 10. This is worth mentioning as all other curves (thick curves in Figure 9 and Figure 10) do not have a common zero-crossing at significant torque.

The reason why the two bearing rings generally show different creeping behavior is the tilting moment of the planetary gear that is caused by the helix angle of gears.

As can be derived from Figure 7, the "overload scenario" applied to the planetary gear during this investigation reduces the effect of planetary tilting. In that figure, the axial forces acting in both tooth engagements cause a mathematically positive tilting moment. Applying the gear load off-centered in the direction shown, the radial forces cause a mathematically negative tilting moment.

Using the equations 1 and 2, the tilting moments from the given gear geometry, the applied torque and the measured off-center positions for the load application can be calculated.

$$M_{ax} = F_{ax} * d \qquad \textit{(Eq. 1)}$$

$$M_{off-center} = F_{rad} * (x_{load,sg} - x_{load,rg}) \qquad \textit{(Eq. 2)}$$

In these equations, F_{ax} is the axial force in a tooth engagement, F_{rad} the radial force, d the pitch circle diameter and $x_{load,sg/rg}$ the off-centered position for the resulting gear force of the sun gear ("sg") or ring gear ("rg"). M_{ax} is the tilting moment from axial forces and $M_{off\text{-}center}$ the tilting moment resulting from off-centered gear load application.

From this, it can be shown that the tilting moment of the planetary gear would be compensated for about 50 mm of off-centered load application.

However, to have equal load application on both bearings, the planetary gear would have to be non-deformable – not a realistic condition for thin-walled planetary gears in wind turbine gearboxes. Nevertheless, the

"overload scenario" presented leads to a partial compensation of the tilting moment and it is speculated to be the reason why the bearings behave very similar regarding creep over a wide torque range.

Up to date, the international literature offers no investigations regarding the creep behavior of planetary bearings under off-centered load distributions in the tooth engagements. Therefore, a comparison of the findings presented here is not possible regarding this aspect.

5. Conclusion

This contribution presents experimental results for planetary bearing outer ring creep obtained from a component test bench specifically designed for this purpose. The two double-row, full-complement test bearings – type "SL185030" – have an outer diameter of 225 mm and are used in wind turbines of up to 2 MW. Therefore, this publication is the first detailed investigation of planetary bearing outer ring creep for this size range.

Different creeping behavior of the two outer rings of the investigated bearing arrangement was found: The generator-sided bearing ring tends to show more roller-induced ring creep whereas the rotor-sided ring shows more gear creep. This behavior correlates well with investigations of a 2.75 MW wind turbine performed on a system test bench. The influence of torque on outer ring creep was shown to be nonlinear and supports literature findings which state that depending on the load level, one of the two mechanisms bearing ring creep and gear creep dominate.

In addition, the influence of off-centered gear-load distributions in the tooth engagements of the planetary gear on outer ring creep was evaluated. Strain gauge measurements show the off-centered load distribution for axis inclinations of 60 µm and 120 µm. Regarding the creep behavior, the 60 µm inclination lead to both bearing rings showing very similar behavior. It was observed, that the creep speed of both bearing rings was close to zero at approximately 50% torque – for gearbox designers this might be a way to reduce ring creep when refurbishing damaged planetary gear stages.

At full axis inclination of 120 µm, the creeping behavior of the two bearing rings was almost inverted compared to the centered measurements.

Acknowledgements

This research was funded by the German Federal Ministry for Economic Affairs and Energy as part of the project „PlaBeD – Planetary Bearing Design". The authors thank the ministry for this funding. The authors also thank the project partners Schaeffler and Winergy/Flender for the provided insight and expertise which greatly assisted the research carried out.

Supported by:
Federal Ministry for Economic Affairs and Energy
on the basis of a decision by the German Bundestag

References

[1] Burger, Bruno (2020): Öffentliche Nettostromerzeugung in Deutschland im Jahr 2019 (engl.: public net electricity generation in Germany in 2019), Fraunhofer ISE, Online available at https://www.ise.fraunhofer.de/content/dam/ise/de/documents/news/2019/Stromerzeugung_2019_2.pdf, last visited Apr. 5th, 2020.

[2] Walford, C.A. (2006): Wind Turbine Reliability: Understanding and Minimizing Wind Turbine Operation and Maintenance Costs, Sandia Report SAND2006-110, online available at https://energy.sandia.gov/wp-content/gallery/uploads/SAND-2006-1100.pdf, last visited Jun. 24th, 2020.

[3] Brooks, Rick (2016): Lessons Learned: Common Wind Turbine Bearing Failures, Costs & Solutions, Wind O&M Canada 2016, Toronto, Nov 29th-30th, 2016, online available at https://www.windpowerengineering.com/wind-turbine-common-failures-solutions/, last visited Jun 24th, 2020.

[4] Lubenow, Kai et al. (2019): Requirements for wind turbine gearboxes with increased torque density with special attention to a low-noise turbine operation, Conference Proceedings: Conference for Wind Power Drives CWD 2019, Aachen, ISBN: 978-3-7481-7867-5.

[5] Dimov, Genadi et al. (2018): Untersuchungen des Wanderverhaltens von Wälzlagern in schrägverzahnten Planetenrädern (engl.: Investigations of the bearing creep behavior in helical planetary gears), 2018 Final report in FVA-Heft Nr. 1281.

[6] Bauer, E.; Wikidal, F.; Gellermann, T. (2005): Überblick über Schäden am mechanischen Strang von Windenergieanlagen (engl: Overview of damages in the mechanical drive train of wind turbines), Conference Proceedings: Drive Train Technology Conference ATK 2005, Aachen, ISBN: 3-86130-417-1, pages 1-21.

[7] Maiwald, Andreas (2019): Special creeping movements of drive train components in wind power gearboxes, Conference Proceedings: Conference for Wind Power Drives CWD 2019, Aachen, ISBN: 9783748178675, pages 67-78.

[8] Gnauert, Jonas et al. (2020): Investigation of the load distribution on a planetary carrier bearing of a wind turbine gearbox to identify trigger for ring creep, Conference Proceedings: Bearing World 2020.

[9] Schlüter, Felix M. et al (2019): Correlation of Planetary Bearing Outer Ring Creep and Gear Load Distribution in a Full-Size Wind Turbine, In: NAWEA/WindTech 2019 Conference, Journal of Physics: Conference Series, doi: 10.1088/1742-6596/1452/1/012062, online available at https://iopscience.iop.org/article/10.1088/1742-6596/1452/1/012062/pdf, last visited Jun. 24th, 2020.

[10] van Kuik, G. A. M. et al. (2017): Long-term research challenges in wind energy – a research agenda by the European Academy of Wind Energy, Wind Energy Science 1,1-39, doi: 10.5194/wes-1-1-2016, online available at: https://www.wind-energ-sci.net/1/1/2016/wes-1-1-2016.pdf., last visited Jun.24th, 2020.

[11] Babbick, Till; et al. (2010): Lagersitze. Beanspruchungsgerechte Auslegung von Wälzlagersitzen unter Berücksichtigung von Schlupf- und Wandereffekten (engl.: Bearing sears. Design fit for purpose of roller bearing seats considering slip and creep effects), Final Report in FVA-Heft Nr. 956.

[12] Bosse, Dennis et al. (2018): Loads on drive train components of wind turbine generators, Final report in FVA-Heft Nr. 1325.

[13] International Organisation for Standardization (2012): Auslegungsanforderungen für Getriebe von Windenergieanlagen (engl.: Design requirements for wind turbine gearboxes), Berlin: Beuth, 2012 (61400 - part 4).

[14] Aul, Eduard et al. (2008): Wälzlagerwandern. Wandernde Wälzlager Innen- und Außenringe unter verschiedenen Einsatzbedingungen. (engl.: Bearing creep: creeping roller bearings. Inner and outer rings under different operation conditions), Final Report in FVA-Nr. 852.

[15] Schlüter, Felix M. et al. (2019): Aktive mechanische Variation der Breitenlastverteilung einer WEA-Planetenradlagerung (engl.: Active mechanical variation of the gear load distribution in a wind turbine planetary bearing), Conference Proceedings: Dresdner Maschinenelemente Kolloquium DMK 2019, ISBN: 978-3-96548-055-1, pages 617-632.

[16] Kissling, Ulrich (2019): Auslegung von Profilkorrekturen für asymmetrische Zahnräder (engl.: Design of profile modifications for asymmetric gears), Conference Proceedings: Dresdner Maschinenelemente Kolloquium DMK 2019, ISBN: 978-3-96548-055-1, pages 219–238.

[17] Oster, P.; Winter, H. (1979): EDV-Programm zur Ermittlung der Zahnflankenkorrekturen am Ritzel zum Ausgleich der lastbedingten Zahnverformungen. (engl.: Compensation of load-dependent tooth deformations: EDP program for the determination of tooth flank corrections on pinions), Final Report in FVA-Nr. 30.

A Fatigue Life Model for Roller Bearings in Oscillatory Applications

Georg Breslau[1], Berthold Schlecht[2]

[1] *Institute of Machine Elements and Machine Design, TU Dresden, georg.breslau@tu-dresden.de*
[2] *Institute of Machine Elements and Machine Design, TU Dresden, berthold.schlecht@tu-dresden.de*

Abstract – For certain applications, rolling bearings do not perform a complete rotation but only an oscillation at a defined amplitude. Common examples are universal joints, pitching systems of wind turbines or piston pin bearings. In such a case the calculated basic bearing life can be corrected by an oscillating life coefficient a_{osc}. This article presents a unified calculation approach for oscillating roller bearings based on the theory of LUNDBERG and PALMGREN, which is compared to the methods of RUMBARGER / JONES and HOUPERT. The relations derived in this work are based on the formulas for calculating the basic dynamic load rating according to the standard. For oscillating motion smaller than the critical amplitude, a more practical calculation method is presented, compared to RUMBARGER / JONES. The approach for larger amplitudes given by HOUPERT was revised, improved and corrected for $\varepsilon \leq 1$. As an application example, the bearing of the universal joint in a cardan shaft is analyzed. Therefore, a calculation approach to determine the dynamic equivalent bearing load is presented. Eventually, it is shown how the life coefficient varies in relation to the oscillation amplitude.

Keywords – oscillation motion, life prediction method, dynamic equivalent load, universal joints

1. Introduction

The rating life calculation of rolling bearings in oscillating motion is currently still insufficiently investigated. However, there are some research studies on experimental tests of oscillating bearings. THIEDE [18] and BOSSE [1] have evaluated the influence of grease lubrication on the rating life by varying the operating parameters such as temperature, oscillation amplitude and frequency. At present, this topic is still being researched e.g. SCHWACK [15] carried out experimental investigations on the wear behavior of oscillating bearings on model test rigs and large-diameter bearings. For all these rig tests mainly small oscillation amplitudes were investigated. While these experimental studies emphasize the importance of lubrication and wear behavior, this paper focused on determining the rating life due to rolling contact fatigue. The rating life of oscillating bearings was mainly examined by HARRIS [4], RUMBARGER/JONES [11] and HOUPERT [7]. This paper contributes to a more precise calculation by adapting these existing methods.

Nomenclature

a_{osc}	[−]	life coefficient for oscillating motion
a_{P}	[−]	life coefficient for oscillating load
b	[mm]	half contact width
e	[−]	WEIBULL slope
D_{pw}	[mm]	pitch diameter
D_{we}	[mm]	roller diameter
$\mathrm{d}V_{\psi}$	[mm^3]	elementary small race volume
$\mathrm{d}\psi$	[rad]	elementary small race angle
C	[N]	radial dynamic load rating of the ring
C_{r}	[N]	radial dynamic load rating
F_{L}	[N]	resulting bearing force (joint force)
F_{N}	[N]	nominal radial bearing force
F_{P1}	[N]	leverage force from M_{T1}
F_{P2}	[N]	leverage force from M_{T2}
F_{Z}	[N]	additional force
g, r	[−]	load distribution function of (ψ, ε)
h	[mm]	yoke span width
J_{r}	[−]	radial load integral
$J_{\theta_{\mathrm{a}}}$	[−]	load integral for oscillating motion of the circumferentially loaded ring
$J_{\theta_{\mathrm{a}},\psi}$	[−]	load integral for oscillating motion of a single volume (ψ)
J_1	[−]	load integral for continuous rotation of the circumferentially loaded ring
J_2	[−]	load integral for continuous rotation of the stationary loaded ring
$J_{2,\mathrm{red}}$	[−]	J_2 for reduced stress volume
L	[h]	life in continuous rotation
L_{osc}	[h]	life in oscillatory application
l_{r}	[mm]	race length
$l_{\mathrm{r,osc}}$	[mm]	stressed race length for oscillation
M_{T1}	[Nm]	input torque
M_{T2}	[Nm]	output torque
N_{rot}	[−]	load cycles (full rotation)
N_{osc}	[−]	load cycles (full oscillation period)
p	[−]	load-life exponent
P	[N]	dynamic equivalent load
Q_{eq}	[N]	dynamic equivalent element load
Q_{max}	[N]	maximum element load
T, t	[s]	time
Z	[−]	number of rolling elements
α	[rad]	nominal contact angle
β	[rad]	flexion angle
γ	[−]	auxiliary value $D_{\mathrm{we}} \cos\alpha / D_{\mathrm{pw}}$
ε	[−]	load zone parameter
θ	[rad]	oscillation angle
θ_{a}	[rad]	oscillation amplitude
θ_{crit}	[rad]	critical oscillation angle
θ_{dith}	[rad]	dither angle of the oscillating ring
θ_{RE}	[rad]	dither angle of the rolling element
φ_1	[rad]	rotation angle yoke G_1
ϕ_{m}	[−]	load modification factor
ψ	[rad]	orbital location angle
ψ_{l}	[rad]	load zone angle
1		index: circumferentially loaded ring
2		index: stationary loaded ring

More than 70 years ago, the LUNDBERG and PALMGREN fatigue model [8], [9] laid the foundation for the dynamic load rating and rating life calculation of rolling element bearings. By means of an equivalent load, the rating life can be calculated for any reliability under certain operating conditions. One of the requirements is the continuous rotation of the bearing. For rolling bearings in oscillating applications, such as drawn cup needle roller bearings in universal joints, this fatigue model is not valid anymore. However, the ISO 281 [1] contains no guidelines or references for calculating the rating life of oscillating bearings. This problem was particularly examined in 1968 by RUMBARGER and JONES [11], who analyzed the results of life tests of 388 caged needle roller bearings under combinations of load, speed, and amplitude of oscillation with WEIBULL statistics. They adjusted the load rating equation for small oscillation angles $\theta_a \leq \theta_{crit}$, where the stressed areas of the raceway do not overlap, thus considering the reduced stressed volume. This idea leads to a simplified life coefficient, which is introduced by RUMBARGER [10].

For distinction of cases, the critical angle θ_{crit} of the oscillation amplitude θ_a is calculated by the relative angle between raceway and cage. Independent of which ring oscillates, the critical angle is given by

$$\theta_{crit} = \frac{2\pi}{Z\,(1 \pm \gamma)}. \qquad \textit{(Eq. 1)}$$

This angle is different for both raceways, the upper sign refers to the inner and the lower sign to the outer ring. Consequently, θ_{crit} is always larger for the outer ring and therefore representative. The angle θ_{crit} depends both on the number of rolling elements Z and the geometry parameter γ. Figure 1 shows how many rolling elements are required to exceed a critical angle of the outer ring. For example, at amplitudes of less than 10° over ~40 rolling elements would be required to exceed θ_{crit}, which is especially not possible for smaller needle roller bearings.

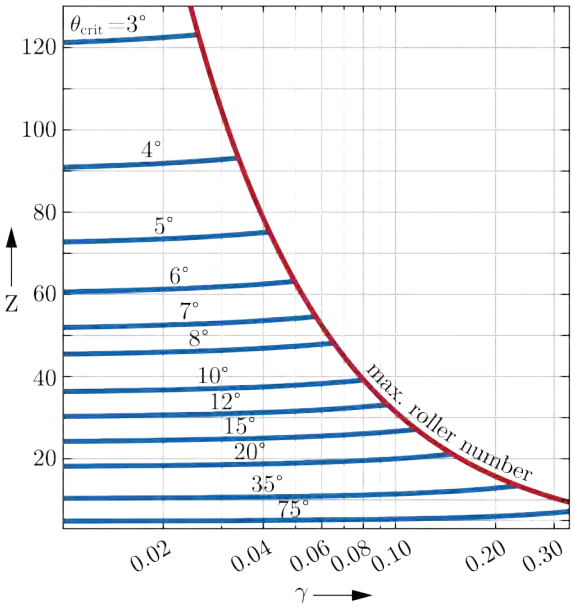

Figure 1: Critical oscillation amplitude of the outer ring

In 1999, HOUPERT [7] developed a calculation approach for oscillating bearing motion based on the LUNDBERG/PALMGREN model, restricted to $\theta_a > \theta_{crit}$. It considers the reduced number of load cycles on the circumferentially loaded ring within the load zone and an equivalent load for each position on the raceway. HOUPERT's life model was referenced e.g. in [14], [17], and [19] and is also discussed in HARRIS' textbook [4]. However, during an intensive and thorough revision of the HOUPERT model, an inconsistency was found which leads to an overestimation of the rating life for load distributions with $\varepsilon \leq 1$. The example of an oscillation amplitude of 180° is suitable for describing the problem. As with continuous rotation, each position of the raceway also passes through the entire load zone, but twice, see Figure 2.

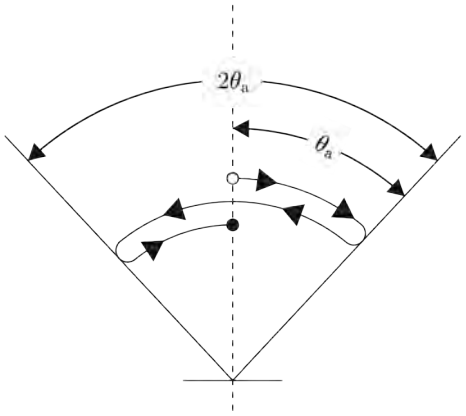

Figure 2: Oscillation period with amplitude θ_a

This results in a load zone independent life coefficient $a_{osc} = 0.5$, which is determined by the ratio of lives for oscillation L_{osc} in relation to continuous rotation L.

$$a_{osc} = \frac{L_{osc}}{L} \qquad \textit{(Eq. 2)}$$

In contrast to $a_{osc} = 0.5$ for $\theta_a = 180°$, the calculation approach of HOUPERT yields values of $a_{osc} > 1$ depending on ε. The editor and the authors have kindly suggested and accepted to let Dr. Houpert add a discussion chapter. This will give Dr. Houpert the opportunity to explain and correct his errors in [7], discuss some conceptual modeling differences and show a few additional results obtained since 1999. As explained by HOUPERT the reason for this inconsistency is a decisive error in [7], which was also noticed and corrected by the authors in [13]. In the Equation 30 of [7] the denominator $2\theta_a$ was used instead of the auxiliary function $H(\psi, \theta_a)$. Furthermore, the factor 2π was missing in equation 32 of [7], which can be considered as a typing error, since it has no influence on the calculation results of HOUPERT. For this reason, the results of [7] are still correct for a load zone of $\varepsilon \geq 1$, since the entire raceway is loaded and thus $H(\psi, \theta_a)$ is equal to $2\theta_a$. Moreover, HOUPERT used the life exponent $p = 10/3$ in combination with a WEIBULL slope of $e = 1.5$. These values are used at Timken Company for both rating life equation and load rating equation but do not correspond to the ISO standard exponents used for roller bearings. As the calculation is based on the LUNDBERG/PALMGREN model or the load rating

equation, it is advisable to use the parameters according to [2] and [3], with $p = 4$ and $e = 9/8$. It should be noted that the use of the exponent $p = 10/3$ is only permitted for the rating life equation but not for the load rating equation. In particular for needle roller bearings, it was already experimentally proven in [11] that a life exponent with $p = 4$ applies. This can also be explained by the fact that, due to the length of the roller, there is a line contact with a rectangular pressure surface rather than a point contact. Finally, it should also be noted that HOUPERT [7] does not refer to RUMBARGER/JONES [11]. This article takes up the basic idea of comparing the basic rating life for continuous rotation and oscillating motion of a bearing with same geometry under otherwise identical conditions. Thus, the rating life equation can be simplified. The work is based in part on a previously published article by SCHLECHT and BRESLAU [13]. The knowledge of the relations between the probability of survival, number of load cycles, stressed volume and load, contributes to a better understanding of the approaches presented hereafter. In the papers [7] and [11] a derivation of the life and load rating equations is presented as an introduction, so that the authors refrain from this and refer additionally to the publications [8] and [9]. In the following, the bearing rings are considered separately, not according to inner and outer ring, but in general regarding the load type. The term circumferentially loaded ring means that the applied load rotates or oscillates relative to the ring, whereas the stationary loaded ring is stationary relative to the applied load.

2. Continuous Rotation

2.1. Circumferentially Loaded Ring

The basic rating life depends on the dynamic radial load rating, the life exponent and the dynamic equivalent bearing load, whereby the latter is identical for oscillating motion.

$$L = \left(\frac{C}{P}\right)^p \qquad \textit{(Eq. 3)}$$

$$L \sim C^p \qquad \textit{(Eq. 4)}$$

According to [8], for the load rating of the circumferentially loaded ring it is established, that

$$C_1 = Z\, Q_c \frac{J_r}{J_1} \cos\alpha\,, \qquad \textit{(Eq. 5)}$$

where compared to oscillating motion only the load integral J_1 and the load rating of the single contact Q_c are different. For the dynamic load rating Q_c, only the load cycle number of the raceway overrolling N_{rot} must be considered, this leads to

$$C_1 \sim {N_{rot}}^{-\frac{1}{p}} {J_1}^{-1}\,. \qquad \textit{(Eq. 6)}$$

The number of load cycles for one full rotation yields

$$N_{rot} = Z\left(\frac{1 \pm \gamma}{2}\right). \qquad \textit{(Eq. 7)}$$

This leads to the following proportional equation

$$L \sim {N_{rot}}^{-1} {J_1}^{-p}\,. \qquad \textit{(Eq. 8)}$$

2.2. Stationary Loaded Ring

For the stationary loaded ring, the same number of load cycles applies according to Eq. 7. The only difference is the dynamic equivalent load, which is described by J_2 and leads to

$$L \sim {N_{rot}}^{-1} {J_2}^{-p}\,. \qquad \textit{(Eq. 9)}$$

The required load integrals J_1 and J_2 for continuous rotation are given by

$$J_1 = \left[\frac{1}{2\pi}\int_{-\pi}^{\pi} g(\psi,\varepsilon)^p \,\mathrm{d}\psi\right]^{\frac{1}{p}} \qquad \textit{(Eq. 10)}$$

and

$$J_2 = \left[\frac{1}{2\pi}\int_{-\pi}^{\pi} g(\psi,\varepsilon)^{p\,e} \,\mathrm{d}\psi\right]^{\frac{1}{p\,e}}, \qquad \textit{(Eq. 11)}$$

where the normalized load distribution as a function of the parameter ε is given by

$$g(\psi,\varepsilon) = \begin{cases} r(\psi,\varepsilon)^{\frac{10}{9}} & \text{if } r(\psi,\varepsilon) > 0 \\ 0 & \text{if } r(\psi,\varepsilon) \le 0 \end{cases} \qquad \textit{(Eq. 12)}$$

with

$$r(\psi,\varepsilon) = \left[1 - \frac{1}{2\,\varepsilon}\,(1 - \cos\psi)\right]. \qquad \textit{(Eq. 13)}$$

3. Oscillating Motion

3.1. Case 1: Low Oscillation Amplitudes $\theta_a < \theta_{crit}$

The following calculation approach is based on RUMBARGER and JONES. However, the derivation of the calculation equation according to [11] is complex and impracticable. Therefore, the following section presents a better comprehensible method of calculating the rating life coefficient. On the one hand, it is considered that the loaded raceway volume is reduced and on the other hand, that only two load changes occur during one oscillation period.

$$N_{osc} = 2 \qquad \textit{(Eq. 14)}$$

The Figure 3 shows the stressed volume, which does not overlap for low oscillation amplitudes $\theta_a < \theta_{crit}$.

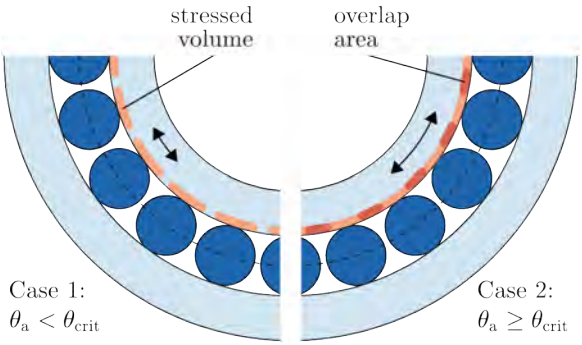

Figure 3: Case distinction [19]

Regarding the dynamic equivalent load, both rings are assumed to be stationary loaded due to the low oscillation amplitude independent of the load type. Thus, the equivalent load is also determined by J_2 for the circumferentially loaded ring. In addition, the load integral J_2

applies to the reduced stressed volume, which is decreased in inverse proportion to the loaded raceway length $l_{\mathrm{r,osc}}$. This ratio can be expressed by

$$\frac{l_{\mathrm{r,osc}}}{l_{\mathrm{r}}} = \frac{\theta_{\mathrm{a}}}{\theta_{\mathrm{crit}}}. \qquad \textit{(Eq. 15)}$$

Using this proportional relationship, the reduced load integral $J_{2,\mathrm{red}}$ is determined by

$$J_{2,\mathrm{red}} = J_2 \left(\frac{\theta_{\mathrm{a}}}{\theta_{\mathrm{crit}}}\right)^{\frac{1}{pe}}. \qquad \textit{(Eq. 16)}$$

From this the basic rating life follows for the proportional equation

$$L_{\mathrm{osc}} \sim {N_{\mathrm{osc}}}^{-1} {J_{2,\mathrm{red}}}^{-p}. \qquad \textit{(Eq. 17)}$$

The life coefficient is calculated in relation to Eq. 9 according to Eq. 2 for a stationary loaded ring by

$$a_{\mathrm{osc},2} = \frac{N_{\mathrm{rot}}}{N_{\mathrm{osc}}} \left(\frac{\theta_{\mathrm{a}}}{\theta_{\mathrm{crit}}}\right)^{-\frac{1}{e}}. \qquad \textit{(Eq. 18)}$$

The substitution of Eq. 7, Eq. 14 and Eq. 1, gives

$$a_{\mathrm{osc},2} = \frac{Z\,(1 \pm \gamma)}{4} \left(\frac{\theta_{\mathrm{a}}\, Z\,(1 \pm \gamma)}{2\pi}\right)^{-\frac{1}{e}} \qquad \textit{(Eq. 19)}$$

and for $e = 9/8$

$$a_{\mathrm{osc},2} = \frac{[Z\,(1 \pm \gamma)]^{\frac{1}{9}}}{4} \left(\frac{2\pi}{\theta_{\mathrm{a}}}\right)^{\frac{8}{9}} \qquad \textit{(Eq. 20)}$$

is found. If the ring is circumferentially loaded, then

$$a_{\mathrm{osc},1} = \frac{[Z\,(1 \pm \gamma)]^{\frac{1}{9}}}{4} \left(\frac{2\pi}{\theta_{\mathrm{a}}}\right)^{\frac{8}{9}} \left(\frac{J_1}{J_2}\right)^{p} \qquad \textit{(Eq. 21)}$$

holds true. According to the product law of probability, the coefficient a_{osc} for the entire bearing can be calculated as combination of the lives with previously determined load ratings C_1 and C_2 of the rings by

$$a_{\mathrm{osc}} = \left[\left(a_{\mathrm{osc},1} \left(\frac{C_1}{C_{\mathrm{r}}}\right)^{p}\right)^{-e} + \left(a_{\mathrm{osc},2} \left(\frac{C_2}{C_{\mathrm{r}}}\right)^{p}\right)^{-e}\right]^{-\frac{1}{e}}. \qquad \textit{(Eq. 22)}$$

This equation is only valid for roller bearings with the exponents $p = 4$ and $e = 9/8$. In [10] RUMBARGER introduced another case distinction, called dithering. It is valid for extremely small amplitudes, where the oscillating roller does not exceed the range of its own pressure ellipse. The same equations are used in a report by Harris et al. [5]. However, RUMBARGER has only related the angle to the bearing cage. The correct equation for the calculation of the dither angle can be determined, e.g by the rotational angle of the rolling element. Independent of which ring rotates, the absolute value of the rotation angle can be defined by

$$|\theta_{\mathrm{RE}}| = \cos\alpha\, \frac{\theta_{\mathrm{dith}}}{2} \left(\frac{1}{\gamma} - \gamma\right). \qquad \textit{(Eq. 23)}$$

The dither angle of the rolling element is given by

$$\theta_{\mathrm{RE}} = \frac{2\,b}{D_{\mathrm{we}}} = \frac{2\,b\,\cos\alpha}{D_{\mathrm{pw}}\,\gamma}. \qquad \textit{(Eq. 24)}$$

For the oscillating bearing ring the dither angle becomes

$$\theta_{\mathrm{dith}} = \frac{4\,b}{D_{\mathrm{pw}}\,(1-\gamma^2)}. \qquad \textit{(Eq. 25)}$$

By specifying a maximum pressure of 4000 MPa, the half contact width for rolling bearing steel is estimated by

$$b \approx 0.035\, D_{\mathrm{we}}\,(1 \pm \gamma). \qquad \textit{(Eq. 26)}$$

The upper sign refers to the outer ring and the lower sign to the inner ring. The substitution of Eq. 26 into Eq. 25 yields

$$\theta_{\mathrm{dith}} \approx \frac{0.14}{\cos\alpha}\, \frac{\gamma \pm \gamma^2}{1-\gamma^2}. \qquad \textit{(Eq. 27)}$$

For oscillation with ($\theta_{\mathrm{a}} < \theta_{\mathrm{dith}}$) the risk of false brinelling and fretting corrosion is very high. With reference to [5], it is recommended to avoid the operation at these very small oscillation angles. For this reason, no calculation method is presented for such a case.

3.2. Case 2: High Oscillation Amplitudes $\theta_{\mathrm{a}} \geq \theta_{\mathrm{crit}}$

In the following, the equations for calculating the coefficient a_{osc} based on a corrected and extended life model are presented. The model is valid for $\theta_{\mathrm{a}} \geq \theta_{\mathrm{crit}}$, for smaller amplitudes the RUMBARGER method must be used. Basically, a distinction is made according to the load on the respective bearing ring whether the load is stationary or rotates in relation to the ring.

3.2.1. Stationary Loaded Ring

In an oscillating bearing, the equivalent load Q_{eq} of the stationary loaded ring is identical to that for continuous rotation. Only the number of load cycles depends on the oscillation amplitude and is considered by

$$N_{\mathrm{osc}} = Z\, \frac{1 \pm \gamma}{2}\, \frac{2\,\theta_{\mathrm{a}}}{\pi}. \qquad \textit{(Eq. 28)}$$

For the proportionality equation of the rating life it is found

$$L_{\mathrm{osc}} \sim {N_{\mathrm{osc}}}^{-1} {J_2}^{-p}. \qquad \textit{(Eq. 29)}$$

The life coefficient is calculated in relation to Eq. 9 according to Eq. 2 for a stationary loaded ring by

$$a_{\mathrm{osc},2} = \frac{N_{\mathrm{rot}}}{N_{\mathrm{osc}}} = \frac{\pi}{2\,\theta_{\mathrm{a}}}. \qquad \textit{(Eq. 30)}$$

The same equation is presented in [5] and [7].

3.2.2. Circumferentially Loaded Ring

In most applications the load rotates in relation to the inner ring, which is subjected to higher pressures and consequently has a lower probability of survival than the outer ring. For this reason, HOUPERT only considered the circumferentially loaded inner ring when deriving the rating life coefficient in [7]. For an exact determination of the rating life, a calculation for both rings depending on the load types is recommended.
The calculation of the ring with rotating load is more complex, since not only the number of load cycles changes, but also a separate dynamic equivalent load Q_{eq} has to be considered for each rolling element position ψ on the raceway. The following Figure 4 shows, that the stress of an elementary ring volume

dV_ψ under circumferential load depends on the orbital position ψ and the oscillation amplitude θ_a.

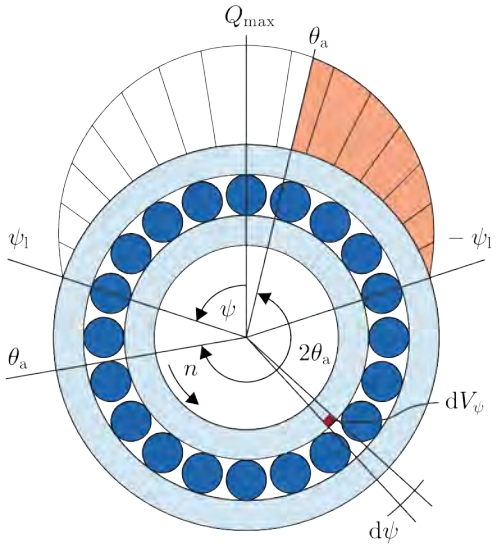

Figure 4: Visualization of the load integral $J_{\theta_a,\psi}$ for a ring position ψ and oscillation amplitude θ_a [7]

Compared to continuous rotation, where each volume element passes through the entire load zone and thus the equivalent load is described by J_1, with oscillation a separate load integral must be calculated for each volume, which is introduced with $J_{\theta_a,\psi}$.

$$Q_{eq} = Q_{max}\ J_{\theta_a,\psi} \qquad \textit{(Eq. 31)}$$

For an oscillating bearing motion, the following load integral is found

$$J_{\theta_a,\psi} = \left[\frac{1}{2\,\theta_a}\int_{\psi-\theta_a}^{\psi+\theta_a} g(\psi,\varepsilon)^p\,d\psi\right]^{\frac{1}{p}}. \qquad \textit{(Eq. 32)}$$

This results in a different dynamic equivalent load for each position, so that different probabilities of survival are obtained. These probabilities are combined according to the product law by the same way as for the load integral J_2. The load integral of the entire bearing ring is given with

$$J_{\theta_a} = \left[\frac{1}{2\,\pi}\int_{-\pi}^{\pi} {J_{\theta_a,\psi}}^{p\,e}\,d\psi\right]^{\frac{1}{p\,e}}. \qquad \textit{(Eq. 33)}$$

For the proportionality equation of the rating life it is found

$$L \sim {N_{osc}}^{-1}\,{J_{\theta_a}}^{-p}. \qquad \textit{(Eq. 34)}$$

The life coefficient is calculated in relation to Eq. 8 according to Eq. 2 for a circumferentially load ring by

$$a_{osc,1} = \frac{N_{rot}}{N_{osc}}\left(\frac{J_1}{J_{\theta_a}}\right)^p = \frac{\pi}{2\,\theta_a}\left(\frac{J_1}{J_{\theta_a}}\right)^p. \qquad \textit{(Eq. 35)}$$

For a better illustration, two calculation examples are given for $\psi_l = 45°$. The diagrams show the resulting values for J_{θ_a} and the relative equivalent load $J_{\theta_a,\psi}$ as function of the position angle ψ. For reference, the value for continuous rotation is given with $J_1 = 0.5556$. The Figure 5 shows the results for an oscillation amplitude $\theta_a = 65°$, resulting in a load integral with $J_{\theta_a} = 0.5689$.

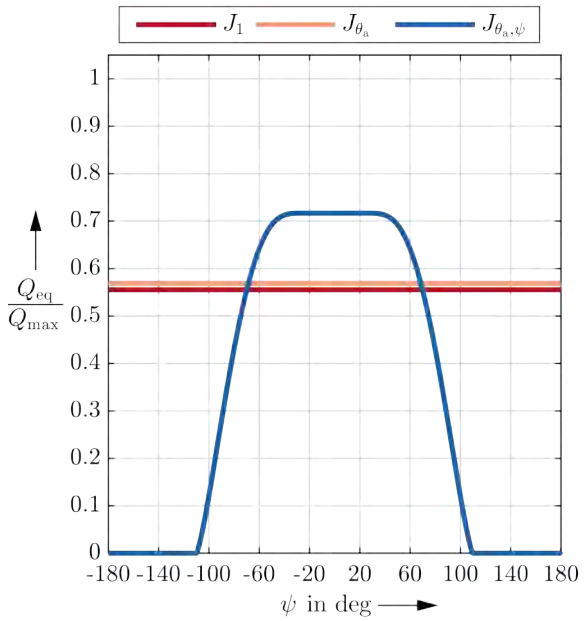

Figure 5: Example for the dynamic equivalent load of the circumferentially loaded ring, with $\theta_a = 65°$ and $\psi_l = 45°$

By reducing the oscillation amplitude in Figure 6 to $\theta_a = 1°$, the value of the load integral $J_{\theta_a} = 0.5863$ approaches the value of $J_2 = 0.5864$, since the load case is rather stationary. The function $J_{\theta_a,\psi}$ becomes similar to the load distribution with decreasing amplitude, so that the value for $\psi = 0$ approaches the maximum rolling element load Q_{max}. Consequently, a stationary loaded ring can be assumed. This confirms the assumption which was made by RUMBARGER and JONES in [11] for very small amplitudes.

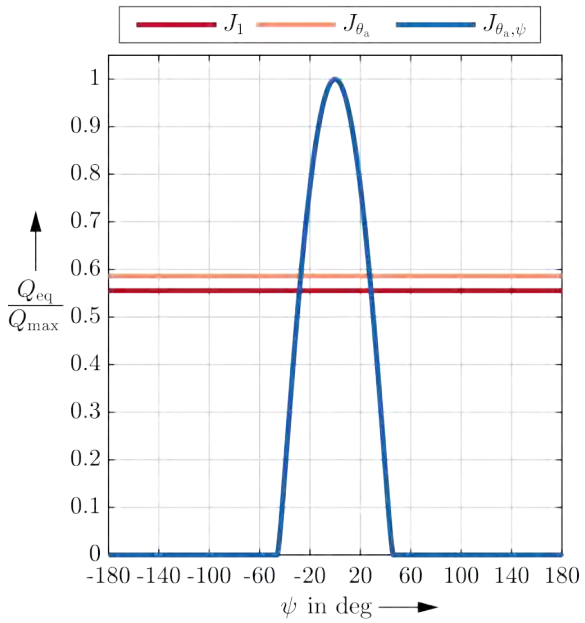

Figure 6: Example for the dynamic equivalent load of the circumferentially loaded ring, with $\theta_a = 1°$ and $\psi_l = 45°$

According to equation Eq. 35, the life coefficient is the product of two terms. The first one is identical to the case of a stationary loaded ring and is only dependent on the amplitude, while the second one is additionally dependent on the load zone parameter. The results are

shown in Figure 7. Obviously, the second term has less influence and must be considered only for smaller amplitudes. This diagram differs significantly from the one shown in [7] by HOUPERT. This becomes clearer at an amplitude of 180°, where the life coefficient is exactly 0.5, independent of the load zone parameter.

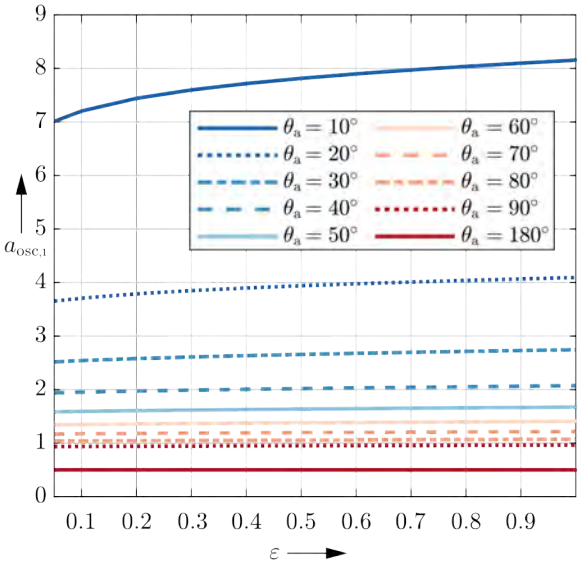

Figure 7: Life coefficient for oscillation ($\theta_a \geq \theta_{crit}$)*, with* $p = 4$ *and* $e = 9/8$

Since there is a low dependency on the load zone parameter ε, which is usually between 0.2 and 0.5 for radial loaded bearings, the rating life coefficient can be specified using a universal load distribution. In accordance with the standard a load integral of $J_r = 0.2$ is assumed for normal bearing clearance in operation (p. 39 in [6]), which is based on a load zone extension of $\psi_l = 65°$. For this value, the Table 1 shows the coefficients for both rings depending on the amplitude.

Table 1: Life coefficient for oscillation ($\theta_a \geq \theta_{crit}$) *and a load zone extension of* $\psi_l = 65°$

amplitude θ_a in deg	life coefficient for oscillation	
	circumferentially loaded ring $a_{osc,1}$	stationary loaded ring $a_{osc,2}$
10	7.5824	9.0000
20	3.8425	4.5000
30	2.6054	3.0000
40	1.9880	2.2500
50	1.6160	1.8000
60	1.3662	1.5000
70	1.1863	1.2857
80	1.0503	1.1250
90	0.9436	1.0000
180	0.5000	0.5000

The calculation approach is applicable for all amplitudes of ($\theta_{crit} < \theta_a$) without restrictions. Even if the oscillation amplitude θ_a exceeds π, the load distribution is calculated correctly by Eq. 12. For example, an amplitude of $\theta_a = 4\,\pi$ results in a life coefficient $a_{osc} = 0.125$, since the load zone is completely passed through 8 times. The calculation of a coefficient for the entire bearing depends on γ and is determined, as for the low amplitudes, by Eq. 22.

4. Life Coefficient for Non-Uniform Loads

Besides the motion of the bearing rings, the external load on the bearing can also be non-uniform. The dynamic load $F(t)$ of an oscillation or a generic procedure is described by the dynamic equivalent load P. Therefore, the determination of P is done by the linear accumulation of damage according to the MINER rule. This is calculated in the similar way as the load integral J_1 according to Eq. 10.

$$P = \left[\frac{1}{T}\int_0^T F(t)^p \, \mathrm{d}t\right]^{\frac{1}{p}} \qquad \textit{(Eq. 36)}$$

However, this equation is only valid for a constant bearing speed, otherwise the integral must be related to the angle of rotation. For a dynamic load during an oscillating bearing motion with the same period, it is found

$$P = \left[\frac{1}{2\,\theta_a}\int_{-\theta_a}^{\theta_a} F(\theta)^p \, \mathrm{d}\theta\right]^{\frac{1}{p}}. \qquad \textit{(Eq. 37)}$$

Just as with the load integrals, the equivalent load can be related to a nominal load F_N and defined as a dimensionless number. For this purpose, the load modification factor ϕ_m is introduced by

$$\phi_m = \left[\frac{1}{2\,\theta_a\,F_N}\int_{-\theta_a}^{\theta_a} F(\theta)^p \, \mathrm{d}\theta\right]^{\frac{1}{p}}. \qquad \textit{(Eq. 38)}$$

The following expression is used to determine a life coefficient from the load modification factor.

$$a_P = {\phi_m}^{-p} \qquad \textit{(Eq. 39)}$$

5. Application Example: Universal Joint

Universal joints are used to connect and transmit rotary motion of two axes inclined to each other. The diagram of a universal joint is shown in Figure 8. The joint connection between the journal and yoke eye is usually realized by needle bearings. These bearings transmit the forces resulting from the torque between the yokes and perform an oscillating bearing motion depending on the flexion angle β. The oscillation amplitude required to calculate the coefficient corresponds to the flexion angle of the cardan shaft, $\beta = \theta_a$. However, in addition to the oscillating motion, the special aspect in calculating the rating life of these bearings is the non-uniformly acting radial force. The basic idea is to calculate the load rating and basic rating life separately for the inner and outer raceways. In the case of the universal joint it must be considered, that the basic dynamic load rating on the outer raceway is calculated for a circumferential load by C_1 and on the inner raceway for a stationary load by C_2, see [7] or [2]. A closer investigation of the cardan shaft kinematics and an evaluation

of the bearing forces as function of the oscillation angle θ shows that the bearing forces F_L are not constant and differ with respect to the yokes G_1 and G_2.

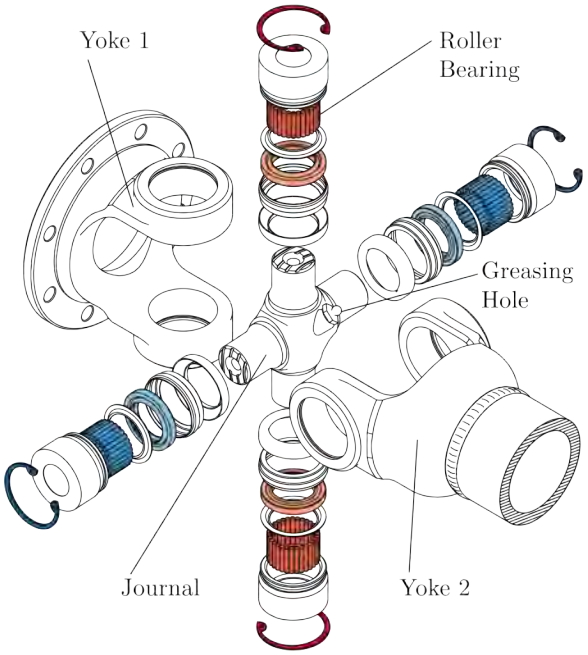

Figure 8: Diagram of a universal joint [12], red bearings belong to yoke 1 the blue ones to yoke 2

This requires the analysis of the internal joint forces, which are shown in the Figure 9 for two different positions. The equilibrium of moments on the journal shows that the bearing forces F_L are identical for both yokes at any time and it is found

$$F_L(\varphi_1) = \frac{M_{T1}}{h}\sqrt{1+\sin^2\varphi_1\ \tan^2\beta}\ . \qquad \textit{(Eq. 40)}$$

However, to determine a dynamic equivalent load, the oscillation angle θ depending on the angle of rotation φ_1 of yoke 1 is also required. The oscillation angle of yoke 1 is given by

$$\theta = \arctan(\sin\varphi_1\ \tan\beta) \qquad \textit{(Eq. 41)}$$

and for yoke 2 by

$$\theta = \arctan\left(\frac{\cos\varphi_1\ \sin\beta}{\sqrt{1-\cos^2\varphi_1\ \sin^2\beta}}\right). \qquad \textit{(Eq. 42)}$$

These equations are used to describe the bearing force as a function of the oscillation angles. A corresponding diagram is shown in Figure 10 for a flexion angle of $\beta = 45°$. By elimination of φ_1 and transformation the following equations are obtained at yoke 1 by

$$F_{L1}(\theta) = F_{P1}\sqrt{\tan^2\theta + 1} \qquad \textit{(Eq. 43)}$$

and at yoke 2 by

$$F_{L2}(\theta) = F_{P1}\ \cos\theta\ \sqrt{\tan^2\beta + 1}. \qquad \textit{(Eq. 44)}$$

In Figure 10 both functions are related to the nominal bearing force $F_{P1} = M_{T1}/h$. The dynamic equivalent load is derived from equation Eq. 37 and determined by

$$P = \left[\frac{1}{2\,\beta}\int_{-\beta}^{\beta} F_L(\theta)^p\ \mathrm{d}\theta\right]^{\frac{1}{p}}. \qquad \textit{(Eq. 45)}$$

In accordance with the equation Eq. 38, this yields the load modification factor ϕ_{m1} for yoke 1, with

$$\phi_{m1} = \left[\frac{1}{2\,\beta\,F_{P1}}\int_{-\beta}^{\beta}[F_{L1}(\theta)]^p\ \mathrm{d}\theta\right]^{\frac{1}{p}}. \qquad \textit{(Eq. 46)}$$

In the similar way the load modification coefficient ϕ_{m2} for yoke 2 is determined by

$$\phi_{m2} = \left[\frac{1}{2\,\beta\,F_{P1}}\int_{-\beta}^{\beta}[F_{L2}(\theta)]^p\ \mathrm{d}\theta\right]^{\frac{1}{p}}. \qquad \textit{(Eq. 47)}$$

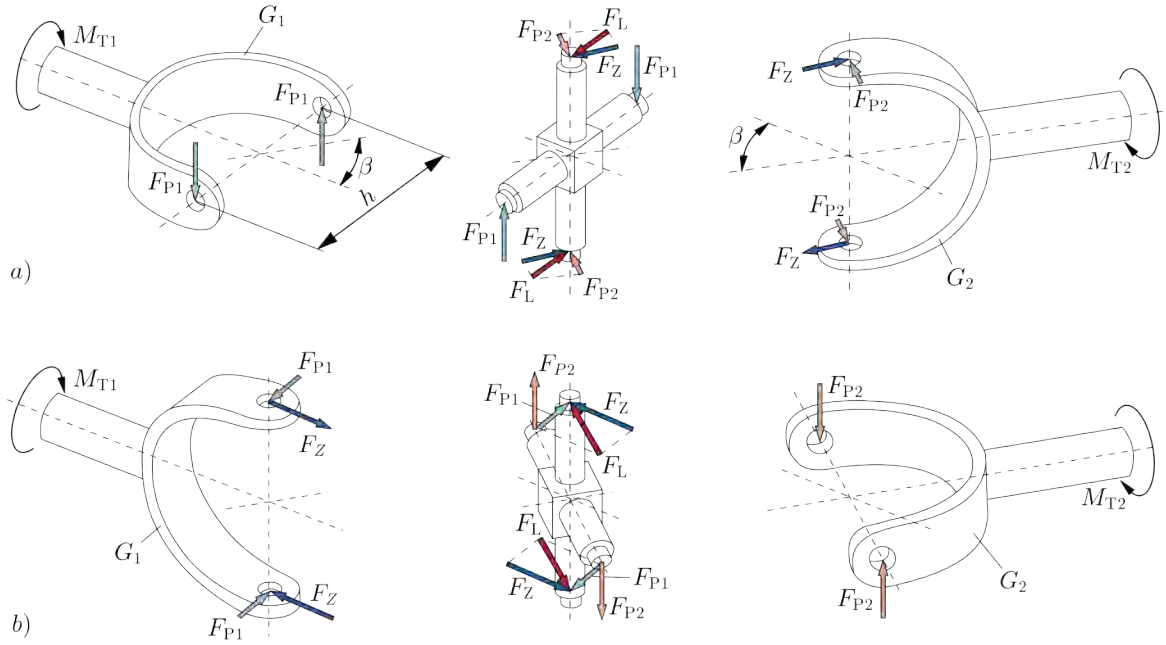

Figure 9: Yoke forces of a universal joint: in a) for $\varphi_1 = 0°$ and in b) for $\varphi_1 = 90°$ [16]

A similar approach can be found in [16] pp. 118 by SEHERR-THOSS et al. However, they neglect the additional force F_Z and calculate only an equivalent load of F_{P2}, which does not represent the actual bearing load.

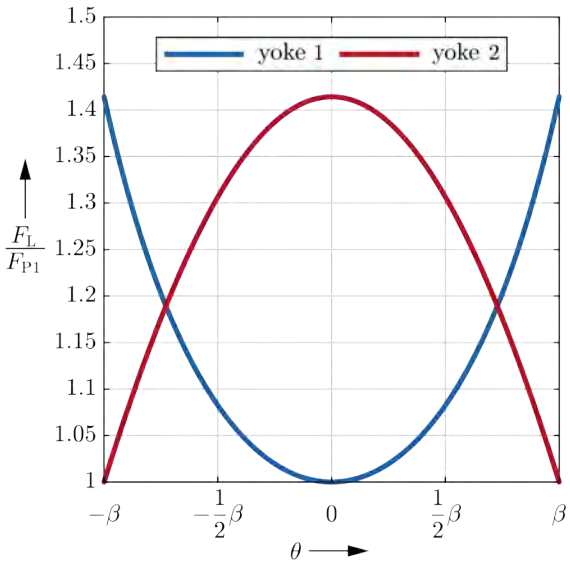

Figure 10: Bearing forces as function of the oscillaion angle

Although the integrals of Eq. 46 and Eq. 47 can be solved analytically, the antiderivatives are too complex in practical application. For this reason, the integrals are solved numerically, and the results are listed in Table 2 for different life exponents. Concerning the needle roller bearings, a life exponent of $p = 4$ is generally used, see [11]. Therefore Figure 11 shows the load modification factors as a function of the flexion angle, provided that the universal joints are set up in a Z-arrangement. For this arrangement, the bearings of yoke 2 are always subject to higher loads. In contrast, the length of the intermediate shaft in the W-arrangement has an additional influence on the bearing load of yoke 1. Here the authors focus on the Z-arrangement and refer to [16] pp. 145 for a derivation of the equations valid for the W-arrangement.

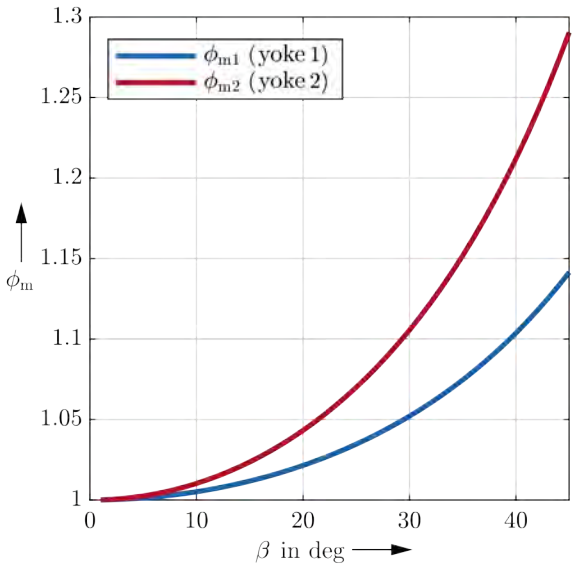

Figure 11: Load modification factor ϕ_m, for $p = 4$ in Z-arrangement

Furthermore, the inertial forces caused by the intermediate shafts with a high moment of inertia can also be included in the determination of the bearing forces due to the non-uniform rotation. As can be seen in Table 2, there is a strong dependence between the load modification factors on the flexion angle, which can be neglected for $\beta < 10°$. This results according to Eq. 39 in the following rating life coefficients of Table 3 for both yokes, depending on the flexion angle of the cardan shaft.

Table 2: Load modification factor ϕ_m

flexion angle β in deg	point contact		line contact				
	$p = 3$		$p = 10/3$		$p = 4$		
	ϕ_{m1}	ϕ_{m2}	ϕ_{m1}	ϕ_{m2}	ϕ_{m1}	ϕ_{m2}	$F_{L,max}/F_{P1}$
3	1.000	1.001	1.000	1.001	1.000	1.001	1.001
6	1.002	1.004	1.002	1.004	1.002	1.004	1.006
9	1.004	1.008	1.004	1.008	1.004	1.008	1.012
12	1.007	1.015	1.007	1.015	1.007	1.015	1.022
15	1.012	1.024	1.012	1.024	1.012	1.024	1.035
18	1.017	1.034	1.017	1.035	1.017	1.035	1.051
21	1.024	1.048	1.024	1.048	1.024	1.048	1.071
24	1.031	1.064	1.031	1.064	1.032	1.064	1.095
27	1.040	1.082	1.041	1.083	1.041	1.083	1.122
30	1.051	1.105	1.051	1.105	1.052	1.106	1.155
33	1.063	1.130	1.064	1.131	1.065	1.132	1.192
36	1.078	1.161	1.078	1.161	1.080	1.163	1.236
39	1.094	1.196	1.095	1.197	1.097	1.199	1.287
42	1.113	1.237	1.114	1.238	1.118	1.241	1.346
45	1.135	1.285	1.137	1.287	1.141	1.290	1.414

Table 3: Life coefficient a_p

flexion angle β in deg	line contact			
	$p = 10/3$		$p = 4$	
	a_{P1}	a_{P2}	a_{P1}	a_{P2}
3	0.998	0.997	0.998	0.996
6	0.994	0.988	0.993	0.985
9	0.986	0.973	0.984	0.967
12	0.976	0.952	0.971	0.942
15	0.962	0.925	0.954	0.911
18	0.945	0.893	0.934	0.873
21	0.925	0.856	0.910	0.829
24	0.902	0.814	0.883	0.780
27	0.876	0.767	0.851	0.727
30	0.846	0.717	0.816	0.669
33	0.814	0.664	0.778	0.609
36	0.778	0.608	0.735	0.547
39	0.739	0.550	0.690	0.484
42	0.697	0.491	0.641	0.422
45	0.652	0.431	0.589	0.361

The rating life of both raceways is calculated using the coefficients for oscillating motion and load. For the trunnion (inner ring) the coefficient is determined by Eq. 30 & Eq. 20 and for the drawn cup (outer ring) by Eq. 35 & Eq. 21. Subsequently, the oscillation coefficients are calculated for an example bearing as a function of the amplitude by the calculation approaches for $\theta_a \geq \theta_{crit}$ and $\theta_a < \theta_{crit}$. If the amplitude is between the critical angles of the inner and outer ring, then the coefficient is calculated using both approaches. Thus, in case of $\theta_a = \theta_{crit}$ the calculated coefficient must be same for both methods. According to this Eq. 14 is obtained by substituting Eq. 1 in Eq. 28. The life coefficient as a function of the oscillation amplitude is shown in Figure 12 for an example bearing.

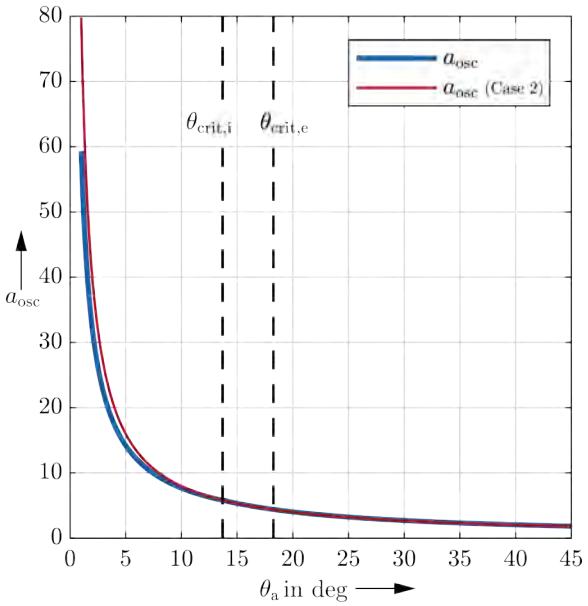

Figure 12: Life coefficient as a function of θ_a with: $\varepsilon = 0.5$, $Z = 23$ and $\gamma = 0.1429$, stationary load on the outer ring

For the critical oscillation amplitudes, no discontinuities occur, which proves that the modelling approaches are compatible with each other. Furthermore, the coefficients increase progressively with decreasing amplitude if the critical angle is exceeded. Furthermore, it is investigated which results are determined if only the calculation approach of case 2 is used and the critical range is ignored. Compared to the coefficients a_{osc} of the combined approaches small deviations occur if the amplitude θ_a is below $\theta_{crit,e}$. To enable a better comparison, the ratio of the coefficients is calculated from both curves. If the amplitude θ_a falls below the critical angle $\theta_{crit,e}$, the function of the lifetime coefficient a_{osc} shows a very small, negligible step. This is caused by the assumption of a point load for the circumferentially loaded ring, in this case the inner ring. The values of the a_{osc}(corr.)-curve are calculated by the Eq. 21 using J_{θ_a} instead of J_2, similar to Eq. 35.

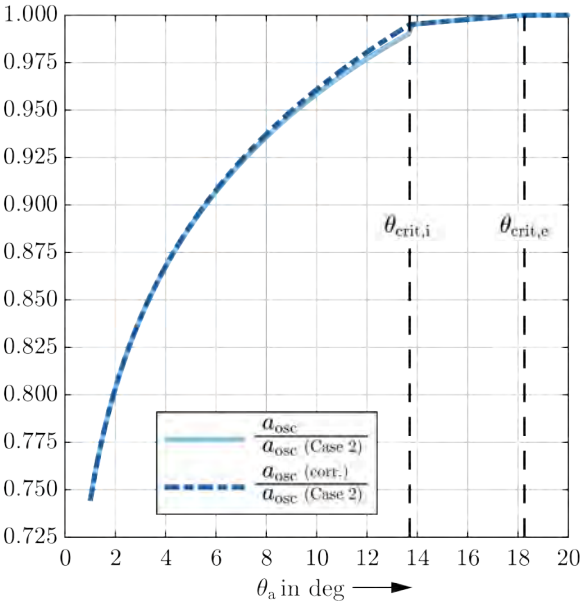

Figure 13: Ratio of the life coefficient curves from Figure 12

To ensure a better comparability, the life coefficient of the example bearing in Figure 11 and Figure 13 have been calculated for a stationary load on the outer ring. For the universal joint application example, a calculation must be made for a circumferential load on the outer ring. Finally, the modified rating lives of the bearings on yoke 1 for trunnion (index i) and drawn cup (index e) are calculated as follows

$$L_{10m,1i} = a_{P1}\, a_{osc,2} \left(\frac{C_i}{F_{P1}}\right)^p, \qquad \textit{(Eq. 48)}$$

$$L_{10m,1e} = a_{P1}\, a_{osc,1} \left(\frac{C_e}{F_{P1}}\right)^p. \qquad \textit{(Eq. 49)}$$

Since the inner raceway of the universal joint bearing is subjected to a stationary load, the coefficient $a_{osc,2}$ is used and consequently for the outer raceway $a_{osc,1}$. The rating lives $L_{10m,2i}$ and $L_{10m,2e}$ of yoke 2 are calculated in the same way, by using a_{P2}. Eventually, the separate modified rating lives of both parts are combined statistically in a common rating life of the complete bearing.

$$L_{10m,1} = \left(L_{10m,1i}{}^{-e} + L_{10m,1e}{}^{-e}\right)^{-\frac{1}{e}} \qquad \textit{(Eq. 50)}$$

Such a combination of rating lives is also valid for bearing assemblies. In this way, the lives of the individual needle roller bearings are combined to obtain the life of the entire universal joint.

$$L_{10\mathrm{m}} = \left(2\,{L_{10\mathrm{m},1}}^{-e} + 2\,{L_{10\mathrm{m},2}}^{-e}\right)^{-\frac{1}{e}} \qquad \textit{(Eq. 51)}$$

The resulting rating life is significantly lower, compared to a single bearing. This can be explained by the fact that if four bearings transmit a force in parallel, the probability of failure is higher compared to a single bearing. Therefore, if the same reliability of 90 % is required as for individual bearings, these must in turn satisfy a higher probability of survival then 90 %.

6. Conclusion

Starting with the theory of LUNDBERG and PALMGREN in [8] a novel life coefficient equation for an oscillating roller bearing was derived. The presented calculation method is derived from the approach of RUMBARGER and JONES [11] for low oscillation angles. Based on the work of HOUPERT [7] an improved and corrected approach was presented for high oscillation angles. Both methods were derived by means of the integrals J_1 and J_2, known from the rating load equation according to [2] and [3] or [6]. The application example was used to show that both methods can be combined and provide the same results for the critical amplitude θ_{crit}. As the life coefficients are calculated separately for each ring, it was shown how the rating lives or coefficients can be statistically combined to obtain a prediction of the entire bearing. This is of special interest if the outer ring is circumferentially loaded and not as usually the inner ring. This paper provides a simple application of the calculation model by means of practical equations as well as tables and diagrams. The only restriction associated with this calculation approach is the assumption, that the lubrication conditions of the oscillating bearings remain unchanged, compared to continuously rotating ones. It is questionable, whether an effective lubricating film will form, especially at low oscillation amplitudes. Therefore, mainly greases are used, which are optimized for mixed and boundary friction. In addition to the lubricant film, suitable greases form separating layers on the contact surfaces, which separate friction partners from each other and prevent adhesion ([1], p. 2). In particular, for low oscillation amplitudes, the risk of wear increases due to false brinelling and fretting corrosion. If the investigated bearing fails due to wear rather than roller contact fatigue, the presented calculation method cannot be applied. In such a case, the lubricant conditions must first be improved. To enable a credible validation of the results, very time-consuming tests of grease-lubricated rolling bearings at low speeds would be necessary to minimize the influence of the lubricant.

As an example of an oscillatory application, the drawn cup needle roller bearing of the universal joint was chosen. Besides the oscillating motion, a non-uniform bearing load must be considered for these bearings. For this purpose, the bearing forces were derived as a function of the oscillation angle, and a dynamic equivalent load was calculated. This equivalent load can be expressed as load modifying factor or directly as life coefficient. Together with the coefficient for oscillating motion a modified rating life can be determined separately for each raceway. These lifetimes can be statistically combined to obtain a rating life for the entire bearing. The rating life of the entire universal joint is determined in a similar way. The methods presented in this paper can be applied to any bearing that is subject to oscillating motion or non-uniform load. Furthermore, the approaches are also suitable for ball bearings.

References

[1] Bosse, H., Müller F., 2003, “Oszillierende Bewegungen: Schmierungsverhalten bei oszillierenden Gleit- und Wälzbewegungen“, Forschungsvereinigung Antriebstechnik e.V, (315/I).

[2] DIN, 2010, “Wälzlager – Dynamische Tragzahlen und nominelle Lebensdauer (ISO 281:2007)“, DIN ISO 281:2010-10, DOI: 10.31030/1718715.

[3] DIN, 2010, “Wälzlager – Erläuternde Anmerkungen zur ISO 281 - Teil 1: Dynamische Tragzahlen und nominelle Lebensdauer (ISO/TR 1281-1:2008/Cor.1:2009)“, DIN SPEC 1281-1:2010-05, DOI: 10.31030/1625622.

[4] Harris T. A., Kotzalas M. N., 2006, Essential Concepts of Bearing Technology, CRC Press, Boca Raton, DOI: 10.1201/9781420006582.

[5] Harris T. A., Rumbarger J. H., Butterfield C. P, 2009, “Wind Turbine Design Guideline DG03: Yaw and Pitch Rolling Bearing Life”, Office of Scientific and Technical Information (OSTI), DOI: 10.2172/969722.

[6] ISO, 2008, “Rolling bearings – Explanatory notes on ISO 281 – Part 2: Modified rating life calculation, based on a systems approach to fatigue stresses”, ISO/TR 1281-2:2008-12.

[7] Houpert L., 1999, “Bearing Life Calculation in Oscillatory Applications”, Tribology Transactions, 42(1), pp. 136–143, DOI: 10.1080/10402009908982200.

[8] Lundberg G., Palmgren A., 1947, “Dynamic capacity of rolling bearings”, Acta Polytechn. No. 7, Mech. Engng. Series, 1(3).

[9] Lundberg G., Palmgren, A., 1952, “Dynamic capacity of roller bearings”, Acta Polytechn. No. 96, Mech. Engng. Series, 2(4).

[10] Rumbarger, J. H., 2003, “Simplification of Dynamic Capacity and Fatigue Life Estimations for Oscillating Rolling Bearings”, Journal of Tribology 125 No. 4, pp. 868–870, DOI: 10.1115/1.1576424.

[11] Rumbarger J. H., Jones A. B, 1968, “Dynamic Capacity of Oscillating Rolling Element Bearings”, Journal of Lubrication Technology, 90(1), pp. 130–138, DOI: 10.1115/1.3601528.

[12] Schlecht B., 2015, Maschinenelemente 1, Pearson Studium, Hallbergmoos, ISBN 3868942688.

[13] Schlecht B., Breslau G., 2019, “Lebensdauerberechnung von Wälzlagern in oszillierenden Anwendungen“, Dresdner Maschinenelemente Kolloquium.

[14] Schmelter R., 2011, “Über die Lebensdauerberechnung oszillierender Wälzlager“, Mitteilungen aus dem Institut für Maschinenwesen der Technischen Universität Clausthal, 36, pp. 35–42.

[15] Schwack, F., 2020, "Untersuchungen zum Betriebsverhalten oszillierender Wälzlager am Beispiel von Rotorblattlagern in Windenergieanlagen", Gottfried Wilhelm Leibniz Universität, Diss., DOI: https://doi.org/10.15488/9756.

[16] Seherr-Thoss H. C., Schmelz F., Aucktor E., 2002, Gelenkwellen, Springer, Berlin Heidelberg.

[17] Stammler M., Reuter A., Poll G., 2018, "Cycle counting of roller bearing oscillations - case study of wind turbine individual pitching system", Renewable Energy Focus, 25, pp. 40–47, DOI: 10.1016/j.ref.2018.02.004.

[18] Thiede, K. U., Deters, L., 2003, "Oszillierende Bewegungen: Wirkung von Schmierstoffen bei langsamen oszillierenden Gleit- und Wälzbewegungen", Forschungsvereinigung Antriebstechnik e.V, (315/II).

[19] Wöll L., Jacobs G., Kramer A., 2018, "Lifetime Calculation of Irregularly Oscillating Bearings in Offshore Winches", Modeling, Identification and Control: A Norwegian Research Bulletin, 39(2), pp. 61–72, DOI: 10.4173/mic.2018.2.2.

Discussion

Luc Houpert *(Bearing and Tribology Consultant, Wettolsheim, France, luc.houpert@orange.fr)*

Let me first congratulate the authors for having picked up some subtle inconsistencies in the results shown in [7] and for having written an excellent paper about a complex topic.

By coincidence, I started on April 2020 some consulting activities on the same topic with the Fraunhofer IWES department (via a cooperation with Mr. Oliver Menck and Dr. Matthias Stammler) and Mr. Menck noticed the same anomalies in my 1999 published results.

The good news is that I found since only one single error in [7] to fix for solving all observed inconsistencies. Many additional results have been obtained in 2020 and will be described in a near future in a joint paper with Mr. Menck.

I would like to thank the authors for giving me the possibility of explaining my error and correction, discussing their model and debating for example on what I consider as two authors' conceptual errors which have fortunately and by coincidence no consequence on their presented results.

I also would like to thank Dr. Stammler for the permission given to show some preliminary results obtained in the frame of a project sponsored by IWES.

Finally, this discussion may hopefully help the readers to get some additional explanations about how the bearing life can be calculated in continuous rotating and oscillatory application cases.

Description of the number of stress cycles and loaded arc to use

Although I fully agree with the final results presented in this paper, I would like to mention some of my conceptual disagreements on a few provided explanations.

For example, Eq. (7) giving the number of stress cycles N_{rot} only applies to a 180 degree loaded zone.

N_{rot} is proportional to $2.\psi_l/2\pi$, (the loaded arc being $2.\psi_l$), but $2.\psi_l$ will disappear later on when using the product $Q_{eq}^{p.e} * N_{rot}^{e}$ with $2.\psi_l$ appearing at the denominator when defining Q_{eq}^{p}.

I agree with the number of stress cycle N_{osc} for the stationary loaded ring described in Eq. (28) as constant for each elementary volume $dV(\psi)$ (located at any orbital angle ψ) and proportional to $2.\theta_a/\pi$ or $2*2.\theta_a/(2.\pi)$.

But the same N_{osc} is also used by the authors in Eq. (34) when studying the oscillating ring.

As described in [7], the number of stress cycles for an elementary volume $dV(\psi)$ located at angle ψ on the oscillating ring cannot be constant and simply proportional to $2.\theta_a/\pi$ or $2*2.\theta_a/(2.\pi)$.

It is in reality proportional to $2*H/(2.\pi)$, H being the loaded arc (in radian or degree) that an elementary volume $dV(\psi)$, initially located at the orbital position ψ, will endure during one oscillation . H can be calculated numerically as done in [7], see equation (28) and Figure 4 of Ref. [7]:

$$H(\psi,\theta) = \int_{\psi-\theta}^{\psi+\theta} h(\psi).d\psi \quad \text{with } h(\psi)=1 \text{ if } Q(\psi)\neq 0 \quad \text{or } h(x)=0 \text{ if } Q(\psi)=0 \qquad \textit{(Eq. 52)}$$

In Figure 4 of the current paper, if (ψ, θ_a and ψ_l) are equal to about 225 or -135 degrees (for ψ), 125 degrees and 45 degrees respectively, then H is equal to about 35 degrees (for ψ = -135 degrees).

An analytical relationship for H or number of cycles, only applicable to the case $\theta_a > \psi_l$ (θ instead of θ_a will be used next) has been given in Table 1 of [7], and can now be extended to all cases (see next Table 4), including the case not considered analytically in 1999 where two partial incursions of $dV(\psi)$ in the load zone (by its two ends) occur:

Table 4: Analytical relationships valid for $-\pi \le \psi \le \pi$ and $\theta \le \pi$

$\lvert\psi\rvert \le \lvert\theta-\psi_l\rvert$	$(\theta-\psi_l) \le \lvert\psi\rvert \le (\psi_l+\theta)$	$\lvert\psi\rvert \ge \psi_l+\theta$
$H = 2.Min(\psi_l,\theta)$	$H = (\theta+\psi_l-\lvert\psi\rvert) + Max(0, \lvert\psi\rvert+\theta+\psi_l-2.\pi)$	$H = 0$

H is therefore a function of ψ since it can be nil, or increase linearly with ψ when the elementary volume enters partially the loaded zone the during one oscillation, or can be constant (corresponding to a flat zone in Figure 14) and equal to $2.\theta_a$ (or $2.\psi_l$ if $\psi_l < \theta_a$) when the elementary volume $dV(\psi)$ is continuously located in the loaded zone. Figure 14 shows one example of two flat zones:

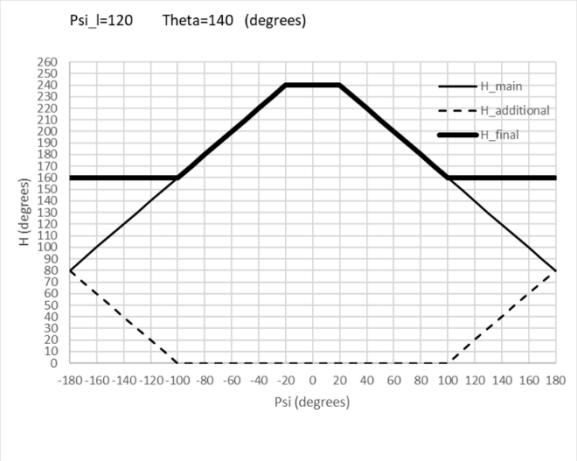

Figure 14: Example (ψ_l = 120 and θ = 140 degrees) corresponding to the existence of two flat zones.

The standard or main flat zone is 240 degrees in this example and correspond to the $Min(\psi_l,\theta)$.

A second flat zone (here 160 degrees) is possible when a second incursion in the other end of the loaded zone is causing an additional H (represented by the *Max* function in Table 4) which compensates the decrease of the main H.

As a result, the number of stress cycle of a given point on the oscillating inner ring cannot be considered as constant and simply proportional to $2.\theta_a$, but should be seen as proportional to H itself function of ψ, ψ_l and θ_a.

Description of the equivalent load

The second conceptual error is about how the equivalent load of the rotating or oscillating ring is defined.

When using the Miner's rule for defining the equivalent load of the rotating or oscillating ring, a discrete summation (replaced later by an integral) of Q^p should be used with at the denominator: $2.\psi_l$ in continuous rotation or the loaded arc angle H in oscillatory applications:

$$Q_{eq} = \left(\frac{1}{2.\psi_l}.\int_{-\psi_l}^{\psi_l} Q^p\,.d\psi\right)^{\frac{1}{p}} \quad \text{or}$$

$$Q_{eq}(\psi) = \left(\frac{1}{H}.\int_{\psi-\theta_a}^{\psi+\theta_a} Q^p\,.d\psi\right)^{\frac{1}{p}} \qquad \textit{(Eq. 53)}$$

Q_{eq}^p can be seen as the average value of Q^p, average value obtained using an integral (as represented in Figure 4 of this paper, but integral to divide by H (and not $2.\theta_a$ as done in Eq. (32) for obtaining the average value of Q^p before raising the result to the exponent $1/p$).

$2.\psi_l$ should therefore appear at the denominator of J_1 in Eq. (10), (11) and (33) while and H should appear at the denominator of $J_{\theta_a,\psi}$ in Eq. (32).

The authors show in Figure 5 the distribution of Q_{eq} for the case corresponding to θ_a = 65 degrees and ψ_l = 45 degrees.

Fig. 15 shows the results obtained when using the new definition of Q_{eq} (defined with H instead of $2.\theta_a$ at the denominator):

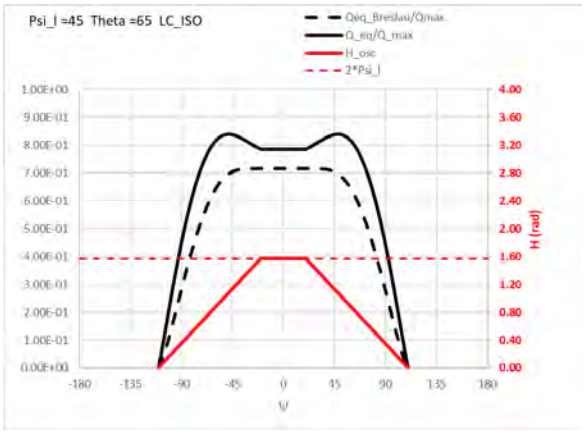

Figure 15: Distribution of Q_{eq} for ψ_l = 45 degrees and θ_a = 65 degrees

Final survival probability

When calculating the probability of survival in Eq. (34) using the product $Q_{eq}^{p.e} * N_{osc}^e$, H appears at the denominator in Q_{eq}^p and numerator in N_{osc}, (while the authors used twice $2*\theta_a$), so that it will cancel out and disappear.

The good news is that the same result (and cancellation) is of course obtained when using twice $2*\theta_a$ (or $2.\pi$ or *1,* the number *1* having no physical sense) instead of H explaining why, by coincidence, the final life results published in this paper are correct.

The inconsistency noticed by the authors in [7] is simply due to the fact that $2.\theta_a$ (instead of H) was unfortunately used in [7] for defining Q_{eq}, while H was correctly used for defining N_{osc}, so that the numerator and denominator could not cancel.

Readers may wonder why spending so much effort calculating H while it will cancel when defining the final survival probability and bearing life. The initial reason is that using H appeared conceptually sound, but a second reason appeared quite useful too: the analytical calculations of the loaded arc H, with its lower and upper bounds, helped obtaining accurate integrals using a reduced number of points, here 101 points (hence 10, 201 points when conducting a double integral as shown in Eq. 54).

Let's here also cite two additional typo errors found in [7]: the factor $2.\pi$ was missing in Equation (32) (not in the calculations) and the factor 60 was missing in the last line before the conclusion chapter (not a few lines before) when defining the equivalent speed to use for calculating a lubrication factor in oscillatory application.

Note that since H disappeared, it is now possible to express in a relatively simple manner the final oscillation factor applicable to the oscillating inner ring (when the oscillating angle exceeds the critical angle):

$$a_{osc\_IR} = \frac{(2.\pi)^{\frac{1}{e}}}{2} \cdot \frac{\int_{-\psi_l}^{\psi_l} \left[1 - \frac{1-\cos\psi}{2.\varepsilon}\right]^{n.p} d\psi}{\left[\int_{-\pi}^{\pi} \left\{\int_{\psi-\theta}^{\psi+\theta} \left[1 - \frac{1-\cos\psi'}{2.\varepsilon}\right]^{n.p} . d\psi'\right\}^{e} . d\psi\right]^{\frac{1}{e}}} \qquad \text{(Eq. 54)}$$

where the function in the squared bracket is nil outside of the loaded range ($-\psi_l$, ψ_l), n is the Hertzian exponent (equal to 10/9 for roller bearing and 1.5 for ball bearing), p is the load life exponent (equal to 10/3 for Timken roller bearing, 4 for ISO roller bearing and 3 for Ball Bearing) and e is the Weibull slope (equal to 1.5 for Timken roller bearing, 9/8 for ISO roller bearing and 10/9 for Ball bearing).

Also note the use of a double integrals at the denominator due to the integration of $Q_{eq}(\psi)$, $Q_{eq}(\psi)$ being itself an integral to define for each ψ as a function of ψ_l and θ_a.

New results obtained:

It is now possible to correct Figure 5 and 6 published in [7] and to replace them by Figure 16 and 17:

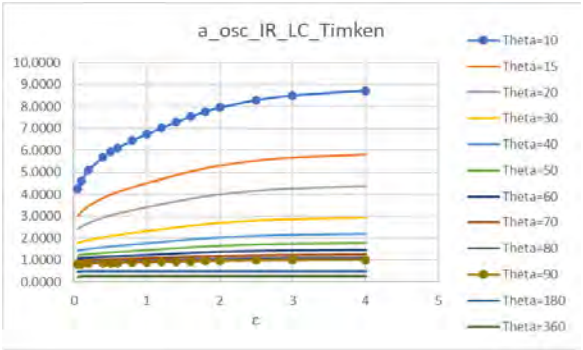

Figure 16: New Figure replacing Figure 5 published in [7]

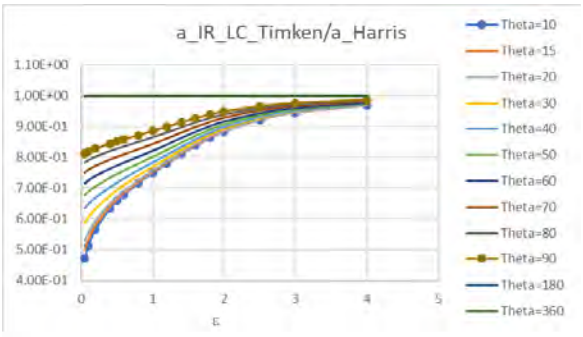

Figure 17: New Figure replacing Figure 6 published in [7]

Figure 18 is also added next for completeness and can be compared to the authors' Figure 7, confirming similar results:

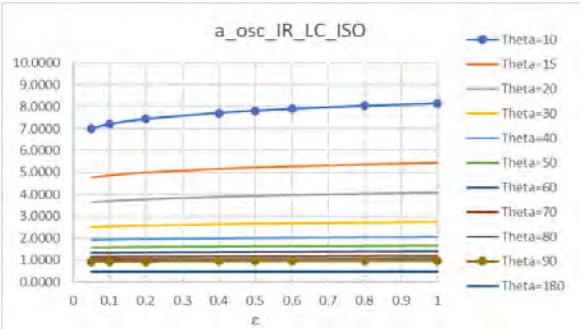

Figure 18: Inner race oscillation factor to compare to Fig. 7

Also Table 5 can be compared to Table 1 for comparing the oscillation factor a_{osc_IR} to $a_{osc,1}$ (calculated with ε = 0.2887 or ψ_l = 65 degrees), confirming identical results.

Table 5: Results obtained to compare to Table 1.

θ_a (deg)	ψ_l
	a_{osc}
10	7.5824
20	3.8425
30	2.6054
40	1.9880
50	1.6160
60	1.3662
70	1.1863
80	1.0503
90	0.9436
180	0.5000

A few additional results obtained

The joint paper to write with Mr. Menck will show all details (that cannot be described here) about the new models and results obtained.

Among the additional results, let's cite: the development of an oscillation factor accounting for both inner oscillating ring and outer stationary ring and the development of appropriate oscillation factor curve-fitted relationships (different for Roller and Ball Bearing) accounting for the oscillation angle θ, load zone parameter ε, geometrical parameter γ and osculation factors f_i and f_o (of the inner and outer race respectively when studying ball bearing). Also, the critical angles will be considered in both analytical and curve-fitted relationships.

Beside Table 4 and Equation (54) already given, this discussion gives me however the opportunity of showing some of them, thanks to the permission given by Dr. Stammler.

Some additional comparisons between our new results to the authors' ones can therefore also be offered in this discussion chapter.

Account for the stationary outer ring:

The account for the stationary outer race is done by describing analytically all outer race parameters (pressure, contact width, number of stress cycles, volume and finally survival probability) as a function of the inner race ones, leading to a parameter call B representing the ratio $ln(S_o)/ln(S_i)$.

More details can be found in a chapter I was invited to write for Ref. [20].

Using the subscript i for the inner race and o for the outer race, the final survival probability then reads:

$$\ln(S) = \ln(S_i).(1 + B_{LC}) \quad \text{with}$$
$$B_{LC} = \left(\frac{1+\gamma}{1-\gamma}\right)^{-\frac{c+h-3+2.e}{2}} . \left(\frac{L_o}{L_i}\right)^{\frac{1-c+h}{2}} . \left(\frac{1}{2}\right)^{1-e} . \frac{K_{bo}}{K_{bi}^e} \qquad \textit{(Eq. 55)}$$
$$B_{LC} = \left(\frac{1+\gamma}{1-\gamma}\right)^{-\frac{c+h-3+2.e}{2}} . \left(\frac{1}{2}\right)^{1-e} . \frac{K_{bo}}{K_{bi}^e} \quad \text{if} \quad L_o = L_i(\text{in } ISO)$$

where the exponent h is equal to 7/3 and c is equal to 34/3 for Timken roller bearing and 31/3 for ISO Roller bearing while K_{bi} and K_{bo} are integrals (function of ε only) used for defining the equivalent load of the rotating inner race and stationary outer race respectively. L is the effective roller – race length.

A similar relationship can be given for Ball Bearing using γ and the race osculation ratio for defining B_{PC}.

B is also be used for expressing the life of the stationary outer race as a function of the rotating inner race one.

In an oscillatory application, the oscillating inner ring life is obtained by correcting its continuous rotating life by the previously described inner ring oscillation factor, while the stationary outer ring life is obtained using its continuous rotating life corrected by the Harris factor ($a_{Harris} = 90/\theta_{\text{degree}}$).

It can then be shown that the final oscillation factor combining both rings reads:

$$a_{osc\_IR+OR} = a_{osc} = a_{osc\_IR} . \left(\frac{1+B}{1+\left(\frac{a_{osc\_IR}}{a_{Harris}}\right)^e . B} \right)^{\frac{1}{e}} \qquad \textit{(Eq. 56)}$$

This relationship has already been used in [4] for producing Figure 11.28 and 11.29 with unfortunately an incorrect value of a_{osc_IR} in some cases.

Figure 11.29 should for example be replaced by Figure 19 (corresponding to $L_o = L_i$ and $\gamma = 0.1$).

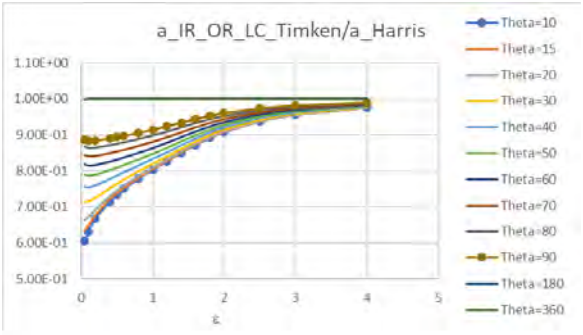

Figure 19: Final oscillation factor corresponding to Timken Roller bearing (with $\gamma = 0.1$)

When using ISO Line Contact exponents, one obtains Figure 20 and 21 (again with $\gamma = 0.1$):

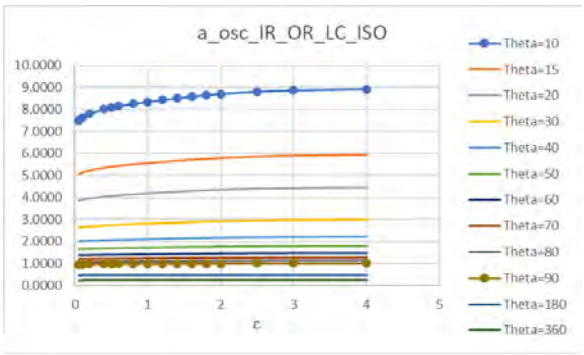

Figure 20: Final oscillation factor obtained using ISO Line Contact exponents (and $\gamma = 0.1$)

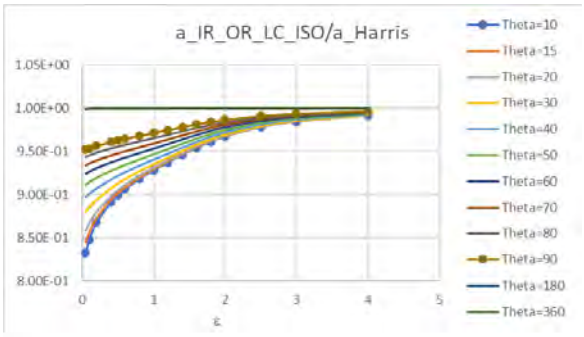

Figure 21: Final oscillation factor obtained using ISO Line Contact exponents (and $\gamma = 0.1$)

It is also possible to easily account for the critical angle by simply correcting the previously calculated oscillation factor a_{osc_IR} and a_{osc_OR} (called a_{Harris} previously) by a coefficient called f_θ:

$$a_{osc\_IR\_or\_OR} \rightarrow f_{\theta\_i,o} . a_{osc\_IR\_or\_OR}$$
$$\text{when } \theta_a \geq \theta_{crit_i,o}: f_{\theta_i,o} = 1$$
$$\text{when } \theta_a < \theta_{crit\_i,o}: f_{\theta\_i,o} = \left(\frac{\theta}{\theta_{crit\_i,o}}\right)^{1-\frac{1}{e}} \qquad \textit{(Eq. 57)}$$

It is now also interesting to compare in Figure 22 the results obtained using Eq. (56) without or with Eq. (57) to the ones shown in Figure 12, thanks to Mr. Breslau

for sharing his results. It can be observed that identical results are obtained.

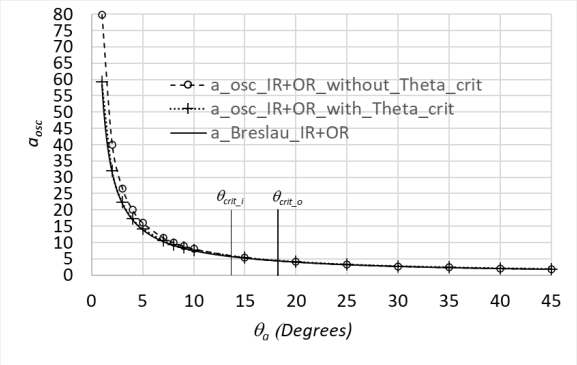

Figure 22: Results obtained using ISO LC exponent, $\varepsilon = 0.5$ and $\gamma = 0.1429$, compared to Fig. 12

Curve-fitted relationships

Finally, useful sets of curve-fitted relationships will be suggested in our joint paper for roller (LC_Timken and LC_ISO) and ball bearing.

As a preliminary information, it can be said that two sets of curve-fitted relationship will be suggested in Table 6.

In the latter relationship, a single mean critical angle (*360/Z* in degree) is also used for defining f_θ.

Note the small effect of θ on the final ratio when θ is small ($0.015374*\theta_{\text{degree}}$ being small in front of 1.6458).

Additional references:

[20] Houpert, L., 2013, "Rolling Bearing Dynamic Rating: Bearing Dynamic Capacity". In: Wang Q.J., Chung YW. (eds) Encyclopedia of Tribology. Springer, Boston, MA. https://doi.org/10.1007/978-0-387-92897-5_101139

Table 6: curve-fitted relationship

A very accurate one using curve-fitted relationship for a_{osc_IR} and K_{bo}/K_{bi}^{e} (used in B), allowing to account for the effect of γ, f_i and f_o on the final oscillation factor, for example:

$$a_{osc\_IR\_LC\_ISO\_cf} \approx f_{\theta\_i}.\frac{90}{\theta_{\text{degree}}}.\left\{1 - exp\left(-(0.014686 * \theta_{\text{degree}} + 1.3771) * \left(\frac{\varepsilon}{0.05}\right)^{0.036493*\varepsilon + 0.13258}\right)\right\} \quad \textit{(Eq. 58)}$$

$$B_{LC\_ISO} \approx \left(\frac{1-\gamma}{1+\gamma}\right)^{5.9583} \cdot (1 + 0.12973 * \varepsilon^{-0.36716}) \quad \textit{(Eq. 59)}$$

$$a_{osc\_LC\_ISO} \approx a_{osc\_IR\_LC\_ISO\_cf} \cdot \left(\frac{1 + B_{LC\_ISO}}{1 + \left(\frac{a_{osc\_IR\_LC\_ISO\_cf}}{f_{\theta\_o}.a_{Harris}}\right)^{\frac{9}{8}}.B_{LC\_ISO}}\right)^{\frac{8}{9}} \quad \textit{(Eq. 60)}$$

A simplified one in which γ has been fixed to 0.1 (and $f_i = f_o$ for Ball Bearing), for example:

For $\gamma = 0.1$:

$$\frac{a_{osc\_IR\_LC\_ISO\_cf}}{f_\theta.a_{Harris}} \approx 1 - exp\left(-\left(0.015374 * \theta_{\text{degree}} + 1.6458\right) * \left(\frac{\varepsilon}{0.05}\right)^{0.034617*\varepsilon + 0.11229}\right) \quad \textit{(Eq. 61)}$$

with $a_{Harris} = \frac{90}{\theta_{\text{degree}}}$

Authors Closure

The authors present in the current paper on the one hand a corrected calculation approach according to [7] and on the other hand also an improved, more comprehensible derivation of the equations. This refers primarily to the omission of the function $H(\theta_a, \psi)$ to describe the covered angle within the load zone. The calculation approaches presented in this paper are based on the derivation of the dynamic load rating with the load integrals J_1 and J_2 according to LUNDBERG and PALMGREN in [8] and [9]. The authors object to the accusation of two conceptual errors and provide a justification and explanation in the following.

The calculation model presented in the current paper is partly based on an article from Nov. 2019, which was also published by the authors, [13]. This conference article discusses the inconsistencies in [7] for the first time and presents a corrected calculation approach.

The derivation of the equations is based on [7] also using the function $H(\theta_a, \psi)$. Further investigations have shown, as in Dr. Houpert's discussion chapter, that $H(\theta_a, \psi)$ is canceled out in the final equation for calculating the coefficient and is therefore not needed. The objective of the authors was, inter alia, the more comprehensive derivation without the auxiliary function $H(\theta_a, \psi)$. For this purpose, the calculation in the current paper is based on the load capacity equation by a load integral analogous to J_1 and J_2.

Statement on accused conceptual errors

In the current paper the load cycles of the circumferentially loaded bearing ring are described, as for the stationary loaded ring, according to Eq. 28. This means that all load cycles are counted even outside the load zone and regardless of whether a load $Q(\psi)$ is zero. Consequently, for all elementary small race volumes

$\mathrm{d}V(\psi)$ the number of load cycles is constant and proportional to $2\theta_\mathrm{a}$. In [7], however, only the load cycles within the load zone are counted and the equivalent load is also only determined for the covered angle within the load zone, described by $H(\theta_\mathrm{a}, \psi)$. The difference is that in this current paper all load cycles during a full oscillation ($-\theta_\mathrm{a} \leq \theta \leq \theta_\mathrm{a}$) are counted and the integral is also determined over the whole range of $2\theta_\mathrm{a}$. According to the MINER rule, it is valid to consider the load cycles with a load of 0 N. By taking the zero loads into account, the equivalent load is lower than the load calculated by Dr. Houpert, but it considers all load cycles (including zero loads). Finally, both approaches lead to the same fatigue and consequently to the same probability of survival of an elementary small volume $\mathrm{d}V(\psi)$. For this reason, identical rating life coefficients a_osc result for both approaches The conformity of the results in this paper with the results of Dr. Houpert is therefore traceable and no coincidence.

Note regarding the Eq. 53 of discussion chapter by Dr. Houpert: The approach in this current paper is based on the load integral J_1 according to LUNDBERG and PALMGREN. The integral J_1 describes the dynamic equivalent load relative to the maximum load Q_max for a circumferentially loaded ring. Regardless of the load zone, the integral is related to the entire circumference (denominator: 2π) and not only to $2\psi_\mathrm{l}$, see Figure 23.

$$Q_{ei} = \sqrt[3]{\frac{1}{2\pi}\int Q^3(\psi)\,d\psi} = Q_\mathrm{max}\,J_1 \quad \ldots\ldots\ldots\ldots\ldots\ldots \quad (88)$$

Figure 23: Dynamic equivalent load equation according to LUNDBERG and PALMGREN, p.26 in [8]

Therefore, the load rating equation of LUNDBERG and PALMGREN considers all load cycles, even outside the load zone. If only the load cycles within the load zone are counted, then J_1 would be related to the load zone angle by the denominator $2\psi_\mathrm{l}$.

Further results for comparison

For comparison with the results of Dr. Houpert, the following table summarizes the coefficients $a_{\mathrm{osc},1}$ for different load zone angles ψ_l and oscillation amplitudes θ_a. The same results can be found in Table 3 of [13] depending on the load zone parameter ε.

Table 7: Results for $a_{\mathrm{osc},1}$ ($p = 4$ and $e = 9/8$)

θ_a [°]	ψ_l [°]													
	25	30	35	40	45	50	55	60	65	70	75	80	85	90
10	6.9936	7.0855	7.1723	7.2534	7.3290	7.3994	7.4648	7.5257	7.5824	7.6354	7.6848	7.7311	7.7743	7.8146
20	3.6474	3.6726	3.6980	3.7233	3.7484	3.7731	3.7970	3.8202	3.8425	3.8638	3.8842	3.9036	3.9220	3.9394
30	2.5146	2.5260	2.5374	2.5489	2.5603	2.5718	2.5831	2.5944	2.6054	2.6163	2.6268	2.6371	2.6470	2.6565
40	1.9361	1.9427	1.9492	1.9557	1.9623	1.9687	1.9752	1.9816	1.9880	1.9942	2.0004	2.0064	2.0123	2.0181
50	1.5824	1.5866	1.5909	1.5951	1.5994	1.6036	1.6077	1.6119	1.6160	1.6200	1.6240	1.6279	1.6317	1.6355
60	1.3426	1.3456	1.3486	1.3516	1.3546	1.3575	1.3604	1.3633	1.3662	1.3690	1.3718	1.3745	1.3772	1.3798
70	1.1688	1.1710	1.1733	1.1755	1.1777	1.1799	1.1821	1.1842	1.1863	1.1884	1.1905	1.1925	1.1945	1.1964
80	1.0367	1.0385	1.0402	1.0419	1.0436	1.0453	1.0470	1.0487	1.0503	1.0519	1.0535	1.0551	1.0566	1.0581
90	0.9328	0.9342	0.9356	0.9369	0.9383	0.9397	0.9410	0.9423	0.9436	0.9449	0.9462	0.9474	0.9486	0.9498
180	0.5000	0.5000	0.5000	0.5000	0.5000	0.5000	0.5000	0.5000	0.5000	0.5000	0.5000	0.5000	0.5000	0.5000

Oscillation factor combining both rings:

The combination of the coefficients for both bearing rings (inner and outer ring or stationary and circumferentially loaded ring) is done by equation Eq. 22. Only the load ratings of the respective bearing rings (C_1 and C_2) and the load rating (C) of the entire bearing are required. These load ratings can be calculated according to LUNDBERG and PALMGREN by [8]. The comparison carried out by Dr. Houpert in Figure 22 shows a very good conformity for amplitudes of $\theta_\mathrm{a} \geq \theta_\mathrm{crit}$. According to [20], the combination of the coefficients by Dr. Houpert leads to the same results as the approach presented in this current paper by Eq. 22.

Curve-fitted relationships:

The calculation model presented in this paper is based on two approaches: RUMBARGER [11] and HOUPERT [7]. The computation model is to be regarded however as one single model with case distinction. Indeed, it is important that the kind of results of a method or model is easily accessible to application engineers.

The authors have refrained from curve fitting, since in most cases the use of look-up tables or reading in diagrams is regarded as sufficient. Figure 7 shows, that due to the low nonlinearities a linear interpolation of the characteristic curves would be applicable. However, a curve-fitting relationship seems to be very useful for low oscillation amplitudes ($\theta_\mathrm{a} < 10°$), due to the high non-linearity in this range. As can be seen in Figure 12, the continuous characteristic curve is well suited for curve fitting. Therefore, it is pleasing that Dr. Houpert has already found an approach to calculate the coefficients with an analytic approximation equation. Nevertheless, the reader is encouraged to use the calculation approach presented in this paper. Especially since the numerical solution can easily be achieved with software like MATLAB.

The Influence of Mechanical Stresses on the Diffusion and Accumulation of Hydrogen in a Cylindrical Roller Thrust Bearing

Iyas Khader[1,2], Dominik Kürten[2], Andreas Kailer[2]

[1] *Department of Industrial Engineering, German Jordanian University, P.O. Box 35247, 11180 Amman, Jordan,* iyas.khader@gju.edu.jo

[2] *Fraunhofer Institute for Mechanics of Materials IWM, Wöhlerstraße 11, 79108 Freiburg, Germany,* dominik.kuerten@iwm.fraunhofer.de, andreas.kailer@iwm.fraunhofer.de

Abstract– Steel rolling elements in bearings are known to undergo premature failure due to brittle flaking or what is also known as white structure flaking. This failure mode is associated with the formation of white etching cracks (WEC) and white etching areas (WEA). Literature findings point out to the mechanism resulting in early brittle flaking as a form of hydrogen-assisted fatigue; hence, the term hydrogen assisted rolling contact fatigue (HARCF) was coined. Understanding the factors affecting the diffusion and subsurface accumulation of hydrogen in bearing steel is crucial to developing measures to mitigate or completely eliminate its detrimental effect.

In this work, a finite element simulation model of a cylindrical roller thrust bearing (CRTB) was created. The simulations enabled studying the diffusion of hydrogen and obtaining qualitative information pertaining to stress-assisted diffusion in tribological loading under the influence of residual stresses. The simulations revealed rather insignificant hydrogen accumulation due to stress-assisted diffusion in comparison to concentration gradient driven diffusion. On the other hand, residual stresses had an evident influence on the subsurface accumulation of hydrogen. The overlap between regions undergoing high stresses and those showing high concentrations of accumulated hydrogen points out to the triggering mechanism of HARCF.

Keywords – Hydrogen diffusion, residual stresses, roller bearings, hydrogen-assisted rolling contact fatigue, WEA/WEC.

1. Introduction

Premature damage in bearings in the form of brittle flaking is still an open area of research and the causes for its occurrence are discussed quite diversely. There is a plethora of examples in the literature discussing the mechanisms of brittle flaking and despite some contradictions (cf. Harada et al. [1]) there is general consensus that it is a form of hydrogen-assisted fatigue [2, 3, 4, 5, 6]; hence, the term hydrogen assisted rolling contact fatigue (HARCF) was adopted. It was shown in several studies that hydrogen forms in rolling contact due to tribochemical reactions between the lubricant and the steel surface [7, 8, 9, 10, 11, 12] or from additives or contaminants [10, 13, 14, 15] present in the lubricant. The release of hydrogen and formation of hydrocarbon byproducts due to lubricant degradation was confirmed through in-situ measurements using vacuum tribometers [12, 16, 17, 18] and electrochemical cells [19, 20].

HARCF is manifested by inter-crystalline crack growth in the subsurface region of the bearing [17] and brittle flaking (also known as white flaking or white structure flaking), which causes spalling. In many occurrences, HARCF is associated with the presence of white etching cracks (WEC) and microstructural alterations known as white etching areas (WEA), which have been explained in light of crack-face rubbing during over-rolling [21, 22]. Although HARCF has not been confirmed as the only root cause of premature WEC-associated failure, it was observed that the formation of WEC was strongly exacerbated in hydrogen-charged samples once reaching specific concentrations as concluded by the work of several researchers [4, 23, 24, 25, 26]. For instance, Hamada and Matsubara [26] reported premature flaking, the occurrence of distinct microstructural changes and WEC formation in hydrogen pre-charged samples tested in rolling-sliding contact; under identical testing conditions the same effects could not be reproduced at lower hydrogen concentrations. Recently, Liang et al. [27] showed by means of rolling contact fatigue tests on bearing steel that hydrogen facilitates the formation of voids and what the authors described as "typical hydrogen-assisted cracks"; hydrogen pre-charged samples showed higher void and crack length density and longer cracks in comparison to uncharged samples. Ruellan et al. [27] attempted to give an overview of the root causes of early damage associated with WEC formation. In a more recent work, this type of damage was correlated with the lubricant formulation [29] rather than specific additives. Besides HARCF, WEC failures were attributed to adiabatic shearing, corrosion fatigue cracking and inclusions (cf. Stadler et al. [29]). WEC-associated failure is known to occur significantly earlier than predicted by standard bearing lifetime calculations [29]. Statistical data on parts revealing WEC failure showed a steeper failure probability slope than that obtained for bearings undergoing classical rolling contact fatigue (RCF) (typical telltale signs of RCF are discussed in [30]), thus, indicating significantly smaller scatter in lifetime data.

Hydrogen uptake in metals normally takes the form of atomic or ionic hydrogen. A review of hydrogen ingress mechanisms in bearing steel is found in [31]. Within this context, we assume that the most predominant mechanism is due to lubricant degradation and decomposition. Diffusible hydrogen, which may as well be trapped at microstructural defects such as

lattice defects and grain and phase boundaries, is known to induce material degradation in steel in what is known as hydrogen embrittlement [44]. The most prominent theories attempting to explain hydrogen-induced degradation are hydrogen enhanced decohesion (HEDE) and hydrogen-enhanced localized plasticity (HELP) .

Modeling hydrogen diffusion in tribological contact is a challenging task, which may shed light on the causes of premature failure. It was shown in early studies that hydrogen accumulates at regions undergoing tensile stresses such as crack tips [28, 29, 30]. Winzer and Khader [31] modeled hydrogen diffusion and trapping in a twin-disk tribological contact using a weakly-coupled finite element (FE) model. It was shown that stress-assisted diffusion plays a minor role in the accumulation of hydrogen. Kadin [32] simulated the effect of compressive residual stresses on hydrogen diffusion and described their effect in enhancing surface to subsurface transport of hydrogen. In a recent study, Khader et al. [33] showed the effect of residual stresses on the diffusion and subsurface accumulation of hydrogen. It was concluded that certain residual stress profiles may lead to intensified subsurface hydrogen accumulation.

Several researchers have measured residual stress profiles in bearing components [34, 35, 36, 37, 38, 39, 40]. Of particular interest were the X-ray diffraction (XRD) measurements conducted by Voskamp et al. [34], Voskamp and Mittemeijer [38] and Dommarco et al. [35]. Voskamp et al. [34], Voskamp and Mittemeijer [38] reported results on 6309-type deep groove ball bearing inner rings. The tested material was SAE 52100 bearing steel predominantly tempered martensitic with 10-15 vol.% retained austenite and about 3-5 vol.% globular cementite with hardness of 850 HV30. Dommarco et al. [35] conducted the measurements on 9.53 mm diameter rods. The tested material was SAE 52100 bearing steel, martensitic hardened and tempered at various temperatures with hardness values ranging between 58.5 HRC and 62.5 HRC. The published data represented residual stress profiles as function of depth. Prior to testing, the profile in unused through-hardened bearing steel was generally comprised of a compressive stress field on the surface and a tensile stress field in the subsurface (blue curve in *Figure 1*). The residual stresses in [40, 44] were additionally measured following rolling contact fatigue tests carried out at maximum Hertzian contact stresses of 3.3-3.8 GPa. Over-rolling resulted in changing the initial residual stress profile to a one comprised of two compressive stress fields surrounding a tensile stress field in the near-surface region (maroon curve in *Figure 1*).

The aim of this work is to provide an analysis of diffusible hydrogen accumulation in a cylindrical roller thrust bearing (CRTB) in the absence of trapping. This analysis sheds light on a mechanism directly related to hydrogen assisted rolling contact fatigue (HARCF). Hydrogen transport was modeled through two distinct

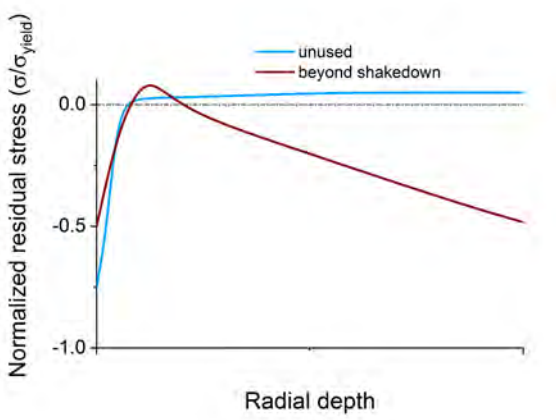

Figure 1: Residual stress profile on the surface and in the subsurface of through hardened bearing steel [34, 38, 35].

mechanisms: (i) concentration gradient driven diffusion and (ii) stress-assisted diffusion. The focus here will be on the influence of various residual stress profiles on the accumulation of subsurface hydrogen.

2. Finite element modeling

A finite element (FE) simulation model was created in Abaqus® to study the diffusion of hydrogen under the influence of various residual stress fields. The developed simulation model is a weakly-coupled, i.e., sequential mechanical-diffusion, two-dimensional extension of the fully-coupled three-dimensional model developed in a previous work [33]. In this work, a structural mechanics simulation was carried out to obtain residual stress profiles, the results of which were then imported into a diffusion simulation. This procedure enables obtaining concentration profiles as function of internal stresses. Notwithstanding the geometrical limitations imposed by modeling the system in two dimensions, this simplification allows for a better understanding of the influence of contact loading on residual stresses and how the latter affects hydrogen diffusion in bearings. Thanks to the manageable model size, two dimensional modeling allows conducting parametric studies. The verification of the Abaqus mass transfer internal code may be consulted in [45].

2.1. Mesh and boundary conditions

A two dimensional section of a cylindrical roller thrust bearing (CRTB) with the dimensions of the commercial bearing FAG 81104-TV was modelled in Abaqus® as shown in *Figure 2*. The average element dimensions in the contact zone were 30 µm×10 µm. The geometry comprised of a section of a roller (diameter Ø = 4.5 mm and length L = 4.5 mm) and the upper and lower raceways. To discretize the geometry, second-order eight-node plane-stress quadrilateral elements (CPS8) were used. A fine mesh was created in the vicinity of the contact zone while discretizing the rest of the geometry with a coarser mesh thus, keeping the size of the model rather manageable.

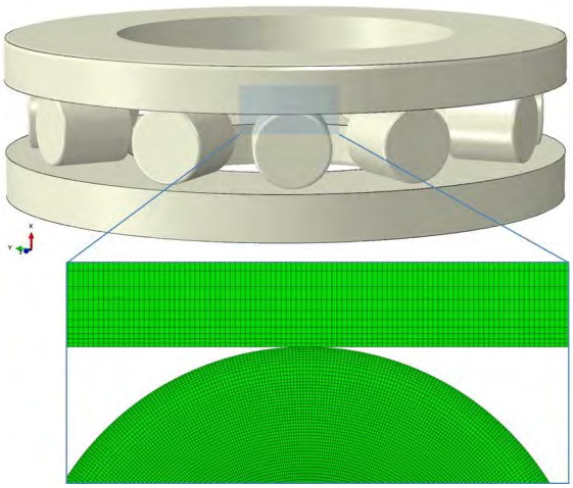

Figure 2: Two-dimensional section of the bearing FAG 81104-TV showing the FE-mesh.

A normal load of 180 N/mm was applied to the upper ring; thus, assuming a line contact, results in a maximum Hertzian contact pressure of 1.7 GPa. Both the upper and lower rings were fixed and the roller was rotated about its axis at an angular velocity of 62.8 rad/s. Coulomb friction was adopted to model friction between the roller and the raceways; the coefficient of friction was assumed constant with a value of $\mu = 0.05$. This value was obtained from a series of measurements carried out on a thrust-bearing tribometer using the same type of bearings and lubricated with a commercial fully-additivated transmission oil with kinematic viscosities of $KV_{40\,°C} = 64.0$ mm^2/s and $KV_{100\,°C} = 9.5$ mm^2/s [33]. It should be pointed out that the friction coefficient measured in full bearing tests has many sources other than solid-to-solid contact (e.g., lubricant viscosity) and hence, does not follow the definition of the friction coefficient according to Coulomb.

For the simulation of diffusion second-order eight-node mass diffusion elements (DC2D8) were used. The stresses were imported from the structural mechanics simulation as initial conditions. Since no knowledge pertaining to either hydrogen flux or hydrogen surface concentration is available, diffusion was assumed to occur uniformly across the roller surface by defining a flux of $J = 10^{-7}$ ppm·mm^2/s. The value was chosen based on a sensitivity analysis carried out to ensure no hydrogen is accumulated in the center of the roller, since hydrogen diffusion from steel into the atmosphere remains unknown. The diffusion period was set to 18×10^3 s. By setting this constraint, diffusion was achieved without having to fix the concentration of surface nodes.

2.2. Residual stresses

The residual stress profiles in the roller were implemented in a preliminary simulation step by applying predefined temperature fields at specific nodes. These boundary conditions were released towards the end of the step to obtain a uniform temperature distribution of 25° C throughout the material and a residual-stress profile in an equilibrium state.

Three residual stress distribution profiles were tested in the simulations as shown in *Figure 3* and detailed as follows:

I. Residual stress free material, exemplified by the black long-dashed curve in *Figure 3*

II. Through-hardened bearing material in its virgin state. Surface machining and heat treatment, resulting in temperature gradients, induce compressive residual stresses on the surface and tensile residual stresses in the subsurface; this profile is denoted by compression-tension (CT) and represented by the blue solid curve in *Figure 3*

III. Bearing steel beyond the shakedown phase with accumulated subsurface plastic strain due to over-rolling. The material lies under two compressive stress fields (on the surface and further down in the subsurface region) surrounding a weaker tensile stress field in the near-surface region. This profile is denoted by compression-tension-compression (CTC) and represented by the green dotted curve in *Figure 3*

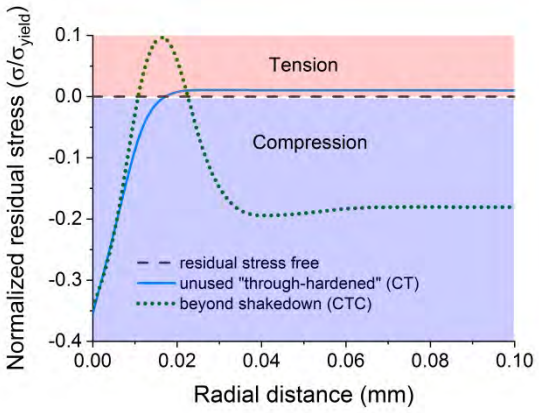

Figure 3: Residual stress distribution profiles implemented in the FE model.

2.3. Diffusion equations

The governing equations for mass diffusion are an extension of Fick's second law. The model accounts for two diffusion mechanisms, namely, (i) diffusion due to the presence of concentration gradients of the diffusing species in the base material and (ii) diffusion driven by stress gradients. The diffusion equation obeys the principles of mass conservation given in the form

$$\frac{\partial}{\partial t}\int_V \bar{C}\,dV + \int_{\partial V} \boldsymbol{n}\cdot\boldsymbol{J}\,dS = 0 \qquad \text{(Eq. 1)}$$

where t is the diffusion time, V is any volume whose surface is S, $\mathbf{n}$ is the outward normal to S, $\bar{C}$ is the total molar concentration of hydrogen and $\boldsymbol{J}$ is the flux.

Assuming a constant temperature, the constitutive expression of the flux is given by [28]

$$\boldsymbol{J} = \frac{D_L \bar{V}_H \bar{C}}{RT}\nabla\sigma_h - D_L\nabla\bar{C} \qquad \text{(Eq. 2)}$$

where D_L is the lattice diffusivity of hydrogen, $\bar{V}_H$ is the partial molar volume of hydrogen dissolved in the host material, σ_h is the hydrostatic stress given by ($\sigma_h = -trace(\boldsymbol{\sigma})/3$), R is the ideal gas constant, T is the absolute temperature in kelvin and $\nabla\sigma_h$ and $\nabla\bar{C}$ are the spatial gradients of the hydrostatic pressure and molar concentration, respectively. Within this context, the form presented in *Eq. 2* assumes a negligible concentration of trapped hydrogen in the base material; this assumption was verified for hardened steel 100Cr6 in Kürten et al. [41] by calculating the ratio of trapped to released hydrogen.

2.4. Material constants and simulation parameters

Elastic-plastic material behavior with kinematic strain-hardening was used to model bearing steel (100Cr6). An elastic modulus of E = 200.2 GPa [33] and a Poisson's ratio of ν = 0.3 [42] were used to define the elastic response. Plasticity was incorporated by assuming an initial yield strength of σ_0 = 750 MPa [43] and a linear kinematic strain hardening modulus of H = 185.5 GPa [33], which should give good approximation with measured values up to a plastic strain of ϵ^{pl} = 0.005.

The parameters used in implementing the hydrogen diffusion model are listed in *Table 1*.

Table 1. Material data required for the diffusion model

Property	Unit	Value	Source
Lattice diffusivity (D_L)	mm²/s	1.1×10^{-3}	[44, 45, 46]
Initial hydrogen concentration (C_0)	ppm	1.5	-
Hydrogen flux (J)	ppm·mm²/s	10^{-7}	-
Ideal gas constant (R)	mJ/mol·K	8.314×10^{3}	-
Temperature (T)	K	293.15	-
Partial molar volume (pmv) of dissolved hydrogen in pure iron [unstrained lattice] ($\bar{V}_H$)	mm³/mol	2.0×10^{3}	[47, 48, 49]
Lower and upper values for $\bar{V}_H$	mm³/mol	2.0×10^{3}, 4.0×10^{3}	-

An arbitrary initial hydrogen concentration in steel was set to 1.5 ppm. This value is considered somewhat high as hydrogen concentration in commercial bearing steel may be as low as 0.4 ppm [56] and typically about 1.0 ppm [8, 22]. As shown in *Table 1*, the partial molar volume (pmv) of dissolved hydrogen in steel ($\bar{V}_H$) is given for the unstrained lattice of the host metal. Unlike the diffusion coefficient which is independent of the stress state, the pmv is sensitive to local stress fields [50] and thus, lattice expansion due to elastic stress fields may result in accommodating more hydrogen into the metal [46]. The pmv of hydrogen in iron is about $\bar{V}_H = 2.0\times10^3$ mm³/mol for the unstrained lattice; however, depending on the vacancy concentration in the host material, values as high as $\bar{V}_H = 16.3\times10^3$ mm³/mol [46] were reported in the literature for the elastically distorted lattice. Moreover, depending on the type of alloy under consideration the pmv may attain different values, for instance Guedes et al. [51] reported values much higher than that in pure iron for martensitic steel alloys. Hence, in this work, and for comparison purposes, a lower value of $\bar{V}_H = 2.0\times10^3$ mm³/mol and an upper value of $\bar{V}_H = 4.0\times10^3$ mm³/mol will be adopted in the simulations.

3. Results

3.1. Mechanical solution

To simulate the evolution of residual stresses with over-rolling, a simulation was created with a residual stress profile CT, as reported in the literature, and exemplified by the blue solid curve in *Figure 3*. This stress profile resembles that of an unused through-hardened bearing. By applying a load of 180 N/mm, the initial contact stress was 1.63 GPa and the maximum von Mises stress appeared approx. 40 µm below the surface with a peak value of 925 MPa; *Figure 4*.

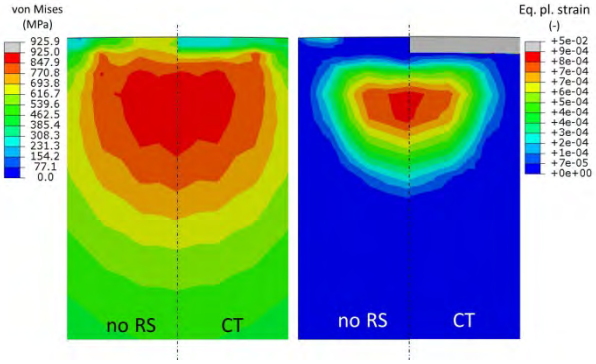

Figure 4: von Mises stress and equivalent plastic strain distributions in the depth of the roller for residual stress free material (no RS) and residual stress profile CT.

To compare this case with a residual stress free material (no RS), the latter was simulated and the results were as follows: The maximum contact stress was 1.73 GPa, which is within 5% of the value obtained from a Hertzian contact solution, and the von Mises stress showed identical values and location to the case with a CT stress profile. Since the developed stresses in the subsurface exceed the initial yield strength of the material (σ_0 = 750 MPa), it is expected that subsurface plastic strain will build up and accumulate.

The initial contact cycle gave rise to fully-contained (i.e., plastically deformed material surrounded by material undergoing only elastic strains) equivalent plastic strain with a maximum value of $\epsilon^{pl} = 9\times10^{-4}$ (refer to *Figure 4*).

During the running-in phase, the bearing material will undergo shakedown, during which subsurface plastic

strain will be accumulated and may even reach the surface in the form of microplasticity. It is hence, expected that residual stresses change from compression on the surface and tension in the subsurface (i.e., compression-tension: CT, exemplified by the blue solid curve in *Figure 3*) to compression on the surface, tension in the immediate subsurface and compression further below in the subsurface (i.e., compression-tension-compression: CTC) as reported in the literature [34, 38, 35] and exemplified by the green dotted curve in *Figure 3*. To examine this proposition, a structural-mechanics simulation with an initial compression-tension (CT) residual stress profile was run for durations of 50 and 100 stress cycles, respectively. The resulting residual stress were plotted against the radial distance in the roller and compared to the initial stress profile as shown in *Figure 5*.

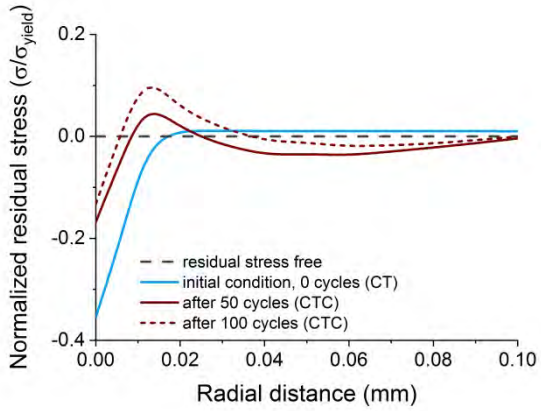

Figure 5: Residual stress profiles obtained from the simulations.

The simulation shows that after 50 stress cycles the residual stress profile changes from CT (blue solid curve in *Figure 5*) to CTC (maroon solid curve in *Figure 5*) and showing reduced compression on the surface. After 100 stress cycles, the compression on the surface slightly decreases and the tensile stress increases resulting in a CTC profile with a steeper gradient (maroon dashed curve in *Figure 5*).

The residual stress profiles obtained from the structural mechanics simulation were then imported as predefined fields into the hydrogen diffusion model. The simulations of hydrogen diffusion into the roller were thus carried out for the four cases of residual stress profiles depicted in *Figure 5*, i.e., (i) residual stress free, (ii) CT as in an unused bearing, (iii) CTC after 50 stress cycles and (iv) CTC after stress 100 cycles.

3.2. Hydrogen diffusion

The results of the diffusion simulations were obtained as nodal concentration values. These were then normalized to the initial hydrogen concentration in the roller (C_0) and plotted against the radial depth in the roller.

3.2.1. The effect of residual stress distribution

In *Figure 6* the hydrogen concentration profiles in the depth of the roller were obtained for the four predefined residual stress profiles shown in *Figure 5*.

In a residual stress free material (black long-dashed curves in *Figure 5* and *Figure 6*), the hydrogen concentration shows a decrease by increasing radial depth. For the case CT (blue solid curves in *Figure 5* and *Figure 6*), which resembles an unused through-hardened bearing, the hydrogen is repelled from the surface into the subsurface and thus, shows slightly higher concentration below the surface.

After 50 stress cycles (maroon solid curves in *Figure 5* and *Figure 6*), the simulation indicates an increased subsurface accumulation of hydrogen, which is exacerbated after 100 cycles (maroon dashed curves in *Figure 5* and *Figure 6*) reaching a value of almost 2.5 times its original concentration in the material at a depth of approx. 12 µm below the surface.

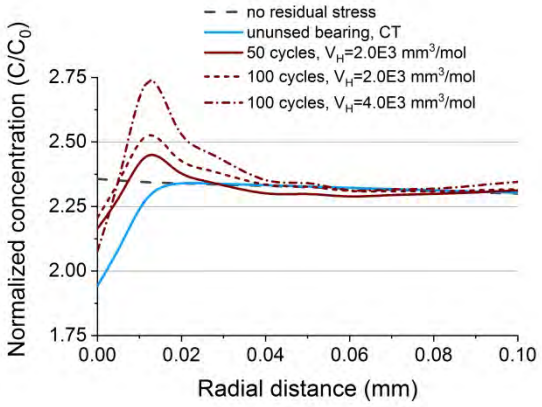

Figure 6: Hydrogen concentration profiles in the depth of the roller.

3.2.2. The effect of the pmv of hydrogen in steel

To study the effect of the pmv of hydrogen in steel, its value was increased to $\bar{V}_H = 4.0\times10^3$ mm^3/mol, which may occur due to elastic stress fields. The hydrogen concentration profile for this case (maroon dot-dash curve in *Figure 6*) showed the value of subsurface accumulated hydrogen to have increased to 2.75 times its original concentration after 100 stress cycles.

3.2.3. The effect of the stress gradient

By going back to *Eq.* 2, it is shown that in fact it is the stress gradient rather than the stress magnitude that provides the driving force for stress-assisted diffusion. To investigate the influence of the stress gradient on the accumulation of hydrogen, the diffusion simulation was carried out with an initial residual stress profile of compression-tension-compression (CTC) as the one depicted in *Figure 3*. As opposed to the CTC-type stress gradients obtained after 50 and 100 stress cycles, this stress profile is characterized by a steep gradient between its compressive and tensile components; such residual stress profile is expected to develop in the bearing well beyond the shakedown phase as reported in the literature.

The results of this simulation is plotted in *Figure* 7 and compared to the results of the simulation results. For this steep stress profile, the subsurface hydrogen accumulation exceeds 3.25 times its original concentration in the material.

For the sake of comparison, the normalized von Mises stress profiles in the unused state (0 cycles, CT) and after 100 stress cycles are plotted against the radial distance in the depth of the roller in *Figure* 7. The von Mises stress profile shows two distinct features regarding its peak between zero and 100 stress cycles: (i) it shifts its position towards the surface of the material and (ii) it increases its value by approx. 20%.

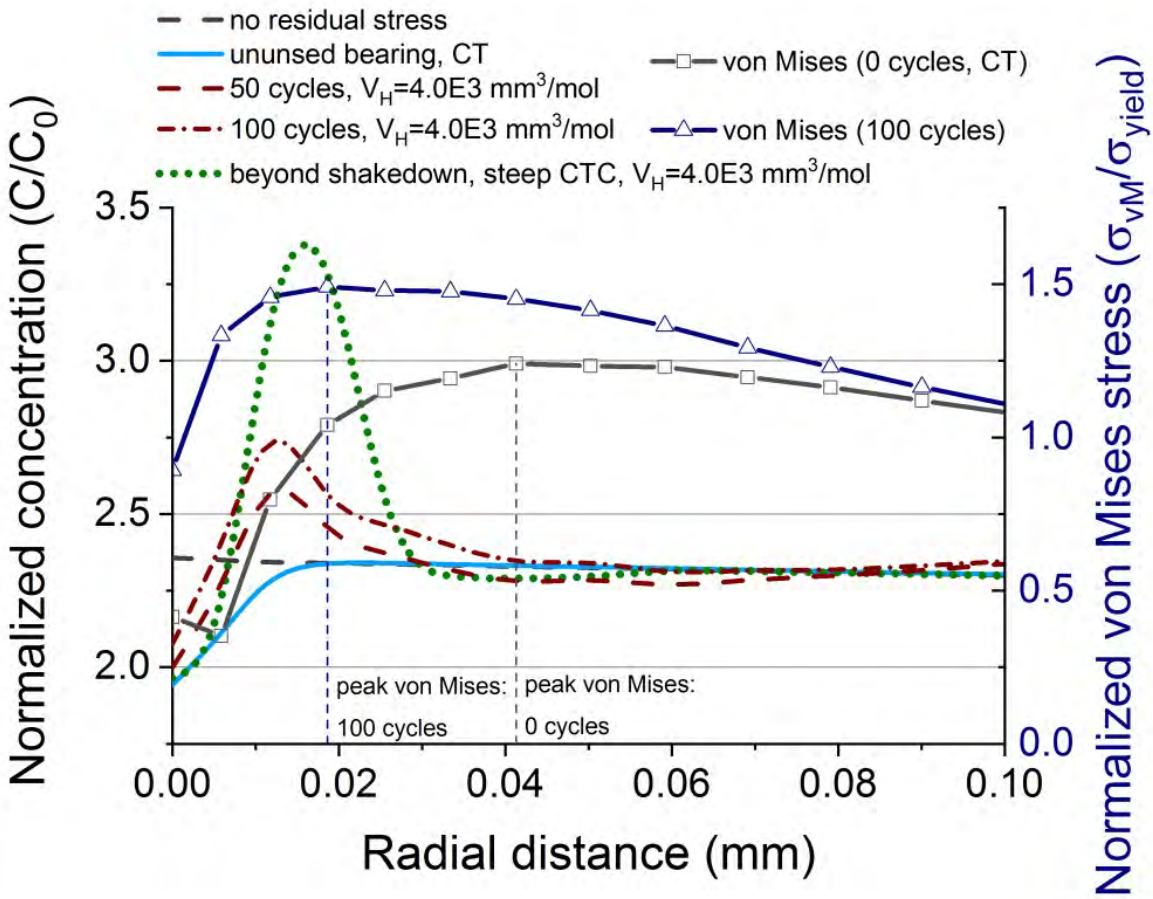

Figure 7: Normalized hydrogen concentration and von Mises stress profiles in the depth of the roller.

4. Discussion

The slight difference in contact stress (below 5%) between the simulation model and the Hertzian contact solution is attributed to: (i) the incorporation of friction and (ii) plasticity in the FE-model, whereas the Hertzian contact model by definition assumes a frictionless elastic contact.

During over-rolling and the associated shakedown of the bearing steel, plastic deformation accumulates below the surface causing the residual stress distribution profile to change from compressive stress on the surface and tensile stress in the subsurface (compression-tension, CT) into two compression stress fields on the surface and in the subsurface surrounding a tensile stress field in the near-surface region (compression-tension-compression, CTC). The results obtained thus far (*Figure 5*) confirm the literature findings [34, 38, 35] that describe such an alteration in residual stresses.

The presence of compressive residual stresses on the surface contributes to the accumulation of subsurface hydrogen. This is in line with the findings of Kadin [32], in which the researcher demonstrated that compressive surface residual stresses enhance surface to subsurface transport of hydrogen. The results of the current study indicate that the presence of residual stresses in the unused bearing may not only drive hydrogen transport but also intensify its subsurface accumulation due to the evolving stress state as a consequence of over-rolling.

The presence of surface compressive residual stresses caused a decrease in hydrogen concertation on the surface compared to the residual-stress-free state (compare "unused bearing, CT" with "no residual stress" in *Figure 6*). After 50 stress cycles, a zone of tensile stress surrounded by an upper and lower zones of compressive stresses is developed due to over-rolling and accumulation of subsurface plastic strain (refer to *Figure 5*). The presence of a tensile stress region surrounded by two compressive stress regions created a preferential path for the subsurface transport of hydrogen causing its repellence from the compressive zones and accumulation in the tensile zone; (compare "50 cycles" with "unused bearing, CT" in *Figure 6*).

Given the uncertainty regarding the partial molar volume of dissolved hydrogen in steel (pmv), lower and upper values for $\bar{V}_H$ of 2.0×10^3 mm^3/mol and 4.0×10^3 mm^3/mol were evaluated. By considering the flux equation (*Eq. 2*) it is apparent that increasing the pmv results in more prominent stress-assisted diffusion leading to more sensitivity to stress gradients. This effect is shown when comparing the results of the 100-cycle simulations carried out with different $\bar{V}_H$ values (*Figure 6*).

Despite the limitation of the current model, especially its crude treatment of boundary conditions pertaining to hydrogen ingress, it clarifies the mechanism of hydrogen accumulation in regions known to undergo fatigue damage due to subsurface stresses. It should be noted that the influence of traps (e.g., dislocations and vacancies) on hydrogen trapping was deliberately not taken into consideration in this model. By disregarding the effect of trapped hydrogen, it was shown here that the accumulation of subsurface hydrogen is essentially independent of trapping. Nevertheless, it should be noted that deformation-induced traps may have an influence on the total hydrogen concentration in the material as demonstrated in previous studies [31, 33] as elevated concentrations of trapped hydrogen are expected to appear within the plastic zone.

In light of these results it may be concluded that a threshold hydrogen concentration for a ductile-to-brittle-transition may be required to trigger crack formation and premature bearing failure. Such a value was reported in the literature to be as low as 1.5 ppm [52] in α-Fe. To put these results in a bigger picture, a critical combination of mechanical stress (in the vicinity of the peak von Mises stresses) and a certain degree of material degradation/embrittlement is required to prompt premature damage. The subsurface distribution of von Mises stresses is thus, shown in *Figure* 7.

In its initial state (0 cycles) the stress profile matches the typical distribution arising in rolling contact with low friction forces. With the progressive accumulation of plastic strain and its consequent strain hardening, the peak von Mises stress shifts its position towards the surface (compare 0 cycles with 100 cycles in *Figure* 7) an thus, approaches the zone of highest hydrogen accumulation in the material; this overlap may contribute to the acceleration of fatigue processes. It was reported by Spriestersbach and Kerscher [53] that microstructural changes in bearing steel, described by the authors as fine granular area (FGA), may be directly correlated with the local plasticity zone predicted by the von Mises criterion, hence, pointing out to the mechanism of formation of FGA. This corroborates the findings of a more recent study [8], which confirmed that telltale features of HARCF such as WEC, from which brittle flaking initiates, appear predominantly in the vicinity of the peak von Mises stresses. It should be however noted that tracing the locations of early signs of damage, such as initiation sites of WEC, is difficult to accomplish experimentally due to the inability to accurately estimate of the minimum number of stress cycles until the first signs of damage appear; the location is also very challenging to predict by numerical simulations due to the sudden changes occurring to the stress state once discontinuities, caused by crack formation, are present in the material.

It was shown in this work that residual stresses induced by machining and hardening processes have a substantial effect on the subsurface accumulation of

hydrogen in bearing steel. Tensile residual stresses such as those present at crack tips or at the tips of inclusions (cf. Al-Tameemi and Long [53]) may also contribute to elevated concentrations of accumulated diffusible hydrogen. In a study conducted by Errichello et al. [55], it was reported that through-hardened bearings fail by cracks that propagate radially and display WEA as sign of microstructural alterations, whereas, carburized steel bearings, that have higher amount of retained austenite and whose residual stress profile is entirely compressive, show higher fracture resistance and tend to fail by macropitting. Nevertheless, reported cases of case-carburized bearings failing due to WEC are present in the literature [64, 65].

The results presented in this study validate those obtained in a previous study [33], in which residual stress profiles were solely based on literature data. The applicability of the developed model to lifetime assessment of real bearings would be greatly improved by considering more realistic boundary conditions pertaining to hydrogen ingress in addition to credible measurements of residual stresses.

5. Conclusions

In this work a weakly-coupled mechanical-diffusion simulation was conducted to study the influence of mechanical stresses on the diffusion and accumulation of hydrogen in a bearing contact. The following is concluded:

- The simulations highlighted that over-rolling and accumulation of subsurface plastic strain, during bearing operation, lead to an alteration of residual stresses. A residual stress profile of compression on the surface and tension in the subsurface will change to compression-tension-compression due to rolling contact.
- Subsurface plastic deformation caused by rolling contact causes the peak von Mises stress to change its value and shift its position towards the surface of the bearing component.
- The presence of residual stresses with a positive gradient (compression to tension) promotes the subsurface transport of hydrogen and its accumulation in the tensile stress region.
- The overlap of high subsurface hydrogen concentration (promoted by residual stresses) and high mechanical stresses (in the vicinity of the peak of von Mises stress) sheds light on the mechanism of hydrogen assisted rolling contact fatigue (HARCF) in bearing steel.

6. References

[1] H. Harada, T. Mikami, M. Shibata, D. Sokai, A. Yamamoto and H. Tsubakino, "Microstructural changes and crack initiation with white etching area formation under rolling/sliding contact in bearing steel," *ISIJ International,* vol. 45, no. 12, pp. 1897-1902, 2005.

[2] K. Tamada and H. Tanaka, "Occurrence of brittle flaking on bearings used for automotive electrical instruments and auxiliary devices," *Wear,* vol. 199, pp. 245-252, 1996.

[3] M.-H. Evans, A. Richardson, L. Wang and R. Wood, "Effect of hydrogen on butterfly and white etching crack (WEC) formation under rolling contact fatigue (RCF)," Wear, vol. 306, no. 1-2, pp. 226-241, 2013.

[4] N. Kino and K. Otani, "The influence of hydrogen on rolling contact fatigue life and its improvement," *JSAE Review,* vol. 24, no. 3, pp. 289-294, 2003.

[5] T. Endo, D. Dong, Y. Imai and Y. Yamamoto, "Study on Rolling Contact Fatigue in Hydrogen Atmosphere - Improvement of Rolling Contact Fatigue Life by Formation of Surface Film," in *Tribology and Interface Engineering Series*, vol. 48, D. Dowson, M. Priest, G. Dalmaz and A. Lubrecht, Eds., Elsevier, 2005, pp. 343-350.

[6] Y. Imai, T. Endo, D. Dong and Y. Yamamoto, "Study on rolling contact fatigue in hydrogen environment at a contact pressure below basic static load capacity," *Tribology Transactions,* vol. 53, pp. 764-770, 2010.

[7] D. Kuerten, N. Winzer, A. Kailer, W. Pfeifer, R. Spallek and M. Scherge, "In-situ detection of hydrogen evolution in a lubricated sliding pin on disk test under high vacuum," *Tribology International,* pp. 324-331, 2016.

[8] D. Kürten, I. Khader, R. Raga, P. Casajús, N. Winzer, R. Spallek, M. Scherge and A. Kailer, "Hydrogen assisted rolling contact fatigue due to lubricant degradation and formation of white etching areas," *Engineering Failure Analysis,* vol. 99, pp. 330-342, 2019.

[9] M. Ratoi, H. Tanaka, B. Mellor and J. Sugimura, "Hydrocarbon lubricants can control hydrogen embrittlement," *Scientific Reports,* vol. 10, p. 1361, 2020.

[10] B. Han, J. Binns and I. Nedelcu, "In situ detection of hydrogen uptake from lubricated rubbing contacts," *Tribology Online,* vol. 2, pp. 450-454, 2016.

[11] M. Kohara, T. Kawamura and M. Egami, "Study on mechanism of hydrogen generation from lubricants," *Tribology Transactions,* vol. 49, pp. 53-60, 2006.

[12] R. Lu, I. Minami, H. Nanao and S. Mori, "Investigation of decomposition of

hydrocarbon oil on the nascent surface of steel," *Tribology Letters,* vol. 27, no. 1, pp. 25-30, 2007.

[13] R. Lu, S. Mori, T. Kubo and H. Nanao, "Effect of sulfur-containing additive on the decomposition of multialkylated cyclopentane oil on the nascent steel surface," *Wear,* vol. 267, pp. 1430-1435, 2009.

[14] R. Lu, S. Mori, H. Nanao, K. Kobayashi and I. Minami, "Study on decomposition of multialkylated cyclopentane oil with sulfur-containing additive on the nascent steel surface," *Tribology Online,* vol. 2, pp. 105-109, 2007.

[15] E. Esfahani, S. Soltanahmadi, A. Morina, B. Han, I. Nedelcu, M. C. van Eijk and A. Neville, "The multiple roles of a chemical tribofilm in hydrogen uptake from lubricated rubbing contacts," *Tribology International,* p. 106023, 2019.

[16] P. A. Bertrand, "Low-Energy-Electron-Stimulated Degradation of a Multiply Alkylated Cyclopentane Oil and Implications for Space Bearings," *Tribology Letters,* 2010.

[17] D. Kuerten, Einfluss der tribochemischen Schmierstoffoxidation auf die wasserstoffinduzierte Wälzkontaktermüdung, PhD Thesis, Fraunhofer Verlag, 2015.

[18] D. Kürten, I. Khader and A. Kailer, "Tribochemical degradation of vacuum-stable lubricants: A comparative study between multi-alkylated cyclopentane and perfluoropolyether in a vacuum ball-on-disk and full-bearing tests," Lubrication Science, pp. 1-9, 2020.

[19] E. Esfahani, A. Morina, B. Han, I. Nedelcu, M. C. van Eijk and A. Neville, "Development of a novel in-situ technique for hydrogen uptake evaluation from a lubricated tribocontact," *Tribology International,* vol. 113, pp. 433-442, 2017.

[20] N. Oberle, T. Amann, D. Kürten, R. Raga and A. Kailer, "In-situ-determination of tribologically induced hydrogen permeation using electrochemical methods," *Proceedings of the Institution of Mechanical Engineers, Part J: Journal of Engineering Tribology,* 2019.

[21] R. Vegter and J. Slycke, "The role of hydrogen on rolling contact fatigue response of rolling element bearings," *ASTM International,* vol. 7, p. 12, 2010.

[22] H. Bhadeshia, "Steels for bearings," *Progress in Materials Science,* vol. 57, no. 2, pp. 268-435, 2012.

[23] H. Uyama, H. Yamada, H. Hidaka and N. Mitamura, "The effects of hydrogen on microstructural change and surface originated flaking in rolling contact fatigue," *Tribology Online,* vol. 6, no. 2, pp. 123-132, 2011.

[24] M. Oezel, A. Schwedt, T. Janitzky, R. Kelley, C. Bouchet-Marquis, L. Pullan, C. Broeckmann and J. Mayer, "Formation of white etching areas in SAE 52100 bearing steel under rolling contact fatigue – Influence of diffusible hydrogen,," *Wear,* vol. 414–415, pp. 352-365, 2018.

[25] M. Curd, T. Burnett, J. Fellowes, J. Donoghue, P. Yan and P. Withers, "The heterogenous distribution of white etching matter (WEM) around subsurface cracks in bearing steels," *Acta Materialia,* vol. 174, pp. 300-309, 2019.

[26] H. Hamada and Y. Matsubara, "The influence of hydrogen on tension-compression and rolling contact fatigue properties of bearing steel," NTN Technical Review, vol. 74, pp. 54-60, 2006.

[27] X. Liang, G.-H. Zhao, J. Owens, P. Gong, W. Rainforth and P. Rivera-Díaz-del-Castillo, "Hydrogen-assisted microcrack formation in bearing steels under rolling contact fatigue," *International Journal of Fatigue,* vol. 134, p. 105485, 2020.

[28] A. Ruellan, F. Ville, X. Kleber, C. Burnet, D. Girodin and J. Cavoret, "Understanding white etching cracks in rolling element bearings: Formation mechanisms and influent tribochemical drivers," *Proceedings of the Institution of Mechanical Engineers, Part J: Journal of Engineering Tribology,* vol. 229, no. 8, pp. 886-901, 2015.

[29] A. Ruellan, K. Stadler, J. Jelita Rydel and H. Ryan, "The influence of lubricant formulation on early thrust and radial bearing damage associated with white etching cracks," Proceedings of the Institution of Mechanical Engineers, Part J: Journal of Engineering Tribology, 2020.

[30] K. Stadler, Lai, J. and R. Vegter, "A review: The dilemma with premature white etching crack (WEC) bearing failures," in Bearing Steel Technologies: 10th Volume, Advances in Steel Technologies for Rolling Bearings, J. Beswick, Ed., West Conshohocken, PA, 2014, pp. 487-508.

[31] A. Olver, "The mechanism of rolling contact fatigue: An update," *Proceedings of the Institution of Mechanical Engineers, Part J: Journal of Engineering Tribology,* vol. 219, no. 5, pp. 313-330, 2005.

[32] M. A. Stopher and P. Rivera-Diaz-del-Castillo, "Hydrogen embrittlement in bearing steels," *Materials Science and Technology,* vol. 32:11, pp. 1184-1193, 2016.

[33] R. Oriani, "Hydrogen embrittlement of steels," *Annual Review of Materials Science,* vol. 8, pp. 327-357, 1978.

[34] P. Sofronis and R. McMeeking, "Numerical analysis of hydrogen transport near a blunting crack tip," *Journal of the Mechanics and Physics of Solids,* vol. 37, no. 3, pp. 317-350, 1989.

[35] A. Varias and A. Massih, "Hydride-induced embrittlement and fracture in metals - effect of stress and temperature distribution," *Journal of the Mechanics and Physics of Solids,* vol. 50, no. 7, p. 2002, 1469-1510.

[36] A. Krom, R. Koers and A. Bakkar, "Hydrogen transport near a blunting crack tip," *Journal of the Mechanics and Physics of Solids,* vol. 47, no. 4, pp. 971-992, 1999.

[37] N. Winzer and I. Khader, "Hydrogen diffusion and trapping in bodies undergoing rolling contact," *Wear,* vol. 303, no. 1-2, pp. 451-458, 2013.

[38] Y. Kadin, "Modeling of hydrogen transport in static and rolling contact," *Tribology Transactions,* vol. 58, no. 2, pp. 260-273, 2015.

[39] I. Khader, D. Kürten, R. Raga, N. Winzer and A. Kailer, "Modeling hydrogen diffusion in a tribological scenario: A failure analysis of a thrust bearing," *Wear,* Vols. 438-439, p. 203054, 2019.

[40] A. Voskamp, R. Österlund, P. Becker and O. Vingsbo, "Gradual changes in residual stress and microstructure during contact fatigue in ball bearings," *Metals Technology,* vol. 1, no. 7, 1980.

[41] R. Dommarco, K. Kozaczek, P. Bastias, G. Hahn and C. Rubin, "Residual stresses and retained austenite evolution in SAE 52100 steel under non-ideal rolling contact loading," *Wear,* vol. 257, no. 11, pp. 1081-1088, 2004.

[42] V. Güley, A. E. Tekkaya, T. Savaş and F. Özhan, "Experimental investigation of residual stresses after heat treatment and grinding processes in the production of ball bearing rings," *Materials Science Forum,* Vols. 571-572, pp. 27-32, 2008.

[43] C. A. Stickels and A. M. Janotik, "Controlling residual stresses in 52100 bearing steel by heat treatment," *Metallurgical Transactions A,* vol. 11, no. 3, pp. 467-473, 1980.

[44] A. Voskamp and E. Mittemeijer, "State of residual stress induced by cyclic rolling contact loading," *Materials Science and Technology,* vol. 13, no. 5, pp. 430-438, 1997.

[45] B. Gould, M. Paladugu, N. Demas, A. Greco and R. Hyde, "Figure the impact of steel microstructure and heat treatment on the formation of white etching cracks," *Tribology International,* vol. 134, pp. 232-239, 2019.

[46] M. Paladugu and R. Hyde, "Material composition and heat treatment related influences in resisting rolling contact fatigue under WEC damage conditions," *International Journal of Fatigue,* vol. 134, p. 105476, 2020.

[47] D. Systèmes, "SIMULIA User Assistance 2018: Abaqus Verification Guide," Dassault Systèmes Simulia Corp., 2017.

[48] D. Kürten, I. Khader and A. Kailer, "Determining the effective hydrogen diffusion coefficient in 100Cr6," Materials and Corrosion, pp. 1-6, 2020.

[49] C. Acht, M. Dalgic, F. Frerichs, M. Hunkel, A. Irretier, T. Lübben and H. Surm, "Ermittlung der Materialdaten zur Simulation des Durchhärtens von Komponenten aus 100Cr6. Teil 1," *HTM Journal of Heat Treatment and Materials,* vol. 63, no. 5, 2008.

[50] F. Yoshida, "A constitutive model of cyclic plasticity," *International Journal of Plasticity,* vol. 16, no. 3-4, pp. 359-380, 2000.

[51] Y. Efimenko, A. Kuslitskii, D. Chaban, G. Karpenko and B. Movchan, "Effect of electron-beam melting upon the properties of grade ShKhl5 ball-bearing steel," *Fiziko-Khimicheskaya Mekhanika Materialov,* vol. 1, no. 4, pp. 333-335, 1965.

[52] J. Bogkris, W. Beck, M. Genshaw, P. Subramanyan and F. Williams, "The effect of stress on the chemical potential of hydrogen in iron and steel," *Acta Metallurgica,* vol. 19, no. 11, pp. 1209-1218, 1971.

[53] S. Frappart, X. Feaugas, J. Creus, F. Thebault, L. Delattre and H. Marchebois, "Hydrogen solubility, diffusivity and trapping in a tempered Fe–C–Cr martensitic steel under various mechanical stress states," *Materials Science and Engineering: A,* vol. 534, pp. 384-393, 2012.

[54] D. Guedes, A. Oudriss, S. Frappart, G. Courlit, S. Cohendoz, P. Girault, J. Creus, J. Bouhattate, A. Metsue, F. Thebault, L. Delattre, D. Koschel and X. Feaugas, "The influence of hydrostatic stress states on the hydrogen solubility in martensitic steels," *Scripta Materialia,* Vols. 84-85, pp. 23-26, 2014.

[55] J. Choi, "Diffusion of hydrogen in iron," *Metallurgical Transactions,* vol. 1, pp. 911-919, 1970.

[56] H. Hagi, Y. Hayashi and N. Ohtani, "Diffusion coefficient of hydrogen in pure iron between 230 and 300K," *Transactions of the Japan Institute of Metals,* vol. 20, no. 7, pp. 349-357, 1979.

[57] J. Hirth, "Effects of hydrogen on the properties of iron and steel," *Metallurgical Transactions A,* vol. 11A, pp. 861-890, 1980.

[58] L.-C. Hwang and T.-P. Perng, "Hydrogen transport in ferritic stainless steel under elastic

stress," *Materials Chemistry and Physics,* vol. 36, pp. 231-235, 1994.

[59] C. Sturges and A. Miodownik, "The interaction of hydrogen and dislocations in iron," *Acta Metallurgica,* vol. 17, no. 9, pp. 1197-1207, 1969.

[60] J. O. Bockris, W. Beck, M. Genshaw, P. Subramanyan and F. Williams, "The effect of stress on the chemical potential of hydrogen in iron and steel," *Acta Metallurgica,* vol. 19, no. 11, pp. 1209-1218, 1971.

[61] D. K. E. Spriestersbach, "The role of local plasticity during very high cycle fatigue crack initiation in high-strength steels," *International Journal of Fatigue,* vol. 111, pp. 93-100, 2018.

[62] H. Al-Tameemi and H. Long, "Finite element simulation of subsurface initiated damage from non-metallic inclusions in wind turbine gearbox bearings," *International Journal of Fatigue,* vol. 131, p. 105347, 2020.

[63] R. Errichello, R. Budny and R. Eckert, "Investigations of bearing failures associated with white etching areas (WEAs) in wind turbine gearboxes," *Tribology Transactions,* vol. 56, no. 6, pp. 1069-1076, 2013.

[64] K. Stadler and A. Stubenrauch, "Premature bearing failures in wind gearboxes and white etching cracks (WEC)," SKF Evolution, 2013.

[65] R. Budny, "Research on white Etch crack failures and failure prevention," in *AWEA Windpower 2015, May 18-21*, Orlando, 2015.

Finite Element Analysis of Two-step Deep Rolling of Bearing Steel for Expansion and Equalization of Compressive Residual Stress Profiles

Joshua Simon[1], Jürgen Gegner[2,3]

[1] *Faculty of Applied Natural Sciences and Humanities, University of Applied Science Würzburg-Schweinfurt, joshsimon96@googlemail.com*

[2] *Department of Material Physics, SKF GmbH, juergen.gegner@skf.com*

[3] *Institute of Materials Science and Materials Testing, University of Siegen, juergen.gegner@uni-siegen.de*

Abstract – Deep rolling for prevention of frictional cracking and fatigue failure enjoys growing popularity in bearing applications. The conventional process suffers from an outer layer low in compressive residual stress. With decreasing tool diameter, the unwanted skin but also the desired influence depth diminish. Simply enhancing the force acting on a small body to move the impact zone farther into the workpiece is no effective remedy, above all because of excessively rising compressive residual stresses. In the present paper, two-step deep rolling with differently sized and loaded tools is introduced as corrective measure against the weak surface layer. For assessing the influence of process parameters, a finite element analysis is performed on ANSYS 19.2 software. A two-dimensional model of the rolling elements pressed onto a raceway is used for residual stress simulation and engineering. Material response of bearing steel is described by isotropic bilinear elastic-plastic behaviour in the von Mises yield criterion. Initial condition is free of (residual) stress. Reference simulations of single overrolling events reproduce experimental findings. Residual stress redistribution is more complex after the second pass. Four parameter studies are conducted to explore two-step deep rolling. The degree of expansion of the impact width of compressive residual stresses depends on the difference in tool diameter. Simulations furthermore indicate benefit from applying the large rolling element first. Effective shape equalization of the compressive residual stress depth profile is basically promoted by similar Hertzian pressure in both process stages.

Keywords – deep rolling, finite element analysis, residual stress engineering, process development, bearing steel

1. Introduction

Cold working mechanical surface treatments are widely applied to improve fatigue strength and damage tolerance of metal components by inducing compressive residual stresses. Radial Hertzian pressure loading essentially governs deformation by deep rolling, whereas shot peening additionally causes plastic stretching near the surface in response to tangential forces from multiple projectile impacts. Consequential differing development of compressive residual stresses becomes obvious from a comparison of typical depth distributions measured by X-ray diffraction in hardened high strength bearing steel. In Figure 1, the initial state after machining is plotted schematically for reference as well. Deep rolling compressive residual stresses can extend significantly further into the material but are rather low in the outer layer. Although the surface value of about 400 MPa benefits from previous honing, it is considerably lower than approx. 700 MPa after shot peening. Dominant Hertzian pressure effect is reflected in pronounced subsurface compressive residual stress maxima. The size of bombarding particles ($1^{\pm 0.2}$ mm in Figure 1) limits shot peening influence depth.

In recent years, deep rolling has attracted increasing attention for bearing application [1–4]. In contrast to shot peening, which requires subtractive reworking of impact crater waviness (typical R_a roughness of several µm), the burnishing process even boosts surface quality [5]. For assessing life gain in classical rolling contact fatigue on the basis of materials science, it should be considered that compressive residual stresses impede butterfly crack initiation and wing growth occurring under Hertzian pressure p_0 upwards of around 1300 MPa [6], but on the other hand arise independently after few ring revolutions in operation once cyclic (micro) plasticity sets in [1], i.e. at p_0 above 2500 to 3000 MPa. With similar deep rolling pre-treatment, bearing tests provide greater enhancement in the load range 1300 MPa$\leq p_0 \leq$2500 MPa than for $p_0 \geq$3200 MPa [2,3]. Larger effect for roller than ball contact is indicated by the corresponding size of damage risk volume [4]. Higher resistance against spontaneous surface cracking by compressive residual stresses is verified experimentally as well [7].

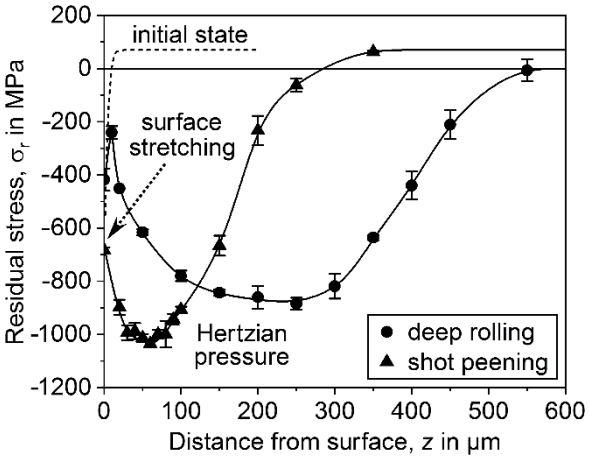

Figure 1: Depth distributions of circumferential residual stress (initial state indicated) after deep rolling and shot peening of surface machined bearing rings out of martensitically hardened 100Cr6 steel.

As the weaker boundary zone (see Figure 1) diminishes improvability of cyclic and static load capacity by deep rolling, corrective measures have been proposed in the literature. The most direct approach is to

remove the near-surface layer up to the peak value of compressive residual stress by subsequent machining [8]. Even if less material is taken off, however, the involved decrease of strengthening depth may be unacceptable particularly for larger bearings. Combined deep rolling and shot peening [9], as suggested by Figure 1, avoids this drawback. Due to resulting surface roughening, the method is inappropriate for bearing applications unless final machining is likewise performed. The alternative of a second deep rolling step at reduced Hertzian pressure with more overturns circumvents this problem [10]. Note that multiple impacts at the same spot increase the subsurface compressive residual stresses from shot peening (cf. Figure 1). It is reported that the maximum is reached rapidly after few collisions [11], which agrees well with findings on repeated deep rolling [1,12]. Because of closer proximity to surface, it is also important that rising number of passes significantly broadens the compressive residual stress distribution [1,13].

In the present paper, another multi-stage deep rolling process is examined. The aim of the study is to estimate numerically the potential for producing a more uniform edge profile of compressive residual stresses. By successively applying rolling elements of different diameter [14], the outer and deeper region can be influenced specifically. Modelling of deep rolling for simulation aided compressive residual stress engineering is based on the triaxially loaded Hertzian contact between two bodies. In the analytical theory, elastic solids and low strains are assumed. A finite element analysis is therefore carried out to involve plastic deformation and residual stress generation.

2. Finite element modelling of a two-step deep rolling process

A measurement based experimental approach to residual stress optimization is a difficult and time-consuming task. Before starting trials, therefore, a finite element analysis (FEA) is an appropriate preparation tool to better understand the effect of process parameters. For this purpose, a two-dimensional (2D) model of multi-step deep rolling is established. The considered plane geometry comprises the raceway to be treated and two rolling bodies. The FEA model is built using the commercial finite element software ANSYS 19.2 with its mechanical APDL solver, as also used for the computation and processing of all results presented in the following. The simulation aims to provide information on the compressive residual stresses during the passes over the hardened steel raceway and the influence of various parameters, such as size of the rolling elements, load and order of application. As discussed above, overrolling with sufficient contact pressure leaves an outer skin of lower compressive residual stress ahead of the subsurface peak. This is in response to the course of von Mises equivalent stress for radial Hertzian loading. If the rolling element size is chosen small to reduce the extent of the border, the desired in-depth effect diminishes accordingly. A large diameter, on the other hand, creates a pronounced weak edge zone. This fundamental restriction is addressed by the examined multi-step process.

Deep rolling can be viewed as a simplified contact problem. Numerical effort and calculation methods are affected by its highly nonlinear nature [15]. ANSYS offers a powerful range of contact tools to carry out such a stress analysis. Deep rolling finite element simulations are available in the recent literature [13,16–18], for instance referring to automotive crankshafts or railway axles.

2.1. Geometries and meshing

For the sake of saving computation time, a 2D model is used to numerically investigate two-pass deep rolling. The reason is that this preliminary study of process development serves the rather qualitative purpose of estimating how the application of differently sized and loaded rolling bodies can influenced the near-surface compressive residual stress state. More practical aspects, such as dealing with overlap or varying track widths of ball tools, are not yet of interest. The model consists of one linear raceway and two circular rolling elements. The latter represent the working tools. To capture the multi-step process in a single simulation, these two rolling elements are superimposed in the model with individual meshes. Note therefore that they represent separate bodies. The raceway reveals a much finer mesh than the rolling elements as the resulting stresses in the workpiece are of primary interest. Figure 2 shows the model geometry. For increased computational accuracy, the mesh of the raceway element (overall thickness: 3.3 mm) is further refined towards the centre of Hertzian contact.

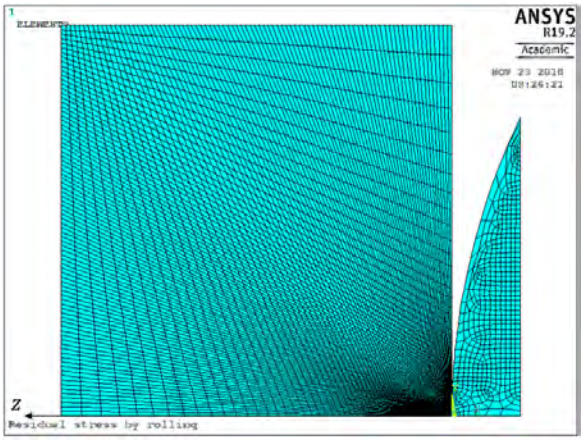

Figure 2: Meshed 2D Model with raceway segment on the left and two overlapping rolling elements (sectors) on the right. The z-axis is directed into the depth of the workpiece.

2.2. Material

All geometries in the model are assigned to bearing steel but with varying Young's modulus E. Higher stiffness (E=300 GPa is a typical value for a ceramic tool) reduces deformation of the rolling elements. The basic material data are given in Table 1. The mechanical behaviour of the bearing steel is characterised in the simulation by an isotropic bilinear elastic-plastic model. Figure 3 schematically illustrates the simplified stress σ vs. strain ε relationship. Note that yield and ultimate strength, $R_{p0.2}$ and R_m, respectively depend on

heat treatment and mechanical processing. Both values set in Table 1 fall in the upper range of bearing steel.

Table 1: Material properties of the raceway (workpiece) and, where mentioned, the rolling elements (tools).

Young's modulus	200 GPa
Young's modulus, rolling elements	300 GPa
Yield strength	2100 MPa
Ultimate strength	2600 MPa
Poisson's ratio	0.3

The residual stresses are calculated by means of the von Mises yield criterion, which is usually chosen in plasticity models. In particular, it describes material response to static and cyclic Hertzian compression appropriately [19,20]. Note that deep rolling residual stresses are caused by local non-uniform micro-plastic deformation.

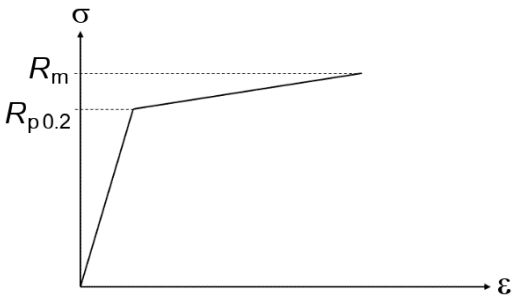

Figure 3: Bilinear elastic-plastic stress-strain curve, yield point and ultimate strength are indicated.

2.3. Contact formulation

Friction is not considered. The core of the simulation is the contact problem between the raceway and rolling element. Its solution is highly complex. The contact formulation comprises the mathematical description of the geometry and the numerical approach. ANSYS provides several algorithms for this purpose. For a Hertzian type contact problem, such as deep rolling, either the pure penalty or augmented Lagrange method are suitable [21]. The former is used as calculation algorithm for the simulation because it leads to good results in practice. This approach also saves computation time due to lower numerical complexity. Contact detection occurs by means of the surface projection-based method [22].

2.4. Boundary and initial conditions

By exploiting the specific geometry, the model is further simplified by a symmetry condition along the radially oriented *z*-axis. At the lower end of the raceway, a fixed support is defined. Load is respectively applied via a displacement of the two rolling bodies towards the raceway element in the negative *x*-direction. By avoiding a force or surface load, the convergence properties of the numerical procedure are significantly improved. For a general interpretability of the simulation results, the initial state is assumed to be free of (manufacturing) residual stresses.

2.5. Solution

Table 2 presents the four steps, into which two-stage deep rolling is divided in the calculation [23]. This way, the process is correctly simulated to evaluate the induced residual stresses.

Table 2: Solution steps.

Step	Solver task
1	Loading of the raceway with rolling element 1
2	Relieved intermediate situation
3	Loading of the raceway with rolling element 2
4	Relieved final situation

All steps must be executed individually by the solver to achieve the intended result. The previous output respectively serves as starting point of the next calculation part because the solutions are superimposed. Main advantage of this subdivision is that the overall and each individual step result can be viewed in one simulation.

The procedure is implemented by displacement of the first rolling body with respect to the raceway in positive and subsequently negative *x*-direction for load application and relief, respectively. To ensure that the workpiece is not influenced by both tools simultaneously, the other rolling element meanwhile remains at rest by "floating" over its surface. This approach can be transferred to the second load case accordingly. Figure 4 reveals the result of such a simulation. The blue area marks induced compressive residual stresses. The maximum (darkest zone) occurs below the surface, in agreement with the depth distribution of Hertzian contact von Mises equivalent stress.

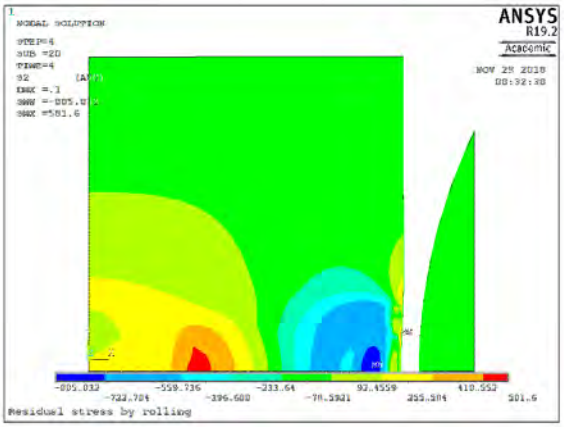

Figure 4: Result of a finite element simulation after step 4, indicating compressive and tensile residual stresses in blue and red, respectively. The rolling (pressing) body is shown on the right, the raceway element on the left. The z-axis is horizontally oriented in the centre of the contact.

3. Results

Before presenting the findings, Table 3-1 provides an overview of the input condition for the performed parameter studies. The two rolling elements of the FEA model are permanently numbered 1 and 2 (see Table 2). This convention emphasizes that each simulation sequence not only involves the corresponding diameters (d_1, d_2) and Hertzian pressures (p_1, p_2) but also the temporal order of loading indicated by an arrow. Table

3-1 thus illustrates the variety of possibilities for applying and (fine-) tuning two-step deep rolling, which makes the present numerical analysis useful for process development and design.

Table 3-1: Scheme of the parameter studies.

Study	Diameter	Hertzian pressure	Order
1	$d_1 > d_2$	$p_1 < p_2$	1 → 2
2	$d_1 = d_2$	$p_1 < p_2$	1 → 2
3	$d_1 > d_2$	$p_1 < p_2$	2 → 1
4	$d_1 > d_2$	$p_1 < p_2$	2 → 1

Note that contact stresses are not read in directly but calculated by the model (see section 2.4.). Sizes of the rolling elements and (non-round) Hertzian pressures used for the parameter studies are given in Table 3-2.

Table 3-2: Rolling element diameters and applied loads (see Table 3-1).

Study	d_1/mm	d_2/mm	p_1/MPa	p_2/MPa
1	9	5	4716	5266
2	9	9	4013	4161
3	9	5	4799	5121
4	9	5	5083	5121

3.1. Simulation examples

The following diagrams consistently refer to the unloaded condition, as stated in steps 2 and 4 of Table 2. Figure 5-1 shows the result of parameter study 1. The residual stress in circumferential direction is plotted against distance from surface. For the first and subsequent second load case (1, 1→2), respectively, diameters d_1=9 mm and d_2=5 mm are set for the rolling elements. Simulation details are compiled in Tables 3-1 and 3-2. Both surface conditions are adjusted in a way that the final exceeds the initial Hertzian pressure applied, i.e. $p_1<p_2$ (order: 1→2).

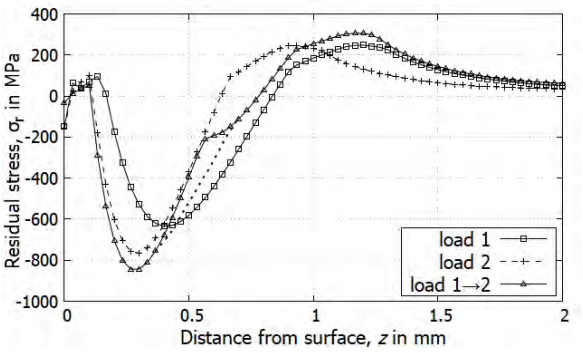

Figure 5-1: Depth profiles of residual stress in circumferential direction, evaluated in the centre of the contact (see Figure 3), for parameter study 1 of Tables 3-1 and 3-2. In addition to the results of initial first (1) and (subsequent) final second (1→2) tool pass, application of load 2 alone (2) is included for reference.

The development of the von Mises residual stress (including plastic material response) in the workpiece raceway for the relieved situations of the analysed two-step deep rolling process of Figure 5-1 (i.e., study 1 of Tables 3-1 and 3-2) is displayed in Figure 5-2. This chart manifests the intended effect on the near-surface zone by the second load (1→2). There is a significant increase of the equivalent stress in the outer layer of z≤0.4 mm, whereas at greater depths changes compared with the previous state are small.

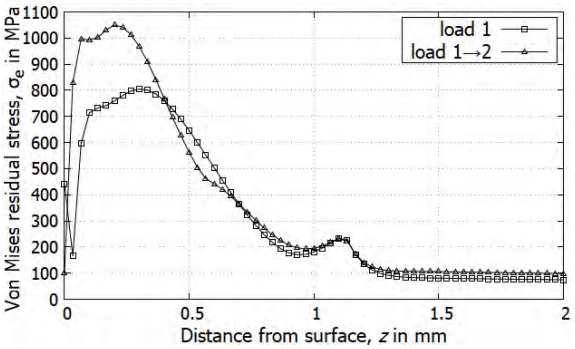

Figure 5-2: Depth distribution of von Mises equivalent residual stress for parameter study 1 (cf. Figure 5-1).

Figure 5-1 indicates that second deep rolling rises the compressive residual stresses substantially near the surface. Due to increased Hertzian pressure ($p_2>p_1$), moreover, the final maximum is about 40% higher.

Mechanical compensation after second loading occurs gradually in the adjacent region. The associated reduction of compressive residual stresses generated previously by the pass of the first rolling element in the inner zone (z≥0.4 mm), however, may be overestimated in the simulation. This assessment is supported by the dashed graph for sole application of load (case) 2, added to Figure 5-1 for comparison. The single-step profiles (1, 2) themselves verify the experimentally well-known correlations that increasing rolling tool diameter expands the impact zone and the position of compression-tension crossover deeper into the material and that larger Hertzian pressures result in higher compressive residual stresses. The nonphysical hump of the terminal curve (1→2) at z≈0.6 mm is related to numerical modelling. The dotted smoothing line assists with estimating the potential benefit of two-step deep rolling according to parameter study 1 over both single-pass processes of load 1 and 2. As the present research focuses on basic correlations, the cause of such obvious numerical inconsistencies (e.g. discretisation) is not further considered. More expanded residual stress redistribution in the second load (pass) mitigates the decrease of the original strengthening depth. This subject is briefly discussed later in the text.

Parameter study 2 of Tables 3-1 and 3-2 aims at indirectly demonstrating the influence of the size of the rolling elements on the residual stresses by choosing both diameters, d_1 and d_2, to be 9 mm. According to the simulation result of Figure 6, the initially induced compressive residual stresses (load 1) are increased and the maximum as well as the inner end of the influence zone are shifted towards larger depth by the second overrolling (1→2) at higher Hertzian pressure. In contrast to Figure 5-1 (study 1), the effect near the surface from the first pass is negligible. Note that the von Mises contact stress for a given Hertzian assembly at any distance (z) increases with load (p_0). In Figure 6, the two-step process (1→2) also does not significantly

raise the impact depth with respect to the included second single-pass reference case (2) of higher pressure. Without shakedown by repeated overturns [1,10], it is the diameter of the rolling element alone that governs the nearest position of subsurface compressive residual stress build-up to a certain magnitude. Expansion of the profile width into the depth for a conventional single tool process occurs only by applying higher Hertzian pressure. Unavoidably associated increase of the compressive residual stress maximum, however, restricts the practical use of this approach. A comparison of both individual load cases (1, 2) in Figure 6 visualizes the basic feature discussed above ($d_1=d_2$, $p_1<p_2$).

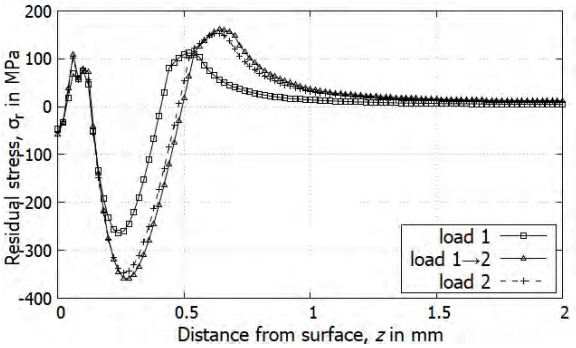

Figure 6: Depth profiles of residual stress in circumferential direction, evaluated in the centre of the contact, for parameter study 2 of Tables 3-1 and 3-2. The distance curve for sole application of load 2 complements the distributions after first (1) and second (1→2) tool pass.

Another accessible influencing factor is the order, in which differently sized rolling elements are applied to the raceway. According to Tables 3-1 and 3-2, parameter studies 1 and 3 are almost identical. It is only the order, in which the larger (1) and smaller (2) rolling element are pressed against the raceway, that actually differs. Figure 7 shows the induced residual stresses after initial (2) and final (2→1) loading. The latter graph is supplemented by a dotted smoothing line (cf. Figure 5-1). The influence depth is significantly increased by the second pass without undesirable changes of the compressive residual stresses in the outer zone.

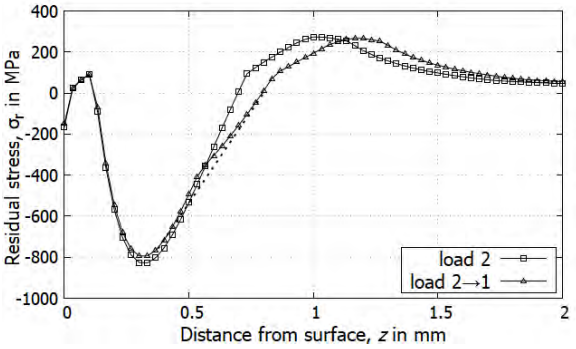

Figure 7: Depth profile of residual stress in circumferential direction, evaluated in the centre of the contact, for parameter study 3 of Tables 3-1 and 3-2.

It is interesting to directly compare the simulation results of study 1 and 3. In Figure 8, the residual stress profiles are smoothed and adjusted at the exit ramp to compensate for numerical inaccuracies. Both curves are rather similar. Whereas Figures 5-1 and 7 illustrate the advantage of two-step deep rolling with regard to improved near-surface coverage and width of the compressive residual stress distributions over the single-stage load 1 and 2 processes, respectively, the suggested increase in efficiency by first applying the large (1→2) rather than the small (2→1) tool needs further investigation for confirmation. Note that the Hertzian pressures of study 1 and 3 are not exactly the same.

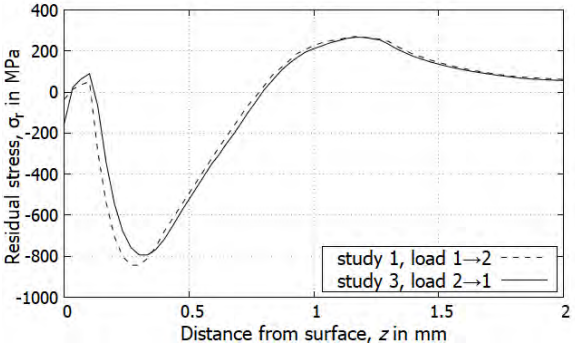

Figure 8: Residual stress comparison of parameter studies 1 and 3 (see Figures 5-1 and 7).

Process performance can finally be tailored effectively by the forces transferred to the raceway through the deep rolling elements. Parameter study 4, defined in Tables 3-1 and 3-2, provides an instructive demonstration. Figure 9 reveals the result of residual stress finite element simulation. The impact of considerably higher final loading than in study 3 (only difference) is obvious from the increased influence depth. As both Hertzian pressures are almost identical ($p_1\approx p_2\approx 5100$ MPa), maximum von Mises contact stresses are either. Hence, the compressive residual stress peaks after load cases 2 and 2→1 are in good agreement (about 800 MPa, note that $p_1<p_2$).

Figure 9 further confirms the benefit of double- over one-step deep rolling. If one refers to the width of the depth zone of compressive residual stress above 400 MPa, this efficiency index rises by a good 50% from 0.38 mm (load 2) to 0.58 mm (2→1). Mutual adjustment of the diameters of the rolling elements and the applied forces (contact pressures), therefore, enables flexible process fine-tuning.

In this context, a last comparison between Figures 6 and 9 is worth drawing. According to Table 3-2, the corresponding parameter studies 2 and 4 reasonably permit distinguishing the effect of an individual tool applied once at two loads onto the raceway surface from a small and large rolling element both employed under the same Hertzian pressure, i.e. $d_1=d_2$, $p_1\neq p_2$ vs. $d_1\neq d_2$, $p_1=p_2$, respectively, on the compressive residual stress distribution. The latter result displayed in Figure 9, therefore, again proves the utility of the upgraded two-step process. Width expansion is completely decoupled from top value enhancement of the residual stress pattern. This influence separation is highly desirable. Note that excessive compressive residual stresses reduce rolling contact fatigue life. For hardened bearing steel, a threshold of about 1000 MPa is reported [24].

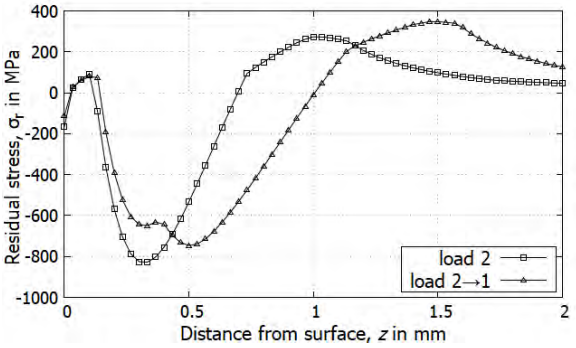

Figure 9: Depth profile of residual stress in circumferential direction, evaluated in the centre of the contact, for parameter study 4 of Tables 3-1 and 3-2.

3.2. Restrictions of the finite element model

A residual stress (σ_r) free initial material condition is assumed in the simulations. In the distance (z) distributions after deep rolling presented above, therefore, compensational redistribution occurs with respect to the $\sigma_r(z)=0$ line. As the workpiece thickness is limited to 3.3 mm in the model, pronounced tension peaks of up to more than 300 MPa are formed after zero crossing. This "overshooting" is just as unrealistic for usual bearing components as exaggerated decrease of compressive residual stresses from first loading in the second pass of two-step deep rolling (see Figure 5-1). Extending the overall thickness of the raceway element, i.e. the distance from surface to fixed support (boundary condition), should further improve the predictions of the finite element analysis.

4. Conclusions

Improvement of product performance is an important driver of technology innovation. Deep rolling for inducing compressive residual stresses in the Hertzian fatigue and friction loaded edge zone currently experiences growing interest in bearing applications. The method of moving a round pressing tool (ball or roller) over the surface of a workpiece is similar to low plasticity burnishing. Advanced computer simulations play a progressive role in process development. In this paper, a finite element analysis using ANSYS is carried out to simulate a two-step deep rolling operation. The intention is to estimate the potential for optimizing the compressive residual stress distribution by smartly combining differently sized and loaded tools. A simplified two-dimensional contact model with bilinear elastic-plastic isotropic material behaviour of the treated bearing steel is created and discussed. The studied parameter constellations include diameters and order of application of the rolling elements as well as Hertzian pressure on the workpiece raceway surface. The effect on width and intensity of the resulting residual stress field is investigated.

High operating speed, cleanliness and combinational variety (e.g. with turning) as well as involved surface smoothing make deep rolling an attractive mechanical strengthening process. Edge weakness of the induced compressive residual stress distribution, however, is a well-known challenge in conventional single-tool practice. Corrective measures proposed in the literature to mitigate this process-inherent disadvantage are discussed. A schematic single-pass deep rolling residual stress profile is depicted in Figure 10. The graph is used to quantify the undesirable skin. With respect to a lower (effectiveness) reference level σ_0 of compressive residual stress, for instance 400 MPa, the weaker boundary layer extends from the surface to a depth z_1. The width of the actual strengthening zone, Δz, thus amounts to $z_2–z_1$. It is worth noting for a single-pass process that the depths $z_1(d)$ and $z_2(p_0)$, respectively, depend essentially on the rolling element diameter d and the applied Hertzian pressure p_0, which is restricted by the material-specific threshold σ_{th} (about 1000 MPa for bearing steel) of maximum (beneficial) compressive residual stress $\sigma_{r,max}(p_0)\leq\sigma_{th}$. Figure 10 concisely illustrates the intrinsic restriction of single-tool/pass deep rolling. It, however, also suggests the approach adopted in the present paper. The numerical simulations indicate that effective width expansion and shape equalization of the compressive residual stress profile can be achieved by the use of two differently sized rolling elements and the application of similar Hertzian pressures, respectively. Note that larger variation in both tool diameters ($\Delta d=|d_1–d_2|$) further increases the influence range Δz. The load on the smaller, near-surface impacting rolling element affects residual stress redistribution in the depth.

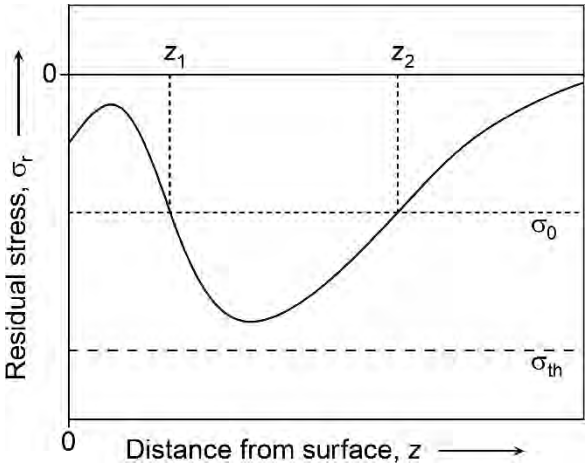

Figure 10: Schematic representation of the residual stress depth profile from single-pass (one tool) deep rolling.

Track widths of differing balls may strongly deviate from each other. A combination (tool) of a small and a large cylindrical roller is therefore easier to use with the proposed two-step process. When applying balls on curved surfaces, however, optimization of the compressive residual stresses only in the (often) highest loaded radius region can be sufficient.

The four finite element parameter studies presented in this paper allow fundamental statements about multi-stage deep rolling. Tool sizes and Hertzian pressures prove to be versatilely appropriate process variables for residual stress engineering. The influence of application order of different rolling elements is not yet

fully clarified but simulations hint at benefit from primarily large and subsequently small diameter. So prepared experimental series are intended for providing further insight into optimized design and fine-tuning of two-pass deep rolling compressive residual stress profiles. The magnitude of an involved increase in hardness H by cold working depends on the heat treatment and mechanical material history. It is of minor relevance to bearing steel condition of $H \geq 58$ HRC. The effect, however, is amplified with decreasing original hardness. Unlike compressive residual stress, no local (redistribution) loss accompanies the second overturn.

Acknowledgment

The authors are grateful to Dr. Werner Horn, SKF Advanced Engineering Competence Centre, for his support and helpful discussions. Permission to publish by SKF is appreciated.

References

[1] S. S. Cretu, M. I. Benchea, O. S. Cretu: Compressive Residual Stresses Effect on Fatigue Life of Rolling Bearings. Proc. IMECE07, 2007 ASME International Mechanical Engineering Congress and Exposition, 11–15 November 2007, Seattle, Washington, USA, American Society of Mechanical Engineers, New York, 2008, pp. 485–490.

[2] A. Pabst, S. Tremmel, S. Wartzack: Investigation of residual compressive stresses in rolling bearing components and their impact on the rating life. Proc. 69th STLE Annual Meeting and Exhibition, 18–22 May 2014, Lake Buena Vista, Florida, USA, Society of Tribologists and Lubrication Engineers, Park Ridge, Illinois, USA, 2014, Vol. 1, pp. 475–478.

[3] F. Pape, O. Maiß, B. Denkena, G. Poll: Computational approach to improve bearings by residual stresses based on their required bearing fatigue life. Int. J. Comp. Meth. and Exp. Meas., Vol. 6, 2018, No. 4, pp. 656–666.

[4] T. Coors, F. Pape, G. Poll: Comparing the Influence of Residual Stresses in Bearing Fatigue Life at Line and Point Contact. Materials Research Proceedings, Vol. 6, 2018, pp. 215–220.

[5] W. Grzesik, K. Zak, M. Prazmowski: Surface Integrity of Hard Turned Parts Modified by Ball Burnishing. J. Mach. Eng., Vol. 12, 2012, No. 1, pp. 18–27.

[6] M. Brückner, J. Gegner, A. Grabulov, W. Nierlich, J. Slycke: Butterfly Formation Mechanisms in Rolling Contact Fatigue. Proc. VHCF-5 (edited by C. Berger, J. Christ), 5th International Conference on Very High Cycle Fatigue, 28–30 June 2011, Berlin, Germany, DVM Deutscher Verband für Materialforschung und -prüfung, Berlin, Germany, pp. 101–106.

[7] J. Gegner, W. Nierlich: Service Loading of Rolling Bearings in Wind Turbine Gearboxes: X-ray Diffraction Material Response Analysis of White Etching Cracks Premature Failures. Tribol. Trans., Vol. 61, 2018, No. 2, pp. 269–278.

[8] J. Fella, O. Beer: Verfahren zur Herstellung von Wälzlagerringen und Wälzlager. German Patent, DE 102015207779A1, filed 28 Apr. 2015.

[9] P. S. Prevey, J. E. Haas: Method and apparatus for improving the distribution of compressive residual stress. United States patent application, US 2008/0081208A1, filed 24 Sept. 2007.

[10] J. Gegner: Verfahren zum Festwalzen eines metallischen Objekts, insbesondere einer Laufbahn eines Wälzlagers. German patent, DE 102015201644B4, filed 30 Jan. 2015.

[11] X. Cheng: Experimental and numerical approaches for improving rolling contact fatigue of bearing steel through enhanced compressive residual stress. PhD thesis, Ohio State University, Columbus, Ohio, 2007.

[12] N. Lyubenova, D. Bähre: Investigation of the surface residual stresses in single and multiple trace deep rolling on flat AISI 4140 specimens. Proc. ICSP-13, 13th International Conference on Shot Peening, 18–21 Sept. 2017, Montreal, Quebec, Canada, pp. 428–433.

[13] N. Lyubenova, D. Bähre: Finite Element Modelling and Investigation of the Process Parameters in Deep Rolling of AISI 4140 Steel. J. Mater. Sci. Eng. B, Vol. 5, 2015, No. 7–8, pp. 277–287.

[14] J. Gegner, U. Krug, A. Olschwski, A. Stubenrauch: Method for producing a track element of a bearing assembly. United States patent, US 9273727B2, filed 25 Oct. 2012.

[15] W. Rust: Nichtlineare Finite-Elemente-Berechnungen: Kontakt, Geometrie, Material. 2nd edition, Vieweg+Teubner, Wiesbaden, Germany, 2011, pp. 235–264.

[16] S. M. Hassani-Gangaraj, M. Carboni, M. Guagliano: Finite element approach toward an advanced understanding of deep rolling induced residual stresses, and an application to railway axles. Mater. Des., Vol. 83, 2015, pp. 689–703.

[17] N. Lyubenova, M. Jacquemin, D. Bähre: Influence of the Pre-Stressing on the Residual Stresses Induced by Deep Rolling. Materials Research Proceedings, Vol. 2, 2016, pp. 253–258.

[18] L. G. A. Fonseca, A. R. de Faria: A deep rolling finite element analysis procedure for automotive crankshafts. J. Strain Anal. Eng., Vol. 53, 2018, No. 3, pp. 178–188.

[19] E. Broszeit, T. Preussler, M. Wagner, O. Zwirlein: Stress Hypotheses and Material Stresses in Hertzian Contacts. Z. Werkstofftech., Vol. 17, 1986, No. 7, pp. 238–246.

[20] J. Gegner, W. Nierlich: Comparison of the Microstructural Changes and X-ray Diffraction Peak Width Decrease during Rolling Contact Fatigue in Martensitic Microstructures. Bearing Steel Technologies, Vol. 9, Advances in Rolling Contact Fatigue Strength Testing and Related Substitute Technologies (edited by J. M. Beswick), Selected Technical Papers, STP 1548, ASTM International, West Conshohocken, Pennsylvania, USA, 2012, pp. 303–328.

[21] L. Nasdala: FEM-Formelsammlung Statik und Dynamik: Hintergrundinformationen, Tipps und Tricks. 3rd edition, Springer, Wiesbaden, Germany, 2015, pp. 227–235.

[22] ANSYS Inc.: ANSYS Mechanical APDL Contact Technology Guide. Canonsburg, Pennsylvania, USA, 2016, pp. 15–60.

[23] J. Simon: Finite-Elemente-Analyse des Druckeigenspannungsaufbaus beim stufenweisen Festwalzen. Bachelorthesis, University of Applied Science Würzburg-Schweinfurt, Schweinfurt, Germany, 2019, pp. 46–50.

[24] E. Schreiber, W. Simon, H.-W. Zoch: Work Hardening of Ball Surfaces. Creative Use of Bearing Steels (edited by J. J. C. Hoo), Selected Technical Papers, STP 1195, ASTM International, West Conshohocken, Pennsylvania, USA, 1993, pp. 81–92.

The Utilization of Production-Related Defects for Improving Operating Properties of Journal Bearings

Lars Friedrich[1], Björn Prase[2], Marko Ebermann[3], Alexander Hasse[4]

[1] *Institute of Design engineering and Drive technology, Chemnitz University of technology, lars.friedrich@mb.tu-chemnitz.de*

[2] *bjoern.prase@mb.tu-chemnitz.de*
[3]*marko.ebermann@mb.tu-chemnitz.de*
[4]*alexander.hasse@mb.tu-chemnitz.de*

The function of hydrodynamic journal bearings is primarily determined by their lubrication gap geometry. Even small deviations in the bearing geometry can lead to a change in the operating properties and in the worst case to bearing failure. Such deviations of the ideal geometry always occur within production. These can be caused, for example, by clamping in a three-jaw chuck - this typically leads to a three-sided uniform thickness geometry (or three-sided-lobe geometry). In order to ensure safe operation of the journal bearings, the shape tolerances are traditionally selected very precisely, which leads to high manufacturing costs.

In this work we follow an alternative approach. We allow larger form deviation values, but orient these when installing the bearing so that negative effects on the operating properties are minimized. The shape deviation investigated is a three-sided-lobe geometry in circumferential direction.

The influence of the orientation of form deviation of hydrodynamic journal bearings were simulated on the basis of the Reynolds equation and evaluated by a worst-case and best-case investigation.

The investigations show that with knowledge of the production-related effects, negative influences of the form deviation can be negated. In addition, a positive influence on the operating properties can be generated by the correct utilization of the form deviations.

The knowledge about the influence of the shape deviation allows to extend the given tolerance data from the standards and thus to widen the production tolerances.

Keywords: journal bearing, form deviations, shape deviation, shape adaption, operating values

1. Introduction

Production drawings require dimensional, form and position tolerances. In order to define these tolerances, the knowledge about their functional influence is required. The function of journal bearings depends largely on the geometry of their hydrodynamic lubricating gap. Shape deviations may result in an early failure of the bearing due to a reduced lubricating gap height or edge carrying. For the technical implementation, ISO 12129-2 gives the permissible shape deviation for thrust rings and shafts [1]. The standards do not provide any information about the tolerance of shape and position deviation of journal bearings. For this reason ISO 12129-2 is often referred to as the reference for journal bearing tolerance.

Investigations focusing on the macroscopic shape deviation of journal bearings show the influence of multi-lobe bearings on the operating values [2]. As a result, these journal bearing forms have been used in industrial practice for a long period of time. Also shape deviations in the microscopic range show a change in operating values [3], [4], [5]. As a result, specific microscopic geometric form deviations were investigated, which had advantages for the operation. These include hyperboloid journal bearings, which are particularly effective against edge-carrying on tilted shafts [6]. Likewise, out-of-roundness deviations show a reduction in wear in journal bearings [7], [8]. If inaccuracies in the manufacturing process are considered, wavy surfaces are a common result. The waviness influence on a rectangular slider bearing [9] and on a hydrodynamic journal bearing [10] can increase the load-carrying capacity depending on the number of waves. The waviness of the journal bearing corresponds to a multi-lobe bearing in the microscopic scale. While the previous works consider the geometric deviation of the cylindrical journal bearing, the geometric orientation was not taken into account. The orientation shows in [11] and [12] an additional influence.

The standards do not define the effects of shape deviations of the bush geometry on the operating values of journal bearings. Therefore, a worst-case analysis is usually carried out for the application. This analysis assumes the form deviation and orientation, which reduces the lubrication gap height the most. For the application, the tolerance zone for the journal bearing is typically derived from the tolerance zone of the shaft from ISO 12129-2. The aim of this work is to eliminate uncertainties regarding the form deviation of journal bearings and to optimize the bearing geometry for operation. For this purpose, a best-case analysis is used to orient the form deviation in such a way that the largest possible lubrication gap height for the operating point is achieved. This work is an extension of the results obtained in [13] and [14].

2. State of the art

The investigations carried out so far show that form deviations have an influence on the operating values of the bearing. The form deviations are caused by inaccuracies in the manufacturing process.

For the practical application, a safe function of the journal bearing is necessary. During operation, it is necessary that some operating values such as the lubrication gap height, which represents the load-carrying capacity, do not fall below specific limit values. In order to guarantee a safe operation of the journal bearing, in any situation, it is required to cover any misalignment of the bearing form deviation that may occur as a result of the manufacturing or assembly process.

Usually, the manufacturing accuracy is therefore increased that a form deviation is kept at a minimum for operation. A misalignment of bearings with a larger form deviation can lead to the limit lubrication gap height being undercut. This means that the bearing operates permanently in the mixed friction area during operation. The wear in the bearing is greatly increased and a failure of the machine element is the consequence.

It is therefore important to keep the lubrication gap height as high as possible.

The problem results from the fact that form deviations must be defined more and more precisely in order to compensate errors in the production and mounting process. These more precise tolerance zones allow the required operating values to be maintained.

This lead to increased costs of the bearing manufacturing process. There is a lack of studies on acceptable form deviations and how the operating values can be ensured without selecting the tolerance zone of the form deviation too small.

ISO 12129-2 includes guidelines for defining form and position tolerances of thrust rings and shafts in journal bearing systems. For a hydrodynamic radial journal bearing made of shaft and bushing, the roundness, straightness and parallelism tolerances are especially critical.

These form deviations can be seen in Figure 1, with the corresponding symbols from the Geometrical Product Specification (GPS) System. The size of the form deviations is described in the figure for the roundness, straightness and parallelism deviation with the parameters t_1, t_2 and t_3.

These form deviations can result in different bearing geometries that deviate from an ideal cylindrical bearing geometry. Each of these geometries affects the convergent lubrication gap and thus the operating parameters compared to an ideal cylindrical bearing geometry. In addition, mixed forms can occur in which, for example, a roundness deviation with a straightness deviation creates a geometry.

In order to investigate the influence of form deviations on the operating values, this work will mainly focus on a roundness deviation (t_1).

The permissible form deviations for journal bearings are derived in this study from ISO 12129-2. However, these specifications only apply to thrust rings and shafts, but not specifically to bearing bushes.

Table 1 shows the acceptable deviation values of t_1, t_2 and t_3 for the form deviations as a function of the lubricating gap height according to ISO 12129-2. This information serves as an orientation for the investigation. The critical case of a lubrication gap height between 5 and 10 µm is assumed.

The exclusion of possible errors in manufacturing and mounting processes, such as a larger form deviation of the bearing running surface or an unfortunate mounting position of this form deviation, requires a larger cost input. By allowing a higher form deviation tolerance zone and a precise definition of the mounting position costs can be cut, but only with knowledge about the influence on the operating values. The aim of the work is to investigate the relationship between a specific form deviation on a journal bearing and its mounting position in order to obtain the best possible operating values.

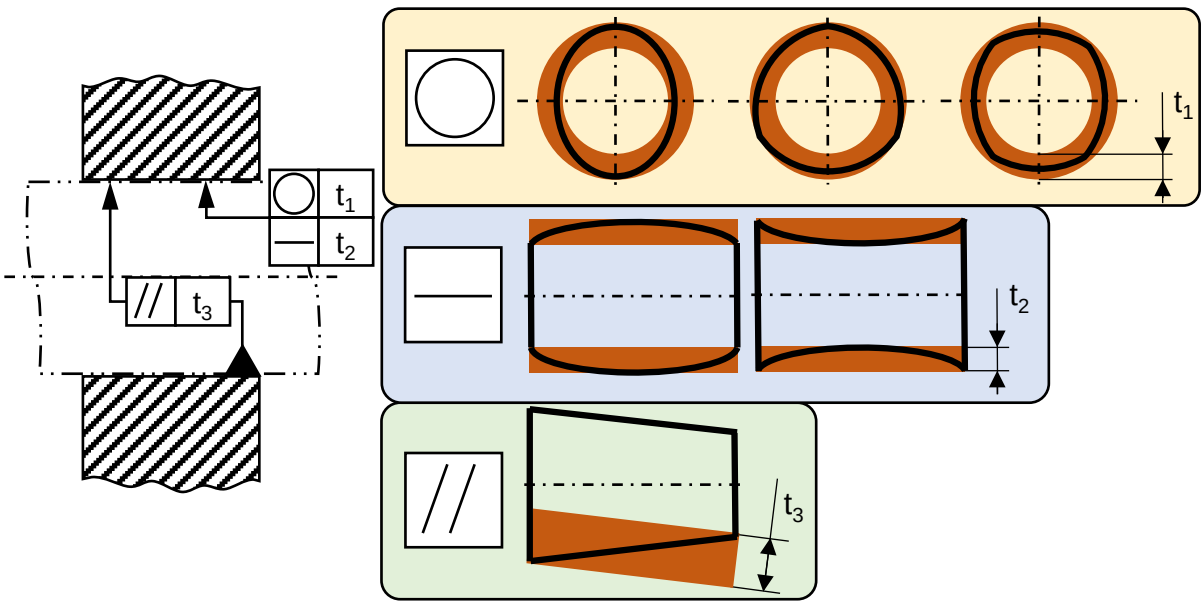

Figure 1: Resulting geometric shapes of journal bearings through form deviation

Table 1: Tolerance values according to ISO 12129-2 [1]

Feature / parameter on drawing			Accuracy grade			
			5	**10**	**20**	**30**
Lubrication film thickness		h_0 in µm	$5 \leq h_0 < 10$	$10 \leq h_0 < 20$	$20 \leq h_0 < 30$	$h_0 \geq 30$
Cylindrical form	Roundness tolerance	t_1 in mm	0,004	0,006	0,01	0,015
	Straightness tolerance	t_2 in mm	0,005	0,01	0,015	0,02
	Parallelism tolerance	t_3 in mm	0,015	0,02	0,03	0,04
Surface roughness		Ra in µm	0,4	0,4	0,63	0,8
		Rz in µm	2,5	4	5	6,3

In order to achieve these goals, a worst-case analysis is first carried out. This can determine how critical a large form deviation and an inaccurate mounting position can be. It is shown that the consideration is necessary, due to the significantly decreasing lubrication gap height.

Additional, a best-case investigation is carried out. This analysis proves that it is worth considering the orientation of the bearing for the operating parameters.

Nevertheless, it must be determined whether the best-case orientation is able to keep the lubrication gap height above a limit value.

Based on these results, the influence of the orientation on the lubrication gap height is investigated, to find a mounting positions, where a safe operation can be guaranteed, even if larger form deviation occurs. Thus, if the shape deviation is known, a mounting position could be defined, which generates a sufficient lubricating gap height even in case of slight angular errors in the mounting process and thus increases the service life of the bearing.

3. Simulation Set up

For the investigation of the roundness deviation a three-sided-lobe geometry is examined by means of simulations. This is one of the most common roundness deviations.

To describe the three-lobe bearing a H3 Polygon according to DIN 32711-1 [15] was used.

Object of investigation is a journal bearing with 30 mm diameter and a B/D-ratio of 0.5. The relative bearing clearance ψ is 2 ‰. The hydrodynamic simulations were carried out with the program ALP3T. A field of 256 points in circumferential direction and 34 points in axial direction describe the geometry of the journal bearing to be simulated, which is the maximum field size that is possible in the standard programme.

Thereby, the degree of deformation is varied. It is assumed, that the form deviation always occupies the maximum space within the tolerance zone. Figure 2 shows a three-sided-lobe shape in the tolerance zone defined by the value of the roundness deviation t_1. The dimension of the value t_1 describes the size of the tolerance zone. In the simulations, the tolerance zone was increased in 0.5 µm steps, starting at 0 µm.

In practical applications, production accuracy of 1µm is already very complex and associated with high costs. A finer definition of the tolerance zone with an accuracy of less than 1µm is economically useful for high-precision applications. For journal bearings, smaller accuracies can achieved with higher production costs. For a more precise resolution within the investigations, a step width of 0.5 µm was therefore chosen. For bearings with a diameter far greater than 30 mm or taller lubrication gap heights as assumed in this study (see Table 1) and used for standard applications, a lower resolution, e.g. in steps of 1 µm, can also be selected.

Additional, the shape orientation have to vary in the simulations. Therefore one peak point is the reference for the orientation. The start position is defined with a peak point along the load direction, the tilt angle φ is zero. The orientation is changed counterclockwise in 86 steps of 1.41° each, until the tilting angle reaches 120° (see Figure 2). Due to the three-sided-lobe geometry, the angular position of 120° corresponds to the geometry at the angular position of 0°.

The angular steps of the investigation are based on the resolution of ALP3T. A maximum of 256 points can be defined in the programme in the circumferential direction. So each field point represents, at a circumferential angle of 360°, an angle of about 1,41° ($360°/256 = 1{,}40625°$). Since every 120° the shape of the same thickness is identical again, 86 steps ($120°/1{,}40652° = 85{,}333$) are needed to examine each orientation of the bearing.

In the simulations, elastic or thermo-elastic deformations were neglected. The bearing bushing was therefore assumed to be rigid.

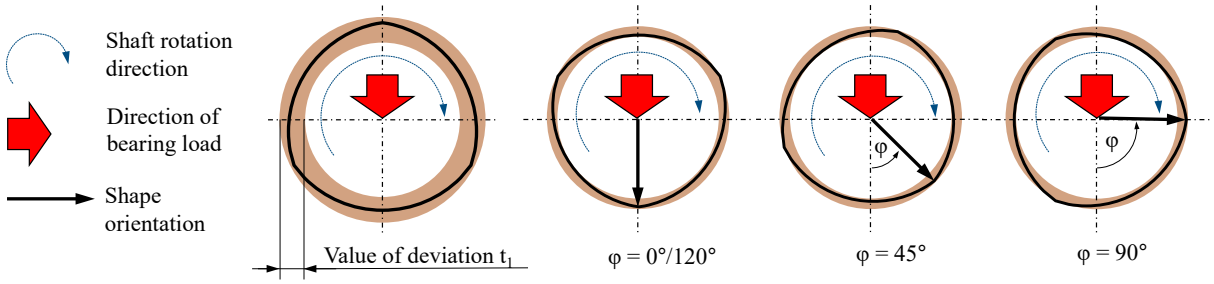

Figure 2: Value of deviation and orientation of the geometric shape

4. Simulations

In the first step of the methodical procedure, a worst-case analysis is carried out. The orientation of the respective form deviation is assumed, which reduces the lubrication gap height most. In the second step, a best-case analysis is carried out, in which the orientation is assumed to be the one that provides the largest lubrication gap height. In the third step, the lubrication gap height is then shown as a function of the angle of rotation for a specific operating condition.

The investigations concentrated on the minimum lubrication gap height. For the examined bearings with a bearing diameter of 30 mm, this is the critical parameter due to the lower relative speed.

Failure due to excessive local pressure occurs mainly in hydrodynamic operation. However, as long as no sufficient lubricating film can be formed, the bearing is still in the mixed friction area and the bearing load is additionally transmitted by the solid contacts between shaft and bushing. Therefore the lubricating gap height at this moment is more critical than the maximum local pressure, due to increased wear.

In comparison to bearings with larger diameters, smaller bearings have a higher heat dissipation, so that thermal failure is less frequent.

Due to the lower relative speed of bearings with smaller diameters, the load-carrying capacity of the bearing is lower, so that the lubrication gap height is in general smaller, compared to larger diameters. This means that there is a greater risk of driving in the critical area of mixed friction.

The influence of form deviation on parameters such as temperature, pressure and stiffness were therefore neglected.

The following results only applies to bearings with a diameter of 30 mm. The influence on the lubrication gap height is given as a percentage change to the lubrication gap height of an ideal cylindrical journal bearing.

4.1. Worst-Case analysis

Object of research is a lubrication gap height between 5 and 10 µm, as this is where wear is most likely to occur due to possible mixed friction. According to ISO 12129 - 2 the maximum allowed roundness tolerance value t_1 is 4 µm. In the simulation, the roundness deviation is varied, while the straightness (t_2) and parallelism (t_3) deviations are neglected and kept at 0 µm.

The simulations were made with three different specific loads p of 0.9 MPa, 1.8 MPa and 2.7 MPa. Each specific load was simulated at five different speeds n, beginning from 2000 rpm to 10000 rpm, in steps of 2000 rpm. Figure 3 shows the minimum lubrication gap heights for a worst-case orientation for p equal to 0.9 MPa, 1.8 MPa and 2.7 MPa, for each value of t_1 from 0 to 10 µm in steps of 0.5 µm.

The results in Figure 3 show, that a worst-case orientation of the form deviation can reduce the lubrication gap height by about 25 %, within the given tolerance zone of 4 µm of roundness deviation, according to the results for 2.7 MPa. At 1.8 MPa and 0.9 MPa and a roundness deviation of 4 µm the reduction of the lubricating gap height is still 20% of the original lubricating gap height of a cylindrical geometry.

With increasing roundness deviation over the given 4 µm, the minimum lubrication gap height decreases further. With a form deviation of more than 8 µm, the lubrication gap height of the bearing under investigation is less than 50% of the cylindrical reference bearing.

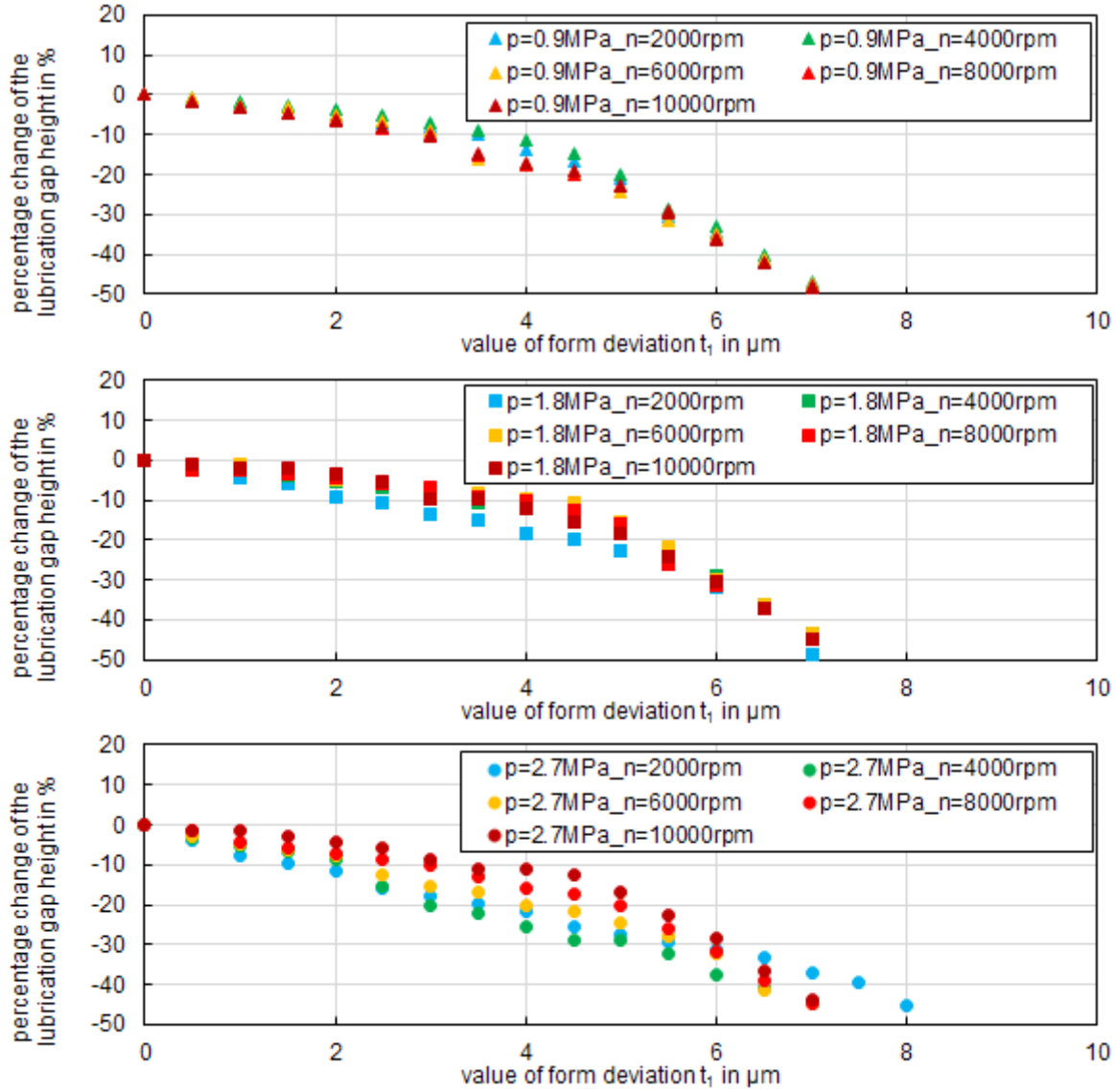

Figure 3: Minimum lubrication gap height of a three-sided-lobe bush at different form deviations in a worst-case orientation scenario for a journal bearing with diameter d=30 mm, wide-to-diameter ratio b/d=0.5 and a relative bearing clearance of $\psi = 2$ ‰

4.2. Best-Case analysis

Figure 4 shows the best-case analysis with the largest possible minimum lubrication gap heights. The shape deviation was again increased from 0 to 10 µm. For each value of the form deviation, the highest lubrication gap height was selected, which resulted from the best possible orientation of the bushing. A form deviation was aimed for in which the lubricating gap height in the best-case orientation achieves the same 25% reduction as shown in Figure 3 for 2.7 MPa in the worst-case analysis.

From the results, it can be seen that at 8 µm roundness deviation a reduction of 25% is achieved for the first time, with a best-case orientation at 2.7 MPa.

At 1.8 MPa and 0.9 MPa, the reduction at 8µm is about 20%, which is on the same level as in the worst-case analysis at 4µm.

Above a form deviation of 8 µm, the reduction of the lubrication gap height is lower due to the best-case orientation.

Furthermore, it is shown that the roundness deviation does not necessarily have a negative influence on the lubrication gap height. At slower speeds with small roundness deviations (of 0 to 4 µm) the best-case orientation can increase the lubrication gap height above the initial value. At higher speeds this is not the case. The positive effect of the form deviation is therefore not only dependent on the orientation but also on the operating point.

With the best-case orientation, the same lubrication gap heights can be assumed for a three-sided-lobe geometry and larger form deviations (of 8 µm) as in the worst-case analysis with smaller form deviations (of 4 µm).

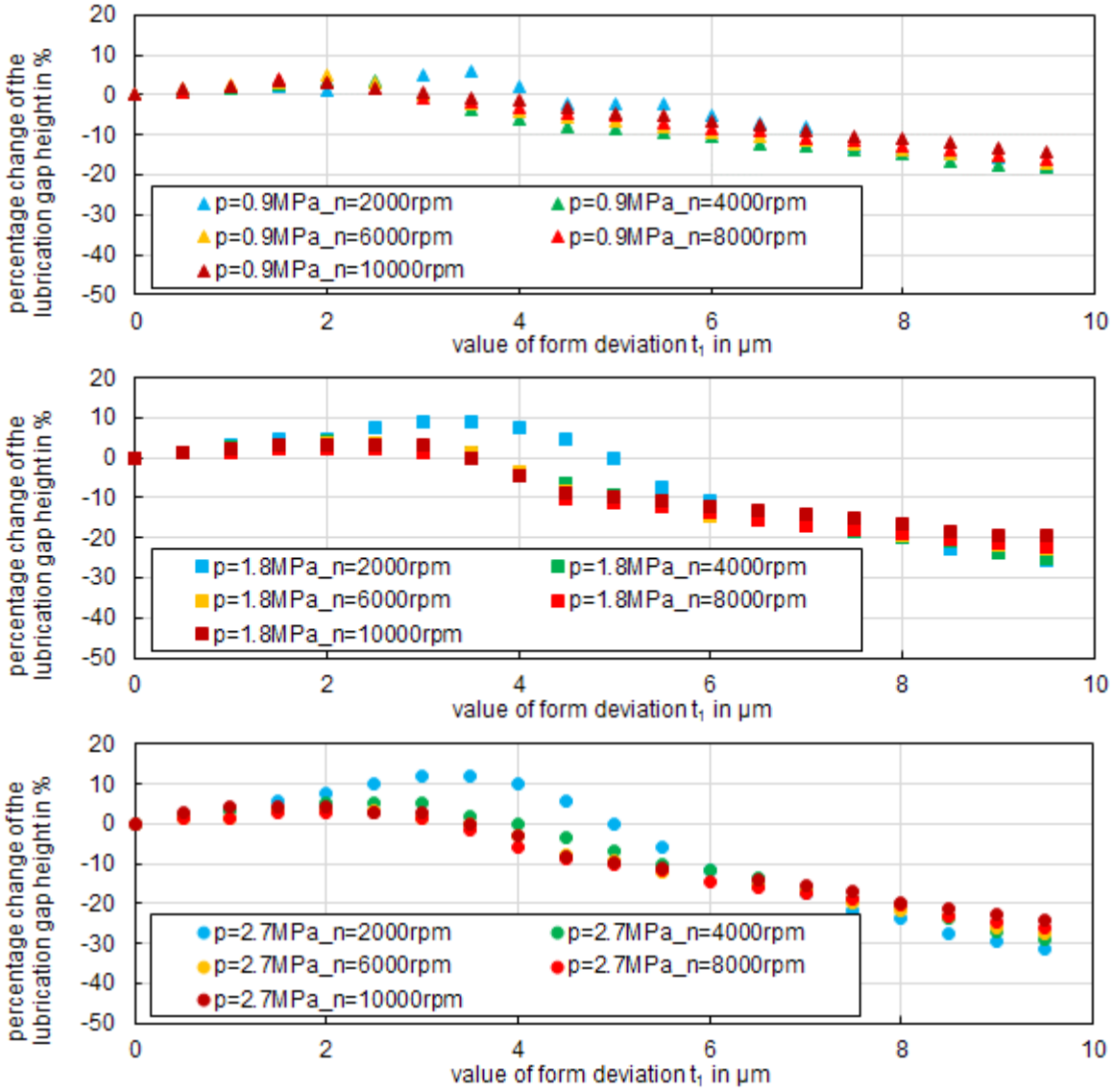

Figure 4: Minimum lubrication gap height of a three-sided-lobe bush at different form deviations in a best-case orientation scenario for a journal bearing with diameter d = 30 mm, wide-to-diameter ratio b/d = 0.5 and a relative bearing clearance of ψ = 2 ‰

4.3. Orientation analysis

The results of the worst-case and best-case analysis do not provide information about the orientation of the geometry. Therefore, Figure 5 shows the percentage changes of the lubrication gap height over the rotation angle φ for the three specific loads of p equal to 0.9 MPa, 1.8 MPa and 2.7 MPa for different form deviations t_1 at a speed n equal 2000 rpm each. Due to the amount of data, the load case with n equal 2000 rpm was chosen to be displayed in the diagram, as this case is the most critical due to the low rotational speed. In addition, only the form deviations of 0, 2, 4, 6 and 8 µm were displayed. The form deviation at 0 µm corresponds to the ideal cylindrical journal bearing.

It can be seen that with an installation angle of φ = 60° - 70° the greatest reduction of the lubricating gap height is achieved. This orientation therefore corresponds to the worst-case orientation. In this installation position, the lubricating gap height is significantly reduced and mixed friction is most likely to occur.

With a mounting position of φ = 30° - 50°, the smallest reduction in the lubricating gap height is shown with the form deviations of 6 to 8 µm. The installation area therefore shows the favorable conditions to ensure reliable operation at higher form deviation (6 to 8 µm). In this mounting position, the negative effect on the lubricating gap height can be reduced for higher form deviations.

With a form deviation of 2 to 4 µm, for this bearing geometry and the corresponding load, there is an improvement in the lubricating gap heights in a range from 0° - 10° and from 110° - 120°. The increase in the lubricating gap height is more noticeable with a higher bearing load. Even with higher form deviations (6 to 8 µm), the reduction of the minimum lubricating gap height is comparatively small in this angular range.

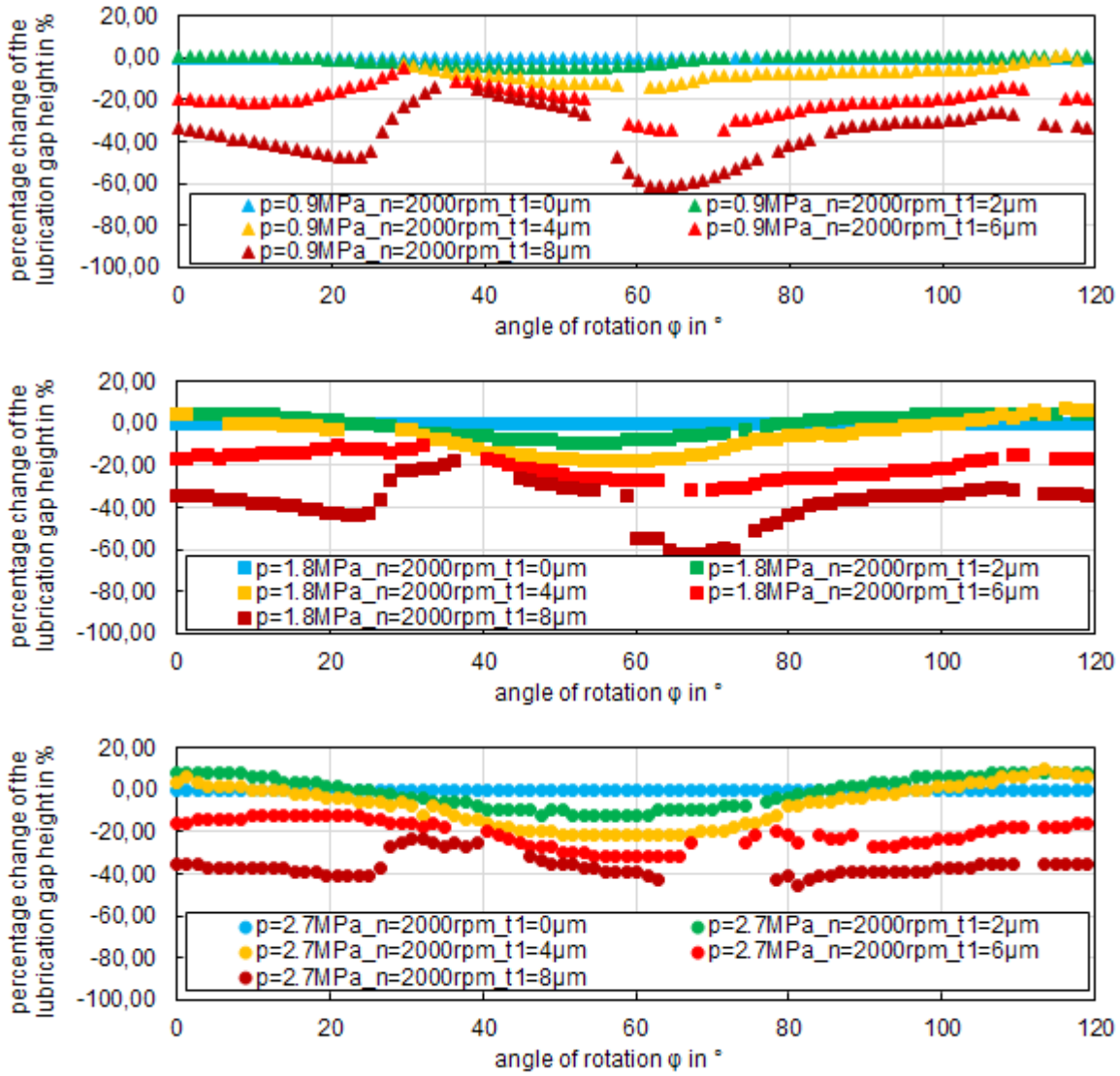

Figure 5: Minimum lubrication gap height of a three-sided-lobe bush at different form deviation values t_1 at different rotation angles φ or a journal bearing with diameter d= 30 mm, wide-to-diameter ratio b/d = 0.5 and a relative bearing clearance of ψ = 2 ‰

5. Conclusions

If the form deviation of the bearing and its orientation is not known, the worst operating condition must be assumed, in which the minimum lubrication gap height is reduced the most. However, if the form deviation is known, the negative influence on the lubricating gap height can be reduced due to its orientation during the mounting process. With a suitable dimension of the form deviation, the lubricating gap height can even be improved compared to circular cylindrical bearing geometries.

Depending on the operating point considered, a best-case analysis can increase the minimum lubricating gap height of the bearings observed by up to 10% with the same utilisation of the tolerance.

Furthermore, in certain load cases, the tolerances from ISO 12129-2 can be extended to 200% (from 4 µm to 8 µm) with a constant lubricating gap height by changing from a worst-case to a best-case installation position.

The following conclusions can be derived from the work:

- Form deviations influence the lubrication gap geometry, whether they have a negative or positive effect on the operating conditions cannot be generally stated;
- Without precise knowledge of the type of form deviation and without knowledge of how the form deviation is oriented in the installation, it must be assumed to be negative;
- For a roundness deviation in the form of a three-sided-lobe shape, an orientation can be selected which improves or only slightly reduces the lubrication gap height.

At this point, it must be made clear that the results only apply to bearings with a bearing diameter of 30 mm, which also have a pure form deviation of a three-sided lobe.

Further investigations must show how other form deviations affect the operating values, like elliptical or multi-lobe roundness deviations, which do not necessarily come from a three-jaw chuck.

In addition, the influences of straightness and parallelism form deviations must be investigated and to what extent the combination of different form deviations can change these operating values.

In further investigations the influence on the operating values temperature and pressure must also be considered.

With the exact knowledge of the form deviation on the running surface of the journal bearing, an orientation can be selected which provides optimal operating conditions.

With a specific geometry in the micrometer range, which cannot be assigned to any conventional geometry, the operating values of the journal bearing can be improved compared to a cylindrical bearing. For this reason it is assumed that for each operating condition the bearing geometry would have to be specifically adapted in order to achieve optimum operating results.

Acknowledgment

This paper was supported by FVA e.V.

References

[1] ISO 12129-2, Plain bearings - Tolerances on form and position and surface roughness for shafts, flanges and thrust collars, Genève/Switzerland: International Organization for Standardization, 2019-04.

[2] P. E. Allaire and R. D. Flack, “Design Of Journal Bearings For Rotating Machinery,” *Proceedings of the 10th Turbomachinery Symposium,* pp. 25-45, 1981.

[3] I. Sherrington and E. H. Smith, “The significance of surface topography in engineering,” *Precision Engineering,* vol. 8, no. 2, pp. 79-87, 1986.

[4] R.S.Srinivasan and K. Wood, “Geometric Tolerancing in Mechanical Design Using Fractal-Based Parameters,” *Journal of Mechanical Design,* vol. 117, pp. 203-206, 1995.

[5] K. Iwamoto and K. Tanaka, “Influence of Manufacturing Error of Roundness for Characteristics of Cylindrical Journal Bearing,” *Life Cycle Tribology,* vol. 48, pp. 751-754, 2005.

[6] S. Strzelecki, “ Operating Characteristics of Heavy Loaded Cylindrical Journal Bearing with variable axial Profile,” *Materials Research,* vol. 8, no. 4, pp. 481-486, 2005.

[7] M. Chernets, O. E. Andreikiv and V. V. Z. N. M. Lebedeva, “A Model for the Evaluation of wear and durability of a plain bearing with small out-of-roundness,” *Materials Science,* vol. 45, no. 2, pp. 279-290, 2009.

[8] M. Chernets and J. Chernets, “Generalized method for calculating the durability of sliding bearings with technological out-of-roundness of details,” *Journal of Engineering Tribology,* vol. 229, no. 2, pp. 216-226, 2015.

[9] D. Hargreaves, “Surface waviness effects on the load-carrying capacity of rectangular slider bearings,” *Wear,* vol. 145, pp. 137-151, 1991.

[10] H. E. Rasheed, “Effect of surface waviness on the hydrodynamic lubrication of a plain cylindrical sliding element bearing,” *Wear,* vol. 223, pp. 1-6, 1998.

[11] P. K. Goenka and J. F. Booker, “Effect of Surface Ellipticity on Dynamically Loaded Cylindrical Bearings,” *Journal of Lubrication Technology,* vol. 105, no. 1, pp. 1-9, 1983.

[12] M. Ebermann, B. Prase and E. Leidich, *Influence of geometric form deviations on operating parameters in hydrodynamic bearings,* Kaiserslautern: FVA Bearing World, 2018.

[13] M. Ebermann, B. Prase, E. Leidich and A. Hasse, “Entwicklung einer Toleranzauswahlmatrix unter Einbeziehung der Betriebseigenschaften zylindrischer hydrodynamischer Gleitlager - Abschlussbericht,” FVA - Eigenmittelvorhaben, Frankfurt am Main, 2018.

[14] M. Ebermann, B. Prase and A. Hasse, “Influence of Geometric Shape Defects on Operating Parameters in Cylindrical Journal Bearings,” in *Proceedings of the ASME 2019 International Mechanical Engineering Congress and Exposition*, Salt Lake City, 2019.

[15] DIN 23711-1: Shaft to collar connection - Polygon profil P3G - Part 1: Generalities and geometry,” Beuth, 2019.

Bearing Selection for High Efficiency Worm Gear Drives

Manuel Oehler [1], Michel Werner [2], Bernd Sauer [3]

[1] *Institute for Machine Elements, Gears, and Transmissions, Technische Universität Kaiserslautern, manuel.oehler@mv.uni-kl.de*

[2] *Institute for Machine Elements, Gears, and Transmissions, Technische Universität Kaiserslautern, michel.werner@mv.uni-kl.de*

[3] *Institute for Machine Elements, Gears, and Transmissions, Technische Universität Kaiserslautern, sauer@mv.uni-kl.de*

Abstract – In worm gearboxes, several machine elements cause different portions of the total power loss. Besides the load-dependent losses of the gears the losses of the bearings on the worm shaft contribute largely to the total power loss. Main reasons are high axial loads and high speeds compared to the worm wheel shaft due to commonly high gear ratios.

In this work, comparative studies are shown in which different bearing setups are applied to a worm gear drive. Example setups are tapered roller bearings or angular contact ball bearings in adjusted bearing arrangement as well as a locating/non-locating bearing arrangement using four-point contact bearing as locating bearing.

A tribological simulation software is used to calculate the load on the worm shaft bearings in axial and radial direction depending on the load situation of the gearbox (torques and speeds at the input and output shaft). Simulative studies show how different bearings perform under several conditions regarding rating life and power loss. Additionally, experimental tests are carried out to show the influence of bearing choice on the total efficiency of the gearbox. It is shown in both simulation and experiment that the use of angular contact ball bearings results in significant lower power losses compared to tapered roller bearings. However, compromises must be accepted regarding the bearing life. One aspect that is not considered in this work is the influence of the bearing selection on the worm shaft deflection under load, which also can play an important role.

Keywords – Efficiency, power loss, worm gears, bearing selection

1. Introduction

Compared to other types of gears, worm gears are characterized by the large gear ratios up to more than 100 that can be realized in one single stage, the simple design, the high overload capacity as well as a low-vibration and low-noise running behaviour [1]. Contrary to the widespread assumption that worm gears are associated with low efficiency, this efficiency has always been comparable to that of other types of gears at low transmission ratios [2]. Technological developments in manufacturing and lubricant technology over the last few decades have made it possible to achieve a large increase in efficiency at all ranges of transmission ratios, which can be seen, for example, in the elimination of fans and fins on gearbox housings. For example, considering gear ratios $i \leq 10$, overall efficiencies of up to $\eta_G = 97$ % can be achieved with worm gears [3]. Nevertheless, the efficiency of worm gearboxes can be increased even further through targeted optimization. The selection of a suitable bearing arrangement concept can make an important contribution to increasing the efficiency of the gearbox.

Here it is purposeful to focus on the bearings of the worm shaft, since comparatively high speeds are present here and high axial forces must be absorbed from the tooth contact. In contrast, the worm gear bearing arrangement mainly absorbs radial forces at significantly lower speeds, depending on the transmission ratio. High axial loads lead to a relatively large amount of sliding friction in the bearing of the worm shaft, where tapered roller bearings (sliding friction in roller end–flange contacts) or angular contact bearings (spinning friction) are commonly used. Accordingly, a large part of the bearing power loss occurs at the position of the worm shaft, whereas the worm wheel bearings make only a small contribution to this.

Investigations into the reduction of gearbox power losses by adapting the bearing arrangement concept have already been shown for various types of gearboxes. Specific measures, such as the use of angular contact ball bearings instead of tapered roller bearings, can increase the gear efficiency in spur gear units [4] and car rear axle gears [5]. Worm gears place different demands on the bearing arrangement than, for example, spur gears, which is why this paper shows how a systematic consideration of bearing power loss and bearing service life can be used to select the most efficient concept for the bearing arrangement of the worm shaft.

2. State of the art

Numerous works by various authors are available on the design and layout of worm gearboxes. In [6], an overview of the design of worms and worm gears with the aspects material selection, manufacturing and efficiency is given. Another comprehensive work on the calculation, design and manufacture of worm gears is [7]. In [8], the design of the gearing is discussed as well as the housing design and the measurement of gearing deviations. Examples and

notes on possible bearing arrangement concepts are described in [9].

A standardized calculation method for determining the friction in the tooth contact of worm gears is described in DIN 3996 [10]. It also contains a method for the general calculation of forces in tooth contact. Standards at the international level are for example [11] and [12]. There, equations are given for efficiency and for the thermal capacity of gearboxes. Tables for selection of gearing geometries as well as calculation rules and examples of load capacity are shown in [13]. In [14] a calculation method for the efficiency of worm gears is included, which is based on empirically determined, speed-dependent coefficients of friction. A comparison of the various standardized calculation methods for efficiency calculation is shown in [15] using worm gears with centre distances of 50 and 150 mm. It becomes obvious that there are very big differences between the different standardized calculation methods as well as between standard and experiment.

Basic works for the computational determination of the efficiency of worm gears are for example [16], [17] and [18].

In [19] experiments on the influence of the lubricant on wear and efficiency are shown and empirical equations for the determination of bearing losses are described. In [20] the load-dependent and load-independent losses of different components in worm gears are determined by means of tests. On the basis of these tests, approximate formulas are derived for the power loss of the bearing at the worm shaft, among other things. The determination of the bearing forces from the gearing forces using the basic rules of engineering mechanics is shown in [21].

3. Power losses in worm gearboxes

In worm gears, losses are caused by the gear teeth, the bearings and the rotating shaft seals. Since there are no clutches or other additional components in common worm gearboxes, other losses can be ignored. According to ISO TR 14179-2 [11], these losses can be divided into load-independent (0) and load-dependent (P).

$$P_V = P_{VZ,0} + P_{VZ,P} + P_{VL,0} + P_{VL,P} + P_{VD} + P_{VX} \quad \textit{(Eq. 1)}$$

In Eq. 1, the index "Z" stands for gearing, "L" for bearing, "D" for seals and "X" for other loss sources.

Under nominal load, the load-dependent losses of the gears $P_{VZ,P}$ are usually responsible for a large part of the losses. However, bearing losses P_{VL} can also contribute significantly to the total losses P_V. In partial load operation, their share can even be greater than that of the gears. The bearings on the worm shaft play a much greater role than the bearings on the worm wheel shaft due to the higher rotational speed and large axial load [20, 22]. The bearing losses in operation can be considerably reduced by a specific design of the worm bearing, thus improving the efficiency of the gearbox.

4. Bearing setups used in worm gearboxes

For the bearing arrangement of the worm shaft, mostly adjusted bearings in X-arrangement or locating/non-locating bearing combinations are used [23]. Since the worm shaft bearings absorb the high axial forces from the gears, tapered roller bearings or angular contact ball bearings are used. Radial loads dominate at the bearing of the worm wheel shaft, which is why deep groove ball bearings are often used here. In the case of bearings of the worm shaft, the most important selection criteria with regard to function are, in addition to power loss, the stiffness of the bearing arrangement and the bearing life.

Notes on the functional selection of bearing arrangements in worm gearboxes can be found in [24], for example.

5. Theoretical studies on various bearing setups

In order to be able to assess various bearing arrangement concepts from the point of view of efficiency, a comprehensive study was carried out. For this purpose, a calculation program was set up which, in addition to calculating the bearing power loss P_{VL} according to the SKF model [25], also allows the modified rating life L_{10mh} of the bearings to be determined according to DIN ISO 281 [26].

The methodology for calculating the bearing power loss and bearing life is described in [22]. With the help of a physical model, the local normal and frictional forces in the tooth contact of worm gears can be calculated. These depend, among other things, on the external load, the gear geometry, the surfaces of the gear teeth and the lubricant used. The bearing forces can be determined from the tooth contact forces, which in turn serve as input values for the bearing power loss and bearing life calculation.

The method for determining the bearing forces by integrating the local forces in tooth contact over all contact lines currently in engagement is described in [27] and [22]. Since the meshing situation and the position of the contact lines of worm gears changes periodically, the bearing forces also fluctuate periodically. For the studies on bearing life and power loss, the bearing forces averaged over all meshing positions were used.

Thus it is possible to evaluate these two target values for different bearing configurations for any worm gearbox under defined conditions.

Fig. 1 illustrates the process of the calculation method from the tribological simulation of the tooth contact to determination of bearing power loss and rating life.

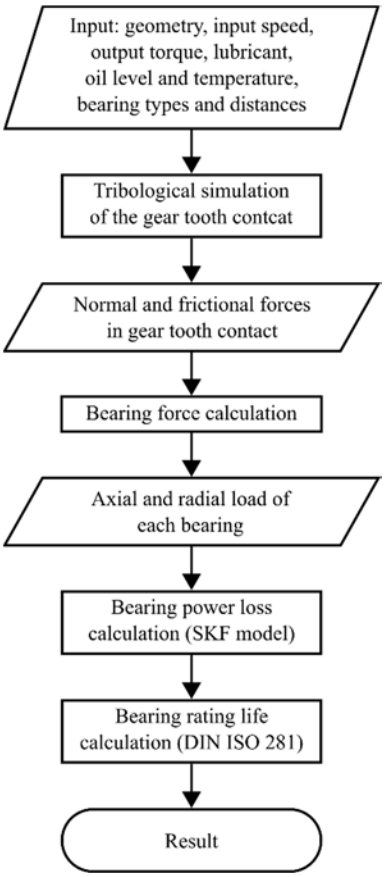

Figure 1: Flow chart to illustrate the process of calculating bearing power losses and rating life

5.1. Gearbox with centre distance 100 mm

Fig. 2 shows the calculated power losses P_V caused by the two bearings of the worm shaft, for different concepts. The following were investigated for a worm gear with centre distance $a = 100$ mm and gear ratio $i = 20$: tapered roller bearings with the designations 31307, 31308, 32207 and 32208 as well as angular contact ball bearings with the designations 7307 and 7308 as adjusted bearings in X-arrangement. Four-point contact bearings with the designations QJ 307 and QJ 308 together with deep groove ball bearings of the type 6307 or 6308 respectively were investigated as locating/non-locating bearing combinations. In addition, the combinations of axial cylindrical roller bearings with the designations 81107 TN, 81108 TN, 81207 TN and 81208 TN with deep groove ball bearings of the type 6307 or 6308 were examined. The light grey bars show the power loss $P_{VL,12}$ of the axially loaded bearing. The dark grey bars show the power loss $P_{VL,11}$ of the axially unloaded bearing. The height of the bars in the diagram therefore shows the total power loss that occurs at the bearings of the worm shaft. The boundary conditions for the calculation were an output torque of $T_{out} = 700$ Nm, an input speed of $n_{in} = 1400$ min^{-1} and an oil sump temperature of $\vartheta_S = 80$ °C when lubricated with a polyglycol oil of viscosity class ISO VG 460.

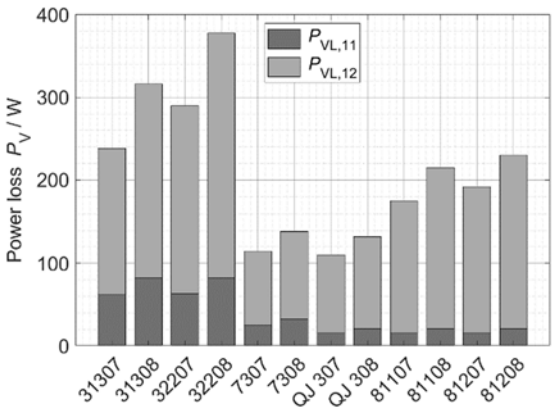

Figure 2: Sum of the calculated bearing power loss P_{VL} of both bearings of the worm shaft and distribution of the losses to the bearings L_{11} (no axial load) and L_{12} (carries axial load) for different bearing arrangement concepts on a worm gear with centre distance a = 100 mm and gear ratio i = 20 operating at an output torque of T_{out} = 700 Nm, an input speed of n_{in} = 1400 min^{-1} and an oil sump temperature of ϑ_S = 80 °C lubricated with a polyglycol oil of viscosity class ISO VG 460 at 80 °C

The evaluation of the power loss calculation shows that the adjusted bearing arrangement with angular contact ball bearings and the locating/non-locating bearing combination with four-point contact bearings are the most efficient variants. In comparison, the use of axial cylindrical roller bearings has higher power losses. Angular contact tapered roller bearing arrangements sometimes result in approximately twice as high losses as those using angular contact ball bearings of the same bore number. Tapered roller bearings of series 313 differ from bearings of series 322 by a larger outer diameter as well as a significantly larger contact angle and show a more favourable behaviour than those with regard to power loss.

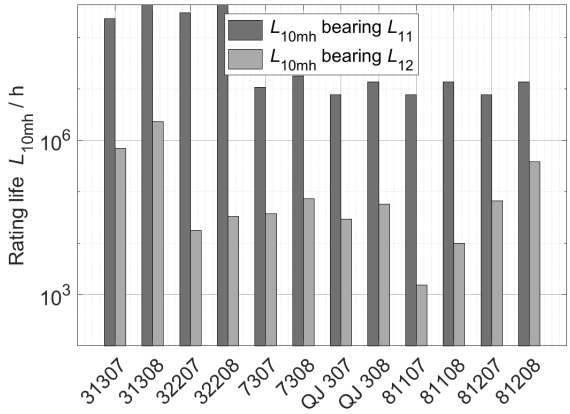

Figure 3: Modified bearing life of both bearings of the worm shaft (L_{11} carries no axial load, L_{12} carries all axial load) for different bearing arrangement concepts on a worm gear with centre distance a = 100 mm and gear ratio i = 20 operating at an output torque of T_{out} = 700 Nm, an input speed of n_{in} = 1400 min^{-1} and an oil sump temperature of

ϑ_S = 80 °C lubricated with a polyglycol oil of viscosity class ISO VG 460 at 80 °C

Fig. 3 shows the modified bearing life L_{10mh} for the bearing arrangement concepts described. According to [26], a contamination coefficient of e_C = 0.5 was assumed for the calculation. A comparison of the modified bearing life L_{10mh} for the axially loaded worm bearing shows that tapered roller bearings of series 313 achieve significantly higher values than the variants with angular contact ball bearings or four-point contact bearings. In the context of power loss, it is evident that the most efficient solutions do not achieve the longest life of all concepts, but the values are still at L_{10mh} > 10,000 h. The use of separate axial and radial bearings in the form of axial cylindrical roller bearings and deep groove ball bearings is neither the best solution from the point of view of service life nor efficiency. In all variants, it has been shown that the selection of a smaller bore number has a positive effect on losses. This effect is particularly clear in the case of tapered roller bearing 313. On the other hand, the modified rating life also decreases with the reduction of the bearing size. Compared with series 322, tapered roller bearings of series 313 have a higher axial load carrying capacity due to the higher contact angle, which is also reflected in the increased rating life.

5.2. Gearbox with centre distance 40 mm

In addition to the gearbox with 100 mm centre distance, a comparatively small gearbox and a large gearbox with identical gear ratio were simulated.

In the following, the results of the simulative study on bearing losses and rating life for a worm gearbox with centre distance a = 40 mm and gear ratio i = 20 are presented.

Tapered roller bearings with the designations 30302 and 30303 as well as angular contact ball bearings with the designations 7302 and 7303 were used as adjusted bearings in X-arrangement. Four-point contact bearings with the designations QJ 202 and QJ 303 together with deep groove ball bearings of the type 6302 or 6303 were investigated as locating and non-locating bearing arrangements. Further combinations of locating/non-locating bearing arrangements, which appear to be particularly useful for smaller gearboxes, are the use of deep groove ball bearings both as locating and non-locating bearings, which was simulated with bearings of types 6303 and 6304. In addition, the combinations of radial cylindrical roller bearings with the designations NU 303 or NU 304 as floating bearings and deep groove ball bearings of types 6303 and 6304 as locating bearings were considered. For the worm gear, deep groove ball bearings of type 6206 were always used as adjusted bearings in X-arrangement.

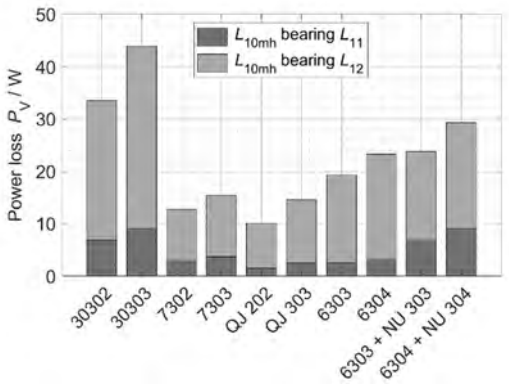

Figure 4: Sum of the calculated bearing power loss P_{VL} of both bearings of the worm shaft and distribution of the losses to the bearings L_{11} (no axial load) and L_{12} (carries axial load) for different bearing arrangement concepts on a worm gear with centre distance a = 40 mm and gear ratio i = 20 operating at an output torque of T_{out} = 50 Nm, an input speed of n_{in} = 1400 min^{-1} and an oil sump temperature of ϑ_S = 80 °C lubricated with a polyglycol oil of viscosity class ISO VG 460 at 80 °C

Fig. 4 and Fig. 5 show the calculated power losses P_V, which occur at the worm shaft bearing, and their respective service life for different concepts. The basis for the calculation is the gearing with centre distance a = 40 mm and a transmission ratio of i = 20. The light grey bars show the power loss $P_{VL,12}$ of the axially loaded bearing. The dark grey bars show the power loss $P_{VL,11}$ of the axially unloaded bearing. The height of the bars in the diagram therefore shows the total power loss that occurs at the bearings of the worm shaft. The boundary conditions for the calculation were an output torque of T_2 = 50 Nm, an input speed of n_1 = 1400 min^{-1} and an oil sump temperature of ϑ_S = 80 °C when lubricated with a polyglycol of viscosity class ISO VG 460.

The evaluation of the power loss calculation shows that the adjusted bearing arrangement with angular contact ball bearings and the fixed/loose bearing arrangement with four-point bearings are the most efficient variants. The variants with tapered roller bearings lead to the largest bearing power losses (see Fig. 4) and both show lower rating life than angular contact ball bearings (see Fig. 5). In this case no recommendation can be made for them. By using identical deep groove ball bearings as locating and non-locating bearings, it is not possible to achieve the lowest power loss values in comparison, but this is the most cost-effective variant. The use of a radial cylindrical roller bearing as a non-locating bearing has no advantages in terms of losses or service life compared to a deep groove ball bearing.

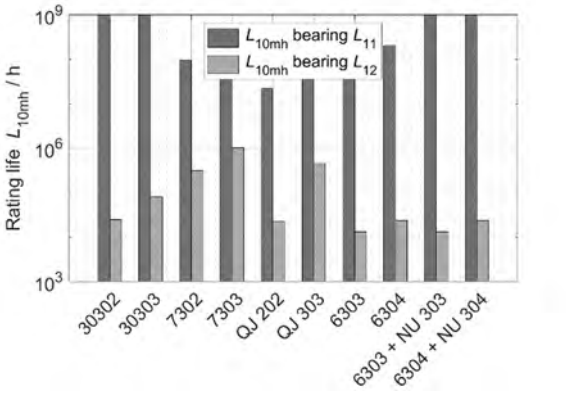

Figure 5: Modified bearing life of both bearings of the worm shaft (L_{11} carries no axial load, L_{12} carries all axial load) for different bearing arrangement concepts on a worm gear with centre distance a = 40 mm and gear ratio i = 20 operating at an output torque of T_{out} = 50 Nm, an input speed of n_{in} = 1400 min^{-1} and an oil sump temperature of ϑ_S = 80 °C lubricated with a polyglycol oil of viscosity class ISO VG 460 at 80 °C

5.3. Gearbox with centre distance 315 mm

In addition to the gearboxes with centre distances of 40 and 100 mm respectively, a gearbox with a centre distance of a = 315 mm and a gear ratio of 20 was selected as an example for a large worm gear. The bearing configurations considered here essentially correspond to the variants that were investigated for centre distance a = 100 mm. Only the bearing size was adapted to the changed shaft geometry and the much higher load.

The boundary conditions for the calculation were an output torque of T_2 = 10,000 Nm, an input speed of n_1 = 1400 min^{-1} and an oil sump temperature of ϑ_S = 80 °C when lubricated with a polyglycol of viscosity class ISO VG 460.

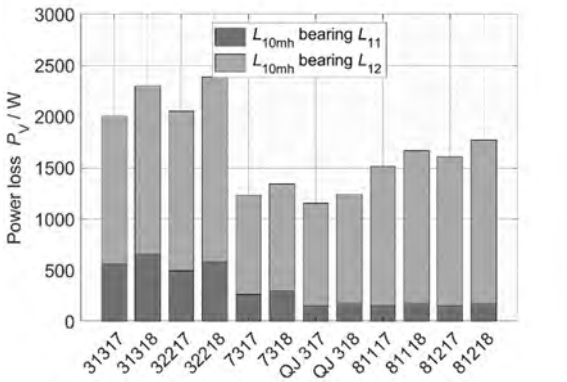

Figure 6: Sum of the calculated bearing power loss P_{VL} of both bearings of the worm shaft and distribution of the losses to the bearings L_{11} (no axial load) and L_{12} (carries axial load) for different bearing arrangement concepts on a worm gear with centre distance a = 315 mm and gear ratio i = 20 operating at an output torque of T_{out} = 10,000 Nm, an input speed of n_{in} = 1400 min^{-1} and an oil sump temperature of ϑ_S = 80 °C lubricated with a polyglycol oil of viscosity class ISO VG 460 at 80 °C

The evaluation of the power loss calculation (see Fig. 6) shows that the adjusted bearing arrangement with angular contact ball bearings and the fixed/loose bearing arrangement with four-point contact bearings are the most efficient variants. Although the variants with tapered roller bearings of series 313 have high power losses, they are also characterized by a long operating life (see Fig. 7). The locating/non-locating bearing arrangement with a type 81218 TN axial cylindrical roller bearing to support the axial force is also a sensible variant. This results in lower losses than with tapered roller bearings, while at the same time ensuring a long operating life.

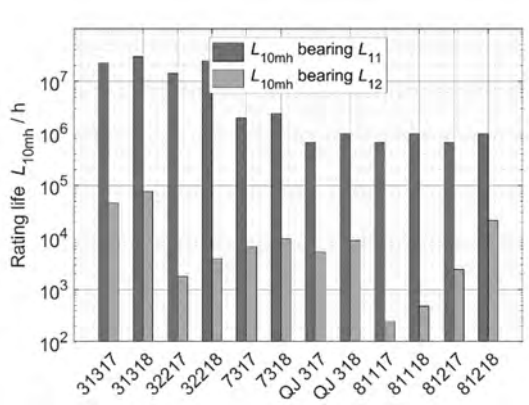

Figure 7: Modified bearing life of both bearings of the worm shaft (L_{11} carries no axial load, L_{12} carries all axial load) for different bearing arrangement concepts on a worm gear with centre distance a = 315 mm and gear ratio i = 20 operating at an output torque of T_{out} = 10,000 Nm, an input speed of n_{in} = 1400 min^{-1} and an oil sump temperature of ϑ_S = 80 °C lubricated with a polyglycol oil of viscosity class ISO VG 460 at 80 °C

6. Experimental setup

6.1. Test bench

In addition to theoretical investigations on the power loss of various bearings in worm gears, extensive experiments were also carried out.

The test bench used is based on two asynchronous machines with a maximum power of 30 kW. The motors are controlled in the electric back-to-back operation in such a way that a speed is specified at the drive motor and a torque is specified at the output motor, which is operated as a generator. The electrical current generated by the output motor in generator operation is fed back into the circuit. The test bench set-up for the investigation of worm gearboxes with a centre distance of a = 100 mm is shown in Fig. 8.

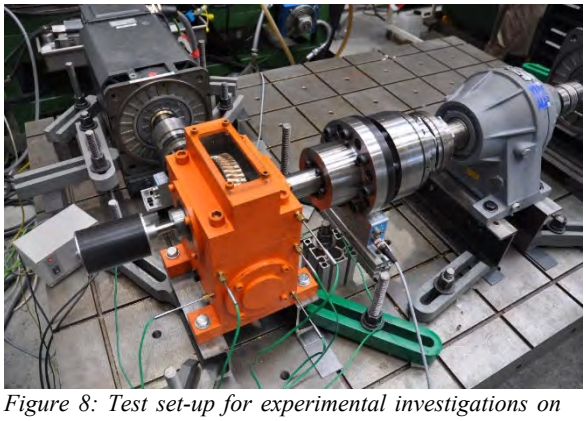

Figure 8: Test set-up for experimental investigations on worm gears with centre distance a = 100 mm and variable bearing concept for the worm shaft

The connections between the driving machine and the worm shaft of the test gearbox and between the reverse transfer gearbox and the braking motor are made by means of metal bellows couplings. A planetary gearbox with a transmission ratio of i = 26.4 is used as a reverse transfer gearbox. This gear has the task of reducing the torque at the output of the test gear in order to avoid exceeding the maximum braking torque of the braking motor. At the input of the test gearbox, the torque T_{in} and speed n_{in} are measured by a non-contact speed and torque measuring system. At the output of the test gear, the torque T_{out} and speed n_{out} are determined with a second torque measuring hub. The overall power loss P_V and the efficiency of the entire gearbox η_G are determined on the basis of these quantities. This is shown in Eq. 2 and 3.

$$P_V = T_{in} \cdot n_{in} - |T_{out} \cdot n_{out}| \qquad \textit{(Eq. 2)}$$

$$\eta_G = (|T_{out} \cdot n_{out}|)/(T_{in} \cdot n_{in}) \qquad \textit{(Eq. 3)}$$

The nominal torque of the input torque measurement system is 200 Nm with an accuracy of 0.05 %. At the output side of the gearbox, a measurement system with a nominal torque of 5,000 Nm and also an accuracy of 0.05 % is installed.

In addition to the rotational speed and torque, the temperature in the oil sump and the mass temperature of the rotating worm gear are measured, which is transmitted by telemetry via a Bluetooth transmitter and receiver.

6.2. Housing of the test gearbox

A housing with a variable bearing concept for the worm shaft was developed to investigate different variants with regard to bearing design and size. Using sleeves with different internal geometries, it is thus possible to realize both adjusted bearing arrangements and a locating/non-locating bearing arrangement with one and the same housing. In addition, the bearing outer diameter can also be selected within reasonable limits. A section display of the housing is shown in Fig. 9.

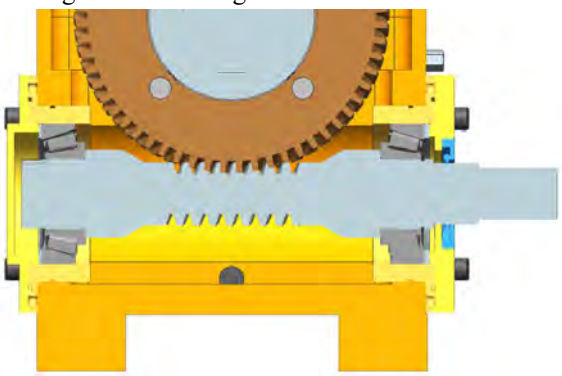

Figure 9: Section display of the housing with a variable bearing concept for the worm shaft and worm gears with centre distance a = 100 mm

- **Test gears**

The geometry of the test gears used in this study is presented in Table 1. The worm was made of case-hardened steel 16MnCr5 (AISI 5115). The worm gear was cut by a fly cutter and was made of bronze CuSn12Ni2-C (UNS C91700). The gears can be described as milled helicoid type, which is defined as flank form ZK according to DIN 3975-1 [28].

Table 1: Geometry of the test gears

Parameter	Symbol	Unit	Value
Centre distance	a	[mm]	100
Nominal gear ratio	i_N	[-]	20
No. of teeth (worm)	z_1	[-]	3
No. of teeth (worm gear)	z_2	[-]	60
Axial module	m	[mm]	2.99
Diameter factor	q	[-]	10.0
Lead angle	γ_m	[-]	16.7
Pressure angle	α_0	[-]	16.5
Addendum modification factor	x_2	[-]	-1.5
Flank form	-	[-]	ZK

- **Lubricants and lubrication used in test**

Two polyalkylene glycol-(PAG) based oils were used as lubricants in this study. These are two high performance gear oils with the product designation "Klübersynth GH-6" and viscosity grades 150 and 460. Table 2 shows an extract from the data sheet of the lubricants.

Table 2: Data of the test lubricants

Parameter	Unit	PG 150	PG 460
Base oil		PAG	PAG
Classification acc. to ISO 12925-1		CKC 150	CKC 460
Viscosity grade	ISO VG	150	460
Kinem. viscosity at 40°C	[mm²/s]	150	460
Kinem. viscosity at 100°C	[mm²/s]	29	71
Density at 15°C	[kg/m³]	1050	1074

The lubrication type used in the tests was oil bath lubrication, whereby the oil level was always at the level of the worm axis. The sump temperature was achieved by heating up as uniformly as possible with the aid of the power loss at a defined operating point. No external heat source or cooling was used.

6.3. Bearing arrangement concepts used in tests

Different bearing arrangements were investigated during the test in this study. In Table 3, the different combinations of bearings at both sides of the worm shaft are shown. It is important to say that only one bearing has to carry all the axial load resulting of the forces in the tooth contact. It depends on the rotational direction of the worm shaft, which bearing is axially loaded and which one is not.

Table 2: Bearing setups at the worm shaft used in tests

Bearing arrangement	Bearing type location 1 (no axial load)	Bearing type location 2 (carries all axial load)
X-arrangement	Tapered roller bearing 32208	Tapered roller bearing 32208
X-arrangement	Tapered roller bearing 31308	Tapered roller bearing 31308
X-arrangement	Angular contact ball bearing 7308	Angular contact ball bearing 7308
Locating/non-locating bearing	Deep groove ball bearing 6308	Four-point contact bearing QJ308

7. Results of experimental investigations

In order to evaluate the influence of different bearing arrangement concepts on the gear efficiency, measurements were carried out at five operating points. The operating points ranged in output torques from 175 Nm over 350 Nm up to 700 Nm. The rotational speed on the input side was adjusted between 700 rpm and 1400 rpm. In addition, the operating temperature ϑ_S and the gear oil were varied. The bearing arrangement concepts used are three adjusted bearing arrangements in X-arrangement and one locating/non-locating bearing arrangement (see Table 3). The following Fig. 10 shows the overall efficiency of the gearbox using different bearing arrangement concepts at the respective operating points, using Klübersynth GH6-150, at an operating temperature of ϑ_S = 60 °C. It can be seen that the two tapered roller bearings lead to a lower efficiency at all operating points than the angular contact ball bearing and the locating/non-locating bearing arrangement, whereby the tapered roller bearing of type 32208 has the lowest value at the operating point n_{in} = 700 min^{-1} and T_{out} = 175 Nm with an efficiency of η_G = 79.5 %. The highest efficiency of η_G = 89.0 % is achieved by the locating/non-locating bearing arrangement at the rated torque of T_{out} = 700 Nm and the speed n_{in} = 1400 min^{-1}.

It can generally be seen that the efficiency increases with increasing speed and increasing load torque, whereby a deviation in the load causes the greatest change. This dependency of the efficiency on load and speed is more pronounced in tapered roller bearings, especially those of type 32208, than in the other two bearing arrangement concepts, with the angular contact ball bearing showing the lowest dependency. For example, the difference between the best and worst efficiency of the tapered roller bearing of type 32208 is 7.6 %, whereas it is only 4.4 % with the angular contact ball bearing.

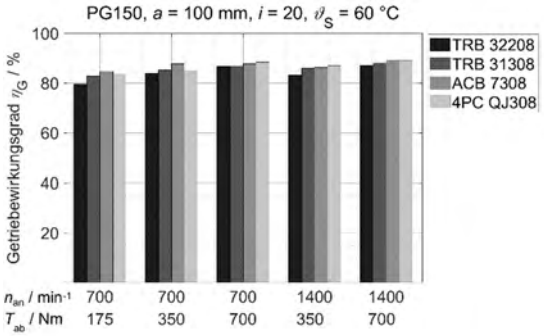

Figure 10: Measured gearbox efficiency η_G for the worm gear with vibratory ground teeth when varying the bearing concepts, with a = 100 mm and i = 20 when lubricated with polyglycol of viscosity class ISO VG 150 at ϑ_S = 60 °C

Fig. 11 shows a comparison of gear efficiency at different operating points at a temperature of ϑ_S = 60 °C, using the high viscosity gear oil Klübersynth GH6-460. The use of an oil with a higher viscosity class leads to slightly higher maximum efficiencies at high loads but also to lower minimum efficiencies at low-load conditions. The lowest efficiency was also achieved here with the tapered roller bearing 32208 at the operating point n_{in} = 700 min^{-1} and T_{out} = 175 Nm. With η_G = 70.9 %, this is almost 20 % below the highest efficiency of η_G = 89.7 %, which was achieved both by the locating/non-locating bearing arrangement and the angular contact ball bearing at the operating point n_{in} = 1400 min^{-1} and T_{out} = 700 Nm which is the nominal load of the gears. As in the previous figure, a strong dependence of the efficiency on torque and speed can be seen. Again, the bearing arrangement concepts with tapered roller bearings are more susceptible to deviations from the nominal torque than the other two bearing arrangement concepts.

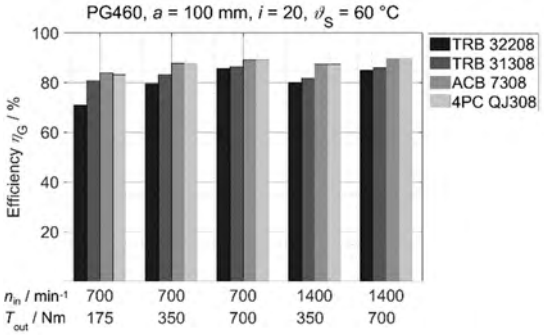

Figure 11: Measured gearbox efficiency η_G for the worm gear with vibratory ground teeth when varying the bearing concepts, with a = 100 mm and i = 20 when lubricated with polyglycol of viscosity class ISO VG 460 at ϑ_S = 80 °C

The difference in efficiency of 14.9 % for tapered roller bearings of type 32208 shows a dependence on the torque (between high and low-load conditions) almost twice as high as in the previous test arrangement. The efficiency difference of the angular contact ball bearing, which was most insensitive to deviations from the nominal torque in the previous test, also increased to 5.8 %.

In Fig. 12, the gear efficiency is shown, analogous to the previous illustrations, when using four different bearing arrangement concepts. The same test gears, again lubricated with Klübersynth GH6-150 at an increased operating temperature of ϑ_S = 80 °C are used.

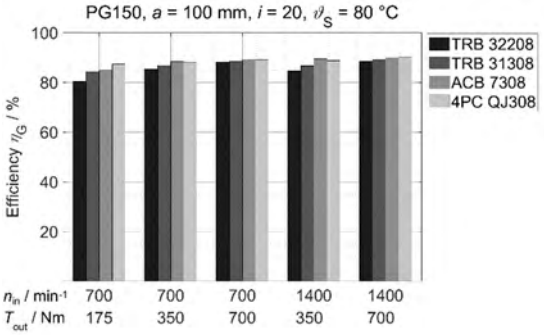

Figure 12: Measured gearbox efficiency η_G for the worm gear with vibratory ground teeth when varying the bearing concepts, with a = 100 mm and i = 20 when lubricated with polyglycol of viscosity class ISO VG 150 at ϑ_S = 80 °C

While the maximum efficiency with η_G = 89.9 % is slightly above that of the test with an operating temperature of ϑ_S = 60 °C, the minimum efficiency with η_G = 76.5 % is significantly worse in this test. Here again, the maximum efficiency was achieved with the angular contact ball bearing, with the taper roller bearing of type 32208 again showing the worst efficiency. However, the dependence of the efficiency on a deviation from the nominal torque is also apparent here and is more pronounced in tapered roller bearings than in the other two bearing arrangement concepts.

Fig. 13 shows a comparison of the efficiencies achieved when using four different bearing arrangement concepts. Again, the same test gears are used and lubrication with Klübersynth GH6-460 at an operating temperature of ϑ_S = 80 °C is applied.

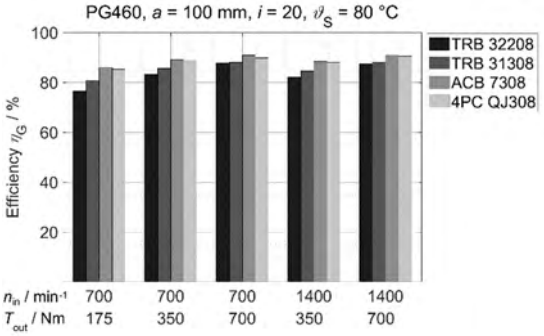

Figure 13: Measured gearbox efficiency η_G for the worm gear with vibratory ground teeth when varying the bearing concepts, with a = 100 mm and i = 20 when lubricated with polyglycol of viscosity class ISO VG 460 at ϑ_S = 80 °C

It can be seen that the gearbox efficiency η_G decreases when the output torque is decreased. The use of tapered roller bearings, in particular bearings of type 32208, results in a greater loss of efficiency than the use of the other two bearing arrangement concepts. In addition, the measured gear efficiency at the operating points with nominal torque in bearings with tapered roller bearings is between 1.6 and

3.4 % below the efficiency that can be achieved with a locating/non-locating bearing arrangement or a bearing arrangement with angular contact ball bearings. The efficiency of these two bearing arrangement concepts is similarly good, although slightly better results can be achieved with the use of angular contact ball bearings than with the locating/non-locating bearing arrangement. At the operating point with nominal torque, the efficiency of the gearbox with locating/non-locating bearing arrangement is between η_G = 89.8 % at a speed of n_{in} = 700 min^{-1} and η_G = 90.5 % at a speed of n_{in} = 1400 min^{-1}.

The use of angular contact ball bearings of type 7308 in an adjusted bearing arrangement in X-arrangement allows overall efficiencies at nominal torque of η_G = 90.9 % at a speed of n_{in} = 700 min^{-1} up to an efficiency of η_G = 91.0 % at a speed of n_{in} = 1400 min^{-1}. A comparison of the efficiencies achieved in this test with those of the test at an operating temperature of ϑ_S = 60 °C shows that the higher operating temperature results in an improvement in efficiency at all operating points. Thus, the maximum efficiency in relation to the test at lower temperature has increased by more than 1 %. The comparison of the different bearing concepts shows that by optimizing the bearing concept within a gearing configuration, an advantage in overall efficiency of up to 3.4 % at the operating point with nominal torque can be achieved. In areas below the nominal torque at n_{in} = 700 min^{-1} and T_{out} = 175 Nm, this advantage even increases to up to 15 % if the initial bearing arrangement with tapered roller bearings of type 32208 is compared with the bearing arrangement with angular contact ball bearings of type 7308. Overall, the differences between the bearing arrangement concepts are smaller if viscosity class ISO VG 150 is used instead of viscosity class ISO VG 460.

8. Summary of the test results

In summary, it can be stated that in all investigations the highest gearbox efficiencies were measured under operating conditions with high output torque. The reason for this is that under these conditions the load-independent losses contribute less to the total losses. This applies to both gear wheels and rolling bearings. Especially in the case of roller bearings, the load-independent losses are relatively high, which is why there are also significantly lower efficiencies in the partial load range compared to operating points under full load. The load-independent losses in oil-lubricated bearings are mainly due to hydraulic losses, which is why lower losses occur at lower lubricant viscosity. This can be achieved either by a higher temperature or a lower viscosity class of the oil.

Under high load, it can be seen that a lubricant with higher viscosity offers advantages in terms of efficiency. This can be explained by the load-dependent losses, which at high output torque are mainly caused by friction in the tooth contact. A higher lubricant viscosity leads here to an increased lubricating gap height. Since worm gear units are always operated locally in the mixed friction area, the number of solid contacts at the roughness peaks is reduced, which in turn reduces the total number of tooth friction.

The effects described above overlap at all operating points investigated, since load-dependent and load-independent losses always occur simultaneously. Depending on the operating point, an optimum for the lubricant viscosity can be determined. Depending on the bearing arrangement, this optimum for roller bearings is at a lower viscosity than for ball bearings, as the experimental results (see chapter 7) show.

The experimental investigations show that selecting an oil viscosity for a worm gearbox can be a conflict between choosing an optimum regarding the bearings on the worm shaft and the tooth contact. The latter rather requires a higher viscosity - especially at high loads -whereas the optimum for the bearings is lower viscosities. A calculation of the lubrication conditions of the worm shaft bearings during the tests shows that the viscosity ratio κ changes significantly depending on the operating conditions applied in the tests. At the operating point with input speed of n_{in} = 700 min^{-1}, viscosity class ISO VG 150 and an operating temperature of ϑ_S = 80 °C the calculated viscosity ratio κ was between 1.5 and 1.7 for all bearings at the worm shaft. At the operating point with best conditions for hydrodynamic lubrication (input speed of n_{in} = 1400 min^{-1}, viscosity class ISO VG 460 and an operating temperature of ϑ_S = 60 °C) the viscosity ratio κ was above 12 for all bearings at the worm shaft. This means, that for the present test gearbox, even at bad lubrication conditions regarding the tooth contact, the bearings at the worm shaft should be lubricated properly. In contrast, when very good lubrication conditions regarding the tooth contact are applied, the bearings are supplied with oil of much higher viscosity than needed and thus produce a high amount of load-independent losses.

All in all, under all the conditions investigated, higher efficiencies can be achieved with ball bearings than with roller bearings. It could be shown that tapered roller bearings of series 313 are better suited than those of series 322 for the application in the worm gear examined. This is due to the larger contact angle that characterizes bearings of series 313. For large axial loads, as caused by the tooth forces in contact with worm gears, bearings with a large contact angle are more suitable than bearings with a small contact angle.

A comparison of the two investigated bearing variants with ball bearings shows that the variant with angular contact ball bearings as an adjusted bearing

arrangement in X-arrangement offers slight advantages in terms of efficiency compared with the locating/non-locating bearing arrangement with a four-point contact bearing as the locating bearing. However, the differences are very small.

A direct comparison between experiment and simulation was not carried out in this case, since the calculation method focusses only on the bearing power losses and the test results show the power loss of the whole gearbox. Nevertheless, all conclusions from the calculation of bearing power losses carried out for the gearbox with centre distance of 100 mm and gear ratio of 20 can be found in the experimental results. Simulation and tests both show that bearing arrangements using angular or four-point contact ball bearings lead to comparable values for the bearing power loss. Using tapered roller bearings is linked with greater power loss than using ball bearings. When using tapered roller bearings to support the worm shaft, both simulation and experiment suggest that bearings with a larger contact angle are preferable to smaller contact angles.

9. Conclusions

In this paper, both simulative and experimental investigations on the influence of different bearing arrangement concepts on the efficiency of worm gears were presented.

By means of a systematic parameter study, bearing arrangement concepts were identified for three different worm gearboxes with centre distances between 40 and 315 mm, which can be usefully applied with regard to both efficiency and bearing life.

By means of tests with a gearbox with centre distance 100 mm on a gear back-to-back test rig it was possible to determine for different operating conditions how individual bearing arrangements of the worm shaft affect the efficiency of the gear.

Under full load, efficiencies of up to 91 % were measured in the tests with an adjusted bearing arrangement in X-arrangement using angular contact ball bearings. This value shows that very efficient drive systems can be realized with modern worm gearboxes providing gear ratios of 20 in one stage.

In addition to energy efficiency, other considerations also play a role in the selection of bearings, even if they have a sufficient service life. These are, for example, the stiffness of the bearing and the guiding accuracy as well as the influence of the bearings on the worm shaft deflection. The mounting and the effort required to adjust the bearing arrangement also influence the decision for or against a bearing arrangement concept.

Acknowledgment

This work was supported by the German Federal Ministry of Economics and Energy (IGF 19461 N) within the framework of the cooperative industrial research and the Forschungsvereinigung Antriebstechnik e.V. (FVA project 729 II).

References

[1] Krause, W., 1993, Konstruktionselemente der Feinmechanik, 2nd ed., Carl Hanser Verlag, München.

[2] Predki, W., Berger, M., Geuß, M., Sievers, B., 2012, “Noch zeitgemäß? Vorteile moderner Schneckengetriebe,” Antriebstechnik 51(3), pp.20–22.

[3] Sellschopp, K., Siebert, A., 2015, “Nie ausschließen - Oder: Sind moderne Schneckengetriebe deutlich besser als ihr Ruf?,” Antriebstechnik 54(4), pp.80–84.

[4] Wolf, T., 2015, “Den CO2-Ausstoß reduzieren - Wälzlager ermöglichen eine Optimierung des Getriebe-Wirkungsgrades.” Antriebstechnik 54(12), pp.54–56.

[5] von Petery, G., 2004, “Kraftstoffersparnis durch maßgeschneiderte Lager für Achsgetriebe von BMW,” Automobiltechnische Zeitschrift - ATZ 106(12), pp.1096–1100.

[6] Crosher, W.P., 2002, Design and application of the worm gear, ASME Press, New York.

[7] Radzecvich, S.P., 2012, Dudley’s Handbook of practical Gear Design and Manufacture, CRC Press, Boca Raton.

[8] Jelaska, D., 2012, Gears and gear drives, Wiley, Chichester.

[9] Dudás, I., 2002, The Theory and Practice of Worm Gear Drives, Butterworth-Heinemann, Oxford.

[10] DIN, 2019, “Tragfähigkeitsberechnung von Zylinder-Schneckengetrieben mit sich rechtwinklig kreuzenden Achsen (Calculation of load capacity of cylindrical worm gear pairs with rectangular crossing axes),” DIN 3996.

[11] ISO, 2001, “Gears—Thermal Capacity. Part 2: Thermal Load-Carrying Capacity,” ISO/TR 14179-2.

[12] ISO, 1999, “Enclosed gear drives for industrial applications,” ISO/TR 13593.

[13] B.S.I., 1963, “Specification for Worm Gearing,” B.S. (British Standard) 721.

[14] AGMA, 1992, “Practice for enclosed cylindrical wormgear speed reducers and gearmotors,” ANSI/AGMA 6034-B92.

[15] Turci, M., Ferramola, E., Bisanti, F., Giacomozzi, G., 2016, “Worm Gear Efficiency Estimation and Optimization,“ Gear Technology 4, pp.46–53.

[16] Predki, W., 1982, “Hertzsche Drücke, Schmierspalthöhen und Wirkungsgrade von Schneckengetrieben,” Ph.D. thesis, Ruhr-Universität Bochum.

[17] Bouché, B., 1991, “Reibungszahlen von Schneckengetrieben im Mischreibungsgebiet,” Ph.D. thesis, Ruhr-Universität Bochum.
[18] Magyar, B., 2012, “Tribo-dynamische Untersuchungen von Zylinderschneckengetrieben,” Ph.D. thesis, Technische Universität Kaiserslautern.
[19] Neupert, K., Hösel, T., Höhn, B.R., Winter, H., 1990, “Versuche zum Einfluss der Baugröße auf Wirkungsgrad und Flankentragfähigkeit von Schneckengetrieben unter Berücksichtigung der Schmierstoffviskosität,” FVA 12 III (Heft 312), Forschungsvereinigung Antriebstechnik e.V., Frankfurt/Main.
[20] Nass, U., Predki, W., 1996, “Tragfähigkeitssteigerungvon Schneckengetrieben durch Optimierung der Schneckenradbronze,” FVA 205 (Heft 476), Forschungsvereinigung Antriebstechnik e.V., Frankfurt/Main.
[21] Jürging, M., Predki, W., 1998, “Tragfähigkeitssteigerungvon Schneckengetrieben durch Optimierung der Schneckenradbronze,” FVA 260 (Heft 544), Forschungsvereinigung Antriebstechnik e.V., Frankfurt/Main.
[22] Oehler, M., 2018, “Methodische Ansätze zur Optimierung des Wirkungsgrades von Schneckengetrieben,” Ph.D. thesis, Technische Universität Kaiserslautern.
[23] Oehler, M., Magyar, B., Sauer, B., 2017, “Schneckengetriebewirkungsgrade,” FVA 729 I (Heft 1226), Forschungsvereinigung Antriebstechnik e.V., Frankfurt/Main.
[24] Schlecht, B., 2010, Maschinenelemente 2: Getriebe - Verzahnungen – Lagerungen, Pearson, München.
[25] SKF Group, 2018, “Rolling Bearings,” PUB BU/P1 17000 EN, Göteborg.
[26] DIN/ISO, 2010, “Rolling bearings - Dynamic load ratings and rating life,” DIN ISO 281.
[27] Haag, P., 1991, “Anlaufwirkungsgrade und Selbsthemmungsfähigkeit von ruhenden Schneckengetrieben,” Ph.D. thesis, Ruhr-Universität Bochum.
[28] DIN, 2017, “Begriffe und Bestimmungsgrößen für Zylinder-Schneckengetriebe mit sich rechtwinklig kreuzenden Achsen – Teil 1: Schnecke und Schneckenrad (Definitions and parameters on cylindrical worm gear pairs with rectangular crossing shafts – Part 1: Worm and worm wheel),” DIN 3975-1.

Dynamic Simulation of Full Complement Cylindrical Roller Bearings with a Semi-Analytical Roller End-Flange Contact Detection Method

Marius Wolf[1], Arshia Fatemi[2]

[1] *Corporate Research, Robert Bosch GmbH Renningen, marius.wolf2@de.bosch.com*
[2] *Corporate Research, Robert Bosch GmbH Renningen, arshia.fatemi@de.bosch.com*

Abstract –
For cylindrical and tapered roller element bearings under axial load, the roller dynamics, damage mechanisms and efficiency are strongly impacted by roller end-flange contacts. Multibody simulation is a expedient tool to acquire insights in the influence of roller end-flange contacts on these effects. However, multibody simulation is only applicable in the development process, if the simulation tool has an appropriate runtime.
For an accurate physical model of the roller end-flange contact, it is essential to determine the contact's location and theoretical penetration. In order to increase numerical efficiency of the contact detection without compromising precision, a significantly faster and more stable semi-analytical approach for contact detection within multibody simulation has been developed [1].
In this paper, it is critically investigated how significant the runtime and stability advantages of the new contact detection algorithm [1] *are in context of an entire multibody simulation in comparison with full numerical models.*

[1] *Wolf, M., Sanner A. and Fatemi, A., 2020, "A Semi-Analytical Approach for Rapid Detection of Roller-Flange Contacts in Roller Element Bearings," Proc. Inst. Mech. Eng., Part J.*

Keywords – roller element bearings, roller end-flange contact, contact detection, multibody simulation, dynamic simulation, full complement cylindrical roller bearings, semi-analytical methods

1. Introduction

Dynamic behavior, efficiency and wear of axially loaded cylindrical and tapered roller element bearings (REBs) are strongly effected by normal and friction forces of the roller end-flange contact [2]. In addition, the governing physics of roller end-flange contacts are highly complex, therefore it is a current field of research [2-5].
The universal contact detection algorithms of commercial multibody software are usually not effective enough for specific contact simulation, concerning simulation time [6].
Normal force and radii of curvature are principal input quantities for physical modeling of roller end-flange contacts. These quantities are both functions of the theoretical penetration and location of the contact, which are calculated within the contact detection step. In addition, the resultant torque is highly dependent on the force application points.
However, for actual application of multibody dynamics simulations (MBS) in the development process of new bearings and products, enhanced simulation runtime is also an indispensable necessity besides high accuracy.

In literature, many approaches for contact detection at the roller end-flange interface can be found (see sect. 2). The authors recently developed a new semi-analytical algorithm for precise and efficient contact detection [1]. It was compared to state of the art contact detection methods and its runtime proved to be significantly faster in a laboratory-like environment.
Nevertheless, for physical modeling of normal and friction forces within a REB, a considerable amount of equations needs to be solved (see sect. 3) and integration of the equations of motion needs to be performed. Thus, contact detection is just one among many steps in the MBS of bearings. Therefore, the relative runtime advantages of the new approach [1] could be far less significant in case of actual application within a MBS. This motivates the investigation of the impact of contact detection algorithms on the overall (numerical) performance of dynamic simulation of REB.

In this paper, contact detection refers to determination of the contact location $\boldsymbol{P}_\mathrm{m}$ and theoretical rigid body penetration δ. The contact's location is the midpoint between the contact points $\boldsymbol{P}_i$ of each body:

$$\boldsymbol{P}_\mathrm{m} = \frac{\boldsymbol{P}_1 + \boldsymbol{P}_2}{2}. \qquad \textit{(Eq. 1)}$$

Contact points are always located on the body's outer surface and correspond to the pair of points with minimal distance, if the bodies are not in contact. If contact occurs, the contact points equal the pair of points with maximum penetration. A more precise definition is given by Wolf et al. [1].

2. Roller End-Flange Contact Detection Models

The following section provides a brief overview of the most relevant contact detection models, which are currently available. A more comprehensive review can be found in Wolf et al. [1].

Universal contact detection within commercial MBS programs is mostly based on discretization of the outer contour of bodies into polygons. Contact detection is then carried out, by checking interference for each polygon [6], [7].
While use of this intrinsic contact detection method is easily applied, it does neither fulfill the requirements concerning accuracy nor numerical efficiency.

In order to avoid the above mentioned drawbacks, Gupta [8] developed an approach based on discretization of roller end geometry as a torus and flange geometry as a cone. Theoretical penetration between these figures can be expressed as a function of the torus' angular coordinate. Contact location $\boldsymbol{P}_\mathrm{m}$ equals the location of maximum penetration. It can be determined using standard numerical schemes for finding extrema of a scalar functions.

Koch [9] introduces a comprehensive method based on gradients of the surface's implicit functions (gradient method). It allows for a variable detailed geometrical approximation by using spheres (SP), cones (CO), tori (TO) and polynomials as basic figures (see fig. 1).

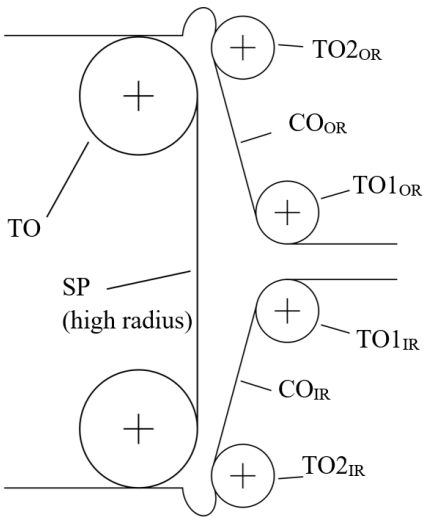

Figure 1: Schematic sketch of a possible roller end and flange geometric approximation at the inner ring (IR) and outer ring (OR).

Three conditions must be fulfilled for the contact points P_1 and P_2:

1. P_1 and P_2 must be located on the body's surface, defined by the implicit function F_i.
2. gradients of F_i must be collinear to each other at P_1 and P_2.
3. gradients of F_i must be collinear to the connecting vector between P_1 and P_2.

For better visualization of these conditions, contact points and gradients for a sphere-cone contact are shown in fig. 2. Eight scalar equations result from the conditions, which need to be solved for six coordinates of the contact points and two scaling factors resulting from the collinearity requirements. This non-linear system of equations is determined and must be solved iteratively.

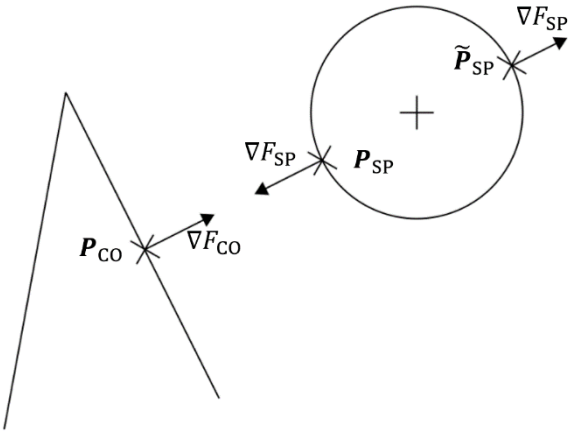

Figure 2: Schematic sketch of the gradient method constraints [9] for a sphere-cone contact. The constraints are fulfilled for all indicated points, yet only $\boldsymbol{P}_\mathrm{SP}$ corresponds to the sphere's actual contact point.

While this approach allows for a very precise approximation of the roller end and flange geometry, its convergence to the correct contact points is not guaranteed, as can be seen in fig. 2. $\boldsymbol{P}_\mathrm{SP}$ and $\widetilde{\boldsymbol{P}}_\mathrm{SP}$ both fulfill the conditions towards contact points, however only $\boldsymbol{P}_\mathrm{SP}$ equals the physical contact point. If the algorithm converges towards $\boldsymbol{P}_\mathrm{SP}$ or $\widetilde{\boldsymbol{P}}_\mathrm{SP}$, depends on the initial guess for iterative solving of the system of equations. Runtime of the gradient method can significantly be reduced within MBS, by storing the solution of the previous time step and using it as the initial guess of the current time step.

The authors recently developed a semi-analytical approach for contact detection in roller element bearings [1]. Analogous to Koch's gradient method [9], it uses a combination of spheres, cones and tori as basic figures to model the roller end and flange geometry as a piecewise function. Planes are represented by spheres with very high radii (see fig. 1). Analytical solutions were derived for sphere-sphere, sphere-cone and sphere-torus pairings. The main idea of the analytical solutions is reduction of the three-dimensional problem into a two-dimensional problem. It can be shown, that the contact points are always located within the plane defined by the sphere's center and rotational axis of the second geometrical figure. Inspection of the contact problem within this plane and the use of trigonometric functions then allows for solving the contact problem with analytical

equations.

Torus-cone contacts are handled similarly to Gupta [8], as described previously in this paper.

For torus-torus contacts, the first step is reduction of the two tori into circles defined by their major radii and determination of the minimal distance. A solution to finding the minimal distance between two arbitrarly located and orientated circles is given by Eberly [10] . Since the distance function is transferred into polynomial form, the global minimum can be determined numerically efficient without convergence issues.

It can be shown, that the actual contact points of the torus-torus problem correspond to the contact points of two spheres located at the contact points of the circle-cirlce problem with radii of the respective torus' minor radius. Finally, the contact points are calculated using the analytical equations derived for the sphere-sphere problem.

The semi-analytical approach [1] was compared to the gradient method of Koch [9] in a laboratory-like environment. In addition of being significantly faster (approx. 37 times), the semi-analytical approach also proved to yield an enhanced numerical stability compared to the gradient method.

3. Simulation Model

A six degree of freedom (DOF) model for simulation of the dynamic behavior of full-complement cylindrical REBs including lubrication was developed.

It allows modeling of dynamic radial and axial loads. Lubrication models for each contact based on rheological lubricant models have been incorporated in the model, since they are essential for the assessment of friction forces.

Normal and tangential forces are calculated for the roller-race, roller-roller and roller end-flange contacts of each roller. Rolling resistance is only considered for roller-race contacts, since roller-roller and roller end-flange contacts are dominated by sliding.

In case of cylindrical REBs, roller-race and roller-roller contacts can be approximated with line contacts. Tilting and skewing of rollers leads to an asymmetric pressure distribution at the contact. This effect and the shape of the rollers are considered by using a roller-slicing technique [11]. Contact detection and load calculation are performed for each slice. For normal and tangential load calculation, each slice is considered as an independent line contact.

The geometrical shape of roller end-flange contacts can vary greatly [2]. In this paper, it is approximated as an elliptical contact.

3.1. Normal Force $\boldsymbol{F}_\mathbf{n}$

3.1.1. Theoretical Penetration

In this paper, theoretical penetration refers to the rigid body penetration and equals the physical deflection at the contact. It is calculated within the contact detection step.

For roller end-flange contacts, the recently developed semi-analytical approach [1] and Koch's gradient method [9] for contact detection were implemented.

For roller-roller and roller-race contact detection, the roller slices and races are modelled as cylinders. Local vectors of the cylinders' geometrical center can be calculated dependent on skewing and tilting using standard geometrical functions.

For calculation of the contact location $\boldsymbol{P}_\mathrm{m}$ and theoretical penetration δ, it is assumed, that the cylinders representing rollers and races are parallel to each other. This allows for a simple analytical contact detection (see fig. 3):

$$\delta = \|\Delta \boldsymbol{r}_\perp\| - (R_1 + R_2) \qquad \textit{(Eq. 2)}$$

$$\boldsymbol{P}_\mathrm{m} = \boldsymbol{r_1} - \boldsymbol{\Delta r}_\perp \left(R_1 - \frac{\delta}{2}\right). \qquad \textit{(Eq. 3)}$$

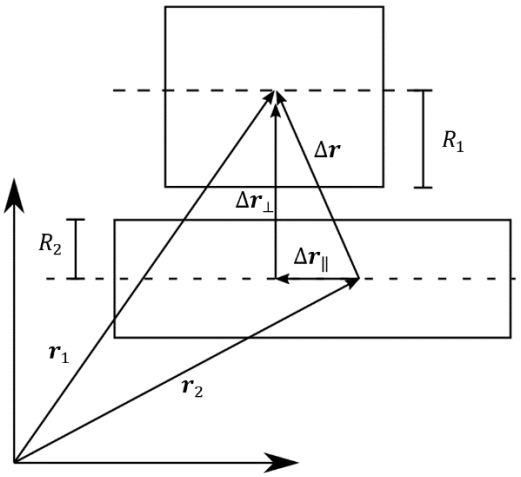

Figure 3: Schematic sketch of generic contact detection for two parallel cylinders.

The assumption of parallel cylinders is valid, since skew and tilt angles are relatively small in cylindrical REBs.

Theoretical penetration is then used in load-deflection relationships to calculate the normal load of each contact (elliptical) or slice (line).

3.1.2. Elliptical Contacts at Roller End-Flange Interface

For elliptical contacts, Hertzian theory is used to calculate the normal force for a given deflection. In order to enable rapid calculation, the approximation formulas given by Brewe and Hamrock [12] are used:

$$F_\mathrm{N} = \pi \kappa E' \sqrt{\frac{\varepsilon\, R'}{4.5} \left(\frac{\delta}{\mathcal{F}}\right)^3} \qquad \textit{(Eq. 5)}$$

with the semi-axis ratio

$$\kappa = \frac{a}{b} \approx 1.0339 \left(\frac{R_x}{R_y}\right)^{0.636}, \quad \textit{(Eq. 6)}$$

the approximated elliptic integrals

$$\varepsilon \approx 1.0003 + 0.5968 \left(\frac{R_y}{R_x}\right), \quad \textit{(Eq. 7)}$$

$$\mathcal{F} \approx 1.5277 + 0.6023 \ln\left(\frac{R_x}{R_y}\right), \quad \textit{(Eq. 8)}$$

the semi-axes of the contact area a and b, the contact's relative principal curvatures R_x and R_y, its effective radius R' and effective Young's modulus E'. Formulas for E' and R' are provided in the nomenclature.

3.1.3. Line Contacts at Roller-Roller and Roller-Race Interface

Hertzian theory does not provide a load-deflection relationship for line contacts. Therefore, a great variety of different relationships were developed over time. A good overview is given for example by Teutsch and Sauer [11]. As recommended by Houpert [13], the approach of Tripp [14] is used.

It follows

$$\delta_i = \left(\frac{2F_N}{\pi l}\right) \cdot \left[\frac{(1-\nu_1^2)}{E_1}\left(\ln\frac{4R_1}{a} - \frac{1}{2}\right) + \frac{(1-\nu_2^2)}{E_2}\left(\ln\frac{4R_2}{a} - \frac{1}{2}\right)\right] \quad \textit{(Eq. 9)}$$

for deflection at the inner ring and

$$\delta_o = \left(\frac{2F_N}{\pi l}\right) \cdot \left[\frac{(1-\nu_1^2)}{E_1}\left(\ln\frac{4R_1}{a} - \frac{1}{2}\right) + \frac{(1-\nu_2^2)}{E_2}\left(\ln\frac{2t}{a} - \frac{\nu_2}{2(1-\nu_2)}\right)\right] \quad \textit{(Eq. 10)}$$

for deflection at the outer ring. Roller-roller contacts are modelled according to eq. 10, since they are also non-conformal contacts.

It should be noted, that Tripp's equations (eq. 9 and 10) cannot explicitly be solved for F_n from a given deflection δ. Yet, a time-consuming iterative solution of the load-deflection relationship is not suitable for MBS. Therefore, a parameter fit with fitting parameters $k_1$and k_2 was performed similarly to Houpert [13] for the roller-roller, roller-outer ring and roller-inner ring contacts:

$$F_n = \frac{l}{k_1} \cdot \delta^{\frac{1}{k_2}}. \quad \textit{(Eq. 11)}$$

3.2. Tangential Force F_t

The resultant tangential friction forces are calculated by weighing the contributions of boundary and elastohydrodynamic lubrication (EHL) regime.

3.2.1 EHL Friction Force F_{EHL}

In this section, the governing equations and assumptions for calculation of the EHL tangential force F_{EHL} are presented.

It is assumed, that the contact area dimensions and the pressure distribution within this area can be modelled using Hertzian formulas. Given the maximum contact pressure p_0, the pressure distribution equals

$$p(x,y) = p_0 \sqrt{1 - \left(\frac{x}{a}\right)^2 - \left(\frac{y}{b}\right)^2} \quad \textit{(Eq. 12)}$$

with

$$p_0 = \frac{1.5\, F_n}{\pi\, a\, b} \quad \textit{(Eq. 13)}$$

for elliptical contacts [15]. The semi-axes of the contact area a and b are calculated using the approximation equations of Brewe and Hamrock [12]:

$$a = \left(\frac{6\,\kappa^2 \varepsilon\, F_N\, R'}{\pi\, E'}\right)^{1/3} \quad \textit{(Eq. 14)}$$

$$b = \left(\frac{6\,\varepsilon\, F_N\, R'}{\pi\, \kappa\, E'}\right)^{1/3}. \quad \textit{(Eq. 15)}$$

For line contacts, pressure distribution equals

$$p(x) = p_0 \sqrt{1 - \left(\frac{x}{a}\right)^2} \quad \textit{(Eq. 16)}$$

with

$$p_0 = \frac{2\, F_n}{\pi\, a\, l} \quad \textit{(Eq. 17)}$$

as the maximum contact pressure. l represents the length of the line contact, which here equals the slice width. Width of the semi-axis a can be calculated via

$$a = \sqrt{\frac{8\, F_n\, R'}{\pi\, E'\, l}}. \quad \textit{(Eq. 18)}$$

Given the pressure distribution, the pressure-induced viscosity increase across the contact area is calculated using Roelands equation [16]:

$$\eta(p,T) = \eta_p \left(\frac{\eta_0(T)}{\eta_p}\right)^{\left(\frac{p_p - p}{p_p}\right)^Z} \quad \textit{(Eq. 19)}$$

with universal parameters $\eta_p = 0.0631$ mPas and $p_p = -196$ MPa.

Base viscosity at ambient pressure η_0 follows from the Vogel equation

$$\eta_0(T) = A \exp\left(\frac{B}{C+T}\right) \quad \textit{(Eq. 20)}$$

with fluid parameters A, B, C.

A homogenous and constant body mass temperature T is assumed for all elements of the REB. This temperature is then used for calculation of the base viscosity η_0. Liu et al. [17] showed, that using the mass temperature is superior to using the supplied oil temperature.

Shear-thinning of the fluid is considered within the simulation by using a Carreau model. For the shear stress τ follows:

$$\tau = \dot{\gamma}\eta \left(1 + \left(\frac{\eta\dot{\gamma}}{\tau_0}\right)^2\right)^{\frac{n-1}{2}}. \quad \textit{(Eq. 21)}$$

The shear rate $\dot{\gamma}$ can be approximated as the ratio of relative tangential velocity u_{rel} and central film height h_{c}:

$$\dot{\gamma} = \frac{\partial u}{\partial z} \approx \frac{u_{\mathrm{rel}}}{h_{\mathrm{c}}} = \frac{u_2 - u_1}{h_{\mathrm{c}}}. \quad \textit{(Eq. 22)}$$

Central film height h_{c} is used instead of the minimum film height, since it represents the major of the contact area and the high pressure area in the contact's center.

For calculation of h_{c}, the dimensionless parameters listed in tab. 1 are introduced. A definition of the required physical input quantities is provided in the nomenclature.

Table 1: Dimensionless parameters used for calculation of film height

Line	Elliptical	
$H = \frac{h}{R'}$	$H = \frac{h}{R_{\mathrm{x}}}$	*(Eq. 23)*
$G = \alpha_{\mathrm{p}}^* E'$		*(Eq. 24)*
$U = \frac{\eta_0 u_0}{E' R'}$	$U = \frac{\eta_0 u_0}{E' R_{\mathrm{x}}}$	*(Eq. 25)*
$W = \frac{F_{\mathrm{n}}}{E' R' l}$	$W = \frac{F_{\mathrm{n}}}{E' R_{\mathrm{x}} l}$	*(Eq. 26)*
$\widetilde{U} = 2\,U$		*(Eq. 27)*
$\widetilde{H} = H \cdot \widetilde{U}^{-0.5}$		*(Eq. 28)*
$M = W \cdot \widetilde{U}^{-0.5}$		*(Eq. 29)*
$L = G \cdot \widetilde{U}^{-0.25}$		*(Eq. 30)*

The viscosity-pressure coefficient α_p^* of the material parameter G (eq. 24) is calculated as proposed by Block [18], [19]:

$$\alpha_{\mathrm{p}}^* = \left(\int_{0.1\,\mathrm{MPa}}^{\infty} \frac{\eta(p = 0.1\,\mathrm{MPa})}{\eta(p)} \mathrm{d}p \right)^{-1} \quad \textit{(Eq. 31)}$$

Since the integral of eq. 31 cannot be solved analytically for the pressure-viscosity dependence stated in eq. 19, it needs to be solved numerically. In order to avoid a time consuming iterative determination during the MBS, a curve fit of its temperature dependency is performed [20]:

$$\alpha_p^*(T) = c_1 \exp(c_2 T) + c_3 \exp(c_4 T). \quad \textit{(Eq. 32)}$$

Film height for line contacts is calculated according to the formula proposed by Moes [21]:

$$\widetilde{H}_c = \left[\left(\widetilde{H}_{\mathrm{IR}}^{\frac{7}{3}} + \widetilde{H}_{\mathrm{IE}}^{\frac{7}{3}} \right)^{\frac{3s}{7}} + \left(\widetilde{H}_{\mathrm{PR}}^{-\frac{7}{2}} + \widetilde{H}_{\mathrm{PE}}^{-\frac{7}{2}} \right)^{-\frac{2s}{7}} \right]^{\frac{1}{s}} \quad \textit{(Eq. 33)}$$

with

$$\widetilde{H}_{\mathrm{IR}} = 3\,M^{-1} \quad \textit{(Eq. 34)}$$

$$\widetilde{H}_{\mathrm{IE}} = 2.62105\,M^{-0.2} \quad \textit{(Eq. 35)}$$

$$\widetilde{H}_{\mathrm{PR}} = 1.28666\,L^{\frac{2}{3}} \quad \textit{(Eq. 36)}$$

$$\widetilde{H}_{\mathrm{PE}} = 1.31106\,M^{-0.125}\;L^{0.75} \quad \textit{(Eq. 37)}$$

$$s = 0.2\left[7 + 8\,exp\left(-2\frac{\widetilde{H}_{\mathrm{IE}}}{\widetilde{H}_{\mathrm{IR}}}\right)\right]. \quad \textit{(Eq. 38)}$$

Roller-roller contacts are an especial case, since they exhibit counter rotation, which results in very small to negligible entrainment velocities. Even though no fluid film is expected for zero entrainment velocities (ZEV) according to eq. 33, experiments and numerical EHL-simulations show the existence of such a fluid film [22]. This lubricant film results from a phenomenon referred to as "viscosity wedge": the variation of viscosity across the film thickness due to thermal effects [23]. Even though ZEV contacts are a current field of research [24-26], no universal empirical analytical formula for the film height of line contacts could be derived yet.

Bakolas et al. [27] present simulation results for minimal film heights for ZEV line contacts in the form of data points within a diagram. Aul [27] interpolates these data points, to obtain a rudimentary film height equation for ZEV line contacts:

$$H = [(g_1^{-0.7} + g_2^{-0.7})^{-1.43s} + (g_3^{-1.45} + g_4^{-1.45})^{-0.69s}]^{\frac{1}{s}} \quad \textit{(Eq. 39)}$$

with

$$g_1 = 0.51\,M^{-0.09} \quad \textit{(Eq. 40)}$$

$$g_2 = 5.5\,M^{0.5} \quad \textit{(Eq. 41)}$$

$$g_3 = 0.06\,L^{1.395} \quad \textit{(Eq. 42)}$$

$$g_4 = 1.04\,M^{0.95}L^{0.08} \quad \textit{(Eq. 43)}$$

$$s = 0.092\left(9.1 + 10\exp\left(-2\,\frac{g_3}{g_2}\right)\right) \quad \textit{(Eq. 44)}$$

For calculation of the speed parameter U $\mathrm{u}_0 = \frac{1}{2}(|u_1| + |u_2|)$ is used for the entraining speed.

Within the simulation both film heights from eq. 33 and eq. 39 are calculated and the greater is then used for calculation of the shear rate $\dot{\gamma}$ (eq. 22). While this method is not yet established in literature, upon the author's knowledge, it is the best currently available published method to model ZEV film thickess of line contacts at system level.

The film height formula proposed by Chittenden et al. is used for elliptical contacts [28]:

$$H_c = 4.31\, G^{0.49}\, U^{0.68}\, W^{-0.073}(1-\beta) \qquad \textit{(Eq. 45)}$$

with

$$\beta = \exp\left(-1.23\left(\frac{\frac{R_y}{R_x}\sin^2\xi + \cos^2\xi}{\sin^2\xi + \frac{R_y}{R_x}\cos^2\xi}\right)^{\frac{2}{3}}\right) \qquad \textit{(Eq. 46)}$$

and ξ as the angle between the direction of entrainment velocity and the major axis of the contact ellipse (see fig. 4).

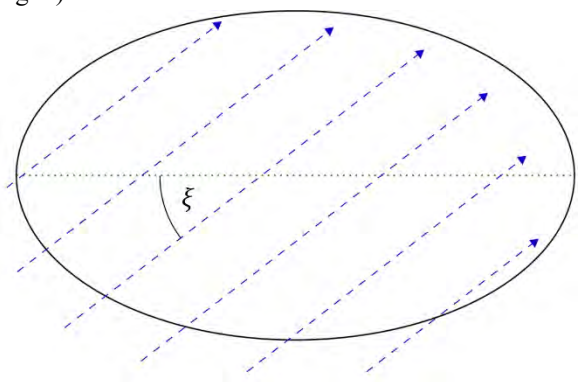

Figure 4: Sketch of the angle ξ between the ellipse's major axis (dotted) and the entrainment velocity field (dashed).

It is assumed, that all contacts are fully-flooded and therefore, no starvation effects on the film height are taken into account. Furthermore, it is anticipated, that shear-thinning and fluid compression can be neglected for calculation of the central film height.

The stated film height formulas in eq. 33 and eq. 45 are only valid for isothermal contacts. Thermal effects are considered using the thermal correction factor ϕ_{th} proposed by Pandey and Gosh for line contacts [29]:

$$\phi_{\mathrm{th}} = \frac{1}{1 + 0.133 \cdot \mathcal{L}^{0.71} \cdot (1 + 5.65 \cdot S^{0.96})} \qquad \textit{(Eq. 47)}$$

with the thermal load parameter

$$\mathcal{L} = \left(-\frac{\partial \eta}{\partial T}\frac{u_0^2}{\lambda_{\mathrm{F}}}\right), \qquad \textit{(Eq. 48)}$$

slide-to-roll-ratio (SRR)

$$S = \frac{u_{\mathrm{rel}}}{u_0} = \frac{2\,(u_2 - u_1)}{u_1 + u_2} \qquad \textit{(Eq. 49)}$$

and λ_{F} as the lubricant's thermal conductivity.

Zhu [30] states, that no thermal correction models are available for elliptical contacts. Therefore, it is assumed, that eq. 47 can also be used as a hypothetical approach for elliptical contacts.

Shear stresses within a fluid cannot exceed a certain, shear-rate-independent, value. This upper boundary is commonly referred to as the limiting shear stress (LSS) τ_{L}. In this paper, the bilinear, temperature-independent, approach of Wang [31] is used for modeling of LSS:

$$\tau_{\mathrm{L}}(p) = \begin{cases} \chi\,(p - p^*) + \tau_{\mathrm{L},0} & \text{if } p < p^* \\ \tau_{\mathrm{L},0} & \text{if } p \geq p^*. \end{cases} \qquad \textit{(Eq. 50)}$$

The final step in calculation of the EHL tangential force F_{EHL} is integration of shear stress distribution over the contact area. Due to the large number of interacting and partially piecewise equations required for calculation of shear stress, an analytical solution of the integral cannot be determined.

Therefore, shear stress is integrated numerically. To ensure an efficient integration, a combination of Gauss-Legendre quadrature and trapezoidal rule is used.

3.2.4. Boundary Friction Force F_{B}

Boundary friction is modelled as Coulomb Friction:

$$F_{\mathrm{B}} = \mu_{\mathrm{B}}\, F_{\mathrm{N}}\, \mathrm{sgn}(u_{\mathrm{rel}}). \qquad \textit{(Eq. 51)}$$

For small SRR, micro slip occurs in an unlubricated contact [32]. The boundary coefficient of friction μ_{B} increases with increasing slip until macro-slip predominates in the contact and μ_B reaches a constant value.

In order to incorporate this phenomenon in the simulation, a simplified model is used. The boundary coefficient of friction μ_B increases linearly with S until a critical value S_0 is reached and remains constant afterwards:

$$\mu_{\mathrm{B}}(S) = \begin{cases} \frac{S}{S_0}\,\mu_{\mathrm{B},0} & \text{if } S < S_0 \\ \mu_{\mathrm{B},0} & \text{if } S \geq S_0. \end{cases} \qquad \textit{(Eq. 52)}$$

In case of small relative and mean velocities, the numerical behavior of F_{B} is undesired, due to abrupt changes of sign of F_{B} (see fig. 5). In order to improve numerical stability, F_{B} is smoothened for $|u_{\mathrm{rel}}| \ll 1$ as shown in fig. 5.

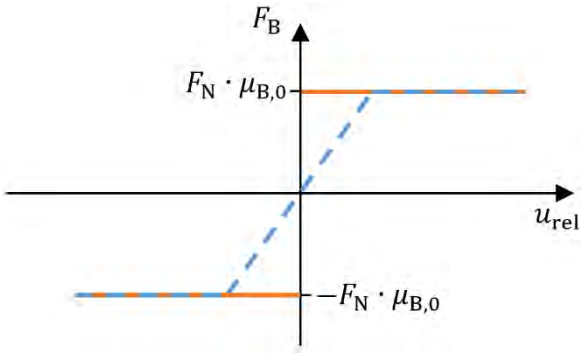

Figure 5: Plot of physical (solid) and smoothened (dashed) boundary coefficient of friction μ_B against relative velocity u_{rel} for $S > S_0$.

3.2.5. Load Sharing in Mixed Lubrication

Mixed and EHL regime are considered. For mixed lubrication the contributions of boundary and EHL regime are weighed using the contact load ratio ϕ according to Zhou and Hoeprich [33]:

$$\phi = \exp\left(-B_{ZH} \cdot \Lambda^{C_{ZH}}\right) \qquad \textit{(Eq. 53)}$$

and

$$F_t = \phi \cdot F_B + (1 - \phi) \cdot F_{EHL}. \qquad \textit{(Eq. 54)}$$

3.3. Rolling Resistance

In addition to friction forces due to relative motion as described in section 3.2., rolling resistance is also considered. Rolling resistance is caused by many physical effects, such as adhesion, hysteresis effects due to plastic deformation, micro-slip, fluid compression in the inlet zone or inlet shear. It creates a torque acting against the direction of rotation.

Since the main kinematic condition of roller-roller and roller end-flange contacts is sliding, rolling resistance is not considered for these contacts.

Similar to calculation of tangential forces, effective rolling resistance is calculated by weighing the contributions of boundary and EHL rolling resistance according to Zhou and Hoeprich [33] (eq. 53 & 54). Boundary rolling resistance due to hysteresis effects for line contacts is calculated via [15]

$$M_B = \alpha_V F_N \frac{2l}{3\pi}. \qquad \textit{(Eq. 55)}$$

EHL rolling resistance is modelled according to Biboulet and Houpert [31]:

$$M_{EHL} = 1.42 \cdot E' R' l R \tilde{U}^{0.5} W^{0.5} \psi \qquad \textit{(Eq. 56)}$$

with

$$\psi = \left(1 + \left(0.966 W^{0.5} \tilde{U}^{-0.25}\right)^{10}\right)^{-0.1}. \qquad \textit{(Eq. 57)}$$

Thermal effects are considered by applying the thermal correction factor from eq. 47 to eq. 56.

4. Benchmarking Study

The performance comparison is conducted by comparing a full-complement cylindrical bearing (bearing B1) simulation (see fig. 6) using the authors' new semi-analytical approach [1] and the gradient method introduced by Koch [9].

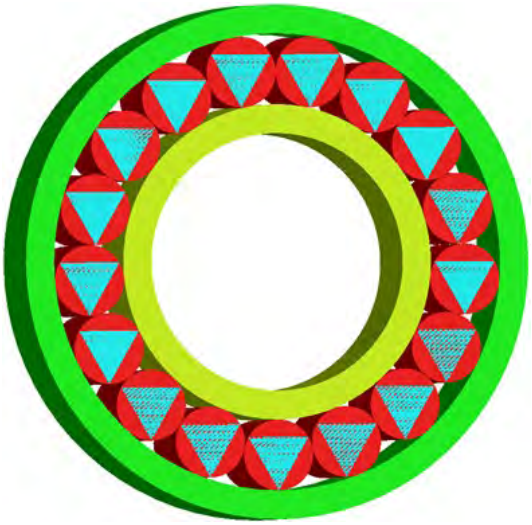

Figure 6: Simulation setup – triangles on rollers are for visualization during post-processing only.

The roller edge is modelled as a torus and the roller end by a convex sphere with high radius in order to represent a plane. The flange is modelled as a cone bounded by two tori at its edges. A sketch of the geometrical approximation can be seen in fig. 1.

The most relevant geometrical parameters are given in tab. 2.

The bearing is lubricated with the reference mineral oil FVA3 and constant radial and axial loads are applied. The relevant lubricant and operating parameters are given in tab. 3. Further lubricant properties can be found in [35].

The simulation includes ramp-up of radial and axial forces, and of the rotational speed of the inner ring. Simulation ends, after two full rotations of the rollers around the bearing at full speed. Inner ring rotation is only allowed in axial direction, while the outer ring is fixed in space. This configuration is chosen to represent a bearing mounted on a very stiff shaft. The rollers are given all six DOF.

For better performance of Koch's method [9], the solution of the contact detection step was stored and used as the initial guess for the iterative contact detection algorithm in the following time step.

Table 2: Load and lubricant parameters of B1

Radial load	Axial load	Rotational speed	Temp.	Viscosity @ 40 °C
5000 N	1000 N	500 rpm	80 °C	81 mPas

Table 3: Geometrical parameters of B1

No. of Rollers	Inner Diameter	Outer Diameter	Opening Angle Flange	Minor Radius TO Roller	Radius Sphere Roller
17	20 mm	29 mm	0.11 °	0.5 mm	5000 mm

5. Results and Discussion

5.1. Precision

Inspection of calculated contact points and theoretical penetration throughout the simulation only reveals differences between the gradient method and the semi-analytical approach within numerical tolerance. Consequently, differences in the resultant forces and torques and consequent kinematics of both simulations are negligible. The identical values for contact points and penetrations throughout the simulation show the equivalence of both methods in terms of precision and are a strong indication for correct implementation of both methods.

It is of high interest, to investigate, which basic figures used for modeling of roller end and flange (see fig. 1) actually got in contact throughout the simulation (see fig. 8 and fig. 9) in order to evaluate detailedness of the geometrical approximation.

It can be seen, that contact between the torus used for modeling the roller and the cone of the respective flange is predominant for both inner (TO-CO_{IR} in fig. 8) and outer ring (TO-CO_{OR} in fig. 9), especially in the load zone. If tilting of the inner ring (IR) is allowed, than other contact pairs occur more often. Herein, tilting refers to a rotational displacement perpendicular to direction of axial and radial force.

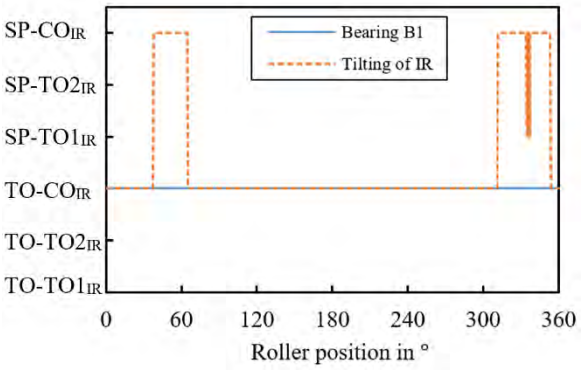

Figure 8: Contact pairings at IR during simulation with and without tilting of IR enabled. For definitions of contact pairs see fig. 1.

This shows, that the simplified geometrical approximation of Gupta [8] in form of a torus and a cone, is a good geometrical approximation. Nevertheless, a more detailed geometric approximation is justified as well. It improves the simulation quality even further, especially in the load-free zone. This is particularly important, since maximum roller slip is determined within the load free zone.

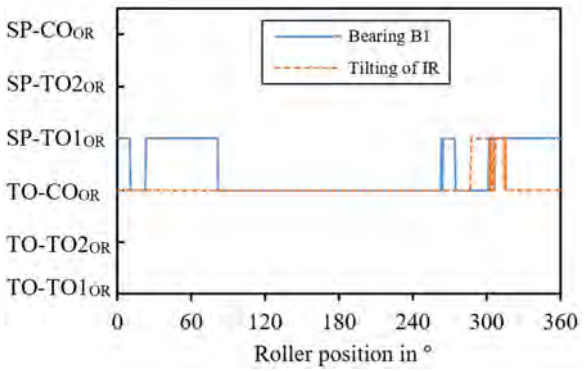

Figure 9: Contact pairings at outer ring during simulation with and without tilting of IR enabled. For definitions of contact pairs see fig. 1.

5.2. Simulation Results

Contact detection models allow incorporation of axial loads into MBS and investigation of their effects on REBs. In this section, some possible applications are presented.

For example, in fig. 10 the bearing frictional torque of B1 is plotted for different constant axial loads. It can be seen, that the bearing frictional torque increases with increasing axial force. This effect can be explained, by increasing friction forces at the flanges (fig. 11).

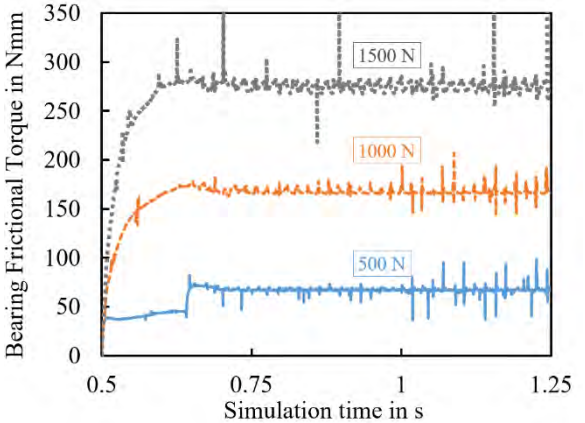

Figure 10: Bearing frictional torque over time for different axial loads. Inner ring rotation ramp-up occurs between 0.5 s and 0.7 s.

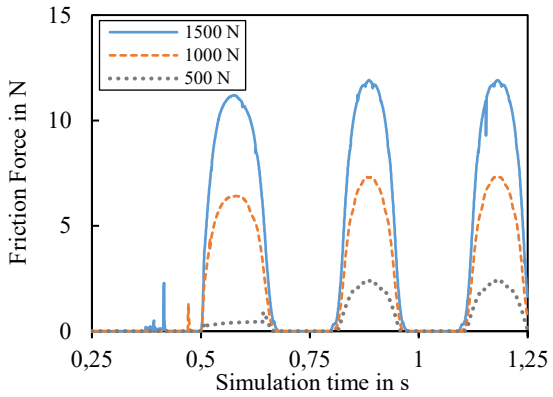

Figure 11: Flange friction force for a single roller over time for different axial loads. Inner ring rotation ramp-up occurs between 0.5 s and 0.7 s.

Furthermore, it can be seen, that the major proportion of the axial force is absorbed by rollers in the load zone (see fig. 12).

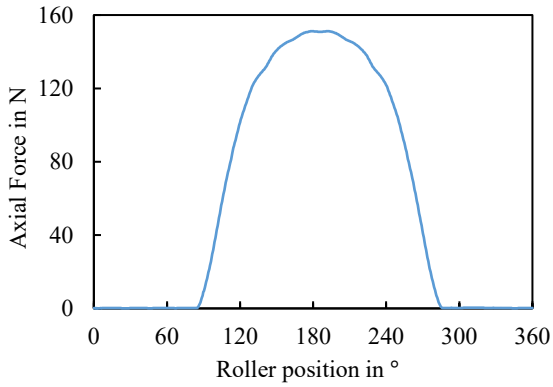

Figure 12: Axial force of a single roller for bearing B1 over roller location.

Radial displacement of inner ring and a positive flange opening angle (see fig. 1 and tab. 3) result in less space in axial direction being left for the rollers within the load zone. Therefore, theoretical penetration and axial load are significantly higher within the radial load zone.

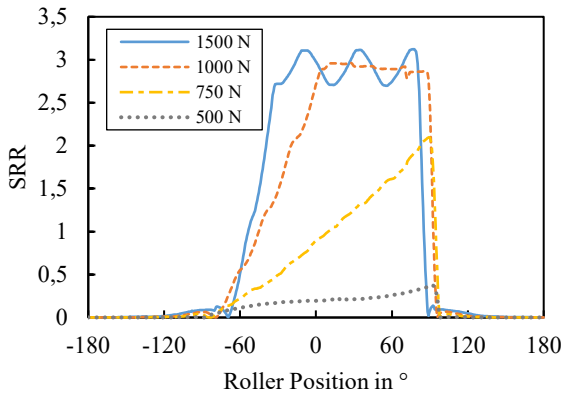

Figure 13: SRR at inner ring over roller position for different axial loads.

Roller slip is the major kinematic effect causing spontaneous non-fatigue damage in REBs, e.g. smearing. The effect of different axial loads on the SRR of rollers can also be studied using the discussed contact detection algorithms (see fig. 13).

5.3. Runtime

The semi-analytical approach reduces runtime of the simulation described in sect. 4 by 35 % compared to a simulation using the gradient method. Therefore, it is shown, that numerical efficiency advantages are still significant, when the new approach is applied within a MBS.

As stated in the introduction, contact detection is just one among many other steps within the MBS of REBs. It is suspected, that its strong impact on the numerical performance results from the large amount of contacts to be evaluated:

Each roller has two possible contact points at the inner flange and two more at the outer flange. Due to the chosen geometrical approximation, for each contact (see fig. 1) six combinations of geometrical figures must be evaluated. Since the bearings consists of 17 rollers, this leads to $17 \cdot 4 \cdot 6 = 408$ contact pairs to be evaluated at each time step.

Numerical performance could be enhanced even further by reducing the number of contacts to be evaluated. Critical analysis of the required complexity of geometrical approximation and of the theoretical possible contact pairs can easily increase numerical performance without the need for new contact detection algorithms.

An example for theoretical impossible contact pairs can be constructed for the geometrical approximation of fig. 1: If the minor radius of the roller's torus is sufficiently large enough and the minor radius of the flange's lower torus is small enough, than no contact between the lower torus and the roller can occur in reality. The roller would get in contact with the cone first and therefore, the number of contacts to be evaluated could be reduced by one third to $17 \cdot 4 \cdot \mathbf{4} = 272$ contacts.

If no change of sign occurs for the axial force, then contact only occurs at the diagonally opposite flanges of inner and outer ring. In this case, the number of evaluated roller end-flange contacts, can be reduced by another 50 %.

Runtime of the gradient method greatly depends on the number of iterations, which are necessary for solving the 8x8 non-linear system of equations. Small differences between the initial guess and solution reduce the number of iterations. Since the solution of the previous time step is used as initial guess of the current time step, it is expected, that runtime of the gradient method is dependent on the step size Δt. Runtime of the contact detection with the gradient

method should be lower for smaller step sizes, since the interim changes of roller and ring spatial displacement become smaller as well.

In order to investigate this hypothesis, the maximum allowed step size $\Delta t_{\max}$ of the simulation is varied and the corresponding relative runtime advantages are plotted in fig. 14.

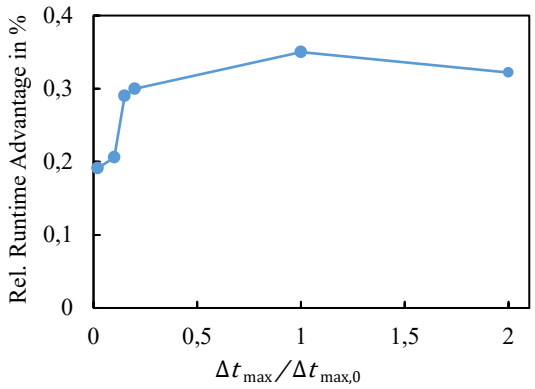

Figure 14: Influence of maximum step size $\Delta t_{\max}$ on runtime advantage of semi-analytical approach. $\Delta t_{\max,0}$ equals the maximum step size with the lowest overall runtime for both methods.

It can be seen, that the runtime advantages are lower for very small time steps. This can be explained, by the lower number of iterations of the gradient method and the independence of the semi-analytical approach from the step size. This insight is relevant, since for relatively stiff systems (e.g. REB with high viscosity oil) a smaller time step size is used within the simulation.

It can be seen, that the new semi-analytical approach's runtime is always lower for realistic maximum step sizes. Even smaller maximum step sizes than shown in fig. 14 lead to unacceptable high total simulation times and were not investigated.

5.4. Practical Consquences in Application of the Semi-Analytical Model

Setting of the first initial guesses of the iterative scheme by Koch [9] at the beginning of the simulation can be quite complex and should not be underestimated. If these values are not chosen correctly, the algorithm does not only converge to a false solution at the first time step (see fig. 2). It is also likely to falsely converge in the following time steps, since the wrong solution will be used as the initial guess of the following time step.

Furthermore, calculation of good initial guesses is especially difficult, if the initial state of the rollers includes skewing and tilting. Accordingly, end users of the MBS must be familiar with the concept of the gradient method.

In addition, concept development for storage of previous solutions should take into account the possibility of race hazard risks.

None of the listed drawbacks exists for the semi-analytical approach [1], though it cannot be ignored, that the gradient method can more easily be extended to include additional basic figures (e.g. polynomials, ellipsoids).

6. Conclusion

The recently developed semi-analytical approach [1] for rapid detection of roller end-flange contacts was compared to the gradient method of Koch [9] for application within a MBS of full-complement cylindrical REB. The bearing simulation includes all six DOF for rollers and rings. Its physical model includes fluid behavior and considers both fluid and mixed lubrication.

Possible applications of dynamic REB simulation were shown and simulation results were presented.

Comparison of the contact detection methods focused on useability, runtime and quality of results.

Main findings of the comparison are:

- There is no compromise in accuracy by using the semi-analytical model [1], since it yields the same trajectories of forces and kinematics as the gradient method [9].
- A more detailed geometrical approximation (see fig. 1) than the torus-cone combination used by Gupta [8] is justified. Fig. 8 and fig. 9 show the occurrence of contacts based on additional combinations of basic figures.
- Application of the semi-analytical approach within MBS reduces runtime of dynamic simulations of REBs compared to the gradient method.
- Runtime advantages are significant (35 % for reference simulation).
- Time step size has an influence on relative runtime advantage. Relative advantages decline for smaller time step sizes.
- The semi-analytical approach has a higher numerical stability, which results in facilitated applicability of the MBS in development processes. Unlike for the gradient method, no knowledge of the working principle of the used contact detection method is required by the end user.

Acknowledgments

The authors would like to thank Prof. Dr. Gerhard Poll (University of Hannover) for helpful and in-depth discussions on modeling of the fluid behavior. Patrick Stuhler, Dr. Nadine Nagler (both Bosch Rexroth AG) and Dr. Timo Kiekbusch (Robert Bosch GmbH) are acknowledged for their general advice on the topic of roller element bearings.

Bibliography

[1] Wolf, M., Sanner A. and Fatemi, A., 2020, "A Semi-Analytical Approach for Rapid Detection of Roller-Flange Contacts in Roller Element Bearings," Proc. Inst. Mech. Eng., Part J.

[2] Wheeler, J.D., 2016, "Non-Elliptical Point Contacts: the Torus-on-Plane Conjunction," Ph.D. thesis, INSA Lyon.

[3] Wheeler, J.D., Fillot, N., Vergne, P., Philippon, D. and Morales-Espejel, G.E., 2016, "On the crucial role of ellipticity on elastohydrodynamic film thickness and friction," Proc. Inst. Mech. Eng., Part J, 230(12), pp. 1503-1515.

[4] Doki-Thonon, T., Fillot, N., Vergne, P. and Morales-Espejel, G., 2012, "Numerical insight into heat transfer and power losses in spinning EHD non-Newtonian point contacts," Proc. Inst. Mech. Eng., Part J, 226(1), pp. 23-35.

[5] Doki-Thonon, T., Fillot, N., Morales-Espejel, G., Querry, M., Phillipon, D., Devaux, N. and Vergne, P., 2013, "A Dual Experimental/Numerical Approach for Film Thickness Analysis in TEHL Spinning Skewing Circular Contacts," Tribol. Lett., 50, pp. 115-126.

[6] MSC Software, 2018, "Adams 2018.1: Online Help," MSC Software, Newport Beach, CA.

[7] Gottschalk, S., Lin, M.C. and Manocha, D., 1996, "OBBTree: A Hierarchical Structure for Rapid Interference Detection," 23rd International Conference on Computer Graphics and Interactive Techniques, Association for Computing Machinery, New Orleans, LA, pp. 171-180.

[8] Gupta, P.K., 1984, Advanced Dynamics of Rolling Elements, Springer-Verlag New York, New York.

[9] Koch, O., 2008, „Dreidimensionale Simulation von kombiniert belasteten Radialzylinderrollenlagern," Ph.D. thesis, Ruhr University Bochum.

[10] Eberly, D., 2019, "Distance to circles in 3D," from https://www.geometrictools.com/Documentation/DistanceToCircle3.pdf

[11] Teutsch, R. and Sauer, B., 2004, "An Alternative Slicing Technique to Consider Pressure Concentrations in Non-Hertzian Line Contacts," Journal of Tribology, 126(3), pp. 436-442.

[12] Brewe, D.E. and Hamrock, B.J., 1977, "Simplified Solution for Elliptical-Contact Deformation Between Two Elastic Solids," Journal of Lubrication Technology, 99 (4), pp. 485-487.

[13] Houpert, L., 2000, "An Engineering Approach to Hertzian Contact Elasticity - Part I," Journal of Tribology, 123(3), pp. 582-588.

[14] Tripp, J. H., 1985, "Hertzian Contact in Two and Three Dimensions," 2473, National Aeronautics and Space Administration (NASA), Cleveland, OH.

[15] Johnson, K.L., 1985, Contact Mechanics, Cambridge University Press, Cambridge.

[16] Hamrock, B.J., Schmid, S.R. and Jacobson, B.O., 2004, Fundamentals of Fluid Film Lubrication, 2nd ed., Marcel Dekker, Inc., New York.

[17] Liu, H.C., Zhang, B.B., Bader, N., Guo, F., Poll, G., and Yang, P., 2019, "Crucial role of solid body temperature on elastohydrodynamic film thickness and traction," Tribology International, 131, pp. 386-397.

[18] Blok, H., 1963, "Inverse Problems in Hydrodynamic Lubrication and Design Directives for Lubricated Flexible Surfaces," International Symposium on Lubrication and Wear, U.S. Atomic Energy Division, Houston, TX.

[19] Vergne, P. and Bair, S., 2014, "Classical EHL Versus Quantitative EHL: A Perspective Part I - Real Viscosity-Pressure Dependence and the Viscosity-Pressure Coefficient for Predicting Film Thickness," Tribol. Lett., 54(1), pp. 1-12.

[20] Fruth, T., 2018, "Vom tribologischen Modellversuch zum Maschinenelement," Ph.D. thesis, University of Kaiserslautern.

[21] Moes, H., 2000, Lubrication and Beyond, University of Twente, Enschede.

[22] Meziane, B., Vergne, P., Devaux, N., Lafarge, L., Morales-Espejel, G.E. and Fillot, N., 2020, "Film Thickness Build-Up in Zero Entrainment Velocity Wide Point Contacts," Tribology International, 141.

[23] Cameron, A., 1958, “The Viscosity Wedge,” ASLE Transactions, 1 (2), pp. 248-253.

[24] Wong, P.L., Zhao, Y. and Mao, J., 2018, “Facilitating effective hydrodynamic lubrication for zero-entrainment-velocity contacts based on boundary slip mechanism,” Tribology International, 128, pp. 89-95.

[25] Zhang, B. and Wang, J., 2016, “Enhancement of thermal effect in zero entrainment velocity contact under low surface velocity,” Proc. Inst. Mech. Eng., Part J, 230(12), pp. 1554-1561.

[26] Zhang, B., Wang, J., Omasta, M. and Kaneta, M., 2016, “Variation of surface dimple in point contact thermal EHL under ZEV condition,” Tribology International, 94, pp. 383-394.

[27] Aul, V., 2014, “Kontaktmodelle zur dynamischen Simulation vollrolliger Zylinderrollenlager,“ Ph.D. thesis, University of Kaiserlslautern.

[28] Chittenden, R. J., Dowson, D., Dunn, J.F., Taylor C.M. and Johnson, K.L., 1985, “A theoretical analysis of the isothermal elastohydrodynamic lubrication of concentrated contacts. II. General case, with lubricant entrainment along either principal axis of the Hertzian contact ellipse or at some intermediate angle,” Proceedings of the Royal Society of London. A. Mathematical and Physical Sciences, 397(1813), pp. 271-294.

[29] Pandey, R. K. and Ghosh, M. K., 1996, “Thermal effects on film thickness and traction in rolling/sliding EHL line contacts - an accurate inlet zone analysis,” Wear, 192(1), pp. 118-127.

[30] Zhu, D., 2013, Encyclopedia of Tribology, Springer, Boston, MA, Chap. Thermal Reduction of EHL Film Thickness.

[31] Wang, D., 2015, “Berechnung der Wälzlagerreibung aufgrund weiterentwickelter rheologischer Fluidmodelle,” Ph.D. thesis, University of Hannover.

[32] Poll, G., 1983, “Der Einfluss der realen Systemeigenschaften auf die Kraftschlussgesetze bei wälzender Relativbewegung,” Ph.D. thesis, Technische Hochschule Aachen.

[33] Zhou, R.S. and Hoeprich, M.R., 1991, “Torque of Tapered Roller Bearings”, Journal of Tribology, 113(3) , pp. 590-597.

[34] Biboulet, N. and Houpert, L., 2010, "Hydrodynamic force and moment in pure rolling lubricated contacts. Part 1: Line contacts," Proc. Inst. Mech. Eng., Part J, 224(8), pp. 765-775.

[35] Laukotka, E.M., 2007, “Referenzölkatalog,” 660, Forschungsvereinigung Antriebstechnik (FVA), Frankfurt am Main.

Nomenclature

Latin Letters

a, b	Semi-axes of contact ellipse
A, B, C	Vogel-parameters
$B_{\mathrm{ZH}}, C_{\mathrm{ZH}}$	Parameters for mixed lubrication
c_i	Fitting parameters for α_{p}^{*}
E	Young's modulus
$E' = 2\left(\frac{1-\nu_1^2}{E_1}+\frac{1-\nu_2^2}{E_2}\right)^{-1}$	Effective Young's modulus
F_{EHL}	EHL friction force
F_{B}	Boundary friction force
F_i	Implicit function of surface *i*
F_{n}	Normal force
F_{t}	Tangential force
G	Material parameter
h_c	Central fluid film height
H	Film height parameter
k_i	Fitting parameters of load-deflection relationship
l	Length of line contact
$\mathcal{L}$	Thermal load parameter
M_{B}	Torque of boundary rolling resistance
M_{EHL}	Torque of EHL rolling resistance
n, τ_0	Parameters of Carreau model
p	pressure
$p_{\mathrm{p}}, Z, \eta_{\mathrm{p}}$	Parameters of Roelands equation
p_0	Max. pressure
$\boldsymbol{P}_i$	Contact point *i*
$\boldsymbol{P}_{\mathrm{m}}$	Contact location
$\boldsymbol{r}$	Location vector
R	Radius
$R' = \left(\frac{1}{R_{\mathrm{x}}}+\frac{1}{R_{\mathrm{y}}}\right)^{-1}$	Equivalent Radius
$R_{\mathrm{x}}, R_{\mathrm{y}}$	Relative principle curvatures
S	Slide-to-roll ratio (SRR)
sgn	Sign function
t	Thickness outer ring
T	Body mass temperature
u_i	Velocity of surface *i*
$U, \tilde{U}$	Speed parameters
$u_0 = \frac{u_1+u_2}{2}$	Entraining velocity
u_{rel}	Relative surface velocity
W	Load parameter

Greek Letters

α_p^{*}	Viscosity-pressure coefficient
α_{V}	Coefficient of boundary rolling resistance
$\dot{\gamma}$	Shear rate
δ	Theoretical penetration
Δt	Time step size of simulation

$\Delta t_{\max}$	Maximum time step size of simulation
η	Viscosity
η_0	Viscosity at ambient pressure
$\Lambda = \frac{h_c}{\sigma}$	Film thickness ratio
μ_{B}	Boundary coefficient of friction
ξ	Angle between entrainment velocity and major axis of contact
σ	Composite root-mean-square roughness
τ	Shear stress
τ_{L}	Limiting shear stress (LSS)
ν	Poisson's ratio
ϕ	Load sharing ratio
ϕ_{th}	Thermal correction factor

Indices and Abbreviations

b	Boundary
c	Central
B1	Reference bearing (see sect. 4)
CO	Cone
DOF	Degree of freedom
EHL	Elastohydrodynamic lubrication
IR	Inner ring
LSS	Limiting shear stress
MBS	Multibody dynamics simulation
REB	Roller element bearing
SP	Sphere
SRR	Slide-to-roll-ratio
TO	Torus
OR	Outer ring
ZEV	Zero entrainment velocity

Surface Mutation of the Bearing Raceway During Electrical Current Passage in Mixed Friction Operation

Simon Graf[1], Bernd Sauer[2]

[1] *Institute of Machine Elements, Gears, and Transmissions (MEGT), s,graf@mv.uni-kl.de*
[2] *Institute of Machine Elements, Gears, and Transmissions (MEGT), sauer@mv.uni-kl.de*

Test results are presented which document the surface mutation of a bearing raceway of an axial bearing during passage of electrical current and operation in the mixed friction area. For the investigation of this matter, a combined mechanical and electrical load is applied to axial bearings of type 51208. For these experiments, the axial test setup of the modified four ball Apparatus, developed in the research project FVA 650 II, is used. The tests are interrupted at specific times and the raceway surface is measured. Therefore, the surface is first cleaned from the lubricating oil by means of an ultrasonic bath. The surface measurement is performed with a confocal microscope at four pre-defined points on the bearing raceway. In order to adjust the identical measurement position for each surface measurement a special recording piece was designed. After completion of the surface measurement the bearing raceway is moistened with lubrication oil and installed in the test bench for further testing. With this methodology it is possible to visualize and evaluate the changes of the measured bearing raceway spots over the test period.

Keywords – bearing currents, surface mutation, mixed friction, contact resistance, grey frosting

1. Introduction

Damages based on the passage of electric current in rolling bearings, such as a damaged raceway or discolored lubricants, have already been observed and described by *Punga* and *Hess* [1], *Fleischmann* [2] and *Keller* [3] since 1907. Based on these works, constructive measures could be developed, which first eliminated the problems of rolling bearing currents. With the increase of the use of high-frequency frequency converters and the associated increased occurrence of variable-speed drive concepts, undesired bearing currents occurred again (i.a. [4], [5]). The reason why these kinds of problems occur by this type of frequency converters is due to the typical steep voltage edges in combination with unfavorable grounding concepts. This leads to the fact that the in [1] described damages occur once again i.a. [6-8]. Figure 1 visualizes a selection of observed damages of bearing raceways and the used lubricant, as described and researched by a couple of researchers [9-13]. This shows the effect of the passage of electric current on the bearing raceway represented by ripples / flutings (1a) and craters (1b), as well as damaged lubricant through oxidation (1c) and discoloration (1d). Here, especially the interaction between the tribological system, defined by the lubricant and the friction condition, and the electrical behavior defined by it plays a decisive role.

The causal relationship between the lubrication condition in a rolling bearing and the kind of resulting rolling bearing current occurring was shown from *Radnai* in [10] and can be visualized and described clearly in figure 2.

There is a dependency between the amount of the occurrence of discharging currents, so-called EDM currents (electric discharge machining), per second, and the temperature is shown. A further boundary condition by that diagram is that the loaded bearing DL link voltage is constant. By increasing the temperature in the test system, the lubrication gap will be reduced, therefore the bearing changes its friction condition from full lubrication to mixed friction. This is shown in Figure 2 with an exemplary lubrication gap course using a second y-axis. The changing in the lubrication gap causes a retroactivity to the electrical system.

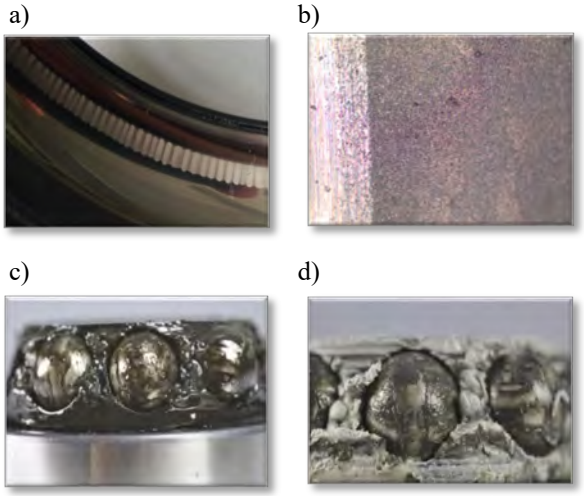

Figure 1: Damages based on electrical bearing currents a) Ripples / flutings b) grey frosting / craters based on electric discharge machining (EDM) c) oxidized lubrication grease d) discolored lubrication grease

By a high gap along with a full lubrication film, the lubricant works like an isolating capacitor. That means that the capacitor the impressed common-mode voltage, characterized by the charging of the capacitor by three voltage impulses followed by three discharging impulses with identical height, can completely hold in the lubricating film. By increasing the temperature, the lubrication gap decreases and so the lubrication film, regarded as the capacitor, is not able to hold the applied voltage completely. This circumstance results in discharging currents in the form of sparks between the raceway and the rolling element. This behavior can be shown in the fact that the three-step build-up of the common-mode voltage is not possible and the voltage collapse during

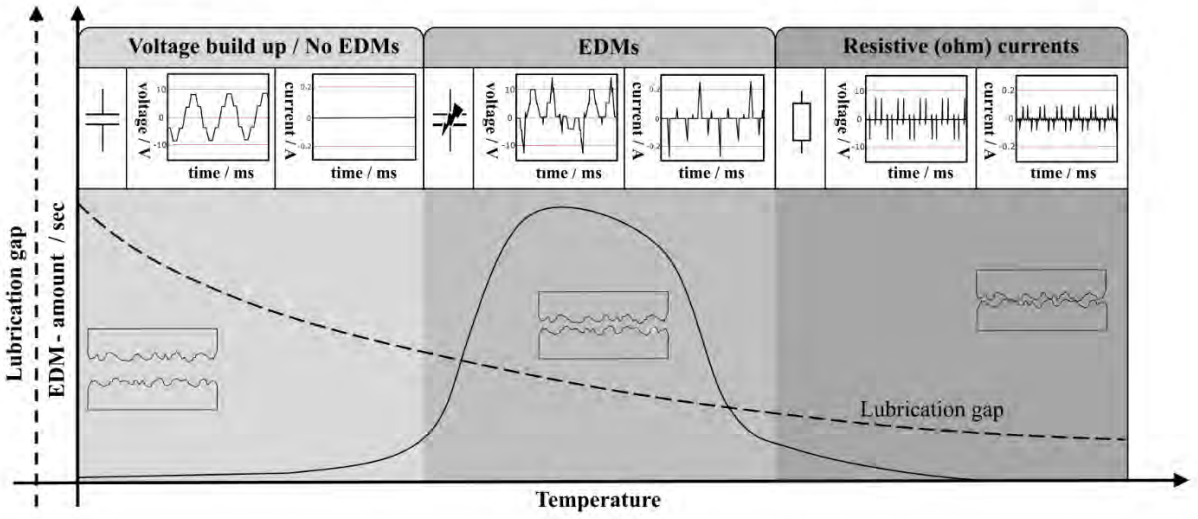

Figure 2: Exemplary illustration of the number of discharge currents (EDM) per second in case of lubrication gap variation due to temperature increase at constant test voltage and illustration of the so defined electrical state and the resulting current / voltage curves

the build-up. As a result of the breakdown, a bearing current occurs. A further reduction of the lubrication gap leads to an operation of the rolling bearing in mixed friction conditions. From the electrical point of view that condition means that the bearing can no longer be described as a capacitor as it is not able to hold the DC link voltage. Instead the voltage flows purely ohmic over the in touch coming roughness peaks. A voltage-build-up as described before is not possible in this condition.

Furthermore [15] could show that a similar graph (corresponding to Figure 2) could be generated by constant temperature and thus a steady lubrication gap height. Therefore, the applied voltage in the system was varied and the electrical system was described by a complex electrical resistance, the impedance. This allows an assessment of the electrical behavior of the resistance (inductive, ohmic, capacitive) via the phase angle. Independent of that, based on the given operation point in combination with the established tribological condition, different kinds of damages can occur more frequently, such as:

- Crater formation [6], [9], [10], [16]
- Ripples [11], [12], [17]
- Changes in the lubricant [6], [9], [10], [13]

which have been investigated in various publications.

The following researches have set the focus to an operation in mixed friction and an associated predominant or pure ohmic behavior of the bearing currents. Conform to *Radnai* [10] EDM discharging is not to be expected. The resulting effects of the additional electrical energy contributed to the system by the passage of electrical current are investigated on the basis of changes in the roughness parameters of the raceway surfaces. Significant for this is in addition to the applied voltage and the discontinuing current, the ohmic contact resistance [18]. This is closely related to the differences between the contact surfaces of contact. Therefore is a difference between the apparent contact area, the supporting contact area, and the effective contact area [19]. The differences between these areas are visualized in Figure 3 a). The inequality between the apparent contact and the supporting contact area depends on the point of view of the surface structure. The assuming of ideal plain contact partners leads to the apparent contact area, considering the real roughness of the surface results in the supporting contact area.

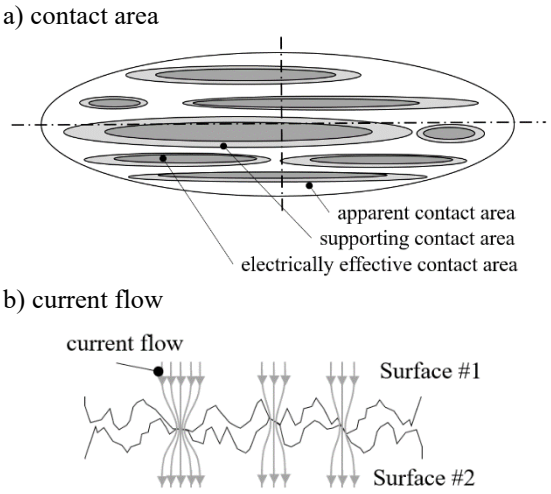

Figure 3: Different parts of the contact resistance a) kinds of contact areas b) current flow throw the constriction resistance

The electrically effective contact surface is a part of the supporting contact surface and ultimately means the electrically active conductive part of the surface (so-called A-spots). The difference between the electrically effective contact area and the supporting contact area is caused by the existence of impurity layers (such as oxidations) on the surface [20]. This leads to a reduction in the electrical conductivity of the contact partner. By considering these, the actual contact resistance is an addition from the surface contamination

resistance based on impurity layers and the constriction resistance. The visualization of the constriction resistance is shown in Figure 3 b). This resistance is evoked due to the roughness in the contact zone and the resulting constriction of the streamlines at the electrical transition between the two components [19]. On the basis of the described electrical properties, corresponding effects on the real surface structure are to be expected, which could be detected and observed during the test period.

2. Methodology and experimental setup

The goal of the presented experimental series is to show and document the influence of the passage of electrical currents to the surface mutation on the raceway of the tested rolling bearing during the experimental period. A further boundary condition is, that the experiment is carried out in the tribology state of mixed friction, so it can be assumed, that only ohmic currents will occur (cf. Figure 2). As a test sample, an axial rolling bearing of the type 51208 (40/68/19) with 14 rolling elements is used. The test samples are loaded with combinations of mechanical (Chapter 2.1) and electrical (Chapter 2.2) loads in a modified four-ball apparatus, the so-called Gerät zur erweiterten Schmierstoffanalyse short GESA (developed in [13] first results in [15] and [21]). The principle test sequence is shown in Figure 4. At predefined test points, the experiment will interrupt and the axial rolling bearing will be disassembled from the test rig to measure the surface with a confocal microscope (Chapter 2.3).

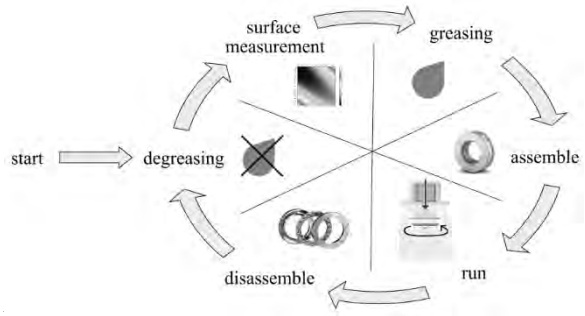

The sample will initially be cleaned up from corrosion protection by an ultrasonic bath with isopropanol. Based on this, the surface is measured in its new state with the confocal microscope. After that, the bearing raceways will moisten with the lubricant, assembled to the test rig and the test run can be started. After a predefined time, the experiment will interrupt again, the axial rolling bearing disassembled, degreased from the lubricant, and remeasured at the confocal microscope. Then the raceways will lubricated with new lubricant, assembled to the GESA and the experiment continued. To make sure that during the whole testing period always nearly the same surface section is measured with the confocal microscope over, a sample holder was constructed which arranges and positions the sample to the used microscope (cf. Chapter 2.3). The cycle described here was carried out in the rhythm of 2h / 2h / 2h and 16 h over a total duration of 72 h.

Furthermore, as a reference test, only mechanical load was applied to estimate the mechanically caused wear of the surfaces. After that, tests were carried out at three different voltage levels (table 1) and a constant switching frequency.

2.1. Mechanical design and boundary conditions

Test bench description

For the following investigations, a model system test rig developed in [13] with the designation GESA (Gerät zur erweiterten Schmierstoffanalyse) was used. This is a test bench adapter, which can be mounted in the test space of a common four-ball apparatus. With this component, shown in Figure 5, an axial rolling bearing can be loaded with a combined electrical, mechanical, and/or thermal load. This test bench has been used for various tests in the context of lubrication examination in combination with mechanical and electrical loads i.a. [13], [15], [17] and [20].

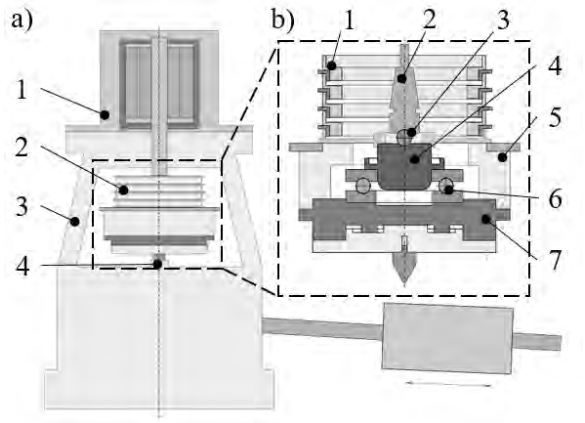

Figure 5: Functional module Gerät zur erweiterten Schmierstoffanalyse GESA a) mounted in the four-ball apparatus (1 driving motor / 2 GESA / 3 housing / 4 axial load punch) b) sectional view of GESA (1 distributing ring / 2 driving shaft / 3 centering ball / 4 shaft / 5 housing / 6 tested bearing / 6a rotating ring / 6b rolling element / 6c stationary ring / 7 bearing ring holder)

With a frictional connection, the driving shaft (b 2) will be connected to the driving motor (a 1) of the four-ball apparatus. The shaft (b 4) is driven by the driving shaft (b 2) over a form closure bygone the distributing ring (b 1). Over the centering ball (b 3) the shaft (b 2) will be centered in its radial direction. By means of a circular line contact defined by the centering ball (b 3) and tapered locating holes on the drive shaft (b 2) and the shaft (b 4), a low-vibration operation of the system is realized. The tested bearing (b 6) is mounted by press fits between the shaft (b 4) and the rotating ring (b 6a), and between the bearing ring holder (b 7) and the stationary ring (b 6c). The distributing ring is an in-house development with up to six distribution channels due to its modular construction (in Figure 5 b 1 five are shown). This is connected to the shaft (b 3) via a flange screw connection. The lowest channel of the distributing ring (b 1) is directly electrical connected over the shaft with the rotating ring (b 6a) of the tested bearing (b 6). Thus the electrical load has to be imprinted via

this channel in the form of the defined voltage - time signal. Furthermore, over this channel a measurement of the bearing impedance is possible, too. The resulting current path results from the contacting and insulation of the individual components to each other over b 1 → b 4 → b 6a → b 6b → b 6c → b 7 → ground. The other components of the GESA are isolated from the current path, by synthetic and ceramic materials. At the GESA the force (0 up to 12 kN), the rotation speed (100 up to 6000 rpm), and the temperature (-10 °C up to 120 °C), of the shaft (b 4) and the bearing ring holder (b 7) can be varied.

Mechanical load

With the modified four-ball Apparatus an axial mechanical load of **2400 N** and a rotational speed of **1000 rpm** is applied to the axial bearing. That results in a maximum Hertzian pressure of ~**1260 MPa** with a Hertzian contact area of **0.19 mm²** on the raceway surface. In combination with the used lubricant, these conditions lead to an operation of the rolling bearing under mixed friction. In this case, the bearing conducts the current purely ohmic.

Lubricant

For lubrication, the non-additive mineral oil OF1.1 (density 0.887 g/cm³, kinetic viscosity 372.3 mm²/s both at 20°C) from the research project FVA 650 II [13] was used. It was selected because strong interactions between the test oil and the surface, as can be expected with an additivated high-performance lubricant, should be avoided. The reason for this approach is, that the influence of tribological active layers to the contact resistance, especially to the surface contamination resistance, should be minimized. This ensures that the influence of the lubricant on the surface mutation is further reduced. Based on this, an investigation of the surface mutation is possible and dependence of the additives in the lubricant is largely excluded.

2.2. Electrical system

Generally, the electrical loads applied to the rolling bearings, are mainly defined by the combination of the driven electric motor with his corresponding frequency converter [6], [7]. By the presented test bench, the electrical voltages and currents from the driving system (Figure 5 a 1) are isolated from the tested bearing. At the Institute of Machine Elements, Gears, and Transmissions (MEGT) at the Technical University Kaiserslautern a series of synthetic frequency converters are available for imposing the electrical bearing load. These are developed and well-tried in the context of the research project 650 I [22] sponsored by the Forschungsvereinigung Antriebstechnik (FVA). The synthetic frequency converters are not used to control the driving asynchronous machines, but they generate variable bearing currents that can be applied directly to the test bearing. By using this methodology, it is possible to vary the mechanical and electrical load on the test object independently of each other. In contrast to a real asynchronous motor, the applied electrical loads to the test bearing can varied independently of each other. These variable electrical parameters are the DC link voltage (up to 60 V), the switching frequency (up to 50 kHz), and the basic electrical frequency of the pulse width modulated voltage (up to 100 Hz). With this system, it is possible to apply different bearing currents independently of the mechanical boundary conditions to the test object.

Table 1: Electrical test matrix including classification parameters for the electrical load

	L6 20 V	L3 40 V	L1 60V
Bearing DC link voltage / V	20	40	60
Bearing voltage / V	3.3	6.6	10.0
Bearing current / A	0.2	0.4	0.6
Bearing current density / A/mm²	0.075	0.15	0.225
Bearing apparent power / VA	0.66	2.64	6

For all the following experiments, a switching frequency of 10 kHz with an electrical basic frequency of 50 Hz was for all selected. The bearing DC link voltage was constant during one test run per test object and was varied between **0 V** / **20 V** / **40 V** and **60 V.** The resulting bearing voltages and bearing currents are summarized in Table 1. Furthermore, the usual evaluation parameters for the electrical bearing load such as the bearing current density conforming to [7] and the bearing apparent power according to [12] are given for the respective load levels.

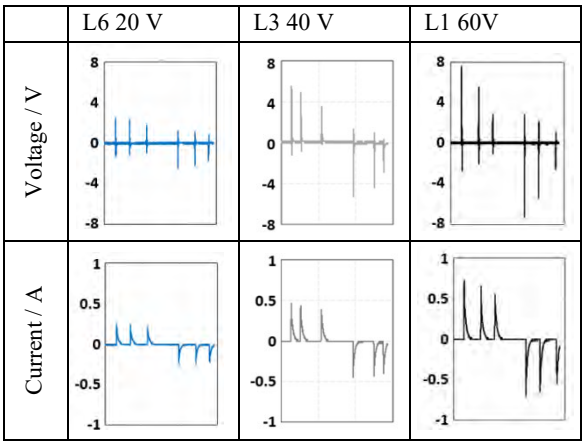

Figure 6: Reached bearing voltages and bearing currents per test series for a voltage build-up

The resulting bearing voltages and bearing currents are visualized for one voltage build-up in Figure 6.

2.3. Surface measurement

A confocal microscope from the company µsurf is used for the measurement of the defined surfaces of the test objects. In contrary to an optical microscope,

which completely illuminates an object as uniformly as possible, a confocal microscope focused the illumination only to a small observing point [23]. To measure an area instead of a point, the so-called Nipkow-disk is used. These disks consist of a hole matrix, which is placed in such a way that the scattered light is not superimposed. Furthermore, a camera is used instead of a simple sensor. By fast rotation of the Nipkow-discs, a flicker-free image can be recorded. Individual focus images are created by varying the distance to the surface. These single images will then be combined to a full parametric 3D-surface. The vertical traverse path must be at least large enough to cover the area from the lowest to the highest point of the surface to be measured [24].

The editing and finishing of the measured surfaces are done with the commercial software MountainsMap © (a product of the company µsurf too). In this step, the system first searches for so-called artifacts, such as reflections or strong measurement deviations of the surface measurement, and eliminates them by means of interpolation. Based on this, the shape is then separated from the roughness for further evaluation. So a plane is created with the superposition of the roughness with the waviness without the shape of the raceway.

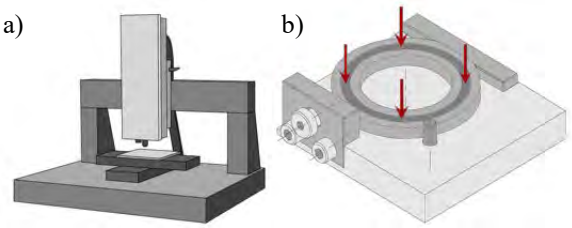

Figure 7: Surface measuring equipment a) confocal microscope with positioning stage which the sample is placed b) sample holder with visualization of possible measurement points

To ensure a better comparison of the roughness at different recording times it is necessary to observe nearly the same surface area on the raceway over the entire testing period. For this function, a sample holder was developed, which positiones and aligns the bearing rings to the confocal microscope. After the alignment of the sample holder at the positioning stage of the confocal microscope, the sample is exactly positioned. This makes it possible to observe the identical surface cutout via automated measuring programs. This device positions the bearing ring over a flat surface and a contact point. Also, the bearing ring is fixed in the sample holder by a spring-loaded pressure element. To clearly define the position, an approximately 1 mm deep circular segment on the outer diameter of the bearing rings is removed by machining, thus creating a plane surface based on which positioning can be carried out. The measured area of the subsequently examined surfaces is 800 µm x 800 µm, by using an objective with twentyfold magnification. The area of the measured surface is defined by 512 x 512 data points.

3. Results and discussion

Based on the previously presented methodology in combination with the presented test benches, the results of the test series are presented and discussed below. The following two lists represent a short compact repetition of the mechanical and electrical boundary conditions used for the experiments.

Mechanical load (constant)

- Axial load: 2400 N
- Rotational speed 1000 rpm
- Hertzian pressure: 1260 MPa
- Hertzian contact area: 0,19 mm²

Electrical load (variable)

- Bearing DC link voltage: 20 V / 40 V / 60 V
- Bearing voltage: 3,3 V / 6,6 V / 10 V
- Bearing current: 0,2 A / 0,4 A / 0,6 A
- Switching frequency: 10 kHz

At this point it should be mentioned again that a reference test was first run under pure mechanical load, on the basis of which the results from the combined mechanical and electrical loads can be compared and classified.

3.1. Typical surface parameter

For a first overview, common surface parameters like

- the mean arithmetic height / *Sa*
- the average square height / *Sq*
- the maximum height / *Sz*

where calculated with the analyzing software MountainsMap, based on the measured surfaces with the used confocal microscope in combination with the developed sample holder. The results of this examination over the testing period are shown in Figure 8. The highlighted points and squares illustrate the real measurement points during the test period. To these moments the experiment was interrupted and conform to the visualized test methodology shown in Figure 4 (dissemble → degreasing the stationary ring → surface measurement → greasing à assemble → start the next cycles) was carried out.

It can be seen in Figure 8 a), that under pure mechanical loads the mean arithmetic height *Sa* and the average square height *Sq* are nearly constant over the testing period. Based on the selected mechanical load level and under consideration of the short experiment duration (72 h) such a course of the surface parameters can be expected by the pure mechanically loaded reference test.

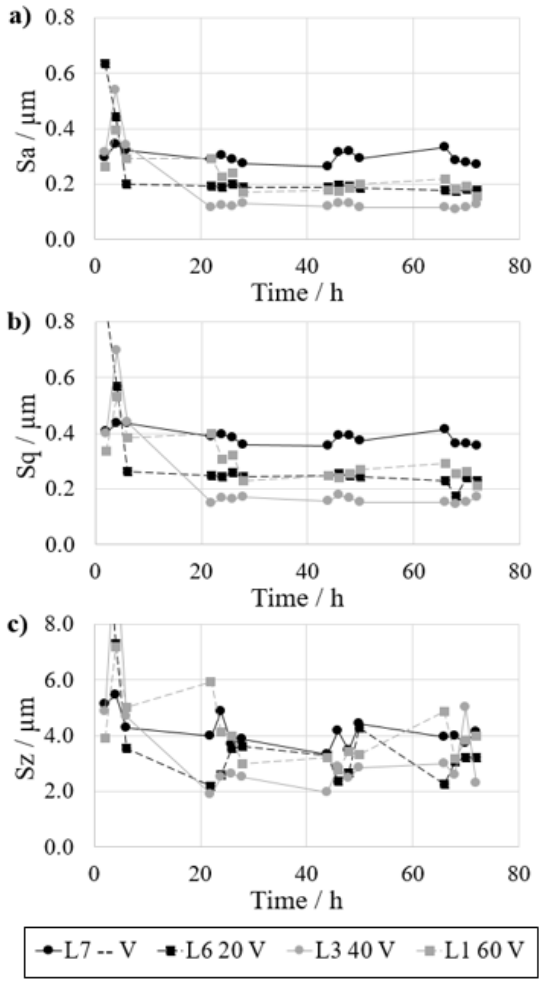

Figure 8: Changing of selected surface parameter over the testing period with highlighted measurement points, naming conform to table X (a) Sa / mean arithmetic height b) Sq / average square height c) Sz / maximum height)

By adding an electrical load, *Sa* and *Sq* (Figure 8 a and b) changes at the very beginning and is on a constant level for the rest of the period. Both of those values decrease more than under the pure mechanical load. This behavior occurs independently of the electrical load level. A clear dependency between the amount of the applied bearing voltage and the arisen surface parameter cannot be detected by this kind of evaluation. The examination of the parameter *Sz* fluctuates very strongly over the test time. For an assessment of the electrical influence on the surface change, this parameter seems to be of little significance. The cause of this can be shown by the definition of the surface parameter *Sz* itself [25]. It is calculated as the length between the lowest surface point and the maximum of the profile. This makes this parameter very disturbing and susceptible to scattering which can also be observed in the evaluation. Furthermore, it can be monitored, that there is no significant influence of the duration of the test cycles (comparing the difference in changing the surface parameters between a 2 h run to a 16 h run) to the calculated surface parameters. Thus, it can be assumed that there is only a little interaction between the methodology of the experiment and the results of the surface measurement.

Even in this form of analysis, it can be assumed that the surfaces are smoothed as a result of the passage of electric current through the bearing. This effect can be observed more detailed by considering the temporal evolution of the histograms of the surface height distribution, shown in the next chapter.

3.2. Surface histograms and contour plots of the surface highness

Building on the previous consideration, more detailed analyses are performed in this chapter. Therefore the influence of the different electrical load levels to the surface mutation will be analyzed and visualized with contour plots. In addition to that, histograms of the surface heights are given too.

Furthermore, an estimation of the surface temperature in the contact area will be done. This estimation is based on electrical surface mutation and the calculated required temperature to deform the roughness in such a manner.

Contour plots

Figure 9 shows the contour plots of the surface heights to selected measure points for the pure mechanical loaded reference test run (L7 –V) and the contours of the experiment with the applied bearing DC link voltage of 60 V (L1 60V). First of all, it should be pointed out again that in the case of the visualized surfaces, the shape of the raceway was filtered and the microscopic image was taken on the raceway. For better comparability, the median plane of roughness is used as a reference plane in the figures. Thus several things can be shown from Figure 9. On the one hand, the function of the positioning device (Chapter 2.3) can be demonstrated because characteristic surface structures can be observed over the entire test duration and the associated mutations on the raceway can thus be described. Over this, the difference in the roughness characteristics between the two tests is clearly visible. The contour plots of the pure mechanical reference test show only small changes in the surface structure and the roughness heights. Compared to that, the results of the L1 60 V experiment, the roughness is reduced significantly (compare Figure 9 L7 –V to L1 60 V at 72 h) and it seems that the forming apparent contact surfaces are more planar.

Apart from this, during the experiments, the typical EDM craters on the measured surface cutouts could not be detected. That indicates an operation in mixed friction on the selected mechanical boundary conditions.

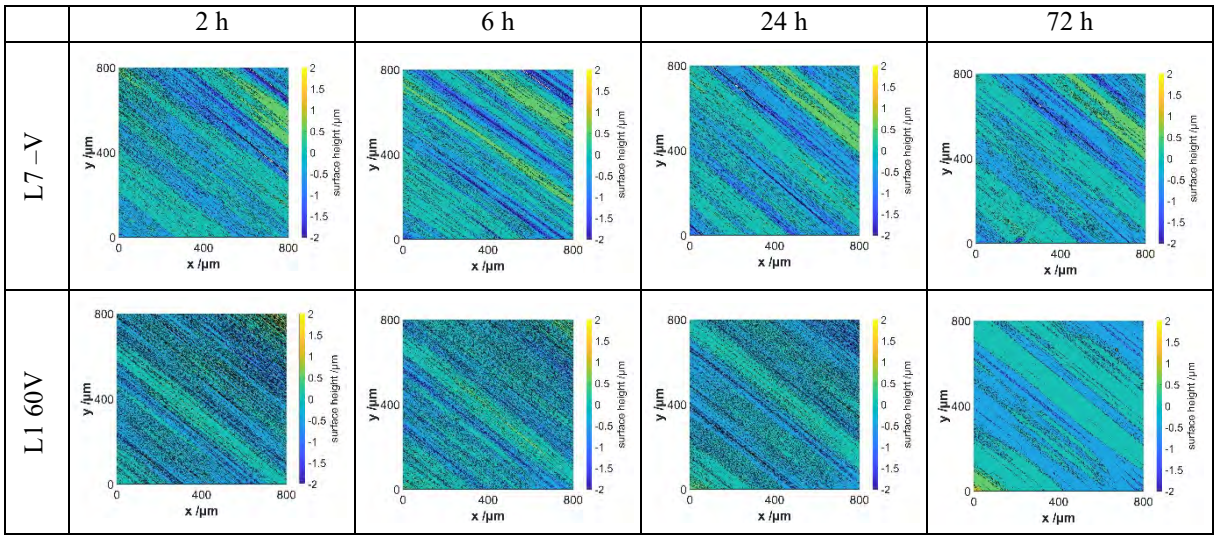

Figure 9: Conform to Chapter 2.3 revised surface contour plots (i.a. shape filter) at selected measurement points for nearly the same surface cutout for pure mechanical (L7 –V) and an exemplary combined mechanical electrical load (L1 60V)

Surface histograms

The histograms of the surface heights of the respective test series provide further information on the surface changes that occur. These are shown in Figure 10 for selected points in time. As with the contour plots, the surface data of the histograms are converted concerning the ideal center plane in order to increase comparability. All histograms of the tests with only mechanical loa d (L7 –V) show a similar shape. With increasing testing time, a small change in the variance (distribution becomes narrower) can be determined. This effect can be seen, when the surface after a testing time of 2 hours and 6 hours is compared. This results in a reduction of data points in the range of about 1 µm. The reason for this is the plasticizing of the highest roughness peaks and shows a typical running-in of a bearing raceway. Again, these data serve as a reference for further consideration of the influence of the passage of current in mixed friction.

When viewing the histograms of the mechanical-electrical test series, the histogram of the series L6 20V at 2h has to be regarded first. There, an incorrect surface measurement with the confocal microscope happens at the specific evaluation point. That is the reason, why the shown data points are strongly noised in such a manner that a reconstruction of the measured surface was no more possible. An influence on the following measurements can be excluded, based on the further course of the surface parameters like *Sa* and *Sq* (Figure 8) and the histograms (Figure 10) of the specific test series (L6 20V). But for the sake of completeness, this noisy histogram is also shown in Figure 10.

While the surface only slight changes in the mechanical reference test cycles (cf. Figure 8 a, b, c; Figure 9 L7 –V Figure 10 L7 –V), a huge difference can be seen in the histograms of the test cycles with the additional electrical load. The clearest effect we see throw the super-position of the mechanical load with an electrical load is that this leads to a strong clustering of the surface heights and a significant reduction of the variance. Furthermore, it seems the range in which the data points are located is also reduced. The range corresponds with the surface parameter *Sz*. In the progression of the *Sz* parameter (see Figure 8) this behavior cannot be detected as clear as in the histograms of the load cases. The reason for this is that al-ready one outlier can cause noise to the maximum height. Furthermore, from the range paired with the variance, it can also be shown that no EDM induced craters are present on the surfaces. These craters would lead to strong outliers on the edges of the histograms, but these are not visible in the figures. Based on these observations, the pure operation in mixed friction can still be assumed.

A clear tendency between the height distribution and the applied electrical load cannot be deduced from the histograms either. As expected, the observed effects of the surface mutation are least pronounced by the lowest electrical load level (L6 20V). This effect can be shown most clearly by clustering the data points around the center plane of the height distribution according to Figure 10 L6 20V 6h / 24h / 72h. This is more distinctive at L3 40V than at L1 60V and L6 20V. Thus, the smoothest surface is achieved with L3 40V. By consideration of the nearly same initial surface distributions (compare Figure 10 L3 40V und L1 60V booth at 2h) of the test cycels L3 40V and L1 60V it seems, that this behavior based on the higher electrical load level by L1 60V is physically illegitimate. Possible other reasons, instead of the differences in the initial surface distribution, for this divergence, are influencing parameters to the contact resistance in the contact between the bearing rings and the rolling elements. This is mainly due to different concentrations of non-conductive elements (e.g. oxides) on the surface and the resulting higher impurity film resistance.

To get more information about the influence of the impurity film resistance to the surface mutation, it is necessary to analyses the chemical elements on the surface in more detail. This is the subject of further research

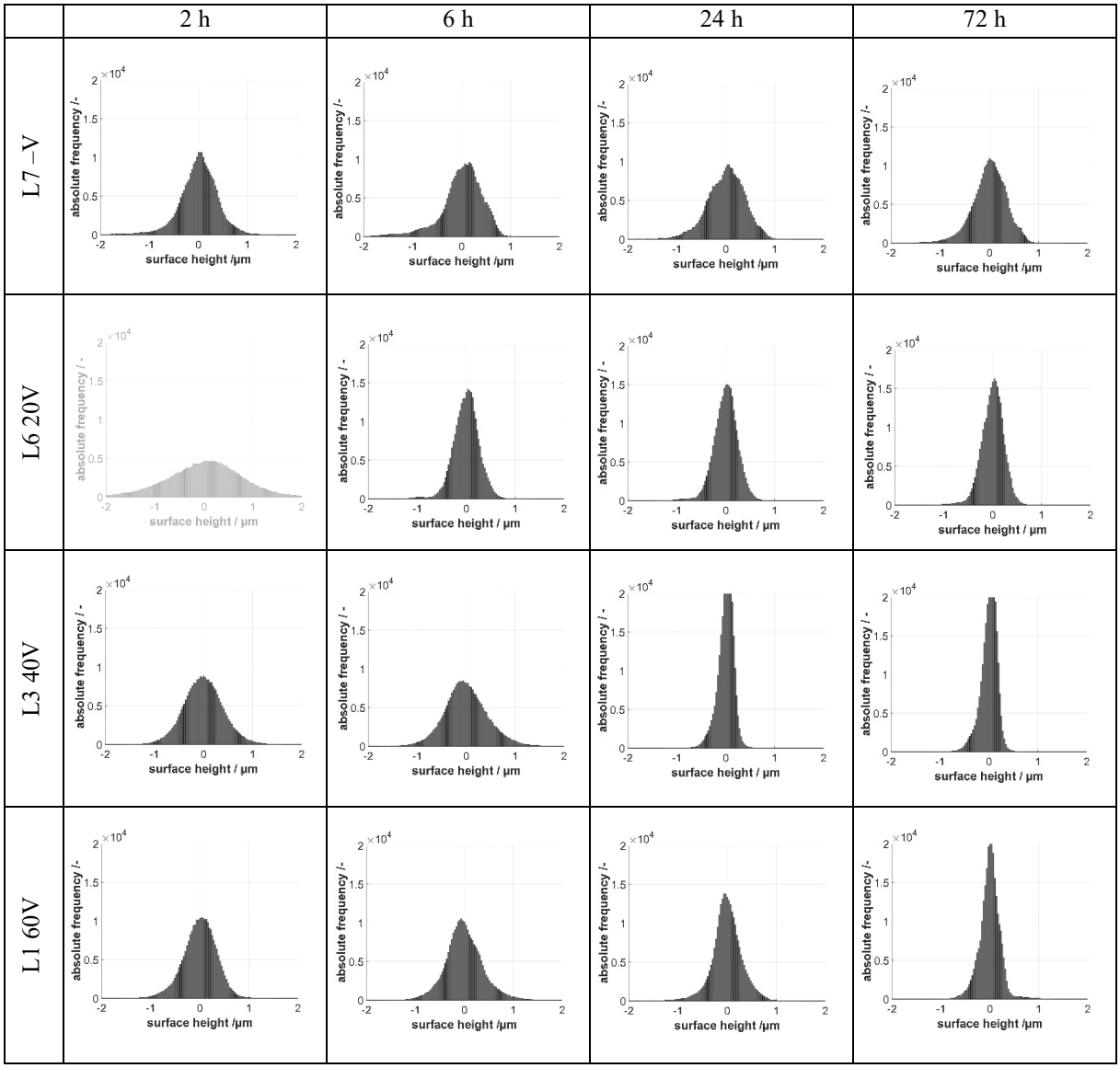

Figure 10: Histogram plots of the surface heights based on the conform to Chapter 2.3 revised surface (i.a. shape filter) at selected measurement points for nearly the same surface cutout for pure mechanical (L7 –V) and the combined mechanical electrical loads (L6 20V / L3 40V / L1 60V)

Estimation of surface temperature

The evaluations of the experiments show, that the rolling contact surfaces get smoother and that this effect occurs as a result of the electrical current passage in an operation of mixed friction. As the main cause of this observation, the local electrical current heat loss that is generated by the passage of the current over the contact resistance between the contact bodies can be assumed. This additional thermal energy leads to a reduction of the yield stress as a result of thermal softening. This allows earlier plastic coating of the roughness peaks, resulting in a smoother surface (compare Figure 9 and 10 at 2 h and 72 h). As a result of the thermal softening, the contact area will increase by the same mechanical load, and this leads to a decrease of the contact resistance. By the reduction of the local contact resistance, less current heat loss will occur [18]. Both of these effects, the increase of the contact area by additional thermal energy and the decreasing of the contact resistance whereby less current heat loss occurs, leading to thermal, electrical, and mechanical equilibration of the surface mutation.

Based on that assumption as a result of the observation of surface changes, the hereby introduced heat energy could be estimated by calculating the thermal softening which is necessary to deform the surface. One method to calculate the softening is to use mathematical material models. A tried and tested material model, which considers thermal effects is the Johnsen Cook material model [25]. This is an empirical model based on experimentally determined material parameters. The Johnson-Cook model gives an equation for the yield stress (equation 1) under consideration of three separate coupled terms.

The first one descript the influence of the plastic strain on the yield stress. The second term takes care of the consideration of the hardening effect by strain rates and the last give the reduction of the yield stress by thermal softening. A further description of this model and the experiments that are queried in order to get the necessary material parameters, are given in [26] and [27].

$$\sigma_F = \left[A + Be_p^n\right]\left[1 + C\ln\left(\dot{e}_p/\dot{e}_0\right)\right] \ldots \\ \ldots \left[1 - \{(T - T_r)/(T_m - T_r)\}^m\right] \qquad \textit{(Eq. 1)}$$

σ_F	von Mises yield stress	$\dot{e}_p$	Plastic strain rate
A	Yield strength	$\dot{e}_0$	Applied strain rate
B	Hardening coefficient	T	Applied temperature
e_p	Plastic strain	T_r	Environmental temperature
n	Hardening exponent	T_m	Melting temperature
C	Strain rate coefficient	m	Thermal softening coefficient

For the following considerations, only the term describing the thermal softening is relevant. This descript the thermal softening as a function of the applied temperature, the environmental temperature, and the melting temperature of the material. Furthermore, an experimental determination of the thermal softening coefficient is needed too. The needed softening parameters from a 100Cr6 bearing steel can be taken form [27] and are given in the following list:

- Yield strength / A = 2033 MPa
- Environmental temperature / T_r = 20 °C
- Melting temperature / T_m = 1500 °C
- Thermal softening coefficient / m = 1.03

The resulting dependence of the yield strength regarding temperature is illustrated in Figure 11. Assuming that the highest Hertzian surface pressure (1260 MPa) leads to plastic deformation. The surface temperature must be around 600°C in order to allow the plastification of the surfaces under the given mechanical load. The higher local pressure due to the rough contact compared to the Hertzian pressure was not considered in this assumption.

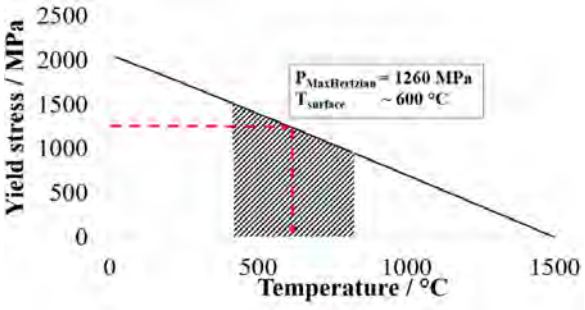

Figure 11: Thermal softening of a 100Cr6 approximated conforming to Johnsen Cook material model

4. Conclusion

Experimentally determined results of surface changes of axial bearings under mechanical and combined mechanical-electrical load were presented. The operation of the bearings was deliberately set to mixed friction, and based on that, EDM currents can be avoided and only ohmic currents will occur. During the experiments, a clear influence of the introduced electrical load on the surface structure of the bearing raceways can be shown.

By calculation of the arithmetic mean of the respective surface parameters from the initial states (2 h measurement point) as reference values, the superposed electrical load leads to a change of the mean arithmetic height *Sa* of 41 % up to 58 % and a changing of the average square height *Sq* between 38 % and 54 %. Under consideration of the changes in the surface parameters of the pure mechanical reference test cycle from about 6% between the initial state and final state the values of the combined mechanical-electrical test cycles are a strong indicator for the relationship between the additional electrical loads and the occurred surface mutation. For the respective load cases, the changes of the surface parameters are documented in table 3. Due to the fluctuating course of the maximum height *Sz* during the test cycles, similar interpretations such as the parameters *Sa* and *Sq* could not be made.

Table 3: Comparison of changes in surface parameters from initial to final state

		L7 –V	L6 20 V	L3 40 V	L1 60 V
Sa	2 h	0.29	0.63	0.31	0.21
	72 h	0.27	0.17	0.12	0.15
	change*	6 %	41 %	58 %	48 %
Sq	2 h	0.40	0.84	0.39	0.33
	72 h	0.35	0.23	0.17	0.21
	change*	6 %	38 %	54 %	44 %
Sz	2 h	5.11	12.50	4.86	3.90
	72 h	4.15	3.20	2.28	3.99
	change*	10 %	31 %	51 %	14 %

*related to the mean value of the condition 2h without the results from L6 20V

Generally it should be noted that the calculated surface parameter are in different kind susceptible to outliers of the measured data points [25]. This can be shown by comparing the histograms in Figure 10 L6 20V and L1 60 V at 72 h. Both measure points have similar values for the mean arithmetic height *Sa* (table 3 L6 20V / *Sa* = 0.17 and L1 60V / *Sq* = 0.15) and the average square height (table 3 L6 20V / *Sq* = 0.23 and L1 60V / *Sq* = 0.21), but are significant differing in the clustering of the data points shown in the respective histograms. This circumstance makes it necessary to include the histograms in the evaluation.

It is conspicuous that no classic damages occurred with the selected mechanical electrical load cases. Instead of this, the surfaces get plainer than in the mechanical reference test. This observation was shown by using contour plots and histograms at selected test times. With these types of diagrams, the changing of the surface parameters can be illustrated in more detail, instead of the curves of the single parameters over the testing time. The strong clustering of the surface data points around the ideal middle plane becomes evident in the histograms. It can also be concluded from the surface plots and the histograms that no EDM discharges with associated cratering on the surfaces occurred, as envisaged in the experimental setup. With this experiment, it could be shown that a different surface mutation occurs during operation in mixed friction than by an operation with full film lubrication and EDM currents. It should be noted that both, EDM discharges and ohmic currents in mixed friction, resulting in a matting of the raceway (Figure 12 a) grey raceway EDM b) grey raceway ohmic). The phenomenon of the grey raceway is referred to in the technical literature as so-called grey frosting. Differentiation according to the electrical effect leading to it has not yet been made. However, this seems advisable in the course of the investigations carried out, since a similar macroscopic effect is based on two different mechanisms and thus requires a more detailed specification. For this purpose, it is proposed to supplement the phenomenon of grey frosting with the responsible electrical effect (grey frosting based on EDM or based on ohmic currents).

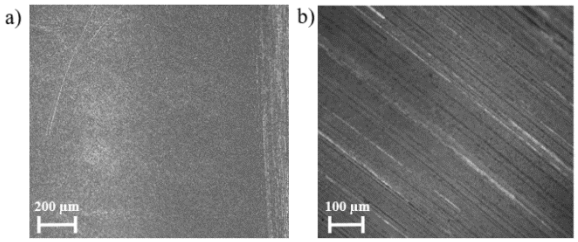

Figure 12: Grey raceway based on different electrical effects a) EDM currents b) ohmic currents

Another observation of the experimental results is, that the transformation of the surface to a stable state from surface mutation and applied electrical load is lastly finished after the measurement points 6 h or 24 h. This corresponds between 216M and 864M switching cycles of the synthetic frequency converter.

A first estimation of the local surface temperature was made based on the relationship between the occurring electrical system in mixed friction and the current heat losses in the contact resistance caused therein. For this purpose, assumptions were made regarding the thermal softening of the bearing ring material, and effects such as inhomogeneous pressure distributions based on the rough surfaces or the influence of tribological layers were deliberately neglected. Therefore it is only a first approximation that has to be specified in more detail in the course of further research based on the available findings.

Acknowledgment

This work was carried out within the framework of the project "Model for the determination of the thermal stress of lubricants as a result of mechanical and electrical loads in rolling contact" (Project No. SA898/25-1), which was financially supported by the German Research Foundation (DFG) e.V.

Special thanks are also due to the company Digital Surf for providing the software MountainsMap

References

[1] Punga, F.; Hess, W.: Eine Erscheinung an Wechsel- und Drehstromgeneratoren, In: Elektrotechnik und Maschinenbau, Nr. 25, S. 615-618, 1907.

[2] Fleischmann, L.: Ströme in Lagern und Wellen. In: Elektrische Kraftbetriebe und Bahnen VII (1909), Nr. 18, S. 352-353

[3] Kellner, J.: Esetek az elektrotechnikai gyakorlatból. Csapágyáramok. (E: Cases from the electrical engineering practice. bearing currents). In: Elektrotechnika Magazin 4 (1911), Nr. 21, S. 309–312

[4] Ammann, C. ; Reichert, K. ; Joho, R. ; Posedel, Z.: Shaft voltages in generators with static excitation systems-problems and solution. In: Energy Conversion, IEEE Transactions on 3 (1988), Nr. 2, S. 409–419.

[5] Kerszenbaum, I.: Shaft currents in electric machines fed by solid-state drives. In: Industrial and Commercial Power Systems Technical Conference, 1992. Conference Record,

Papers Presented at the 1992 Annual Meeting., IEEE Conference Record of the, 1992, S. 71–79

[6] Preisinger, G.: Cause and effect of bearing currents in frequency converter driven electrical motors: Investigations of electrical properties of rolling bearings, Dissertation, Technische Universität Wien, Wien, 2002.

[7] Muetze, A.: Bearing currents in inverter-fed AC-motors, Dissertation, Technische Universität Darmstadt, Shaker, Aachen, 2004.

[8] Zika, T.: Electric discharge damaging in lubricated rolling contacts, Dissertation, Technische Universität Wien, Wien, 2010.

[9] Gemeinder, Y.: Lagerimpedanz und Lagerschädigung bei umrichtergespeisten Antrieben, Dissertation, Technische Universität Darmstadt, Darmstadt, 2016.

[10] Radnai, Benjamin: Wirkmechanismen bei spannungsbeaufschlagten Wälzlagern. Dissertation, Technische Universität Kaiserslautern, 2016, Maschinenelemente und Getriebetechnik Berichte Bd. 20/2016, ISBN 978-3-95974-029-6

[11] Furtmann, A.: Elektrisches Verhalten von Maschinenelementen im Antriebs-strang, Dissertation, Universität Hannover, Hannover, 2017.

[12] Tischmacher, H.: Systemanalysen zur elektrischen Belastung von Wälzlagern bei umrichtergespeisten Elektromotoren, Dissertation, Universität Hannover, Hannover, 2017.

[13] Bechev, D.; Weicker, M.: Methodik zur praxisnahen Charakterisierung von elektrischen Schmierstoffeigenschaften zur Verbesserung der rechnerischen Vorhersage von Lagerströme: FVA-Forschungsvorhaben 650 II Schädlicher Stromdurchgang II, (Forschungsheft wird publiziert), Frankfurt am Main, 2020.

[15] Gonda, A.; Capan, R.; Bechev, D.; Sauer, B. The Influence of Lubricant Conductivity on Bearing Currents in the Case of Rolling Bearing Greases. Lubricants 2019, 7, 108

[16] Bechev, D.; Kiekbusch, T.; Radnai, B.; Sauer, B.: Untersuchung der Auswirkungen von leitenden und nichtleitenden Schmierfetten auf die Oberflächeneigenschaften bei spannungsbeaufschlagten Wälzlagern, In: T+S Tribologie und Schmierungstechnik, Band 65, Ausgabe 3, S. 5-11, 2018.

[17] Bechev, D.; Gonda, A.; Capan, R.; Sauer, B.: Untersuchung der Oberflächenmutationen und der Riffelbildung bei spannungsbeaufschlagten Wälzlagern, 13. VDI-Tagung Gleit- und Wälzlagerungen 2019, Schweinfurt, 2019.

[18] Holm, R.: Electric Contacts – Theory and Application. Heidelberg: Springer, 1967. ISBN: 978-3-662-06688-1

[19] Vinaricky, E.: Elektrische Kontakte, Werkstoffe und Anwendungen. Heidelberg: Springer-Verlag Berlin, 2016. ISBN: 978-3-642-45427-1

[20] Holm, R.: Electric Contacts Handbook. 3. Auflage, Heidelberg: Springer, 1958

[21] Bechev, D.; Capan, R.; Gonda, A.; Sauer, B.: Method for the investigation of the EDM breakdown voltage of grease and oil on rolling bearings, Bearing World Journal, Volume 4, VDMA Verlag GmbH, Frankfurt am Main, 2019.

[22] Radnai, B.; Gemeinder, G.: Untersuchung des Schädigungsmechanismus und der zulässigen Lagerstrombelastung von Wälzlagern in E-Motoren und Generatoren, verursacht durch parasitäre hochfrequente Lagerströme: FVA-Forschungsvorhaben 650 I Schädlicher Stromdurchgang I, Frankfurt am Main, 2015.

[23] Borlinghaus, R.: Konfokale Mikroskopie in Weiß. Berlin: Springer, 2016. ISBN: 978-3-662-49358-8

[24] Keferstein, C.; Marxer, M.; Bach, B.: Fertigungsmesstechnik. 9. Auflage, Wiesbaden: Springer Vieweg, 2018. ISBN: 978-3-658-17755-3.

[25] Johnson, G. R.; Cook, W. H. (Hrsg.); A constitutive model and data for metals subjected to large strains, high strain rates and high temperatures, Proceedings of the 7th International Symposium on Ballistics. 1983. Netherlands

[26] Lakshmana Rao, C.; Narayanamurthy, V.; Simha, K. R. Y.; Applied impact mechanics, Chichester, West Sussex. Wiley, 2016. ISBN: 978-11-1924-180-5.

[27] Bilici, M.A; An investigation on the ballistic behaviour of alumina/aluminium armour structures, Dissertation, University of Ankara, 2007.

[28] EN ISO 25178-2 Geometrische Produktspezifikation (GPS) - Oberflächenbeschaffenheit: Flächenhaft - Teil 2: Begriffe, Definitionen und Oberflächen-Kenngrößen

Full-Size Test Bench Measurements and Validation of a Novel Conical sliding Bearing for the Main Shaft of Wind Turbines

Tim Schröder[1], Amadeus Rolink[1], Georg Jacobs[1], Dennis Bosse[1]

[1] *Chair for Wind Power Drives (CWD), RWTH Aachen University, tim.schroeder@cwd.rwth-aachen.de*

Abstract – This contribution shows an innovative approach concerning a new type of rotor main bearings for wind turbines. The bearing is designed for the specific loads and operating conditions of a wind turbine and includes major novelties in the field of sliding bearing technology.

In contrast to the established radial and axial bearing designs, this bearing is equipped with conical sliding surfaces, inspired by tapered roller bearings. This design has three major advantages. It has the ability to carry axial and radial forces as well as bending moments in one bearing, which allows to design a very short drivetrain so that the power density of the entire system can be increased. Secondly the bearing is designed segmented, so that these segments can be easily exchanged on the tower in the case of failure and no external crane is required, as in the case when replacing fully enclosed roller bearings.

And finally, a novel pad connecting structure is used to ensure a uniform load distribution and to avoid edge wear. This is done without the use of elaborate tilting segments, by a specifically designed elastic connecting structure of the bearing segments. Accounted by the wind typical big dimensions of the bearing it is a challenge to handle system deformations during operation and the tilting of the shaft within the bearing clearance. The flexible designed connecting structure allows the adjustment of each segment position to the actual bearing load and ensures thereby a smooth pressure distribution by a parallel gap between the shaft and the segments.

In the contribution the design and calculation process of such conical sliding bearing and corresponding validation measurements of a full-scale demonstrator test in the application of a wind turbine main bearing will be shown. In order to investigate the new bearing concept under real conditions, an extensive measuring campaign has been carried out on a full-scale 1 MW system test bench. Among other matters the load-bearing properties and the overall bearing performance have been investigated.

Keywords – Wind Turbine, Main Bearing, Conical Sliding Bearing, Journal Bearing, EHD

Introduction

Rolling element bearings currently used in components of wind turbines (WT) often fail well before the planned service life [1 to 3] and are a strong driver of electricity production costs due to the costly replacement.

The WT main bearing in particular, as one of the core components of the drive train, causes very high costs in the event of damage, since the entire drive train of the turbine has to be dismantled for the bearing replacement [4, 5]. Particularly in the offshore sector, the failure of such a main component can quickly jeopardize the economic viability of the entire wind project [6], since replacement requires the use of ship cranes and at least the dismantling of the rotor [7 to 9]. Ship cranes are a significant cost driver, as charter costs are very high at 200,000 - 300,000 € per day [4] and availability for unscheduled operations is poor [10]. In addition, there is the strong dependence on weather, wind and swell, especially in autumn and winter.

That's why in the recent past, a change in technology from roller bearings, to plain bearings has been discussed in order to improve the technical reliability of the main bearing of the wind turbine. However, plain bearings in the area of heavy-duty drivetrains are more established in applications with high rotational speeds (e.g. power plant turbines) or in applications with stationary operating conditions (e.g. propeller shafts of ships). New research results show, however, that plain bearings can be used for the main bearings of wind turbines despite the low rotational speeds and high dynamic loads [11].

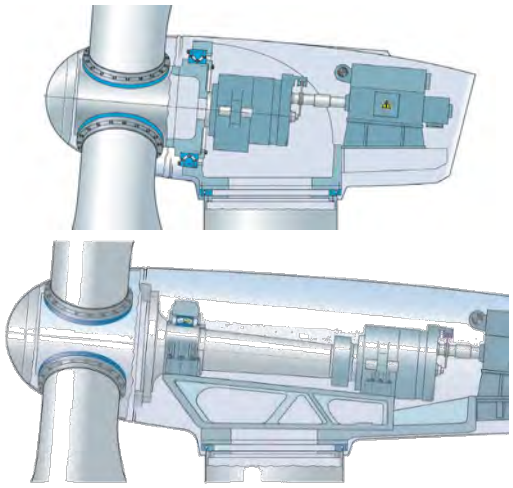

Figure 1: WT drive train with double row tapered roller main bearing (top) [23] and three-point suspension drivetrain (bottom) [23, picture modified]

WT drivetrains with a double row tapered roller main bearing (also called moment bearing), like shown in the top picture of Figure 1, take all wind loads in one compact bearing and have advantages compared to other drivetrain concepts, as the whole drivetrain can be designed very short. That leads to lightweight components (esp. shaft) and a short load

path from the rotor to the tower and the currently demanded power density requirements are met. The bottom picture of Figure 1, shows a classical three-point suspension for comparison.

On the other hand, the big diameter of double row tapered roller main bearings in combination with the high number of rollers can lead to fatigue issues due to the high number of rollovers. Also accounted by the big diameter, it is a big challenge to handle tolerances in the manufacturing process and system deformations during operation. Both have a big influence on the pressure distribution and consequently also on the bearing lifetime [11, 1]. The application of sliding bearings instead of roller bearings offers the chance to dismantle these barriers, which motivated the investigations on a sliding main bearing for this type of WT drivetrain.

The replacement with a tapered (conical) sliding bearing for the application in such a wind turbine promises a high potential from several points of view, as it combines the advantages of a sliding bearings with the advantages of moment bearings:

- The easy exchangeability of individual sliding segments on the tower allows for an increase in availability and a reduction in operating costs.
- The compact design as a tapered moment bearing can handle all loads (forces and bending moment) in one bearing and meets thereby the demands for a high power density.
- Compared to rolling bearings, system deformations are not critical with the appropriate design measures (e.g. tilting pads, elastic connection of the pads).
- Compared to rolling bearings, the segmentability simplifies the scalability to larger diameters.

However, a tapered bearing is largely unknown in sliding bearing technology, since usually pure radial and pure axial bearings with a big supporting width are combined. Design methods and guidelines are available for these designs [ex. 12 to 14], but do not exist for plain bearings with tapered sliding surfaces, so that fundamental investigations are of interest.

The overall objective of this work is therefore to show a procedure for the design of a conical sliding bearing and to validate this by means of a functional verification in original size.

For the selected bearing design, measures to avoid edge wear are necessary for a proper functionality of the bearing. Due to the large bearing diameter and the resulting large absolute bearing clearance, as well as the short supporting width of the tapered bearing, the effect of edge load is increased. An even load distribution and the avoidance of edge loading is particularly important to prevent increased wear. Therefore, the next chapter begins with a description of the bearing design and the measures taken to avoid edge-wear. Then the test rig used to validate the bearing is described.

This is followed by a presentation of the measurement results of the tests carried out, which are used to validate the new bearing concept and the simulations carried out during design process.

1. Bearing Design and Test Setup

In the conceptual design process, simulations of a rigid conical sliding bearing [18] were accomplished, which showed distinctive issues concerning edge wear and high contact pressures, shown in Figure 2.

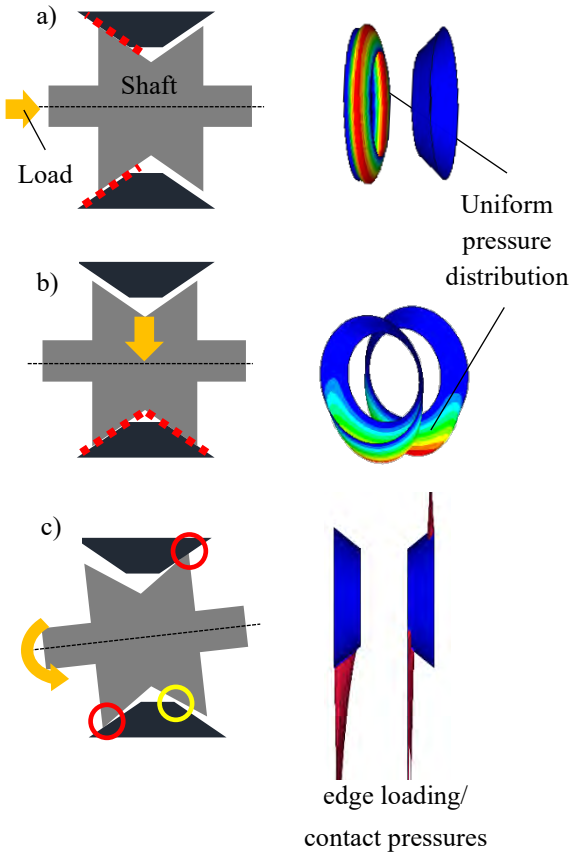

Figure 2: Load- taking capability of a conical sliding bearing

According to the illustrations in Figure 2, a conical sliding bearing is capable to handle axial loads and radial loads applied in the middle of the shaft without any special measures (Figure 2, a,b). This can be seen by moderate and well distributed hydrodynamic pressures as in this cases the bearing gap “closes” parallel. But in the case of bending moments as they show up in wind turbines (Figure 2, c) the shaft tilts slightly within the bearing clearance which leads to high contact pressures and edge wear. This effect is amplified by the short supporting width and the comparatively high bearing clearance due to the large diameter of the bearing [16, 17].

A flexible designed connection structure of the bearing pad allows the pads to follow the movement of the shaft. By a slight deformation of the connecting

structure, a smooth pressure distribution without edge wear and a long durability is ensured (Figure 3).

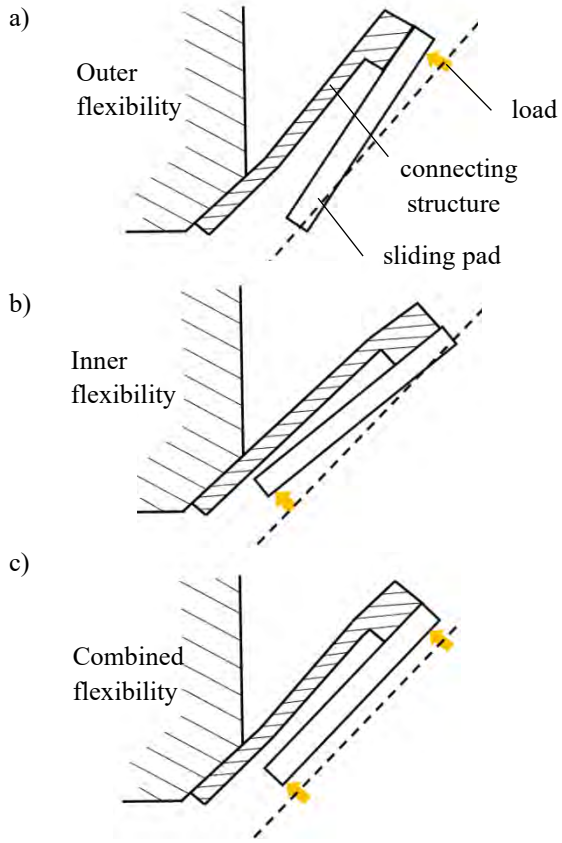

Figure 3: Novel design of pad connecting structure to ensure a uniform hydrodynamic pressure build up without edge wear

Depending on the actual load distribution on each bearing segment, the connecting structure will yield with the outer flexibility (Figure 3, a) and the inner flexibility (Figure 3,, b) to a combined double flexibility (Figure 3, c). By this a "parallel" and well lubricated gap is ensured. Compared to other opportunities to align a bearing pad (for example tilting pads), this design has major benefits in its simplicity and the absence of sensitive bearing joints.

Once the functional principle of this new sliding bearing has been proved by elasto-hydrodynamic (EHD) calculations, a 1MW wind turbine has been chosen as a demonstrator platform to design, simulate and test this bearing in full-scale. Therefore, the hub-loads are calculated by a Co-Simulation of Simpack and Simulink, considering the WT controller and wind conditions according to IEC 61400 [15, 22].

For the design of the bearing, a static design load case (among others), was derived from this, which is shown in the following table.

Table 1: Static Design Load Case

F_x	101,1 kN
F_y	6,0 kN
F_z	-87,0 kN
M_y	100,3 kNm
M_z	79,6 kNm

Concerning these loads a basic geometry was first defined with the help of a pre-dimensioning strategy shown in [18], followed by extensive EHD calculations. This EHD calculations have been performed in order to investigate the design parameters of the bearing and especially the ideal stiffness combination of the "inner" and "outer" flexibility [16, 17].

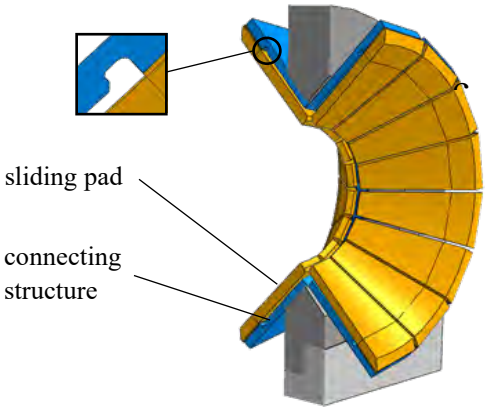

Figure 4: cross-sectional view and picture of manufactured bearing

Figure 4 shows the result of the design process. According to the functional principle, the stiffness of the segment connection (blue part) controls the yielding. The constructional properties of this part (length, thickness, groove (see detail), etc.) are particularly relevant.

On the next page, Figure 5 shows the bearing mounted on the machine carrier of a 1 MW system test bench, where it replaces the original roller main bearing.

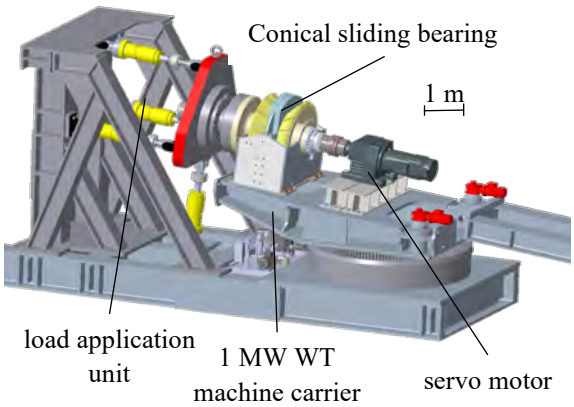

Figure 5: Test setup on CWDs 1 MW System Test Bench

The system test bench is equipped with a hydraulic load application unit. This unit is capable to emulate the forces and bending moments resulting from the wind exposed WT rotor and load values can be set

according to the results of the hub-load analysis. The main bearing absorbs all forces and bending moments directly and without a second bearing point in the gearbox, so that it is possible to simplify the test setup by testing without the main gearbox. A servomotor is installed on the gearbox position, which applies the rotational speed to the bearing.

In order to be able to evaluate the characteristics of the bearing in operation, the bearing is equipped with a large number of different sensors in the test setup.

Temperature sensors are applied to evaluate the global load-bearing behaviour and to detect critical operating conditions at an early stage. For this purpose, two temperature sensors were applied in each of the 32 bearing pads in small bores under the sliding surface. In each sliding segment one sensor is located at the outer diameter and one at the inner diameter, so that information about the local load distribution can be derived and, in particular, any edge loading can be detected early.

Figure 6 shows a picture of a sliding segment including the connection structure with the positions of the two temperature sensors highlighted.

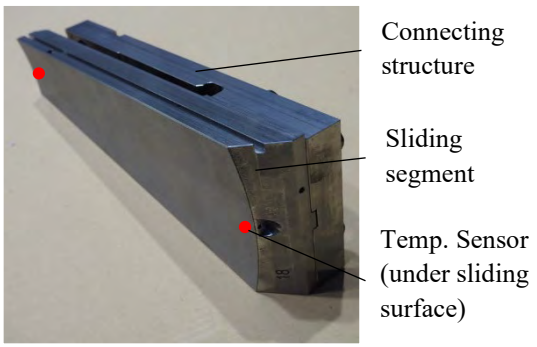

Figure 6: Position of temperature sensors on each sliding segment

In addition, six tactile LVDT (Linear Variable Differential Transformer) displacement transducers are positioned on six of the upper pads to detect the displacement of the segment connection relative to the center carrier. This makes it possible to check whether the actual deformation under load also corresponds to the dimensioning.

In addition to all operating variables of the test bench, the test setup is equipped with a torque sensor between the servo motor and the bearing. Thereby the frictional state (solid friction, mixed friction, fluid friction) can by evaluated.

2. Validation

In order to test the new bearing concept under the real conditions of a wind turbine, a measurement campaign was carried out with the bearing manufactured in original size. The aim is to prove the functionality of such a new sliding bearing in the main bearing. In addition, the necessary data basis will be created to validate the design procedure as well as individual calculation and simulation results.

This chapter therefore describes the experimental work on the manufactured bearing. Chapter 0 starts with the description of the investigations regarding the load bearing behaviour under two selected load scenarios. This is then followed by an evaluation of the deformation behaviour of the elastic connecting structure of the segments in chapter 3.2 and further investigations of the general bearing performance under low rotational speeds in chapter 3.3.

All measurements taken on the test bench are compared with the simulation models which were used for the design process of the bearing. This enables the possibility to validate the models.

The following picture in Figure 7 shows the manufactured bearing without the shaft, which is tested on CWDs 1 MW WT system test bench.

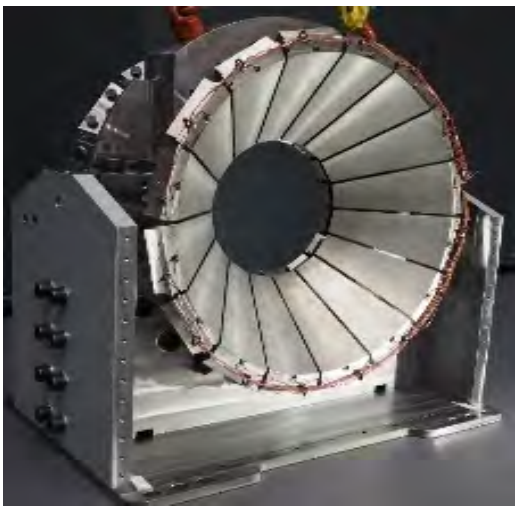

Figure 7: Picture of the manufactured bearing without shaft

2.1. Validation of Load Bearing Behaviour

To validate the new bearing concept, as well as the related EHD-Simulation models, tests from synthetic uniaxial loads (static) to real dynamic loads have been carried out. Temperature sensors, of which one is installed on the outer- and one on the inner position of each pad, are best suited to evaluate the overall load bearing behaviour and the load zone. Of course, also critical operating conditions due to mixed friction or edge wear can be detected at an early stage.

For a better understanding of how the load is distributed over the bearing, a simple synthetic load at nominal rotational speed (28 rpm) is first presented. The thrust is ramped up in 7 steps up to 101 kN, whereby every step is hold for 10 minutes of operation. Figure 8 shows the temperature distribution, in which the continuous lines indicate the temperatures at the end of the last load step (t_1 ; 101 kN thrust). The blue line indicates the temperatures at the outer ring measurement points and the red line shows the

inner ring measurement points. The front sliding surfaces are named V1 to V16 in clockwise direction in view of the opening cone (starting with V1 at 13 o'clock), the rear sliding surfaces analogously with H1 to H16. The dotted lines show the temperatures at the beginning of the test.

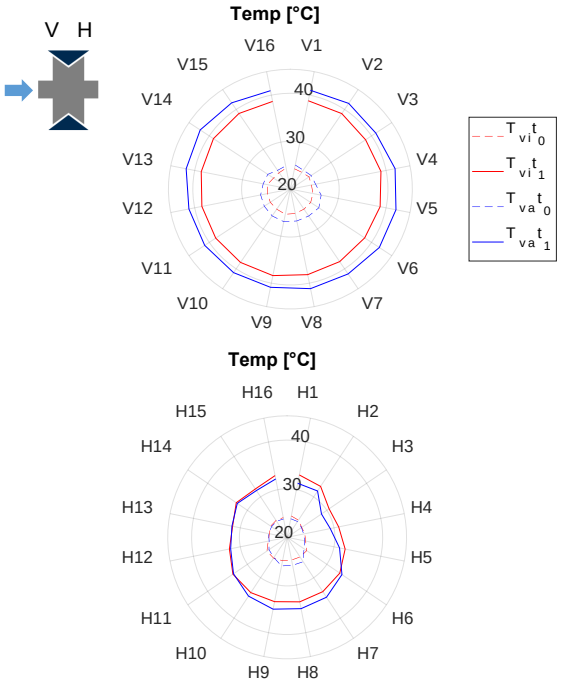

Figure 8: Temperature distribution during uniaxial thrust test (Top: Front Cone with, pad #H1-H16, Middle: Rear cone with pad #V1-V16 [18])

The measurements proof the expectation, that the front pads become warmer as they take the load in the case of pure thrust. Also under pure hydrodynamic conditions the gap between the shaft and the pad is getting smaller in the loaded zone, which results in more liquid friction and a higher heat input into the pad. Figure 8 also shows that the pads are very equally loaded due to the very similar temperature distribution, which is an indicator for proper position tolerances of the bearing pads. The outer ring measurement points generally become a bit warmer (~2-3°C), as the bearing diameter is larger at the outer ring measurement points resulting in a higher circumferential speed. Visible is also the gravity influence on the 1700 kg shaft. In the measurements as well as in the simulation (s.Figure 9) the rear bottom pads become slightly warmer.

The measured temperatures are far below the critical temperatures for plain bearings, which already indicates purely hydrodynamic conditions without mixed friction. According to DIN 31652, empirical values for the maximum permissible bearing temperature are between 90 and 125 °C [48], depending on the type of lubrication, whereby the application limits of the lubricant and the sliding layer material must be observed.

The analysis of the frictional torque confirms this. Despite an increase in the load from 0 kN at the beginning of the test to 101 kN at the end of the test, the frictional torque increases by only 25% from 833 Nm to 1047 Nm during this time. At the same time, the entire oil sump warms up during the test from 25 °C to 33 °C.

A simulation with the built up simulation model and the operating state (101 kN thrust, dead weight, nominal speed) reflects the measurement results, as shown in Figure 9.

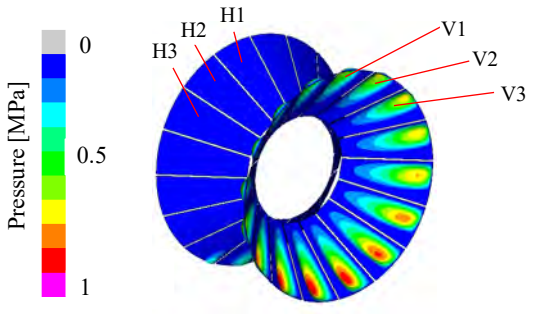

Figure 9: simulation result at 101 kN uniaxial static thrust

The load is also distributed over the front cone in the simulation, whereby the pressure build-up on the outer ring is higher due to the higher circumferential speed. Corresponding to the low measured temperatures, overall very moderate pressures and no peaks due to contact pressures caused by mixed friction can be detected.

Figure 10 shows the load bearing performance under the 4-dimensional design load case according to the loads shown in Table 1.

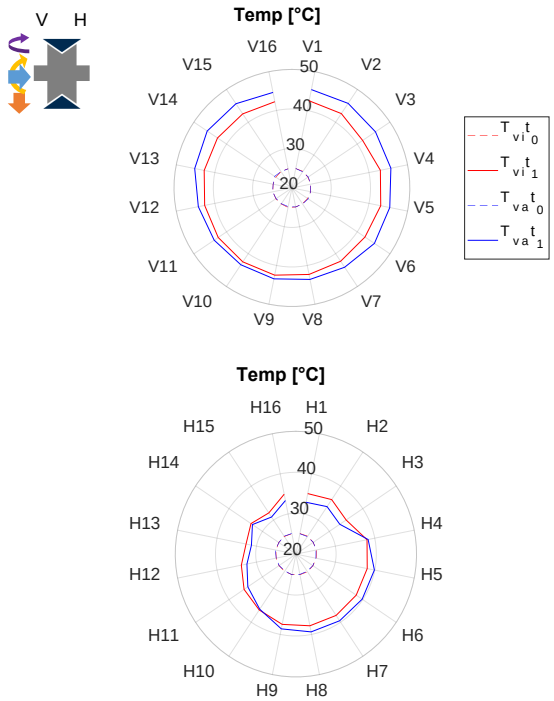

Figure 10: Temperature distribution during 5-DOF Design-Load test [18]

As to be expected, the area of the load zone becomes larger at this higher load and the maximum measured temperatures are also higher. With the same test duration of 110 minutes (compared to pure thrust) and

very similar initial temperatures at the start of the tests, the maximum temperature in this 4-dimensional load case of 46°C is greater than the maximum temperature at pure thrust (42°C).

The simulation result in Figure 11 shows that the load carrying behaviour of the bearing corresponds very well with the measured condition.

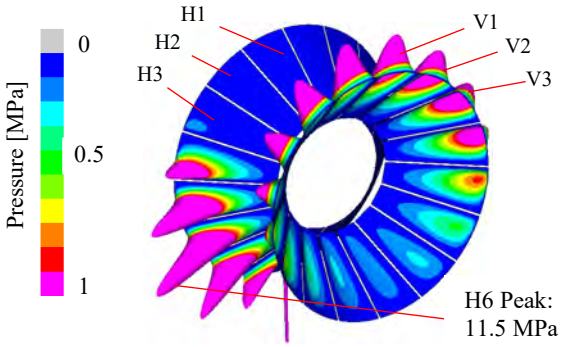

Figure 11: simulation result of related static design load case according to Table 1.

The high simulated pressures with the associated narrow lubrication gap at the rear cone on the segments H5, H6 and H7 would lead to higher temperatures at the corresponding measuring points. However, these sliding segments are located directly in the oil sump, where they experience the best possible cooling from the environment.

Generally the measurement proofs, also according to the simulation, that the hydrodynamic pressure is always distributed evenly over the loaded segments with uncritical hydrodynamic pressures and without any contact pressures. The measured bearing temperatures are also very moderate in all cases.

2.2. Validation of the elastic pad-connection structure

In the previous chapter, it was shown that the bearing ensures uniform load carrying capacity without critical edge loading. Since the adaptation of the sliding segments to the load conditions is realized by the deformation of the connection structure, the deformation behaviour will be analysed and evaluated more precisely in the following.

With the procedure shown in Figure 12, the deformation of the structural components can be determined under consideration of the real hydrodynamic load to the sliding segment.

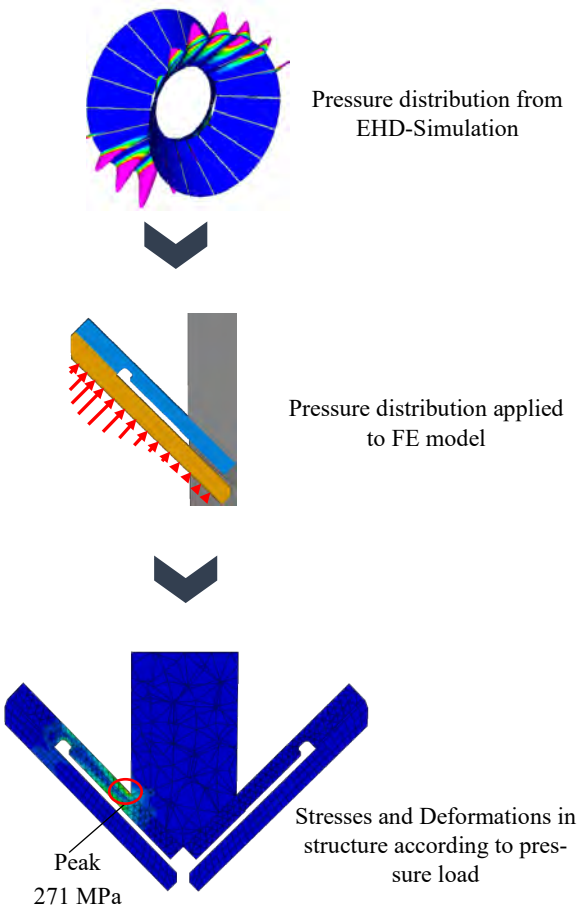

Figure 12: Procedure for determining the deformation behaviour

According to the shown procedure the pressure distribution calculated with the EHD simulation software is discretized via a Matlab script and then applied to the sliding segments as a surface load in the FE software Abaqus. In contrast to a "standard" contact condition between the shaft and the sliding segments, this ensures that the load introduction takes place under consideration of the real, hydrodynamic load.

It has been determined that the maximum, absolute structural deformation occurs under pure bending load, since the smallest number of sliding segments is loaded under this load condition. In the case of simultaneous thrust loading, for example, the influence of the bending moment is reduced because the loading zone increases and thus the number of loaded segments increases. This behaviour is equivalently visible in the test bench measurements. For the evaluation of the elastic behaviour the load case of pure max bending moment (100,3 kNm) is therefore selected.

As expected, the area with the highest stresses is located at the transition from the stiff central structure to the relatively soft segment connections. Here, local stresses of up to 271 MPa occur, which is about 30% of the yield strength of the material used

(1.7225 (42CrMo4); yield strength untempered 900 N/mm²).

The FKM guideline also specifies a material fatigue strength under bending stress (σW,b,N) of 525 N/mm² for this material [19]. Under pulsating bending load (σbSchN), which is even more appropriate for the type dominating load in a WT, a strength of 855 N/mm² is specified [20]. On the one hand, the calculated stresses are far below the critical values and, on the other hand, the loads on the bearing are much lower during most of the operating time, so that the deformation with regard to fatigue can be assessed as uncritical.

A more detailed analysis of the deformation of the segment connection and the absolute displacement of the segments themselves are now of interest. For this purpose, the FE simulation model was provided with "markers" along the segment running surface and on the rear side of the segment connection structure and the displacement relative to the central part of the bearing was read out. The connection of these displacement points then corresponds to a discretized bending line. Figure 13 shows these bending lines of the highest loaded segment V1 under the applied load condition.

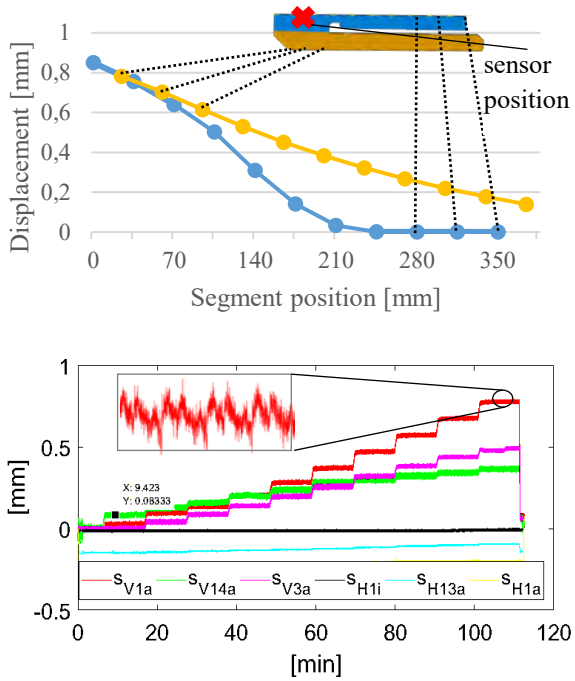

Figure 13: simulated displacement of connection structure and sliding pad (top) and measured displacement at 100.3 kNm uniaxial bending moment

It can be seen that the stiffness ratio has been chosen so that the deformation mainly takes place in the (blue) connecting structure, while the segment itself sees almost no defrmation (as it holds the sensitive sliding material). The displacement of the segment is only determined by the displacement of the connecting structure and along the segment the bending line is almost linear. At the same time, the connecting structure (blue line) deforms as desired "s-shaped" so that a parallel displacement of the sliding segment is possible.

The figure at the bottom of Figure 13 shows the deformation measured by the displacement sensors during a test where pure bending moment is stepwise applied on the bearing to the maximum value of 100.3 kNm.

At this load, the largest displacement of 0.7 mm is measured at the sensor of segment V1 (red line, S_{V1a}). This segment is located clockwise just to the right of the 12 o'clock position and is therefore, as the analysis of the load bearing behaviour under this load case showed, the most heavily loaded.

Considering the sensor position on the back of the connecting structure (blue part) the measured deformation corresponds very good to the simulation.

Despite static operating points with regard to load and speed, all displacement sensors detect a small speed-dependent, circumferential periodic and load step-independent movement with a maximum amplitude of about 25 µm (see detail in Figure 13, bottom). This indicates that the segments also react elastically to manufacturing tolerances, such as roundness deviations of the shaft. This is a great advantage, especially in comparison to rolling bearings, where in this case forced forces quickly occur between the rolling elements and the bearing rings.

2.3. Validation of Bearing Performance under low rotational speeds

In [18] it is shown that the mixed friction limit is passed already at very low rotational speeds whereby normal operation points are far away from this rotational speed so that full lubrication is ensured under nominal conditions. A special focus is now placed on the analysis and evaluation of the wear behaviour during mixed friction at start/stop conditions of the wind turbine. Since under these conditions the hydrodynamic pressure build-up does not completely separate the surfaces, this operating condition is particularly critical.

In order to investigate the properties of the bearing and its coated sliding surface during the start-up processes, these conditions were simulated on the system test bench. For this purpose, the real start-up loads and the associated rotational speed ramp were applied on the bearing in accordance with the load simulation. This procedure is repeated in cycles. In order to shorten the cycle time and thus the overall test duration, the entire run-up to the rated speed (28 rpm) was not tested. The cycle was only run up to a speed of 7.5 rpm, as it had already been demonstrated that higher rotational speeds were not critical regarding mixed friction and wear. Figure 14 shows the applied cycle with driven speed ramp and the measured drive torque.

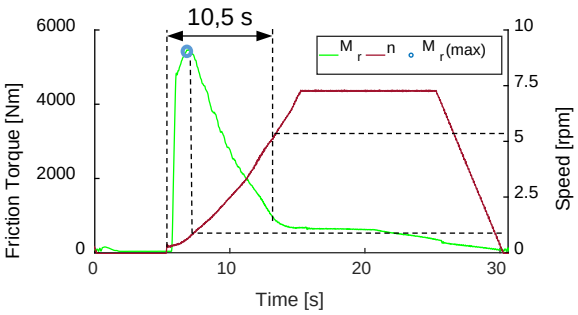

Figure 14: Friction torque and rotational speed during first phase of WT-start up

It can be seen that with the beginning of rotation the measured torque initially increases rapidly. In this phase, the breakaway torque must first be overcome and the friction torque reaches its maximum (M_r(max)) at a speed of 1.1 rpm. From then on, the hydrodynamic separation of the surfaces begins and the solid-contact share of the mixed friction decreases with increasing speed. Despite a further increase in speed, a plateau in the torque curve is reached from 5.1 rpm onwards. This is a reliable indicator that the transition speed is exceeded here and that the range of pure hydrodynamic lubrication is reached. Up to this point, the bearing was operated in mixed friction for 10.5 seconds.

On the next figure, Figure 15, the same curve is shown again in a different time-scale, so that the transition from static friction to liquid friction can be analysed more precisely. Thereby the friction characteristics can be compared to the classical friction behaviour according to [21].

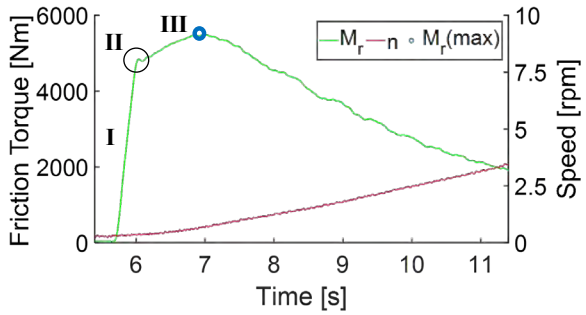

Figure 15: Top: Detailed Friction torque and rotational speed during first phase of WT-start up; Bottom: friction characteristics according to [21]

The illustration shows that despite the comparatively complex bearing geometry with a total of 32 distributed sliding segments, the friction characteristics of classic friction pairings according to [21] can be recognized in the measurement data. In the first phase (I, adhesion) there is no local sliding in the contact surface and the friction moment curve increases linearly [21]. In the second phase (II, breaking free) the transition to sliding takes place and local slippage or adhesion occurs at adjacent surface contact points. The width of this transition increases with the surface roughness present in the friction pairing. The maximum depends on the local deformation in the roughness contact, since the associated plastification increases the adhesive interactions between the contact surfaces [21]. In the third phase (III, "sliding") relative movements take place in the entire contact area of the surface. The coefficient of friction during sliding then depends on the properties of the near-surface boundary area [21].

In total 8000 of these start-stop cycles were carried out and only polishing was detectable on the bearing segments. The arithmetic height (Sa) as characteristic value for the roughness reduced from 7.9 µm to 5 µm, so only a slight smoothing of the surfaces accrued. The number of tested cycles represent already about 40% of the wind turbines lifetime.

3. Summary

The failure of the main bearing in a WT increases the *levelized cost of energy* (*LCOE*) due to the costly replacement. In contrast to the roller bearings used exclusively up to now, plain bearings promise quick and cost-effective replacement on the tower due to their segmentability, without the need to dismantle the rotor and drive train.

The aim of this contribution was to qualify this new bearing technology for the main bearing of WT with theoretical investigations based on simulations and a related experimental validation.

Although state of the art sliding bearing arrangements are usually equipped with pure radial- and axial sliding bearings, this contribution follows and analyses the use of a tapered (conical) sliding bearing arrangement for the main bearing.

The conical design combines the advantages of the established moment rolling bearing (especially compact and light design of the whole turbine, compare Figure 1) with the advantages of sliding bearings (especially exchangeability of segments). Irrespective of the area of application in wind turbines, this design represents a novelty in sliding bearing technology, so no guidelines for the design process are available.

Therefore, in the first part of this paper the design procedure was described. It was shown that this new bearing type has a strong tendency for edge loading, which is mainly due to the tilting of the shaft within the lubrication gap. Due to the large bearing diameter and the resulting large absolute bearing clearance, as well as the short supporting width of this bearing type, this effect occurs more strongly. A double spring-elastic mounting of the sliding segments effectively prevents the edges from being carried and at the same time is characterised by a simple constructional implementation. The use of maintenance-intensive and expensive tilting joints can thus be completely eliminated. The carefully designed stiffness of the segment connection ensures the necessary parallel alignment of the sliding segments to the shaft and thus ensures a uniform load carrying without "edge loading". Through this design measure the space-saving conical design can be implemented in a functional and cost-effective manner.

With the help of extensive EHD simulations the tapered bearing was designed including this new connection structure and was then manufactured in original size to be tested on a 1 MW WT system test bench. Here, a comprehensive measurement campaign was carried out under the real loads and operating conditions of a WT to prove its functionality. Among other things, the load-bearing capacity of the bearing, the deformation of the flexible connection structure of the bearing segments, as well as the mixed friction limit and the start-up behaviour were examined. All the tests carried out delivered results that made it possible to validate the related simulations. For example, the temperature distribution measured in the bearing was used to validate the simulated load-bearing behaviour over all load situations with very good agreement. For the entire operating range, the functional capability for the designed bearing could be proven and, with 8,000

start-up processes tested under real conditions, clearly exceeded expectations with regard to wear behaviour.

Regarding the current state of the art, this work made an important and previously unproven contribution to the design and real-size application of sliding bearings for WT main bearings.

Acknowledgment

The presented investigations are part of the joint project “WEA-GLiTS”, promoted by the German Federal Ministry for Education and Research. The Authors would like to thank their project partners in industry Miba, Zollern BHW and Oerlikon Metco, for the excellent cooperation and support.

References

[1] J. Wenske: Projektbericht "ELAN-Entwicklung innovativer elektrischer Antriebskonzepte für Windenergieanlagen" (2016)

[2] Windkraft Journal: Verbesserung der Lagerzuverlässigkeit in einem Rotorlagersystem (2019)

[3] S. Sheng: Report on Wind Turbine Subsystem Reliability - A Survey of Various Databases (2013)

[4] ErneuerbareEnergien.de: Erneuerbare Energien: Windparkfütterung. Offshore-Kosten sparen, 2015. https://www.erneuerbareenergien.de/archiv/windparkfuetterung-150-3882-85284.html, accessed: 10.06.2020

[5] S. Engström, T. Lyrner, M. Hassanzadeh, T. Stalin, J. Johansson: Tall towers for large wind turbines. Report from Vindforsk project V-342 Höga torn för vindkraftverk (2010)

[6] S. Pfaffel, S. Faulstich, K. Rohrig: Performance and Reliability of Wind Turbines. A Review. Energies 10 (2017) 11, S. 1904

[7] T. Schröder, G. Jacobs, D. Bosse: Sliding moment bearing as a main bearing in wind turbine generators, Conference for Wind Power Drives 2017, Aachen (2017)

[8] T. Schröder, G. Jacobs, D. Bosse, K. Bobzin, M. Öte, T. Königstein, W. Wietheger: Thermisch gespritzte Gleitlagerwerkstoffe für die Rotorlagerung von Windenergieanlagen. Ingenieurspiegel 2016 04, S. 29

[9] K. Bobzin, M. Öte, T. Königstein, W. Wietheger, D. Bosse, T. Schröder: Thermisch gespritzte Gleitlager für die Hauptlagerung von Windenergieanlagen. Antriebstechnisches Kolloqium 2017: Conference Proceedings (2017)

[10] M. Balks, P. B.: Risikobewertung bei Investitionen in Offshore-Windanlagen. Wirtschaftsdienst 94 (2014) 1, S. 26–33

[11] E. Hau: Windkraftanlagen (2008)

[12] ISO7902: Hydrodynamic plain journal bearings under stady-state conditions - circular cylindrical bearings (1998)

[13] Deutsches Institut für Normung e. V.: DIN31652. Hydrodynamische Radial-Gleitlager im stationären Betrieb - Berechnung von Kreiszylinderlagern (1983)

[14] Verein Deutscher Ingenieure: VDI2204: Auslegung von Gleitlagerungen

[15] T. Schröder, G. Jacobs, D. Bosse; Sliding moment bearing as a main bearing in wind turbine generators; Conference for Wind Power Drives 2017

[16] T. Schröder, G. Jacobs, D. Bosse; EHD-Betrachtung eines neuartigen Gleitlagerkonzeptes für das Hauptlager einer Windenergieanlage, FUM 2017

[17] J. Hölzl, T. Schröder, A. Rolink: Innovative Lagerkonzepte und neue Gleitlagerwerkstoffe für den Antriebsstrang von Windenergieanlagen; Schadensmechanismen an Lagern 2018 (VDI)

[18] T. Schröder, G. Jacobs, A. Rolink,D. Bosse; "FlexPad" - Innovative conical sliding bearing for the main shaft of wind turbines, WindEurope 2019

[19] R. Rennert, E. Kullig, M. Vormwald, A. Esders, D. Siegele: Rechnerischer Festigkeitsnachweis für Maschinenbauteile. FKM-Richtlinie (2012)

[20] H. Wittel, D. Jannasch, J. Voßiek, C. Spura: Roloff/Matek Maschinenelemente. Springer Vieweg (2017)

[21] E. Leidich, M. G.: Ermittlung charakterisierender Kennwerte für reibschlüssige Verbindungen. Forschung im Ingenieurwesen 80 (2016) 1-2, S. 71–84

[22] Germanischer Lloyd, Wind Energy Commitee: Guideline for the Certification of Wind Turbines. Rules and Guidelines Industrial Services (2010)

[23] SKF Group: SKF Nautilus advanced bearing arrangements. Simplified mounting and dismounting, increased reliability and enhanced safety (2012)

Measuring the Kinematic Behavior of the Rolling Elements in a Spindle Bearing under Axial and Radial Loads

Prof. Dr.-Ing. Christian Brecher[1], Hans-Martin Eckel[1], Dr.-Ing. Marcel Fey[1], Stephan Neus[1]

[1] *Laboratory of Machine Tools and Production Engineering (WZL), RWTH Aachen University, h.eckel@wzl.rwth-aachen.de*

Abstract – In the field of high-speed spindle bearings, the kinematic conditions in the bearing determine the load carrying capacity and speed suitability. Under the influence of radial loads, contact angle variations occur, which cause varying orbital speeds of the balls over the bearing circumference. If the clearance between the balls and the cage pockets is exceeded, high contact forces between balls and cage can destroy the cage. The calculation of these orbital velocities and thus of the balls advance and retardation is strongly influenced by the frictional conditions in the contacts, which are difficult to determine. Experimental investigations are therefore helpful for a better understanding of this behavior.

For this reason, a photoelectric measuring system was developed to measure the motion of the balls in the bearing. The system works on the principle of a through beam light barrier, where the balls pass the light beam.

In this paper, a spindle bearing of size 7014 with ceramic balls was investigated. The speeds are up to 30,000 rpm with varying axial preloads and radial forces. The results show that, compared to calculated values, a more uniform orbital velocity curve is measured than calculated values indicate. Thus, the ball advance and retardation tend to be lower than the calculations indicate.

Keywords – Bearing Kinematics, Radial Bearing Load, Measurement, Angular Contact Ball Bearing

1. Introduction

The bearing arrangement of a machine tool main spindle is subject to complex load conditions as a result of the process forces. Especially under high rotational speeds and under combined axial and radial loads the kinematics of the balls and their interactions with the raceways and the cage become important [1].

In practice, the bearing arrangement is designed on the basis of maximum occurring pressure and the kinematic conditions in the bearings. Frequently, the kinematic critical values, in particular the ball advance and ball retardation (BaBr), limit the maximum radial load, that can be supported. BaBr describe the leading and trailing motions of the rolling elements in the cage pockets caused by radial or torque loads. This can lead to a great wear and finally a failure of the cage, if the cage pocket clearance is exceeded, such that the forces between cage and balls become significant [2].

In case of high speed machining, practical examples show, that cage damage frequently occurs, but also that the bearings do not fail despite exceeding the calculated kinematic limits under radial loads. This indicates a deviation between the calculated and the real ball motion behavior.

Furthermore, precise known ball speeds help to parameterize friction models for the thermal bearing simulation under various loads. A deep understanding of BaBr under radial load is equally necessary for thermo-elastic and mechanical bearing models.

Previous investigations

Measuring the motion of balls and cage demands high requirements on the measuring technology. Various methods for measuring ball and cage movement are presented below.

The rotational speed and the motion behavior of the cage has been investigated in several studies. In case of pure axial load, the orbital speed of the rolling elements derives from the cage speed.

Roissant measured the rotational speed of the cage by means of light reflection sensors and a measuring scale applied to the front of the cage. The measurements were used to determine the actual rotational speed of the cage and thus of the rolling element set under static axial forces for the validation of bearing friction models. [3]

Choe measures the cage whirling amplitude with fiber optic sensors for the investigation of the dynamic cage behavior under various axial loads and rotational speeds. Interactions between balls and cage are described theoretically and are considered experimentally using different cage pocket clearances. [4]

Herkert uses radioactive isotropy to measure the rotational speed of a roller in a cylindrical roller bearing and additionally measures the cage speed in ball bearings by means of an optical encoder under axial and radial loads. The cage speed provides information about the slipping behavior of the whole ball set. [5]

Falcon measures the contact angles in the bearing under axial load using small transducers placed in the outer ring. The measurement is based on sub-surface measurement of the deformation of the outer raceway by the balls. The measurements were carried out under static axial load. [6]

Haines acquired the contact angle and roll axis in an angular contact ball bearing using a high-speed camera and markings on the balls. The measurements were performed under pure axial load up to a speed of 4,950 rpm. [7]

Krimpmann analyses the kinematics of the rolling elements in a roller bearing under radial load. He uses two inductive displacement sensors to measure the roller skewing behavior and the speed of the rollers. He rules out the use of optical methods due to lubrication. [8]

Inductive measurement, however, only allows the examination of standard bearings with metallic rolling elements. The measurement of the kinematics of high-speed spindle bearings, which are usually fitted with ceramic balls, cannot be carried out with this method.

Kakuta analyses the forces acting on a cage of a ball bearing with the effect of misalignment. To measure the contact force between a ball and the cage in circumferential direction, he has removed a half stem of a cage and mounted instead an L-type measuring block. The measuring block is equipped with strain gauges at the back side which measure the bending strain and therefore the ball-to-cage force. The investigations were carried out with a deep groove ball bearing of size 6310 with misalignment under radial and pure axial loads as well as under moment loads. The maximum speed was 1,600 rpm. The results show that significant contact forces and thus increased BaBr only occur under the influence of misalignment (angle). [9]

The speeds investigated are low compared to high speed applications. Gyroscopic moments, centrifugal forces on the rolling elements and the associated different contact angles between the inner and outer contact are therefore not addressed. A transferability of the results to high speed bearings cannot be assumed.

Holland presents a promising system for measuring the movement of the balls and cage using high speed videography. For the system, the test bearing must be accessible from both sides for illumination and image acquisition. Loading the test bearing with radial or moment loads is difficult. His work shows results under static axial force. [10]

No experimental results could be found for the orbital velocities of the balls under radial load and high speeds. However, knowledge of these speed components, which are uneven over the bearing circumference, is necessary to understand far-reaching effects in the bearing under radial load.

Therefore, a photoelectric measuring system to track the position of the rolling elements along their orbit is introduced. The system has been integrated in a spindle bearing test bench with variable axial thrust loads and radial loads. Due to its robust and compact design, the measuring system can be integrated into a test bench or even in a main spindle.

2. Theoretical consideration of ball advance and retardation

Below, the origin of the ball leading and trailing motion will be briefly explained in order to be able to explain the effects determined in the experimental part.

For a detailed description of the analytical calculation methods of the rolling contacts and the entire bearing, refer to [3; 11; 12].

The orbital velocities of the balls around the bearing axis are fundamental for the ball leading and trailing motion. Figure 1 give an overview of the kinematics of the balls [3]

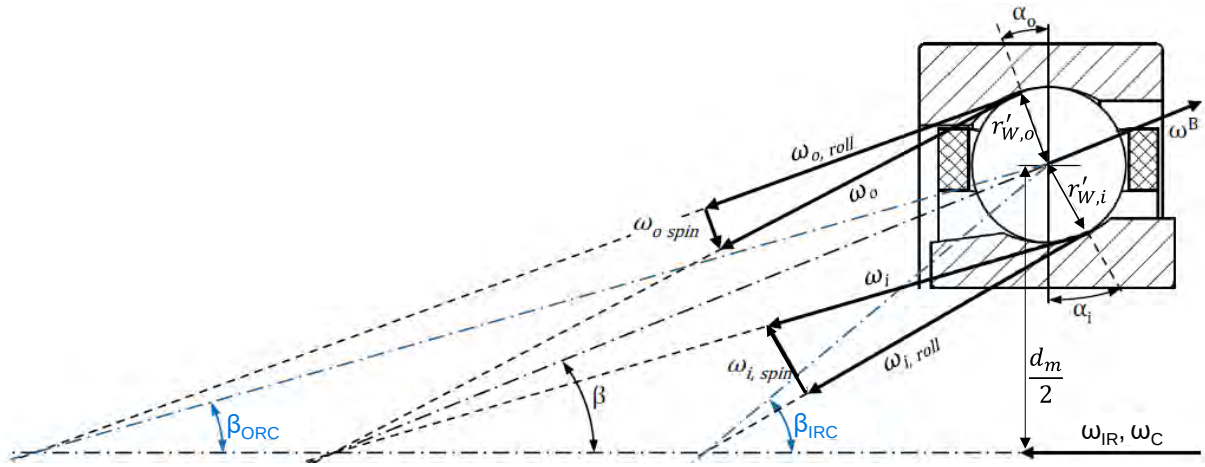

Figure 1: Ball kinematic

The orbital velocity ω_C of the cage respectively of a ball is calculated by Eq.(1) with the rotational speed of the inner ring ω_{IR}, the inner and outer effective Ball radius $r'_{W,i}$, $r'_{W,o}$ and the pitch diameter d_m [11]. The velocity particularly depends on the contact angle distribution over the bearing circumference and thus on the contact angle difference between the inner (α_i) and outer (α_o) contact and the position of the rolling axis with the angle β.

The angle β describes the angle of the rolling axis at which the ball rotates with ω_B. Since a simultaneous pure rolling in both contacts with is not possible, this angle depends on the load and friction conditions in the contacts. The total rolling angular speeds ω_i and ω_o at the inner and outer contact consist of the pure rolling components $\omega_{i,\,roll}$ and $\omega_{o,\,roll}$ and spinning components $\omega_{i,\,spin}$, and $\omega_{o,\,spin}$.

$$\omega_C = \frac{\omega_{IR}}{1 + \frac{r'_{W,i} \cdot (\frac{d_m}{2} + r'_{W,o} \cdot cos\alpha_o) \cdot a_1}{r'_{W,o} \cdot (\frac{d_m}{2} - r'_{W,i} \cdot cos\alpha_i) \cdot a_2}} \qquad (1)$$

with:

$$a_1 = cos\beta \cdot cos\beta' \cdot cos\alpha_i + sin\beta \cdot sin\alpha_i$$

$$a_2 = cos\beta \cdot cos\beta' \cdot cos\alpha_o + sin\beta \cdot sin\alpha_o$$

For simplification, there are the theories of outer race control (ORC) and inner race control (IRC) of the balls at the raceways [13]. The theories represent limiting values while assuming a pure rolling at the respective

control type at the inner or outer contact. At high speeds and low loads, an ORC is likely due to the higher load in the outer contact under the influence of centrifugal forces. Whereas an IRC predominates at low speeds and high loads due to the higher pressures at the inner contact.

In practice, an equilibrium of the inner and outer friction components is achieved so that the position of the rolling axis assumes values between the limit values of the ORC and IRC. Because of the extensive uncertainties to calculate the real rolling axis, the limit values of the ORC (β_{ORC}) and the IRC (β_{IRC}) are to be considered within this experimental analysis. The balls yaw angle β' caused by the gyroscopic moments is assumed to be 0 for simplification [14].

Figure 2 shows the formation of the BaBr.

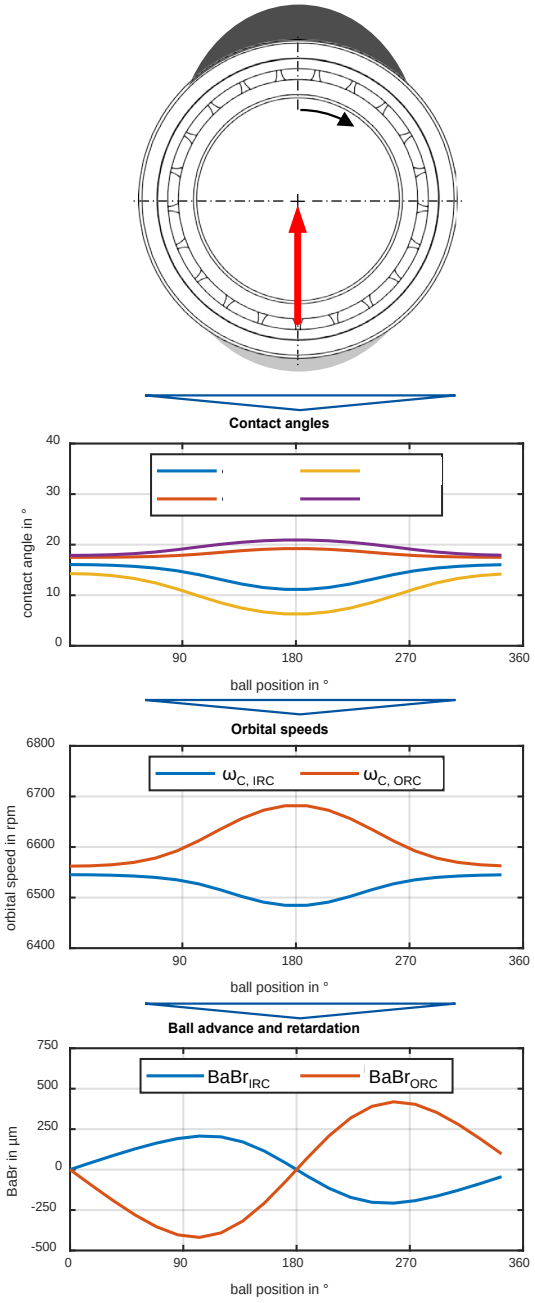

Figure 2: Formation of the BaBr due to radial load

The radial force on the bearing causes an increase of the inner contact angle and a reduction of the outer contact angle mainly in the unloaded zone of the bearing. This process occurs with both ORC and IRC, whereby the contact angle difference is higher in the case of ORC.

According to Eq.(1), the shown orbital velocities for ORC and IRC are obtained. In the loaded zone, the speeds for ORC and IRC show similar values. The speeds in the unloaded zone point in opposite directions. This example shows that knowledge of the actual ball guidance with respect to the angle β is essential for calculating the speeds in the bearing.

Finally, the BaBr over the bearing circumference is calculated by integrating the speeds. Using the IRC as an example, the leading balls are behind the loaded zone and the trailing balls are behind the unloaded zone.

The maximum permissible BaBr is limited by the cage geometry. Hence, Figure 3 shows schematically the positions of the balls, the cage and the outer ring in a load-free and radially loaded state. The example shown is based on an outer ring guided cage corresponding to the test bearing used.

The cage, which is concentric in the initial state, has a clearance of half the cage guidance clearance in radial direction. Accordingly, the balls in the initial state have a clearance of half the cage pocket clearance in tangential direction.

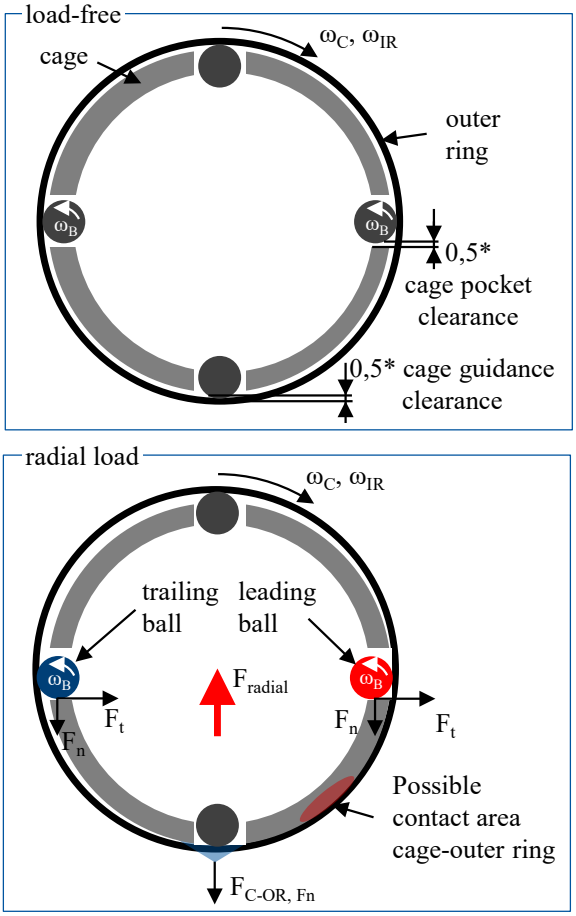

Figure 3: Ball-cage-outer ring interactions

Under the influence of a radial force, the ball behind the load zone may be leading and the ball behind the unloaded zone may be trailing. Therefore, both balls

move downward by half the cage clearance and contact the cage with the normal force F_n.

The cage in turn moves downwards due to F_n until it is guided by the outer ring with the force $F_{C\text{-}OR,\ Fn}$. The two balls are therefore displaced downwards each with half the cage guidance clearance in addition.

The maximum BaBr is the difference between the leading and trailing ball and thus the sum of the cage guidance clearance and the cage pocket clearance. Due to F_n in the ball-cage contacts and the rotation of the balls ω_B relative to the cage, frictional forces F_t act tangential on the cage. The absolute displacement of the cage for the given example is therefore assumed to be in the marked contact area.

3. Measuring setup and test bearing

3.1. Measuring System

The requirements on the system for measuring the BaBr are a precise measurement of the orbital ball positions at high speeds and a good integratability into a test rig or a spindle without affecting its function. Only in this case, measurements with external test forces or in the machine with process forces are possible. Other systems like a high speed camera do not allow this level of integration.

The measuring system is based on the principle of a through beam light barrier (Figure 4).

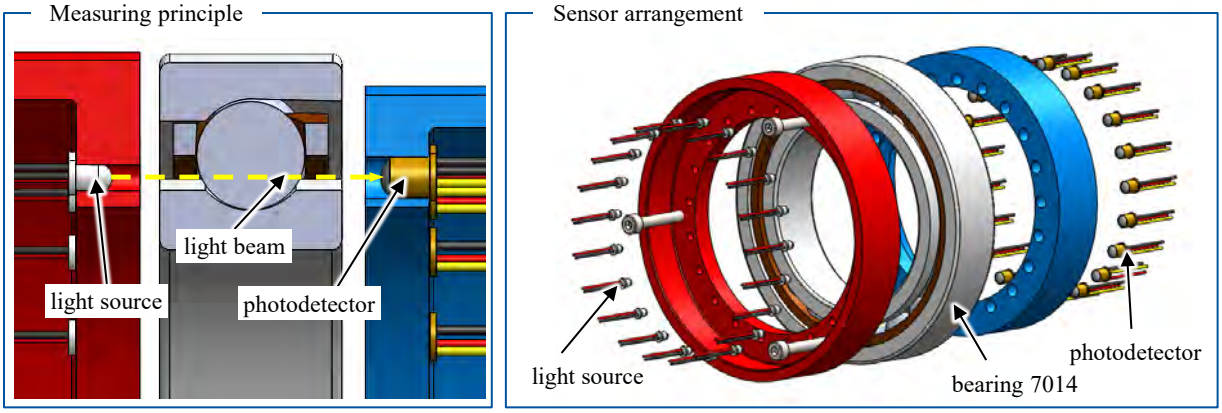

Figure 4: Measuring system

Light sources are used to illuminate the bearing in the area between the inner ring and cage. The light beams are intermittently blocked by the balls. Opposing photodetectors measure these light signals and provide information as to whether a rolling element is in the light beam or not. With this information, the respective position of a rolling element can be calculated. To determine the position, the mean value between the times when a rolling element block and unblock the light beam is used.

To achieve a precise determination of the rolling element position, the photodetectors have a very short circuit time between the bright-dark (270 ns) and the dark-bright (120 ns) transitions. The flanks of these signals must be detected very accurately in time due to a high sampling rate. The signals are therefore sampled at a high frequency of 5 MHz (200 ns between two samples), which is in the range of the sensor switching times. For the used bearing (Table 1), a resolution of 4 µm of the orbital ball positions at the sensor locations can be theoretically achieved at a speed of 10,000 rpm (cage frequency ≈ 71.7 Hz). The measurable resolution just depends on the sampling frequency. The lubrication (e. g. oil film thickness) in case of oil-air lubrication will not significantly affect the accuracy of the measurement. The oil film is thin in comparison to the mentioned resolution and the detection method (mean value between the times when a rolling element block and unblock the light) averages effects like oil film thickness or variable orbits of the balls.

The absolute positions of the photodetectors deviate from the respective ideal positions due to a misalignment of the sensors in the detector ring as well as internal sensor tolerances.

If a ball is now detected at a sensor position, the actual position of the rolling element is displaced by the misalignment of the sensor. To compensate these deviations, the misalignment of the sensors is determined by means of a suitable reference run without radial force, in which no BaBr occur. For this purpose, the movement of a ball around the bearing axis, i.e. passing through all sensors consecutively, is observed. Assuming a uniform movement of the ball around the bearing axis with no BaBr, the detected times (corresponding to the position of the balls at the sensor positions) must have an equal distance.

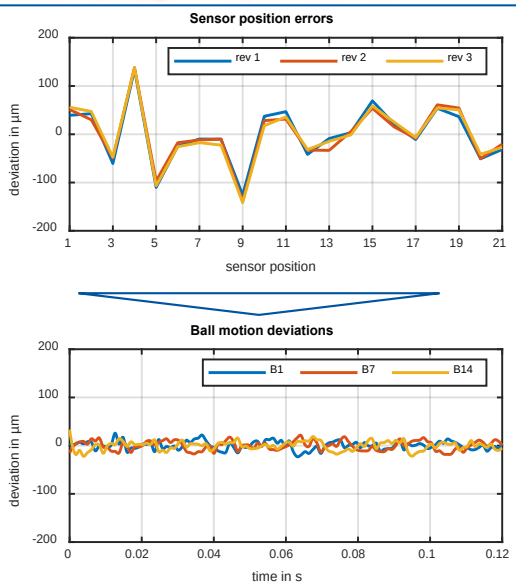

Figure 5: Correction of the sensor position errors

Table 1: Characteristics of the test bearing

Bearing characteristics	
inner diameter: 70 mm	ball diameter: 11.906 mm
outer diameter: 110 mm	pitch diameter: 90 mm
width: 20 mm	cage pocket diameter: 12.5 mm
contact angle: 19°	number of balls: 21

The deviation from the mean value over all detection intervals at each sensor position describes the respective sensor misalignment.

Figure 5 shows the calculated sensor position errors for three revolutions (rev1, rev2, rev3) and the corrected deviations in ball motion for ball 1, 7 and 14 (B1, B7 and B14). The motion of the observed ball in the radial load-free state shows a recurring course over all revolutions. Therefore, the deviation determined at each sensor indicates the sensor position error. As expected, the signals of the ball motion deviations show an even course after correction.

3.2. Test bench and bearing characteristics

The design of the test bench is comparable to an externally driven main spindle. Figure 6 and Figure 7 show the test bench and the bearing arrangement of the spindle including the force ratio of the load unit to the test bearing. The oil-air lubricated test bearing in hybrid design is elastically adjusted against the floating bearing with an axially acting, adjustable hydraulic preload unit. The maximum rotational speed is 30,000 rpm. The spindle can be loaded during operation by a hydraulic actuator acting in radial direction from 0 N to 3,000 N. The resulting maximum radial force at the test bearing is 4,500 N. The force is applied by a load unit and is monitored with an integrated force sensor.

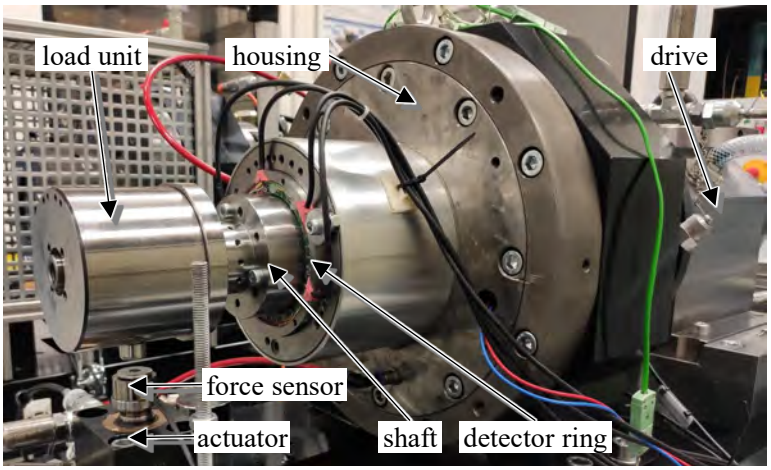

Figure 6: Test bench and measuring system

The rotation of the spindle is separated by a further spindle bearing package inside the load unit and thus enables the tactile application of force to the rotating spindle.

The axial preload force acting on the test bearing is adjusted via the axial preload unit. The geometry of the test bearing is listed in Table 1.

The bearing corresponds to size 7014 with large ceramic balls. The cage pocket clearance is approximately 600 µm and the cage guidance clearance is approximately 500 µm. Therefore, a maximum BaBr of 1.100 µm is expected.

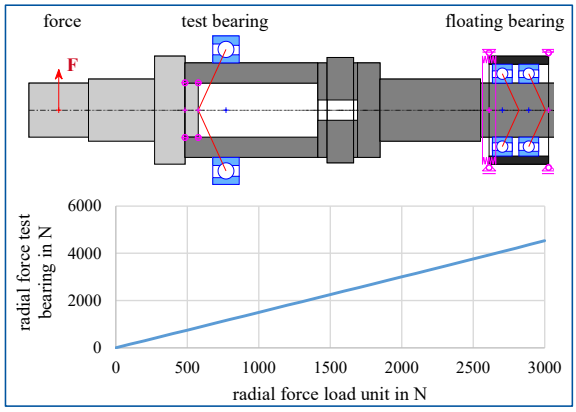

Figure 7: Model of the test bench and force ratio of the load unit to the test bearing

Figure 8 shows the inclination of the bearing rings (angular misalignment) for the forces investigated. The inclination shows a non-linear course from a certain radial force in case of an axial force of 500 N and 1,000 N.

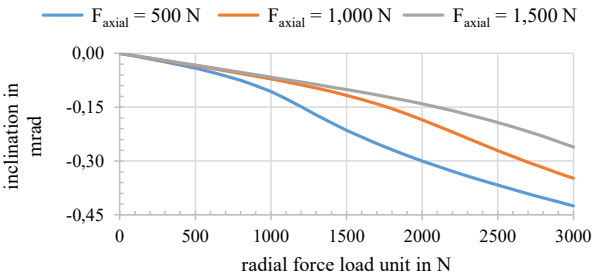

Figure 8: Calculated inclination of the bearing rings for various radial and axial forces at a speed of 9,000 rpm

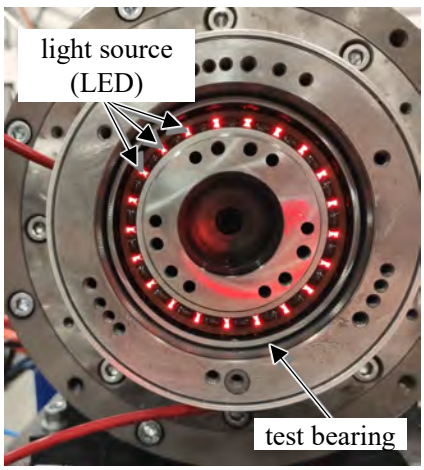

Thus, changes in the bearing kinematics can be expected at radial forces of 1,000 N (F_{axial} = 500 N) and 1,750 N (F_{axial} = 1,000 N).

4. Test procedure and results

4.1. Procedure

During the investigations, the BaBr are measured under different speeds and loads. The speed is increased in steps of 3,000 rpm up to 30,000 rpm for each load condition. The radial force on the load unit is increased in steps of 250 N from 0 N to 3,000 N, whereby the axial preload is varied parametrically from 500 N to 1,000 N and 1,500 N. The radial force direction and therefore the position of the loaded and unloaded zones is in accordance with the calculations in Figure 2.

Even at the maximum speed of 30,000 rpm, the photodetectors show reliable signals without significant false detections, thus ensuring the effectiveness of the system.

4.2. Results

The orbital velocity of the balls around the bearing axis is the decisive factor for the BaBr. Therefore, the orbital speeds for a rotational speed of 15,000 rpm, an axial preload of 1,000 N and varying radial forces of 0 N, 1,000 N, 2,000 N and 3,000 N are analyzed first (Figure 9 to Figure 12).

The measured values for the orbital speeds are compared to the calculated values for the ORC and IRC. Furthermore, the outer and inner contact angles αo and αi as well as the outer and inner contact pressures σo and σi are shown in order to relate these to the measured speeds.

In the radial load-free state (Figure 9), the speed curve shows an expected uniform behavior over the bearing circumference. Due to the high speed, the measured speed is closer to the ORC and follows the results of Roissant [3].

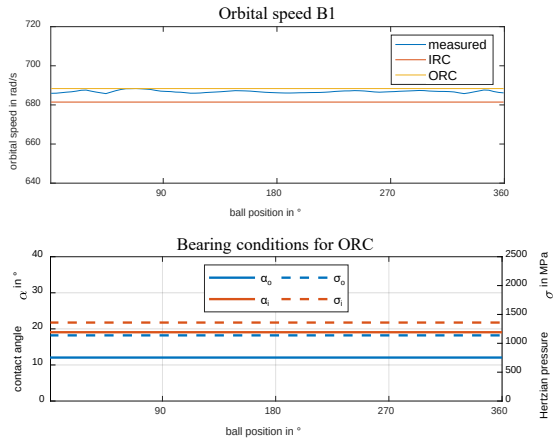

Figure 9: Orbital speeds and contact conditions for: n = 15,000 rpm, axial force = 1,000 N, radial force = 0 N

At the radial force of 1,000 N, the pressures and contact angles do not indicate critical values (Figure 10). In the unloaded zone there are already high deviations between the orbital velocity calculated according to ORC and IRC. In contrast, the measured speed shows a balanced course. When entering the load zone (approximately 270°) the ball experiences an increase in speed and follows the ORC.

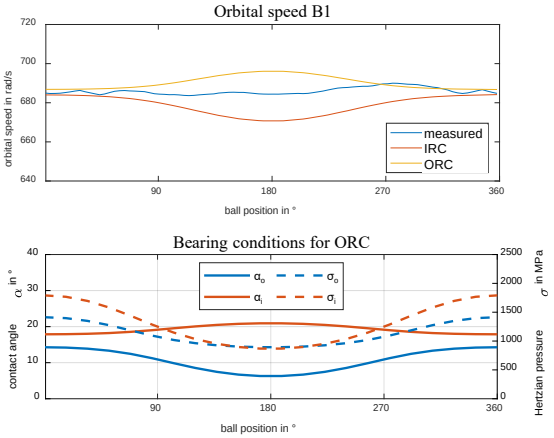

Figure 10: Orbital speeds and contact conditions for: n = 15,000 rpm, axial force = 1,000 N, radial force = 1,000 N (1,500 N at bearing)

At a radial force of 2,000 N (Figure 11), the pressure on the inner contact and the contact angle on the outer contact indicate that the balls in the unloaded zone lift off the inner ring. Due to this high contact angle shear, the speeds calculated according to ORC and IRC also show high deviations in the unloaded area. In the loaded zone (<90°), the balls indicate an increased IRC. According to the IRC, the balls are continuously decelerated up to 120°. At this point, the balls lose contact with the inner ring and don't follow the kinematic guidance any more.

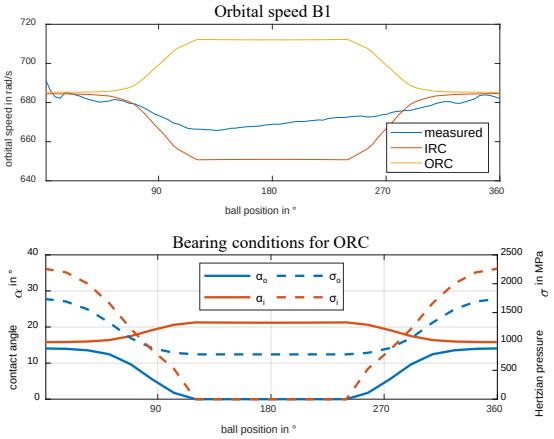

Figure 11: Orbital speeds and contact conditions for: n = 15,000 rpm, axial force = 1,000 N, radial force = 2,000 N (3,000 N at bearing)

Theoretically, the balls must therefore exhibit a pure ORC in this area. However, due to the lack of drive via the inner contact, the balls cannot follow the increased speed of the ORC. The continuous speed increase from 120° may be due to viscous frictional effects between the ball and the inner ring, which drive the ball slightly.

The measured transition at 120°, from which the speed increases slightly, is in good agreement with the position from which the rolling elements lift off at the inner contact.

At the radial force of 3,000 N (Figure 12), the pressures and contact angles indicate that the balls are lifted from the inner contact over a wide circumferential range.

Contrary to the results with a radial force of 2,000 N, the measured speed no longer follows the IRC in the loaded zone. It takes a more uniform course over the bearing circumference. While there is a slight acceleration of the balls at the radial force of 2,000 N in the unloaded zone, the balls are decelerated at the radial force of 3,000 N in this zone. This may be due to the effect, that the balls lift far from the inner contact so that the inner ring no longer drives the balls. The mass inertia of the balls prevents the balls from abruptly reducing the speed.

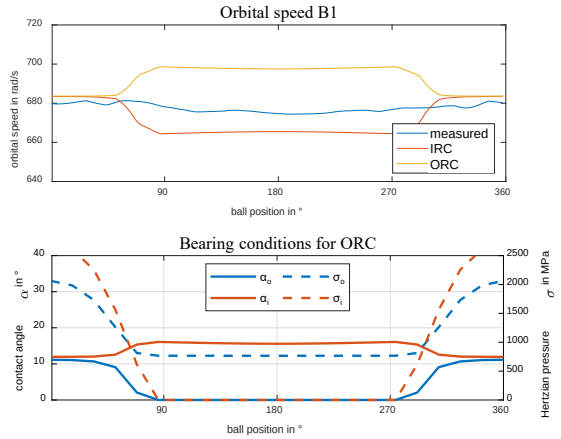

Figure 12: Orbital speeds and contact conditions for: n = 15,000 rpm, axial force = 1,000 N, radial force = 3,000 N (4,500 N at bearing)

An overview of the measured orbital speeds is given in Figure 13. At the speed of 6,000 rpm, the orbital speeds show an even distribution over the bearing circumference in the lower radial force range. At higher radial forces, a field of reduced speed is formed in the unloaded zone.

If the speed is increased to 12,000 rpm, the balls experience a significant acceleration starting at ball positions of 250° when entering the load zone in a radial force range from 1,000 N to 1,750 N. At higher radial forces, a range over the bearing circumference is formed in which the speeds are reduced. At radial forces above 2,500 N, the orbital velocity curve is smoothed again over the bearing circumference.

At a speed of 18,000 rpm, the balls experience an acceleration in the radial force range from 750 N to 1,750 N when leaving and entering the load zone. These increased speeds indicate a stronger ORC (cf. Figure 11)

The speeds at 24,000 rpm show a uniform curve over the entire radial force range, so that BaBr are low here.

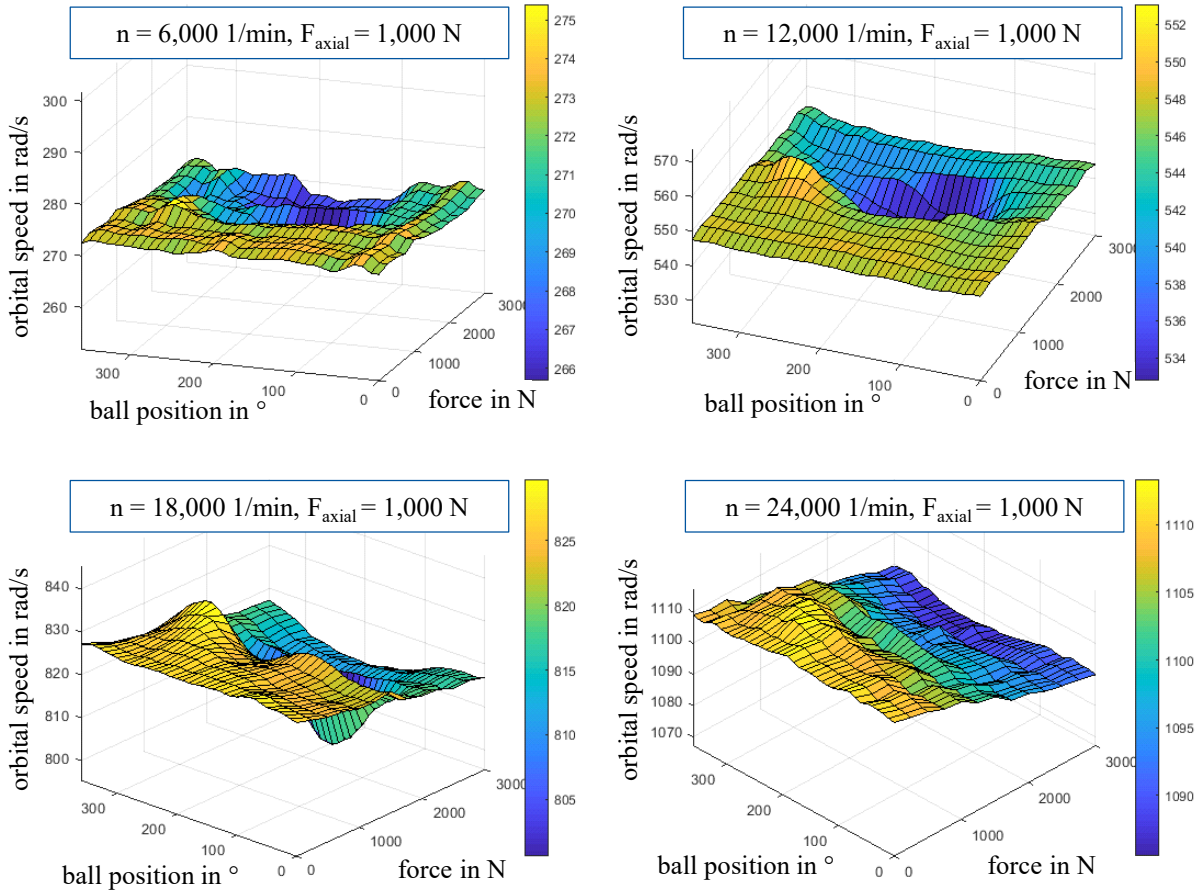

Figure 13: Orbital speeds under various rotational speeds

The deviations of the individual angular ball positions (ball 1 to 21) from the average are shown in

as an example for a speed of 9,000 rpm with an axial force of 1,000 N. The figure shows time sections of a continuous orbital motion of the rolling element set. At a radial force of 1,000 N, a range from B11 to B16 is already formed with small leading motion behind the loaded zone in direction of rotation.

With an increasing axial force, this plateau-shaped field with maximum BaBr values widens and occurs at higher speeds and radial forces. The values for the BaBr in these plateau-shaped fields correspond to the presumed BaBr of 1,100 µm and lead to contacts between the cage and the balls. If the radial force exceeds a certain value at an axial force of 500 N and 1,000 N, the BaBr decrease again. This can be explained by the

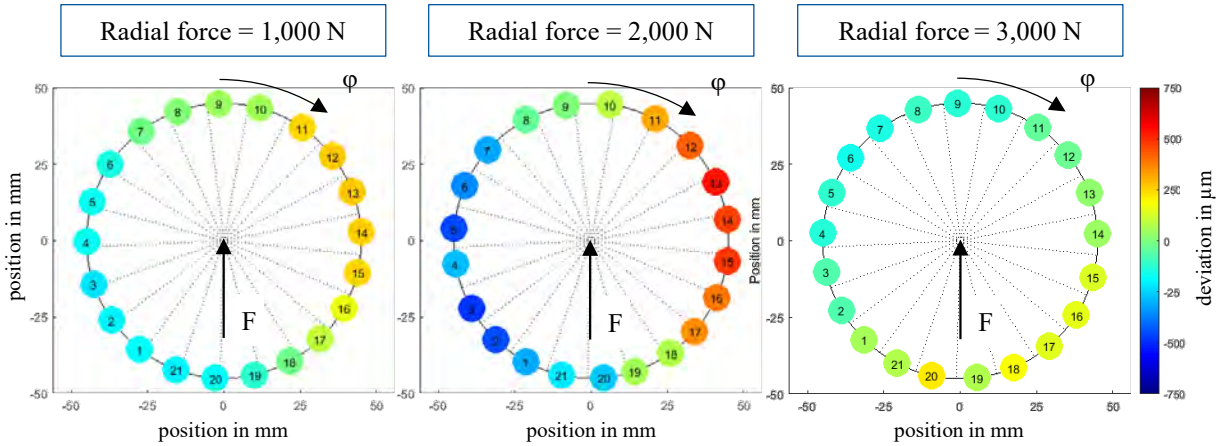

Figure 14: Ball motions for: n = 9,000 rpm, axial force = 1,000 N, radial force = 1,000 N, 2,000 N, and 3,000 N

From B19 to B6 there is a small trailing of the balls. An increase of the radial force to 2,000 N results in significant leading of the balls in the range from B11 to B17. The corresponding trailing motion is noticeable from B20 to B7. The difference of the highest values for the leading and trailing motions are in the range of the expected maximum possible BaBr with approximate 1,100 µm. Remarkable contact forces between the cage and the balls can be expected in this load case. If the radial force is increased to 3,000 N, the values for the leading and trailing motions decrease again. The figure also shows that the areas with maximum advance and retardation are shifted in direction of rotation with increasing radial forces.

Figure 15 shows the BaBr values for each examined operating point. The specified BaBr describe the difference between the maximum advance and retardation over all balls.

At an axial force of 500 N, high BaBr values only occur in a narrow force range from 1,000 N to 1,250 N at speeds above 6,000 rpm.

loss of contact between the balls and the inner race on the unloaded bearing side and thus an undisturbed ORC without forced guidance of the balls between inner and outer race. The results are in accordance with the calculated inclination (Figure 8), which shows a significant nonlinearity at 1,000 N (F_{axial} = 500 N) and 1,750 N (F_{axial} = 1,000 N). In general, the results point out that towards high speeds the BaBr are lower than at low speeds.

At the highest axial force of 1,500 N, the BaBr values are low for the entire speed range up to a radial force of approximate 1,750 N. The high axial preload has a positive influence on the kinematics of the bearing, resulting in the lower BaBr values. From a radial force of approximate 2,000 N, however, there is a wide range of maximum BaBr values over the entire radial force range and even at higher speeds. It is likely that in the plateau-shaped area, the movements of the balls are strongly limited by the cage, such that a high cage load is present.

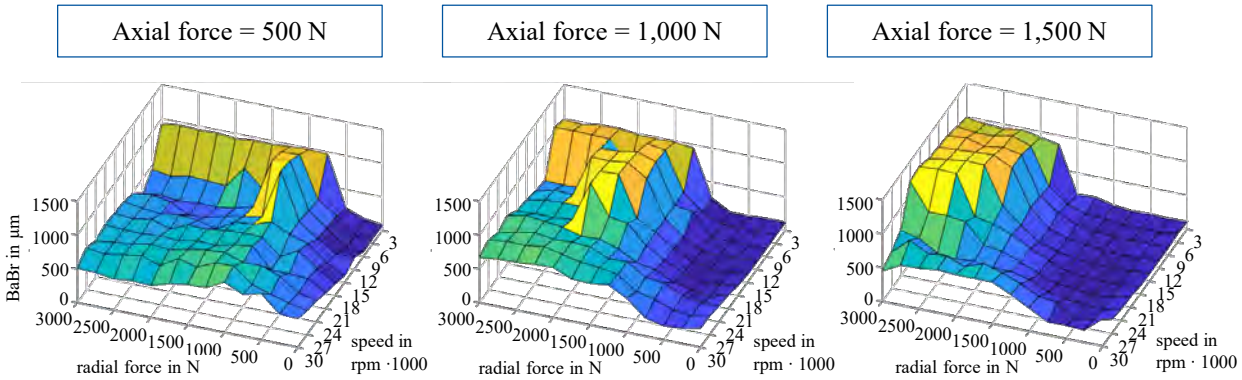

Figure 15: Ball advance and retardation for various loads

Conclusions

A photoelectric system to measure the BaBr was developed and installed in a test bench. The test bearing was subjected to different axial and radial forces. The investigations were performed with rotational speeds up to 30,000 rpm.

The results show, that up to a certain radial force, the BaBr increase at low to medium speeds. In this speed and force range, the values show comparable values to the expected maximum BaBr of 1,100 µm, so that a high load on the cage can be expected. Because the balls lift off the inner contact in the unloaded zone, the value decreases if a certain radial force is exceeded.

The radial force range, where the BaBr increase and decrease is strongly influenced by the axial preload. At higher speeds, the BaBr takes on smaller values again.

In future work, the system will be expanded to include the radial and rotatory position measurement of the cage, so the effects between balls and cage can be examined in detail. Further measurements of the BaBr will be carried out with dynamic, process-like loads and in a milling machine during machining.

Acknowledgment

Supported by Federal Ministry for Economic Affairs and Energy on the basis of a decision by the German Bundestag. The Authors would like to thank the German Federation of Industrial Research Associations (AiF) and the German Machine Tool Builders' Association (VDW) for financial support of the project 18900 N.

Funded in addition by the German Research Foundation (DFG) - Project-ID 174223256-TRR 96 / T01.

References

[1] Wang, Y, Wang, W, Zhang, S., Zhao, Z. (2015): Investigation of skidding in angular contact ball bearings under high speed. Tribology International, 92:404–417.

[2] Kannel, JW, Merriman, T (20.08.1980): SSME TURBOPUMP BEARING ANALYTICAL STUDY, Columbus, Ohio.

[3] Rossaint, J (2013): Steigerung der Leistungsfähigkeit von Spindellagern durch optimierte Lagergeometrien. Dissertation, Werkzeugmaschinenlabor WZL der RWTH Aachen, RWTH Aachen.

[4] Choe, B, Lee, J, Jeon, D, Lee, Y (2019): Experimental study on dynamic behevior of ball bearing cage in cryogenic environments, Part i: Effects of cage guidance and pocket clearances. Mechanical Systems and Signal Processing, 115:545–569.

[5] Kingsbury, E, Walker, R (1994): Motions of an Unstable Retainer in an Instrument Ball Bearing. Transactions of the ASME, 116:202–208.

[6] Falkon, KC, Andrew C. (1969-70): Angular contact ball bearings: Track position at high speeds. Proceedings of the Institution of Mechanical Engineers, 184(19):351–370.

[7] Haines, DJ (1970-71): Second Paper: Observations of ball to track contact angles and inclination of ball rolling axis in an angular contact ball race. Proceedings of the Institution of Mechanical Engineers, 185 30/71:366–372.

[8] Krimpmann, M, Vesselinov, V, Weber, J (2002): Numerische und experimentelle Analyse der Kinematik von Rollenlagern. VDI-Berichte, 1706:377–398.

[9] Kakuta, K (1964): The Effects of Misalignment on the Forces Acting on the Retainer of Ball Bearings. Journal of Basis Engineering, (86):449–456.

[10] Holland, L (2018): Analyse des Bewegungsverhaltens der Komponenten in Spindellagern mittels Hochgeschwindigkeitsvideographie. Dissertation, Technische Hochschule Darmstadt.

[11] Harris, TA, Kotzalas, MN (2007): Essential Concepts of Bearing Technology. 5. Auflage. CRC Press.

[12] Falker, J (2020): Analyse des Betriebsverhaltens von Hochgeschwindigkeits-Wälzlagern unter radialen Lasten. Dissertation, Werkzeugmaschinenlabor WZl der RWTH Aachen, RWTH Aachen.

[13] Jones, AB (1960): A General Theory for Elastically Constrained Ball and Radial Roller Bearings Under Arbitrary Load and Speed Conditions. Journal of Basis Engineering, 82(2):309–320.

[14] Steinert, T (1995): Das Reibmoment von Kugellagern mit bordgeführtem Käfig. Dissertation, Werkzeugmaschinenlabor WZL der RWTH Aachen, RWTH Aachen.

Microinclusions Impact on Steel Balls Fatigue Life

S. Rizzo[1], F. Morosi[1], R. Sesana[2], E. Ossola[2], E. Brusa[2]

[1] *Central Lab – Product Development, Tsubaki Nakashima, Italy*
[2] *DIMEAS, Politecnico di Torino, Italy*

Abstract – Rolling contact fatigue is the main cause of failure in bearings. Among other factors, damage phenomena are related to material properties and manufacturing processes. The damage evolution might be affected by microinclusions present in the material. This influence is related to composition, dimension, shape and location of microinclusions. The relation between microinclusions and fatigue life is investigated for balls undergoing Hertzian pressure fatigue for 100Cr6 steel. Failures are analysed to relate life of rolling elements to the microinclusion parameters.

Keywords – Bearing, Microinclusion, Rolling contact fatigue

1. Introduction

Bearing fatigue life is affected by several damage phenomena, including tribological conditions, surface and sub-surface defects and environmental conditions (temperature, corrosion and humidity) [1]. In optimal working conditions, the main cause of damage is Rolling Contact Fatigue (RCF) [2], which involves surface pitting and subsurface spalling. The main factor affecting sub-surface RCF damage is related to non-metallic inclusions, where the Hertzian contact shear stress is maximum [3]; in fact, inclusions act as stress risers, promoting crack initiation and propagation [4]. For this reason, steelmaking processes have improved steel cleanliness over the last decades [5,6], in order to control non-metallic inclusions (NMI) and oxides [7].

The effect of inclusions on fatigue life, considering the effect of size, shape, location and composition, is described in many studies [8–11]. In [12], experimental and numerical activities explored the stress state in the material around the inclusion, where microstructural changes were observed, referred as "butterfly wings".

Different inclusion sizes (ranging from 8 to 16 μm) were studied, but no strong influence on stress concentration was found. This result is partially in agreement with Gabelli et al. [13], who found that defects smaller than a threshold do not affect fatigue life of high strength steels for bearing manufacturing. In [14], basing on the Eshelby method, the interaction between multiple inclusions (pairs, clusters and stringers) was investigated. This paper presents an investigation on the effect of microinclusions on fatigue performance of a steel alloy (100Cr6) for rolling element manufacturing. This steel is defined in international Standards as UNI 3097 and DIN 17230 as 100Cr6, AISI/SAE as 52100, AFNOR 35-565 as 100C6. Many researches are dedicated to this steel, both with experimental and numerical approaches [7, 13, 15].

The purpose of the present paper is to correlate the bearing life and the incremented stress related to non-metallic inclusions presence in the subsurface of rolling balls during fatigue conditions. Microinclusions composition, shape, aspect ratio, geometry and location are obtained after the ball failure. An analytical model was implemented in a numerical dedicated solver, to relate life of rolling elements to the microinclusion parameters. A dedicated 3D model implementing Eshelby model [16] was developed to estimate the stress distribution around the microinclusion. This analysis introduces new contribution in the improvement of the quantitative estimation of bearing balls life. In particular the quantitative estimation of stress increment due to parameters related to microinclusion is included in life estimation. The estimations are then compared to actual failure cases.

2. Materials and methods

The fatigue performances of rolling elements have been evaluated by rig tests. Twelve cases of failures obtained under identical conditions were taken into account. Rig tests are structured with an electrical motor that drives a rotating shaft on which the inner rings of two double row ball bearings are trapped (figure 1) (inner ring curvature radii R2x = 22.250 mm and R2y = - 6.322mm). The rotary motion of the outer rings was prevented by the external fluted shell. The applied load was purely axial (34.4 kN) and it was guaranteed by a pneumo-hydraulic pistons system; tested bearings were assembled with 7 balls with diameter of 11.112 mm. The maximum pressure obtained on the ball surface from Hertz theory is of 3.8 GPa and the material is 100Cr6 steel. A correct lubrication status was guaranteed by the application of mineral grease. Once reached the ball failure, the evaluation of microinclusion effect on stresses was performed; the Eshelby-Mura model was applied to estimate the stress field surrounding each single microinclusion that was found in the spalling starting point. The stress modification due to a microinclusion is affected by its size, shape and location. Experimental evidence shows that inclusions can appear in pairs, clusters and stringers. The ASTM E45 Standard [17] provides a description for the stringer case, which is considered with a minimum of three particles. In this case, the stringer can be considered as a standalone inclusion with an elongated semi axis that covers the distance from the first to the

last inclusion. In addition, the stress peak at the inclusion boundary is affected by the depth at which the inclusion is located.

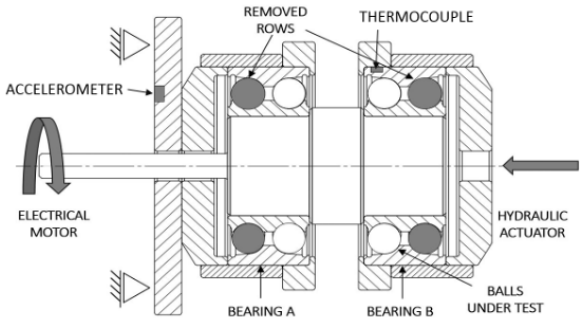

Figure 1: scheme of the test rig

3. Results and discussion

Twelve broken balls coming from the test were analized. In five cases, more than one inclusion was found in the fractured area; it was decided to consider only the one corresponding to the major increase of stress, since it was the worst from the fatigue life point of view. In addition, if inclusions with different chemical compositions were detected, a weighted average of Young's modulus and Poisson's ratio were used in the following calculations.

In figure 2, the nominal stress distribution obtained from the Hertz theory for a homogenous matrix is reported; and then for each single microinclusion, the corresponding calculated stresses were corrected taking into account for the composition, location and dimension of the inclusions experimentally found, by means of the Eshelby code. In particular a dedicated numerical solver was implemented in Matlab environment implementing the Eshelby equations to obtain the stress in the matrix volume around the microinclusion, given dimension, shape, material and position of the microdefect. Results are reported in Table 1. In the same table the calculation of the equivalent Tresca stresses [18] in uniform matrix σ_{nT} and at microinclusion boundaries with Eshelby's model σ_{iT} are reported for each microinclusion, accounting for dimension,

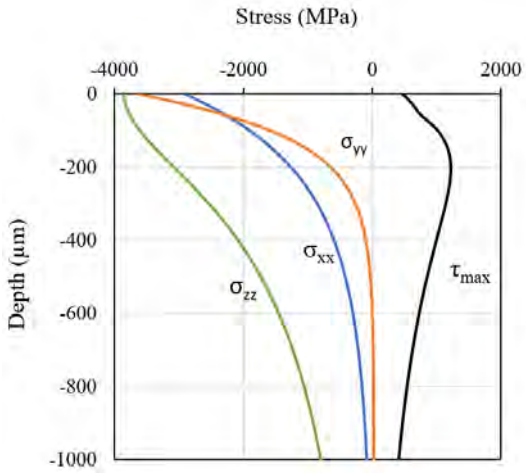

Figure 2 - Subsurface stress distribution under testing conditions (z: radial axis, y and x orthogonal axes)

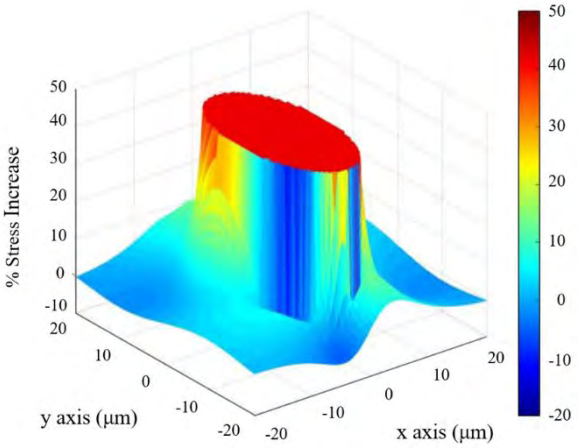

Figure 3 - Simulation of stress distribution around NMI in ball. Case 3 of the 12 failures investigated

shape, aspect ratio, position, and elastic modulus. The percent increment in stress is also reported.

The numerical stress simulation shows a stress gradient in the matrix volume surrounding the microinclusion related to a failure case (see Fig. 3 as an example).

The stress increment due to the microinclusions varies from 17% to 51% for the investigated failure cases.

In Fig. 4 a plot reports nominal (blue curve) subsurface equivalent stresses, calculated considering the contact force on a single ball due to the nominal experimental axial load (34400N). In the same plot, other curves are reported, representing the ideal stresses generated for increasing forces (Hertz load). The blue dots represent the nominal stress for each failed ball, in the point here the crack nucleated. Applying the Eshelby-Mura model, the stress increment due to the microinclusion experimentally found was evaluated (grey arrows). It can be observed that the presence of a microinclusion somehow "extends" the sub superficial volume where stresses become dangerous for crack nucleation in rolling contact fatigue.

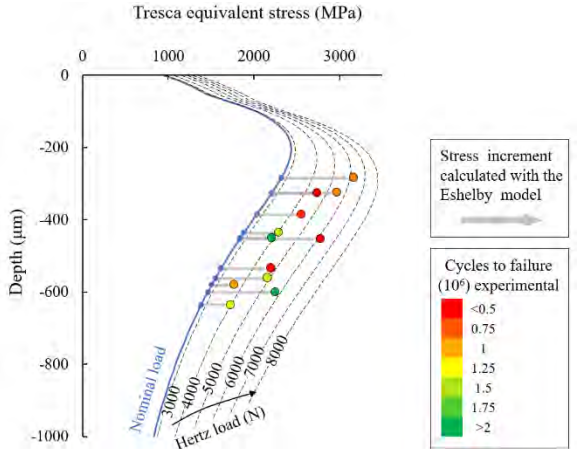

Figure 4 - Subsurface Tresca equivalent stresses calculated with and without microinclusions

This information stresses the critical importance of accounting quantitatively for all the parameters related to microinclusions (shape, dimension, aspect ratio, elastic modulus) and not only of its position for a correct

stress distribution calculation. Further information can be obtained from these results.

In Table 2 the calculated equivalent loads and L_{10} for failed balls are reported. L_{10} parameters are obtained according to Zaretsky model [19]. In rows, the different balls; N_L is the axial load applied to the bearing in the test rig during experimental testing; P_{eqn} is the nominal equivalent axial load, calculated according to catalogue indication for the estimation of the nominal L_{10} (i.e. 0.66 times the axial force acting on the bearing); T_L is the axial force that would produce in a homogeneous matrix the same Tresca stress that is due to the microinclusion, according to Eshelby; L_H is the Hertz load, i.e. the contact load applied to a single, homogeneous ball, generating at the microinclusion depth the same Tresca stress due to microinclusions; L_{10n} is the L_{10} nominal value calculated using the P_{eqn} value, i.e. without considering the effect of microinclusions; in the last column the cycles to failures N_f are reported. It can be observed that failures occurred for microinclusion positioned at depths for which the nominal stress is lower than the maximum nominal stress at the critical depth (2435 MPa @0,205 mm). for 5 over 12 specimens the calculated incremented stress is higher than the maximum nominal one. For the 7 other cases the incremented stress is in the range of 9 and 30% less than the maximum nominal stress at critical depth. The deepest microinclusion which caused failure occurred at 0,636 mm. The estimation of the incremented stress seems to be helpful in identifying a depth interval where microinclusion occur to be critical. This analysis can be extended to other parameters characterizing the microinclusion. A representative example is the shape: if the inclusion can be approximated as an elongated ellipse, the stress peak increment is greater.

This observation is supported by a wide range of inclusion types found in balls, with also different shapes and dimensions.

In [20] a further detailed analysis of the experimental results is reported.

In Figure 5 a failure surface including a microinclusion is reported

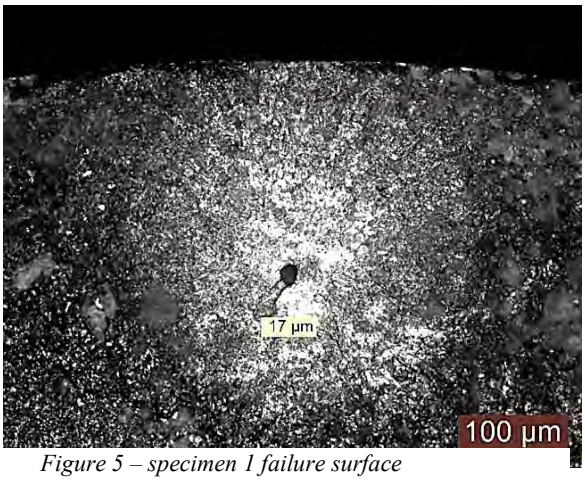

Figure 5 – specimen 1 failure surface

Table 1 - Microinclusions data and calculation results

ID	Composition	Dimension [µm]			Depth	Aspect ratio	σ_{nT}	σ_{iT}	σ_{inc}
		x	y	z	[µm]	xy	MPa	MPa	-
1	TiC (Ti carbide)	1.7	4.3	1.7	-453	0,40	1836	2776	51%
2	Al2O3 (Al oxyde)	1.7	2.7	1.7	-562	0,63	1550	2158	39%
3	Al2O3 (Al oxyde)	7.0	49.0	7.0	-600	0,14	1462	2245	54%
4	Al2O3 (Al oxyde)	12.5	12.5	12.5	-284	1,00	2320	3160	36%
5	TiC (Ti carbide)	4.5	4.5	4.5	-436	1,00	1886	2290	21%
6	Al2O3 (Al oxyde)	12.3	10.0	10.0	-326	0,81	2210	2969	34%
7	Al2O3 (Al oxyde)	3.5	2.0	2.0	-450	0,57	1846	2206	20%
8	Al2O3 (Al oxyde)	2.5	0.5	0.5	-636	0,20	1384	1728	25%
9	Al2O3 (AL oxyde)	4.0	1.0	1.0	-386	0,25	2034	2552	25%
10	CaO (Ca Oxide)	4.0	2.0	2.0	-580	0,50	1508	1768	17%
11	Al2O3 (Al oxyde)	7.5	7.5	7.5	-535	1,00	1616	2200	36%
12	Si+Al+Ca	15.0	15.0	5.0	-327	1,00	2208	2737	24%

Table 2 – Calculated equivalent loads for failed balls

ID	N_L [N]	P_{eqn} [N]	T_L [N]	L_H [N]	L_{10n} (10^6 cycles)	N_f (10^6 cycles)
1	34400	22704	74445	6100	1.51	0.46
2	34400	22704	59800	4900	1.51	1.4
3	34400	22704	39053	3200	1.51	1.94
4	34400	22704	75666	6200	1.51	0.87
5	34400	22704	48817	4000	1.51	1.45
6	34400	22704	67123	5500	1.51	0.46
7	34400	22704	47596	3900	1.51	3.75
8	34400	22704	48817	4000	1.51	1.28
9	34400	22704	53698	4400	1.51	0.61
10	34400	22704	45155	3700	1.51	0.97
11	34400	22704	58580	4800	1.51	0.54
12	34400	22704	54919	4500	1.51	0.87

4. Conclusions

The target of the activity was to evaluate the influence of microinclusions on the fatigue life of rolling balls, accounting for shape, dimension, aspect ratio, location, and Young's modulus of microinclusions. For this reason, the effect on the stress field of balls made of 100Cr6 was investigated.

Many sets of balls were tested in bearings thanks to a dedicated test rig. Furthermore, the fracture analyses were assessed thanks to a gauge meter, an optical microscope, and a Scanning Electron Microscope.

A numerical solver that implements the Eshelby solution for the inclusion problem was developed to analyze the cases above. Some simulations were made to understand the functionalities of the code and the effect of the different parameters: dimension, shape, depth, chemical composition, and configuration were evaluated. Moreover, the code was useful to simulate the stress state of the experimental cases.

Twelve failed balls were considered, for each case all the inclusion properties were found and the stress state around microinclusion was evaluated.

The survey pointed out that inclusions that are shallower than a certain value are not critical for failures, according to [13], and at the same time, no inclusions close to the surface were found, according to the Hertz theory. These aspects suggest that there is a defined depth range for which the inclusion, together with its own properties, is critical.

Further discussion and further development of this approach can follow, considering that the elastic modulus of the matrix changes during damaging processes, according to [3], and thus the estimation of Tresca stress by means of Eshelby model should take into account of this evolving phenomenon or, according to [3], couple the stress fields due to microinclusion and to Hertzian contact. Also, the interaction between microinclusions can be modelled in a more detailed way, above all in the case they have different compositions.

Nomenclature

σ_{nT} *equivalent Tresca stress at microinclusion location*

σ_{iT} *equivalent Tresca stress at microinclusion boundary according to Eshelby model*

σ_{inc} increment of stress from nominal stress without inclusion and with inclusion)

P_{eqn} nominal equivalent axial load, calculated according to catalogue indication

L_{10} catalogue indication of life in millions of cycles

L_{10n} life in millions of cycles calculated using the P_{eqn} value, i.e. without considering the effect of microinclusions

L_H Hertz load, i.e. the contact load applied to a single, homogeneous ball, generating at the microinclusion depth the same Tresca stress due to microinclusions

N_L axial load applied to the bearing in the test rig during experimental testing

N_f cycles to failures

T_L axial force that would produce in a homogeneous matrix the same Tresca stress that is due to the microinclusion

References

Example:

[1] J. Halme and P. Andersson, “Rolling contact fatigue and wear fundamentals for rolling bearing diagnostics - State of the art,” Proc. Inst. Mech. Eng. Part J J. Eng. Tribol., 2010, doi: 10.1243/13506501JET656.

[2] N. K. Arakere, “Gigacycle rolling contact fatigue of bearing steels: A review,” Int. J. Fatigue, vol. 93, pp. 238–249, Dec. 2016, doi: 10.1016/j.ijfatigue.2016.06.034.

[3] T. Beyer, F. Sadeghi, T. Chaise, J. Leroux, and D. Nelias, “A coupled damage model and a semi-analytical contact solver to simulate butterfly wing formation around non-metallic inclusions,” Int. J. Fatigue, 2019, doi: 10.1016/j.ijfatigue.2019.05.029.

[4] N. Tsunekage, K. Hashimoto, T. Fujimatsu, and K. Hiraoka, “Initiation behavior of crack originated from non-metallic inclusion in rolling contact fatigue,” J. ASTM Int., 2010, doi: 10.1520/JAI102612.

[5] Y. Unigame, K. Hiraoka, I. Takasu, and Y. Kato, “Evaluation Procedures of Nonmetallic Inclusions in Steel for Highly Reliable Bearings,” in Bearing Steel Technology-Advances and State of the Art in Bearing Steel Quality Assurance: 7th Volume, 100 Barr Harbor Drive, PO Box C700, West Conshohocken, PA 19428-2959: ASTM International, 2009, pp. 34-34–8.

[6] F. J. Ebert, “Fundamentals of Design and Technology of Rolling Element Bearings,” Chinese J. Aeronaut., 2010, doi: 10.1016/S1000-9361(09)60196-5.

[7] H. Fu et al., “The relationship between 100Cr6 steelmaking, inclusion microstructure and rolling contact fatigue performance,” Int. J. Fatigue, 2019, doi: 10.1016/j.ijfatigue.2018.11.011.

[8] T. Makino et al., “Effect of defect shape on rolling contact fatigue crack initiation and propagation in high strength steel,” Int. J. Fatigue, vol. 92, pp. 507–516, Nov. 2016, doi: 10.1016/j.ijfatigue.2016.02.015.

[9] K. Hashimoto, T. Fujimatsu, N. Tsunekage, K. Hiraoka, K. Kida, and E. C. Santos, “Study of rolling contact fatigue of bearing steels in relation to various oxide inclusions,” Mater. Des., vol. 32, no. 3, pp. 1605–1611, Mar. 2011, doi: 10.1016/j.matdes.2010.08.052.

[10] Y. Murakami and N. Yokoyama, “Influence of Hydrogen Trapped by Inclusions on Fatigue Strength of Bearing Steel,” in Bearing Steel Technology, 100 Barr Harbor Drive, PO Box C700, West Conshohocken, PA 19428-2959: ASTM International, 2009, pp. 113-113–12.

[11] J. Lai, T. Lund, K. Rydén, A. Gabelli, and I. Strandell, “The fatigue limit of bearing steels - Part I: A pragmatic approach to predict very high cycle fatigue strength,” Int. J. Fatigue, 2012, doi: 10.1016/j.ijfatigue.2011.09.015.

[12] S. M. Moghaddam et al., “Effect of non-metallic inclusions on butterfly wing initiation, crack formation, and spall geometry in bearing steels,” Int. J. Fatigue, vol. 80, pp. 203–215, Nov. 2015, doi: 10.1016/j.ijfatigue.2015.05.010.

[13] A. Gabelli, J. Lai, T. Lund, K. Rydén, I. Strandell, and G. E. Morales-Espejel, “The fatigue limit of bearing steels – Part II: Characterization for life rating standards,” Int. J. Fatigue, vol. 38, pp. 169–180, May 2012, doi: 10.1016/j.ijfatigue.2011.12.006.

[14] J. Courbon, G. Lormand, G. Dudragne, P. Daguier, and A. Vincent, “Influence of inclusion pairs, clusters and stringers on the lower bound of the endurance limit of bearing steels,” Tribol. Int., 2003, doi: 10.1016/S0301-679X(03)00076-8.

[15] M. Oezel, T. Janitzky, P. Beiss, and C. Broeckmann, “Influence of steel cleanliness and heat treatment conditions on rolling contact fatigue of 100Cr6,” Wear, 2019, doi: 10.1016/j.wear.2019.04.026.

[16] J.D. Eshelby, “The determination of the elastic field of an ellipsoidal inclusion, and related problems”, Proceedings of the Royal Society A, pp. 376-396, 1957, https://doi.org/10.1098/rspa.1957.0133

[17] ASTM, “E45-18a Standard Test Methods for Determining the Inclusion Content of Steel,” ASTM Int. Conshohocken, PA, www.astm.org, 2018, doi: 10.1520/E0045-18A.

[18] “Mechanical Behavior of Materials“, Global Edition, V edition, N.E. Dowling et al, Pearson Ed. 2019.

[19] E. V Zaretsky, “Rolling bearing life prediction, theory, and application,” NASA Tech. Reports, 2013.

[20] R. Sesana, E. Ossola, S. Pagliassotto, S. Rizzo, E. Brusa, “Influence of microinclusion in life of rolling elements: Experimental, microstructural, analytical and numerical investigation”, International Journal of Fatigue 139 (2020) 1057.